

Creative Commons Attribution 4.0 International (CC BY 4.0)

<https://creativecommons.org/licenses/by/4.0/>

Access to this work was provided by the University of Maryland, Baltimore County (UMBC) ScholarWorks@UMBC digital repository on the Maryland Shared Open Access (MD-SOAR) platform.

Please provide feedback

Please support the ScholarWorks@UMBC repository by emailing scholarworks-group@umbc.edu and telling us what having access to this work means to you and why it's important to you. Thank you.

Offsets between X-ray and Radio Components in X-ray Jets: The AtlasX

KARTHIK REDDY ¹, MARKOS GEORGANOPOULOS ^{1,2}, EILEEN T. MEYER ¹,
MARY KEENAN,³ AND KASSIDY E. KOLLMANN ⁴

¹*Department of Physics, University of Maryland, Baltimore County, 1000 Hilltop Circle, Baltimore, MD, 21250, USA*

²*NASA Goddard Space Flight Center, Code 663, Greenbelt, MD 20771, USA*

³*ADNET Systems, Inc., Bethesda, MD 20817 USA*

⁴*Department of Physics, Princeton University, Princeton, NJ 08544, USA*

(Received ...; Revised ...; Accepted ...)

Submitted to ApJ

ABSTRACT

The X-ray emission mechanism of powerful extragalactic jets, which has important implications for their environmental impact, is poorly understood. The X-ray/radio positional offsets in individual features of jets provide important clues. Extending the previous work in Reddy et al. 2021, we present a detailed comparison between X-ray maps deconvolved using the Low Count Image Reconstruction and Analysis (LIRA) tool and radio maps of 164 components from 77 Chandra-detected X-ray jets. We detect 94 offsets (57%), with 58 new detections. In FR II-type jet knots, the X-rays peak and decay before the radio in about half the cases, disagreeing with the predictions of one-zone models. While a similar number of knots lack statistically significant offsets, we argue that projection and distance effects result in offsets below the detection level. Similar de-projected offsets imply that X-rays could be more compact than radio for most knots, and we qualitatively reproduce this finding with a ‘moving-knot’ model. The bulk Lorentz factor (Γ) derived for knots under this model is consistent with previous radio-based estimates, suggesting kpc-scale jets are only mildly relativistic. An analysis of X-ray/radio flux ratio distributions does not support the commonly invoked mechanism of X-ray production from inverse Compton scattering of the cosmic microwave background but does show a marginally significant trend of declining flux ratio as a function of distance from the core. Our results imply the need for multi-zone models to explain the X-ray emission from powerful jets. We provide an interactive list of our X-ray jet sample at <http://astro.umbc.edu/Atlas-X>.

Keywords: galaxies: active–galaxies: jets–methods: data analysis–radio continuum:
galaxies–X-rays: galaxies

1. INTRODUCTION

It is now generally agreed that practically all galaxies host a supermassive black hole (SMBH, $M \sim 10^6 - 10^9 M_\odot$) at their centers (e.g., Richstone et al. 1998). A small fraction of SMBHs accrete matter and produce intense radiation that covers up to 20 orders of magnitude in frequency. These Active Galactic Nuclei (AGN) sometimes produce collimated double-sided relativistic jets (e.g. Padovani et al. 2017), which are detected in large numbers in the radio. These jets transport energy from sub-parsec scales of the AGN out to kpc and frequently to Mpc scales, well beyond the host galaxy, and play a crucial role in driving the AGN feedback on the host galaxy and cluster (e.g., Fabian 2012), which may affect how structure in the Universe evolves (e.g., Blandford et al. 2019). However, the total power carried by jets is still not well known.

Despite hundreds of known resolved (arcsecond-scale/kpc-scale) radio jets, there were very few resolved jets detected in the optical and X-rays prior to the advent of the *Hubble* and *Chandra* observatories (e.g., Schreier et al. 1979; Butcher et al. 1980; Biretta et al. 1991; Harris et al. 1994). Since the launch of *Chandra* in 1999, over 150 jets have been detected in the X-rays (e.g., Sambruna et al. 2004; Marshall et al. 2005; Massaro et al. 2015) showing in many cases X-ray knot structure roughly coincident with the radio. These detections of jet knots and terminal ‘hot spots’ stimulated optical observations with the Hubble Space Telescope (HST) resulting in over 3 dozen optical jet detections (e.g., Sambruna et al. 2004; Tavecchio et al. 2007; Kharb et al. 2012; Harris et al. 2004a)

For most low-power jets, with the typical ‘plumey’ and edge-darkened Fanaroff & Riley (1974) class I (FR I) morphology, the level and spectrum of the knot X-ray emission seems to be a smooth continuation of the radio to optical synchrotron spectrum (e.g., Marshall et al. 2002; Worrall et al. 2003; Hardcastle et al. 2003, but see Meyer et al. (2018) for a counter-example). In contrast, the powerful, highly-collimated and edge-brightened FR II-type jets exhibit puzzling X-ray characteristics, seen first in the powerful source PKS 0637-752. The latter was the first source *Chandra* detected (Chartas et al. 2000; Schwartz et al. 2000). Its bright and spectrally hard knot X-ray emission is not the high energy tail of knot radio-to-optical synchrotron spectrum, but rather part of a second, high energy spectral component. Synchrotron self-Compton (SSC) and inverse Compton emission by up scattering cosmic microwave background (IC/CMB) photons in equipartition conditions and assuming non-relativistic flow speeds were found to severely under-produce the observed X-rays (Chartas et al. 2000; Schwartz et al. 2000).

Celotti et al. (2001) and Tavecchio et al. (2000) independently noted that at pc scales (probed with very long baseline radio interferometry or VLBI) the jet of PKS 0637-752 exhibits superluminal motion with apparent speed (in units of c) of $\beta_{app} = 13.8$ (Lovell et al. 2000), requiring a minimum bulk Lorentz factor $\Gamma_{min} = \beta_{app}$. By assuming that the bulk Lorentz factor Γ is the same at pc and kpc scales and that the jet is oriented

close to our line of sight ($\theta \sim 1/\Gamma$, where θ is the angle between the jet and the line of sight), they showed that the X-rays could be explained as IC/CMB due to the much higher Doppler boosting¹ (δ) than previously adopted for this mechanism.

The IC/CMB model was quickly adopted as the standard explanation for the high X-ray emission from many FR-II type jets (e.g., Sambruna et al. 2004; Marshall et al. 2005; Jorstad & Marscher 2006; Tavecchio et al. 2007; Miller et al. 2006; Kharb et al. 2012). Despite the popularity of the IC/CMB model, it failed to explain some features of multi-wavelength observations: (i) For a given X-ray spectrum this model predicts a unique gamma ray flux (Georganopoulos et al. 2006) that in most cases is not detected (e.g., Meyer & Georganopoulos 2013; Meyer et al. 2015; Breiding et al. 2017, but see Meyer et al. (2019) for two notable exceptions) (ii) High polarization (on the order of 30%) is observed in the optical spectrum of the jet knots of PKS 1136-135 (Cara et al. 2013); in this source the optical samples the low-energy tail of the high-energy (X-ray) emission component. A high level of polarization is in disagreement with the expected low polarization of IC/CMB emission (Uchiyama et al. 2007). (iii) If we assume that the emission comes from a moving feature, we expect to see proper motions on the order of $\beta_{app} \sim 10$. Contrary to this expectation, an HST proper motion study of the jet of 3C 273 found $\beta_{app} \lesssim 1$ (Meyer et al. 2016). (iv) If we assume that the emission comes from a stationary feature, the cooling time of the X-ray emitting electrons is $\sim 10^6$ years (Harris & Krawczynski 2007), much larger than that of the radio-emitting electrons (Worrall 2009). One would thus expect X-ray jets to extend past the radio, while the opposite is seen to happen in many jets (e.g., Sambruna et al. 2004; Jester et al. 2006). (v) X-ray variability has been detected in a knot in the jet of Pictor A on the order of a few years (Marshall et al. 2010), and possibly even a few weeks (Hardcastle et al. 2016). Such short time scales are incompatible with the enormously longer cooling time of the X-ray emitting electrons under IC/CMB.

Some workers (e.g., Jester et al. 2006; Hardcastle 2006; Clautice et al. 2016), motivated by the problems in the IC/CMB model, favored synchrotron emission from an ad-hoc additional population of energetic electrons (~ 30 -100 TeV). Testing this interpretation requires high-resolution X-ray polarimetry, which is possible with the recently launched Imaging X-ray Polarimetry Explorer (IXPE Weisskopf et al. 2016). In general, both double-synchrotron and IC/CMB models can fit the observed radio to X-ray spectral energy distributions (SEDs), as Cara et al. (2013) demonstrated for PKS 1136-135. It is essential to understand the nature of the knot X-ray emission, as this has a major consequence on the implied total power in the jet. While the IC/CMB model requires Eddington or super-Eddington jet powers, the synchrotron model is sub-Eddington by at least an order of magnitude (Dermer & Atoyan 2004; Atoyan & Dermer 2004).

¹ $\delta = \frac{1}{\Gamma(1-\beta \cos \theta)}$, where β is the speed of the emitting plasma in units of the speed of light, and θ is the angle of the jet to the line of sight

Almost all the discussion in the literature has been implicitly framed in the context of one-zone models, which requires the emission in different frequency bands to be co-spatial. This assumption has been seen not to hold in some cases, where displacements and/or size differences between radio and X-ray knots have been noted (e.g., Sambruna et al. 2004; Jester et al. 2006). X-rays peaking and decaying before the radio were previously reported in some knots of FR-II sources (e.g., Kataoka et al. 2008; Clautice et al. 2016; Harris et al. 2017). Similar offsets between the peaks of radio and X-rays are also seen in FR-I sources like M87 (Marshall et al. 2002), though this is generally attributed to synchrotron cooling effects (e.g., Hardcastle et al. 2001).

The majority of the known radio/X-ray offsets were only noted individually in their respective detection papers, and for the majority of X-ray jets the low number of X-ray counts attributed to the knots and the resulting statistics limited attempts to detect offsets. We addressed this problem using a novel approach based on a statistical tool called Low count Image Reconstruction and Analysis (LIRA, Esch et al. 2004; Stein et al. 2015) to detect offsets from low-count jets in Reddy et al. (2021, hereafter Paper I). In that study we detected offsets in roughly half of the analyzed 22 jets; however the overall frequency of occurrence in the full X-ray jet sample is unknown, and it is not yet clear whether these offsets are exceptions or the norm. In this work, we extend our analysis to the data of all the remaining X-ray jets available in the *Chandra* archive, and compare them to high-resolution radio images, to look for radio/X-ray offsets, where possible. We aim to find whether these offsets represent a norm, and examine any statistical correlations that could illuminate the physical nature of the knots and hotspots.

The rest of this document is organized as follows. Section 2 describes the data sample, reduction and analysis methods. Section 3 describes the results we discuss them in section 4. Appendix B provides brief descriptions for offsets in each source.

The adopted cosmology follows the NASA Extragalactic Database (NED): $H_0 = 67.8$ km/s/Mpc, $\Omega_m = 0.308$ and $\Omega_\Lambda = 0.692$. Spectral index α is given by the flux density, $F_\nu = \nu^{-\alpha}$ and the photon index by $\Gamma = \alpha + 1$.

2. METHODS

2.1. *X-ray Jet Sample*

The initial sample of X-ray jets was taken from a broad literature and archive search, as previously described in Reddy et al. (2021). These include the over 100 sources listed in the XJET² database, the 3CR snapshot surveys (e.g., Massaro et al. 2010, 2015, 2018; Stuardi et al. 2018) and other serendipitous discoveries, totaling 189 sources. In addition, for this paper, we added four detections from Snios et al. (2021), three from Marshall et al. (2018), and one each from Worrall et al. (2020), Connor et al. (2021) and Ighina et al. (2022), bringing the total count to 199 sources.

² <https://hea-www.harvard.edu/XJET/>

These are listed in Table 5 in the Appendix, and is to the best of our knowledge, the complete list of all published X-ray jets detected by *Chandra* at the time of writing this paper. The table lists the common name of the source in column 1, IAU name in column 2, J2000 Right Ascension and Declination in column 3, redshift in column 4, angular scale (kpc/'') in column 5, class of the source (e.g., FR-I, FR-II, quasar) in column 6, and a reference to the previous X-ray observation publication in column 7. In what follows, unless otherwise stated, we group sources classified as FR II or ‘quasars’ (i.e., lobe-dominated quasars or LDQ and core-dominated quasars or CDQ) collectively as FR II-type and all FR I together with BL Lacertae (BL Lac) objects as FR I-type.

In Paper I, we examined 69 of these jets identified as ‘low counts’ jets, where at least one feature was detected with less than 20 counts, in order to apply a specialized low-counts localization analysis in these cases. In that work we were not able to measure offsets for 47/69 due to various shortcomings of the observations or source characteristics (such as lacking a radio core or having no compact X-ray emission). In this paper we re-consider one source from the previous paper with a high-count hotspot (3C 275.1). Of the remaining 130 jets left for this paper, we exclude 52 jets from the analysis for a variety of reasons. (In the Appendix we further describe these sources and the impact of their removal on our conclusions.) In particular, in 17 of these there is no point-like or spatially correlated X-ray/radio feature in the jet, and in 2 sources the short exposure leads to an under-exposed ‘core’ which prevents accurate X-ray/radio alignment. In two cases it is clear that the X-ray emission originates from a thermal medium surrounding the jet rather than from the jet itself – these are 3C 171 (Hardcastle et al. 2010) and 3C 305 (Hardcastle et al. 2012). We also exclude 13 jets at high redshift ($z > 2.2$) because in these cases it is difficult to ascertain whether the X-ray origin is from the jet, a hotspot, or an extended lobe due to the reduced scale and greater foreshortening of the jet. Following Paper I, we only considered jet components without neighboring components in a radius of two native ACIS-S pixels (0.492'') to construct regions large enough to measure their centroids. We excluded ten sources with no component satisfying this criterion. Finally, we did not re-analyze ten sources with known (published) offsets similar to or larger than a single ACIS-S pixel, where instrumental effects are unlikely to produce an offset (see 2.4 for details), or sources where they are already accounted for while measuring offsets. However, these sources are included in our general analysis. In total we newly analyzed 164 components from 77 jets in this paper, joining the 37 features in 22 jets from paper I. With the literature cases, this comes to 226 components from 107 X-ray jets.

2.2. Radio Data

We retrieved radio data mainly from archives of the Very Large Array (VLA) and, in a few cases, from the Australian Telescope Compact Array (ATCA). As the intent

is to detect offsets using *Chandra* X-ray images at a resolution of $\approx 0.25''$, we also selected the radio data to have a similar resolution ($\approx 0.2\text{--}0.4''$). Table 1 provides the details of these observations with the name of the source in column 1, project name in column 2, date of observation in column 3, frequency in column 4, beam size in column 5, and the RMS of the final image in column 6.

Table 1. Details of Radio Observations

Name	Program	Date	Frequency GHz	Beam "×", PA°	RMS 10^{-5}Jy/beam
3C 9	15A-357	2019 Jun 15	14.99	0.15×0.12, -55.58	0.47
3C15	AB0534	1990 May 25	8.40	0.35×0.26, 51.76	2.21
3C 31	AL0405	1996 Nov 13	8.46	0.24×0.22, 167.00	1.04
4C +01.02	AR0197	1989 Jan 08	4.80	0.47×0.39, 18.26	11.80
3C 33	AR0148	1986 Jul 13	4.86	1.54×1.49, -32.53	124.00
3C 47	AB0796	1996 Nov 07	4.84	0.40×0.38, 61.81	2.19
PKS 0144-522	ATCA(C890)	2004 May 08	17.73	0.40×0.40, 0.00	12.10
4C +35.03	AM0221	1987 Aug 15	4.86	0.39×0.36, -20.48	5.26
PKS 0208-512	ATCA(C890)	2002 Feb 01	8.64	1.33×1.21, -26.06	27.40
3C 66B	AA0128	1991 Aug 19	8.21	0.24×0.20, 9.80	2.66

NOTE—Table 1 is published in its entirety in the machine-readable format. A portion is shown here for guidance regarding its form and content.

The VLA observations were calibrated and imaged using the Common Astronomy Software Applications (CASA, [McMullin et al. 2007](#)) toolbox. For VLA data, 3C 286, 3C 48, or 3C 137 were used as flux calibrators, while the sources were bright enough themselves in several cases to be used as phase calibrators. The initial bandpass, and amplitude and phase calibrations were performed using `bandpass` and `gaincal` tasks in CASA, respectively. The calibrated data are mostly imaged using the `clean` task in CASA with the “Briggs” weighting scheme and where we set `robust`=0.5. In a few cases the newer `tclean` task was used with equivalent parameters. Additionally, for JVLA data, we set `nterms`=2 to capture the spectral curvature over the wideband. For ATCA data, the initial calibration was performed using the MIRIAD ([Sault et al. 1995](#)) toolbox following the standard procedures described in the ATCA cookbook. 1934-638 served as the flux calibrator for all the observations. The RFI was flagged using `pgflag` and `blflag` tasks, and amplitude and phase were initially calibrated using `mfcal` and `gpcal` tasks in MIRIAD. The calibrated data were imaged using the Difmap program ([Shepherd 1997](#)) following the same procedure used for the VLA data. Natural weighting was applied in nearly all cases to produce the images. Finally, we measured the radio flux from each component by fitting an elliptical Gaussian model using the 2D fitting tool available in CASA. If the fit did not converge, we estimated the flux by summing the pixel values within a chosen region of interest (ROI) around the component.

Table 2. Details of *Chandra* X-ray Observations

Name	Chandra ObsIDs	Effective exposure ^a (ks)	Modes ^b	counts/s ^c
3C 9	1595, 17088, 18700-1	89.00	F, V	0.021
3C15	17128	116.34	V	0.045
3C 31	2147	44.00	F	0.027
4C +01.02	9281, 10380, 10799	70.30	V	0.163
3C 33	6910, 7200	36.40	F	0.068
3C 47	2129	34.70	F	0.222
PKS 0144-522	10366	5.41	V	0.091
4C +35.03	856	8.20	V	0.020

^aAfter background flare removal, if any.

^bThe observation mode for each obsID where F=FAINT, V=VFAINT. A single value is provided if all the current and subsequent obsIDs have the same mode.

^cAverage of the count rate from each epoch.

NOTE—Table 1 is published in its entirety in the machine-readable format. A portion is shown here for guidance regarding its form and content.

2.3. *Chandra* X-ray Data

We obtained X-ray data from the *Chandra* archives and re-processed them using the standard methods described in *Chandra* data analysis threads. We used calibration information from CALDB 4.9.4 and the Chandra Interactive Analysis of Observations (CIAO, [Fruscione et al. 2006](#)) v4.13 suite for reducing the data. Table 2 summarizes details of the observations used in our analysis with the source name in column 1, *Chandra* ObsID in column 2, the effective exposure time in column 3, observation mode in column 4, and the count rate in column 5.

We inspected the time-binned light curve for each observation and any periods with count rates above the 2σ -level were excluded. Only the events falling between 0.5-7.0 keV are considered, while those falling in regions on the detector with less than 2% of the total exposure time are excluded. For sources with multiple observations, the centroid of the core in each observation, measured using `dmstat`, is aligned to the observation with the maximum of exposures. The aligned observations are merged using `merge_obs` to produce the final merged observation. Following Paper I, we bin all the events files on half-pixel boundaries (bin factor: 0.5) of ACIS-S pixels and set the image size to either 64x64 or 128x128 to comply with LIRA input size requirements, further explained below.

2.4. Measuring X-ray/Radio Offsets with LIRA

Sub-pixel level offsets ($\lesssim 0.3''$) in high-count jets are generally detected by comparing longitudinal radio brightness profiles against their X-ray counterparts, constructed

using sub-pixel images (e.g., Sambruna et al. 2007; Siemiginowska et al. 2007; Perlman et al. 2011; Kharb et al. 2012; Harris et al. 2017) or by measuring X-ray/radio centroid differences (e.g., Sambruna et al. 2004; Worrall & Birkinshaw 2005; Marscher & Jorstad 2011), or visually in simple cases where offsets are similar to or larger than *Chandra*’s resolution (e.g., Kataoka et al. 2008; Hardcastle et al. 2007; Erlund et al. 2007; Perlman et al. 2009). The brightness profile-based method, which is usually applied to the entire jet at once, ignores the possibility that curvature in the jet that may reduce any observable offset below a detectable level at different points along the jet. Although centroid-difference can alleviate this problem by measuring the offset individually for each component independent of the jet morphology, *Chandra*’s point spread function (PSF) and background fluctuations introduce additional uncertainties in offsets, which are unaccounted by this method. Moreover, emission from the PSF of the bright core can add excess emission to nearby components and move their centroid closer to the core, thereby creating false offsets. The same effects can additionally induce false detections of X-ray components themselves in the case of low-count jets, and LIRA was used to examine this possibility for the jets analyzed in Paper I. We extend the approach used in Paper I to high-count jets in this work to estimate the uncertainties in offsets and thereby the significance of their detection.

We refer the reader to Paper I for full details on the method and Esch et al. (2004) and Stein et al. (2015) for a detailed statistical treatment of LIRA. Briefly, LIRA models the observed image as a sum of two model images. The baseline model comprises all user-specified features assumed to be present in the observation. For our case, we use a point source (representing the bright core) overlaid with a flat background for the baseline model. In addition to this there is the “added” model, containing any emission required in excess of the baseline to explain the observation. LIRA applies a Bayesian methodology to infer the posterior distribution of the added model by fitting a superposition of the baseline and the added models to the observation with a user-supplied PSF. Put another way, LIRA reconstructs the observation by convolving the sum of the baseline and the added models with the PSF. It samples the output posterior distribution using Markov Chain Monte Carlo (MCMC) method to produce a series of images of the added model; they represent the brightness distribution of the observation after accounting for effects of the core, background, and the PSF. We compute an offset from each MCMC image using the X-ray/radio centroid difference method to derive its posterior distribution and thereby its associated uncertainty. In this work, we discard the first 1000 iterations as *burn-in*, and generate 2000 MCMC images of the added model. These 2000 images are averaged to produce a core and background subtracted deconvolved image.

2.5. Preparing PSFs and baseline images

We follow a similar procedure used in Paper I to generate PSFs and baseline models for each source. We used the published values of spectral parameters for the core

where available. For the rest, we extracted their spectra using `specextract` command in CIAO and initially fit them using a power-law model in SHERPA (Freeman et al. 2001), with two absorption components, one each for the host galaxy and the Milky Way. If the hydrogen absorption column density (nH) of the host galaxy was poorly constrained in the fit, we only used the Milky Way nH ³ for the absorption component and re-fit the spectra. We used the final spectral model with `trace-nest` command from SAOTrace⁴ v2.0.5 to simulate 100 ray traces through *Chandra*’s optics. We projected these ray traces onto the ACIS-S detector using `simulate_psf` command from CIAO, which used MARX v5.4.0 (Davis et al. 2012) as the backend, and generated a merged event file without applying any sub-pixel event repositioning.

Since the default value of $0.07''$ for the `blur` parameter in `simulate_psf` is known to produce a PSF narrower⁵ than the observation, we generated multiple PSFs by varying `blur` between $0.07''$ and $0.35''$ in steps of $0.07''$ (see also discussion in Paper I). We compared each simulated PSF’s enclosed counts fraction (ECF) with that of the observation and selected the PSF with the least squared error. We binned the final PSF events file to match the pixel boundaries of the observed image. For sources with multiple observations, we summed the PSF of all individual observations to obtain the final PSF. We loaded this PSF in SHERPA and fit a 2D Gaussian model (`gauss2d`) with a flat background (`const2d`) to the observation to generate the baseline model. In addition, as we discuss in the following section, we also generated a baseline model with only a flat background to estimate uncertainties in the location of the X-ray core.

2.6. X-ray/Radio Image Registration

The radio core locations were measured by fitting with a 2D elliptical-Gaussian model in CASA and were localized to within 0.1 mas for all sources. We use the `dmstat` command in CIAO to estimate the centroid of the X-ray core using a circular region. The centroid was computed multiple times by varying the radius and location of the region to minimize any bias from manual selection of regions. In addition, we measured the core’s centroid on MCMC images generated using LIRA with a flat-background-only baseline model (i.e., without subtracting the core). The major axis of the standard deviational ellipse (e.g., Yuill 1971), which encloses 98% of the LIRA derived centroids was as always less than $0.03''$. Furthermore, for all the sources, the offset between `dmstat`-measured and LIRA-measured centroids was always less than $0.05''$. To estimate the uncertainty in the alignment, we conservatively take the sum of the maximum uncertainty in X-ray (`dmstat`+LIRA) and radio core locations in quadrature yielding a value of $\sim 0.06''$. We note the intrinsic dispersion in the X-ray core’s location was absent in the slightly smaller uncertainty estimate of $0.05''$ used

³ Retrieved from WebPIMMS service (<https://heasarc.gsfc.nasa.gov/cgi-bin/Tools/w3nh/w3nh.pl>)

⁴ <https://cxc.cfa.harvard.edu/cal/Hrma/Raytrace/SAOTrace.html>

⁵ See <https://cxc.cfa.harvard.edu/ciao/why/aspectblur.html> for details

in Paper I. However, its conclusions remain unaltered even with the slightly larger estimate as all offsets claimed in Paper I are larger than $0.15''$.

2.7. Measuring X-ray Flux and Spectral Index

Similar to the case of cores, we use the published values of spectral indices and fluxes where available. These values are listed in table 4 along with their respective publications. For the remaining sources, we extracted the emission spectrum using the `specextract` command in CIAO. We fit each spectrum with an absorbed power-law model over the 0.5-7.0 keV energy band and fixed nH to Milky Way value. The counts were grouped to a minimum of one count per bin and WStat statistic was used with Monte-Carlo (`moncar`) optimizer. Once the fit converged, we used the normalization value to estimate the spectral flux density at 1 keV. For sources with poor fits (with no spectral indices listed in table 4), we measured the flux using exposure-corrected LIRA deconvolved images. The aspect histogram and instrument map required to create the exposure map were generated using `asphist` and `mkinstmap` commands in CIAO, respectively. The instrument map was weighted using an absorbed power-law model with $\Gamma = 2$ and appropriate galactic nH value. We summed the individual exposure maps in the case of sources with multiple observations. We divided the averaged LIRA image by the final exposure map to create a flux image with the units of counts $\text{sec}^{-1} \text{ pixel}^{-1}$. The pixel values inside each chosen region were summed to estimate the count flux and were converted to energy flux density at 1 keV using the same spectral model adopted for the instrument map.

3. RESULTS

We show in Figure 1 an example figure for 3C 9 showing the *Chandra* observations (left panel) and LIRA-deconvolved (average of 2000 MCMC images) image (right panel), with radio contours overlaid in green. The dashed-gray circles indicate the regions used to measure the centroids for each knot. In each LIRA deconvolved image, we normalize any residuals in the core region to improve the contrast among features in the jet. The mean centroid for each region is marked with a red X. Similar figures for the remaining 76 sources we have analyzed are given in the Appendix.

In our analysis, an offset was considered to be significant only when the mean of the distribution of offsets measured using individual MCMC images from LIRA was at least 1σ level above $0.15''$, which is a threshold ~ 2 times the estimated X-ray/radio astrometric registration error (taken as $\approx 0.07''$). If multiple unresolved radio peaks existed within a hotspot region with only a single source of X-ray emission, the offset is measured as the distance between the X-ray centroid and the brightest radio peak. With this criterion, we find 94 (from 61 jets) offsets in our sample of 164 features in the 77 jets newly analyzed in this paper. Table 3 summarizes the source and offset counts from Paper I and this work. In Paper I we found offsets in 19/37 features of 15/22 jets analyzed there.

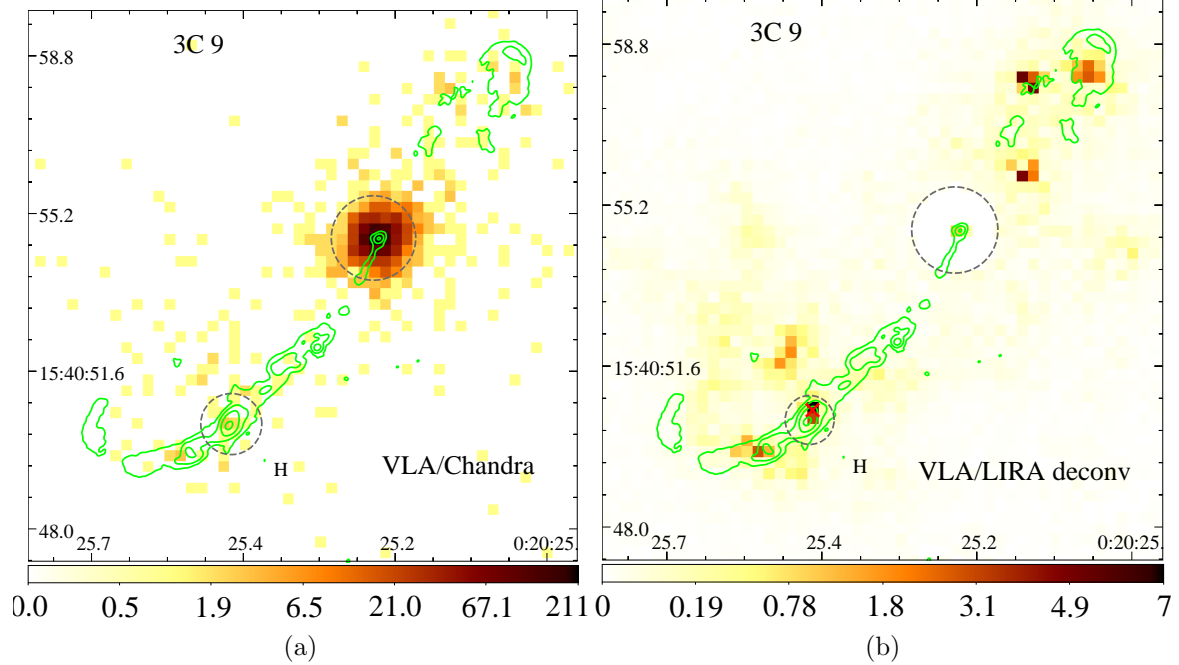


Figure 1. Results for the offset analysis of 3C 9. With the radio contours overlaid on both panels, (a) shows the *Chandra* X-ray image and (b) shows the LIRA deconvolved image. The dashed-gray circles indicate the regions used to measure the centroid for each feature and their respective mean centroids are marked with a red X. The radio contours are given by 0.03, 0.4, 2.0, 6.0, 8.0 mJy beam⁻¹. The complete figure set (75 images) is available in the online journal.

Of the 94 offsets detected in this work, we newly detect 58 offsets from 43 jets, while 36 offsets from 21 jets confirm what was previously reported in the literature. The previously reported offsets were generally identified either visually or based on X-ray/radio centroid differences or using longitudinal brightness profiles although without any proper uncertainty estimates, which we now provide. In addition, we include 15 sources from 9 jets with offsets on the order of an ACIS-S pixel (0.492"); we also include 4 offsets in 3C 273 from [Marchenko et al. \(2017\)](#), which were measured after accounting for the effects of PSF. In addition, we include 6 other features from 3 of these jets under the Co-s category, where within the published uncertainty, estimates, the offsets are consistent with $\leq 0.15''$. Furthermore, although our selection criteria excluded components surrounded by any other feature within 2 ACIS-S pixels, in 18 of such features, we find radio knots co-spatial with distinct X-ray peaks. We tentatively include them under the no-offset category, and are indicated with gray labels on their individual images. This comes to 132 offsets in a total of 226 components where a total of 201 components are analyzed in Paper I and this work.

The default prior for LIRA used in this work is optimized to detect compact sources that causes smooth diffuse (e.g., M87) or resolved sources to appear with a speckled texture in their deconvolutions. That means diffuse emission around point or point-

Table 3. Summary of the sources considered in Paper I and this work.

		Paper I	This work
Analyzed	Jets	22	77 ^a
	Features	37	164
Excluded	Jets	47	52
Offsets found	Jets	15 (68%)	61 (79%)
	Features	19	94
Previously identified offsets	Jets	-	21
	Features	-	36
Newly identified offsets	Jets	15	43
	Features	19	58
Offsets used from reference	Jets	-	10
	Features	-	19

^a Total count including the common source, 3C 275.1.

like sources, if present, may introduce errors in the source’s mean location. However, the associated uncertainty in the localization also increases due to increased fluctuation in the measured offset between individual MCMC draws, thereby suppressing the detection of a false offset. For example, even with a mean offset of $0.69''$, knot K45 in 3C 111 is classified as Co-s because it is still within 1σ of $0.15''$.

For two reasons, diffuse emission cannot solely be responsible for the offsets observed in our study. Most of the analyzed components are isolated where we expect minimal diffuse (inter-knot) emission. Two, diffuse emission must induce offsets in random directions contrary to the observed predominance of a specific offset type (see section 4.1). That means a diffuse component must exist in jet features that always brightens in a preferred orientation to reproduce the observations. However, this is equivalent to a spatially separated emission zone configuration, whose detection is the main focus of this work. Hence we conclude that diffuse emission has little influence on the overall conclusions of this study.

Table 4 summarizes the results of our offset analysis on 77 sources with 164 components. Additionally, we provide the details of 25 sources we included from the literature. The name of the source is provided in column 1, the X-ray feature’s name in column 2, the angular X-ray/radio offset in column 3, along with any reference that noted an offset previously, the sky-projected offset in column 4, and the type of the offset in column 5. We adopt the offset-type nomenclature from Paper I where “Xf” indicates X-ray-first or the X-rays peaking upstream of the radio, “Rf” indicates radio-first or the radio peaking upstream of the X-rays, and “Co-s” or co-spatial indicates the lack of any significant evidence for an offset. Tentative Co-s-types are indicated with a (T). “Amb” or ambiguous offset-type is used for components with an unclear direction of the jet (e.g., 3C 351, Figure 81) or those that lack unambiguous X-ray/radio spatial correlation (e.g., knot or large-scale hot gas). Furthermore, we specify an additional attribute for the offset-type based on the structure of the com-

ponent. “Bnd” indicates a knot lying at a bend in the jet, “Flr” indicates the so-called *flaring point*, commonly found in FR I-type sources (e.g., [Hardcastle et al. 2001](#)), and “Vnsh” if the emission from an FR II-type jet quickly diminishes at the specified location before re-emerging at a hotspot further downstream (e.g., 4C+19.44, [Harris et al. 2017](#)). “Jet-HS” indicates the hotspot presumably produces X-rays when the jet enters the turbulent hotspot region, generally coinciding with a faint radio peak followed by a much brighter radio hotspot. In addition to the results on offsets, we also compile spectral data in Table 4 with radio spectral index (α_r) in column 6, X-ray spectral index (α_X) in column 7, radio frequency in column 8, the corresponding radio flux in column 9, X-ray energy flux density at 1 keV in column 10 and the X-ray/Radio flux ratio ($R = \log_{10}(\frac{\nu_X F_X}{\nu_r F_r})$, flux ratio, hereafter) in column 11.

Table 4. Offset analysis results with spectral data

Name	Component	Offset Type ^b	Offset kpc ^c	α_r	α_X	ν_r GHz	f_r mJy	f_{1keV} nJy	R $\log_{10}(\frac{\nu_X F_X}{\nu_r F_r})$
3C 9	H	0.29 ± 0.09	Xf+Bnd	2.46 ± 0.77		14.99	47.20	0.30	0.10
3C15	B	0.66 ± 0.29	Xf+F _l r	0.92 ± 0.40		8.40	33.20	0.64	0.56
	C	0.14 ± 0.04	Co-s	0.20 ± 0.06	0.90 0.70 ± 0.36 (32)	8.40	8.30	1.10	3.82
3C 31	B	0.77 ± 0.05	Xf+F _l r	0.26 ± 0.02	0.55 1.30 ± 0.20	8.46	6.83	2.45	10.25
4C +01.02	B	0.12 ± 0.07	Co-s+Bnd	0.97 ± 0.56	1.02 0.80 ± 0.30 (1)	4.80	10.04	4.55 (1)	22.85
	SHS	0.40 ± 0.06 (1)	Xf	3.41 ± 0.50	1.02 0.90 ± 0.60 (1)	4.80	114.60	1.72 (1)	0.76

NOTE—Table 1 is published in its entirety in the machine-readable format. A portion is shown here for guidance regarding its form and content.

References—(1) [Kharb et al. \(2012\)](#). (2) [Kraft et al. \(2007\)](#). (3) [Hardcastle et al. \(2004\)](#). (4) [Perlman et al. \(2011\)](#). (5) [Hardcastle et al. \(2001\)](#). (6) [Clautice et al. \(2016\)](#). (7) [Harris et al. \(2004b\)](#). (8) [Hardcastle et al. \(2001\)](#). (9) [Hardcastle et al. \(2016\)](#). (10) [Hardcastle et al. \(2007\)](#). (11) [Stanley et al. \(2015\)](#). (12) [Sambruna et al. \(2006\)](#). (13) [Hardcastle et al. \(2002\)](#). (14) [Wilkes et al. \(2012\)](#). (15) [Meyer et al. \(2018\)](#). (16) [Jester et al. \(2006\)](#). (17) [Marshall et al. \(2002\)](#). (18) [Worrall et al. \(2016\)](#). (19) [Harris et al. \(2017\)](#). (20) [Gelbord et al. \(2005\)](#). (21) [Worrall & Birkinshaw \(2005\)](#). (22) [Brunetti et al. \(2001\)](#). (23) [Kataoka et al. \(2008\)](#). (24) [Kraft et al. \(2005\)](#). (25) [Wilson et al. \(2000\)](#). (26) [Sambruna et al. \(2008\)](#). (27) [Erlund et al. \(2010\)](#). (28) [Godfrey et al. \(2012\)](#). (29) [Worrall et al. \(2012\)](#). (30) [Perlman et al. \(2009\)](#). (31) [Tavecchio et al. \(2007\)](#). (32) [Kataoka et al. \(2003\)](#). (33) [Siemiginowska et al. \(2003b\)](#). (34) [Siemiginowska et al. \(2012\)](#). (35) [Wilson & Yang \(2002\)](#). (36) [Jorstad & Marscher \(2006\)](#). (37) [Kataoka et al. \(2003\)](#). (38) [Sambruna et al. \(2004\)](#). (39) [Jorstad & Marscher \(2004\)](#). (40) [Marscher & Jorstad \(2011\)](#). (41) [Siemiginowska et al. \(2007\)](#). (42) [Perlman et al. \(2011\)](#). (43) [Marchenko et al. \(2017\)](#). (44) [Pyrzas et al. \(2015\)](#). (45) [Worrall et al. \(2012\)](#).

Of the 94 detected offsets, we find 75 Xf-type offsets, 13 with the Bnd-type, 4 with the Flr-type, 11 with Jet-HS type; 9 features show the Rf-type offset, 2 with the Bnd-type, 2 with the Vnsh-type. Figure 2 shows the histogram of sky-projected offsets in our sample for knots (left panels) and hotspots (right panels), where the top and bottom panels show the offsets in arcseconds and kpc, respectively. The average magnitude of sky-projected knot-offsets is $0.59 \pm 0.79''$ (1.79 ± 1.44 kpc) in FR II-type sources, $0.58 \pm 0.29''$ (0.81 ± 1.04 kpc) in FR I-type sources, and $1.13 \pm 1.77''$ (3.17 ± 3.21 kpc) in hotspots. The observed high dispersion in the offsets is expected as the jets in our sample span a wide range of orientations (see section 2.1) and redshifts. Put

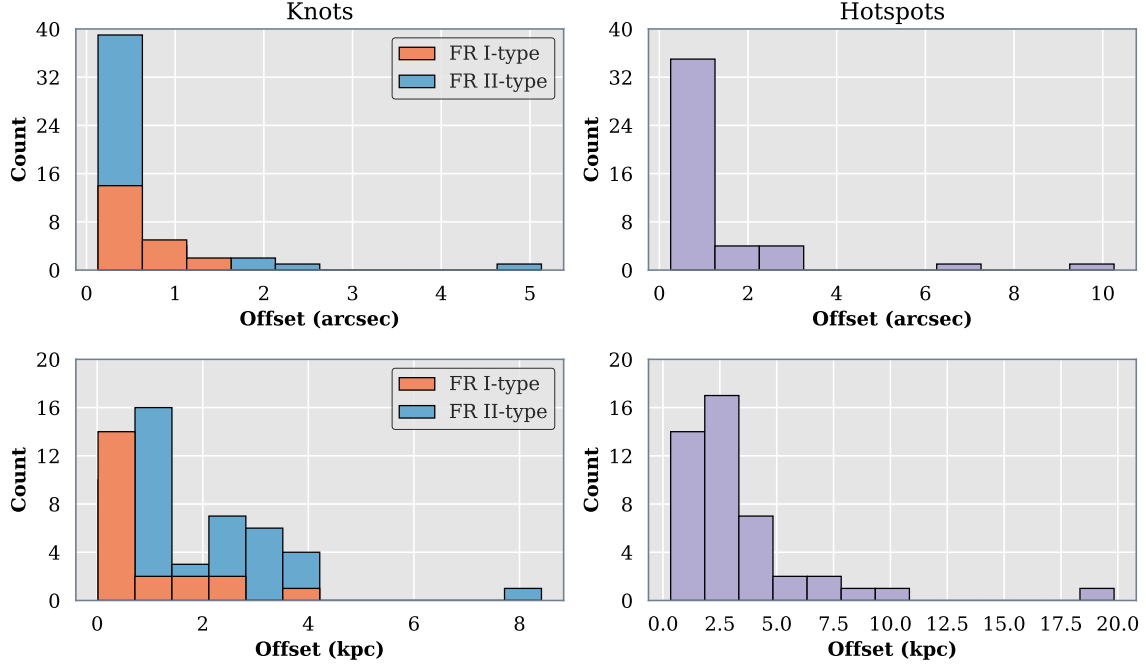


Figure 2. Histograms of the sky-projected offsets in knots and hotspots. Left panels show histograms of offsets in knots for the FR-I and FR-II types and the right panels show histograms for offsets in hotspots. The units of offsets are arc second and kpc in the top and bottom panels, respectively.

another way, even an identical intrinsic offset can observationally produce a wide range of offsets due to projection and distance effects.

3.1. New X-ray Feature Detections

Combined with the high resolution of *Chandra*, our X-ray image deconvolution using LIRA has allowed us to quantify offsets while accounting for the effects of core and background, which is unavailable to traditionally used longitudinal profile or centroid-based methods. For example, we detected an offset in the hotspot of 3C 454.3, located at $\approx 5''$ from its extremely bright blazar core. Here, the wings of the core's PSF inevitably introduce an uncertainty in the centroid of the hotspot, but our method is able to overcome this interference. Besides offsets, our deconvolutions have also revealed new features in jets, undetected in their previous analyses. In a few cases, we also detect features buried within the PSF of the core. Below we briefly comment on the new detections in individual sources.

3C 66B (Figure 23): In addition to an X-ray peak associated with the radio knot A, we also detect two distinct X-ray peaks between knots x and B, which, however, lack clear radio counterparts. The one closer to the core lies between knot x and the upstream edge of knot A. The other peak, further downstream, lies on the eastern edge of knot B, where the radio contours appear gently deflected around it, suggesting it may be a stationary obstacle shocked by the jet (e.g., Kraft et al. 2000;

Hardcastle et al. 2003). This detection is consistent with the need for two or more spectral components to explain knot B’s complex X-ray spectra (Hardcastle et al. 2001).

PKS 1229-02 (Figure 61): We detect a new X-ray knot roughly upstream of the radio knot C, which lies at an apparent bend in the jet. Interestingly, the upstream region of radio C also shows a spike in the rotation measure (see Fig. 3 in Russell et al. 2012). This spike suggests a bend-induced shock presumably produces the X-rays in the jet (e.g., Worrall & Birkinshaw 2005). A relatively fainter X-ray feature is also detected further down the jet, beyond which the jet appears disrupted. This morphology suggests a stationary obstacle possibly interacts with the jet and gently disrupts it (for example, see Evans et al. 2008), while presumably producing the X-rays.

PKS 1335-127 (Figure 66): We detect the X-ray counterpart to the radio knot A, which lies $\sim 1''$ to the southeast of the core.

4C +19.44 (Figure 67): Besides all the knots except S2.0, We also detect distinct X-ray features between knots S4.0-S5.3, S5.3-S8.3, and S10.0-S11.2, along the outer edges of the jet where the radio contours curve inside. This structure suggests these features are possibly stationary obstacles, for example, hot gas clouds, gently *pinching* the jet. These features match the locations where the transverse X-ray brightness profile of the jet deviates from its mean position angle, presented in Figure 2 of Harris et al. (2017). We newly detect two X-ray features in the jet region (previously referred to as S25.7 in Harris et al. (2017)) upstream of the southern hotspot. We label the northern feature as S25.7, and the southern feature as SHS-a where the jet presumably enters the turbulent hotspot region.

3C 78 (Figure 25): We detect the X-ray counterpart to the radio knot C.

4C +21.35 (Figure 59): We detect an X-ray knot $\sim 0.2''$ upstream of the radio knot C2, which lies at an apparent bend in the jet.

4C +28.07 (Figure 24): We detect two X-ray knots co-spatial with two radio knots, C and D, respectively. A new X-ray feature is also detected upstream of NHS-a, where the jet presumably enters the turbulent hotspot region.

PKS 1202-262 (Figure 56): We detect a clear knotty structure in the X-rays with three knots co-spatial with radio knots B, C, D, respectively. Although we detect two more X-ray features further downstream of knot D, they lie midway between the radio knots, making their radio association ambiguous. This knotty structure is contrary to the observed relatively flat longitudinal brightness profile, presented in Figure 9 of Perlman et al. (2011), which originally led the authors to believe IC/CMB primarily produces the X-rays.

3C 270.1 (Figure 57): Our deconvolved X-ray image shows a $\sim 1''$ (8.7 kpc) bar-like structure upstream of the southern radio hotspot, previously seen in the western hotspot of Pictor A (Hardcastle et al. 2016). This structure presumably indicates

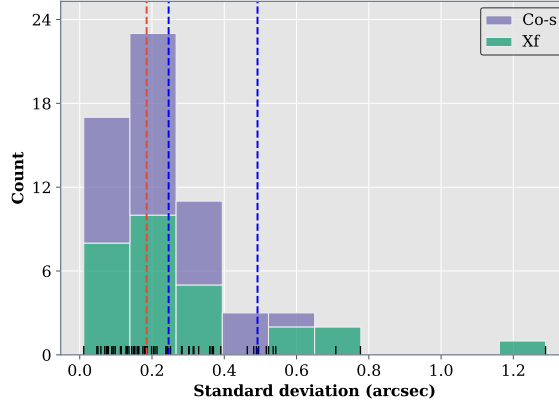


Figure 3. Histogram of the standard deviation of knot regions on deconvolved images for Xf (green) and Co-s-type (gray) knots. The two blue-dashed lines locate the half and single ACIS-S pixel sizes, and the red-dashed line indicates the median of the distribution.

the location where the jet impacts the turbulent hotspot region and produces X-rays along its entire cross-section.

3.2. Are X-ray knots resolved?

Throughout the literature on X-ray jets, the sizes of knots required to calculate various jet parameters, for example, equipartition magnetic fields, have been inferred using radio data (in the image or UV planes) mainly due to their well-characterized PSFs (e.g., Kataoka & Stawarz 2005). A few attempts have been made to infer the sizes of knots in the X-rays, for example, by comparing the radial profiles of observations and simulated PSFs (e.g., Kataoka et al. 2008; Marchenko et al. 2017). However, firm conclusions could not be made due to the imperfect knowledge of *Chandra*'s PSF.

Despite these imperfections, we can examine whether the X-ray knots are resolved or not by studying the standard deviation of knot regions in LIRA-deconvolved images. We estimate the standard deviation as:

$$\sigma = \sqrt{\frac{1}{N} \sum_{\text{pixel } i} n_i (x_i - \bar{x})^2} \quad (1)$$

where x_i is the location of the i^{th} pixel, n_i is its pixel value, and N is the sum of all pixel values. Here we only consider knots in FR-II-type jets as they are the main focus of our work. Figure 3 shows the histogram of standard deviation of all the knot regions. The median of the distribution (red-dashed line) is less than the half ACIS-S pixel size (0.246"), and about 90% of the knots lie below single ACIS-S pixel size (0.492"), both indicated with blue-dashed lines. That means emission from the majority of the knots is mostly confined to a single image pixel, which supports our assumption that we can generally treat knots as point (unresolved) or point-like sources. For knots with values greater than a single pixel, the source may be intrinsically extended.

Larger standard deviations may also result in sources with low signal-to-noise ratios (SNR) or with mismatched PSFs. For comparison, the typical standard deviation for the cores with high SNRs is about $0.03''$, consistent with a point source. However, due to the spatio-spectral dependence of *Chandra*'s PSF, the PSF simulated for the core and input to LIRA may not always match the emission from knots. Hence, their emission may be smeared in the deconvolved images, resulting in a larger variance even for actual point sources.

4. DISCUSSION

We analyzed a large sample of X-ray jets with the main aim of constraining the nature of X-ray emission from FR II-type jets on kpc scales, and obtained several lines of constraints in the form of offsets. While offsets argue for two or multi-zone models, the formation mechanism of knots and their internal structure are other important uncertainties in understanding how they emit X-rays. Although a few multi-zone models have been considered in the literature to reconcile the predictions of IC/CMB with the observations (e.g., Jester et al. 2006; Tavecchio 2021a), they are generally found to require unrealistic conditions (e.g., Jester et al. 2006) in the jet, and lack a mechanism to explain offsets. Below we discuss the statistics of the observed offsets and explain them using a knot description based on previous works (Stawarz et al. 2004; Kataoka et al. 2008, and references therein) that suggest knots represent separate moving parts of the jet, and estimate their bulk Lorentz factor under this scenario. We then use X-ray/radio flux ratios as a means to test whether IC/CMB can be the dominant mechanism with the limits of the current sample.

4.1. *Knot-Offsets in FR II-type jets*

Including offsets from Paper I and those directly taken from the literature, we find that the Xf-type offset is the majority type of offset observed in knots of FR II-type sources (48 out of 114). The Rf-type offset occurs only in a few cases (8 out of 114). These Xf-type offsets clearly contradict the X-ray/radio co-spatiality required by *any one-zone* IC/CMB interpretation, including the IC/CMB one.

To first order, Rf-type offsets in knots of FR II jets are compatible with a multizone IC/CMB scenario, where the X-rays (produced by electrons with $\gamma \sim 10$) can extend past the radio ($\gamma \sim 10^4$) due to their larger radiative lifetimes. However, their peculiar morphology combined with additional evidence suggests that in these cases the X-ray emission is not from the jet itself. For example, the Rf-type offset found in knot C of 4C+11.45 (Figure in 4.15 Paper I) appears at an apparent bend in the jet and is surrounded by Ly α clouds. The X-rays may be produced by the surrounding clouds, shock-heated by the jet which is being deflected, leading to an Rf-type offset. Similarly, Knot C in PKS 1030-357 (Figure 47) and knot S17.7 in 4C+19.44 (Figure 67) show an Rf-type offset with an unusual structure: the radio and X-ray emission from the jet rapidly declines with the X-ray emission persisting slightly further downstream than the radio (indicated with “+Vnsh” in Table 4).

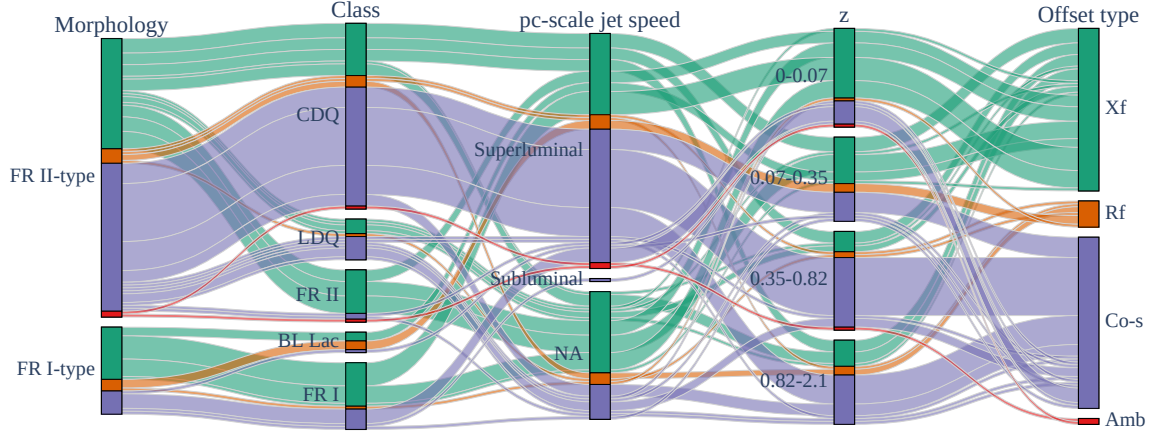


Figure 4. Categorical parallel-coordinates plot for the offsets in knots of FR II-type and FR I-type sources. Each stripe constitutes a group of knots with identical value in each coordinate and are colored according to the offset-type. Starting from the left, the coordinates are source type, sub-classification, pc-scale jet speed, redshift range, type of the offset.

A previously cold gas may be deflecting the jet away from our line of sight, thereby diminishing its observed emission (e.g., [Mendoza & Longair 2001](#)), while the jet shock-heats the cloud, which produces the X-rays (e.g., [Worrall et al. 2016](#)). Such shock-heated clouds presumably exhibit a thermal X-ray spectrum which can be tested with deeper observations.

Although many knots show significant offsets, a large fraction (56 out of 114) have radio & X-ray positions consistent to within errors (within $0.15''$), which may appear to satisfy the co-spatiality condition that one-zone models require. However, using these knots as evidence for one-zone emission is limited by several factors, including projection and distance effects, and limited instrumental resolution. To examine the importance of these effects, we construct a *categorical-parallel-coordinates* plot, shown in Figure 4 for all the knot-offsets in FR II-type sources (as well as FR I knots for completeness). Each “stripe” represents a group of one or more knots with the same attributes across all the coordinates and are color-coded based on the offset type. Starting from the left, the coordinates are namely, (i) the source type (FR I or FR II), (ii) the sub-class (e.g., CDQ or LDQ), (iii) the pc-scale jet speed (superluminal for $\beta_{app} > 1$ and subluminal for $\beta_{app} \leq 1$), (iv) the redshift, divided into four quartiles, and (v) the offset-type.

The class-coordinate shows that the CDQ-knots, which come from closely aligned jets, comprise the majority of the Co-s-type knots. The LDQ class, although less populous than the CDQ class, has a similar fraction of Xf/Co-s-types. Conversely, the knots in FR II-jets, which come from misaligned jets, predominantly possess the Xf-type offset. Furthermore, the z-coordinate indicates that the fraction of Co-s-type knots increases with redshift, which is expected as the CDQs mostly populate the two higher-redshift quartiles. That means Co-s-type knots possibly belong to the Xf-type

class, and a combination of projection and distance effects may be foreshortening their observable offsets to below *Chandra*’s resolution.

On the other hand, the Co-s-type knots may also be intrinsically different from their Xf-type counterparts and may result in different spectral properties. To examine this scenario, we adopted the 2-sample Anderson-Darling (AD) test (Scholz & Stephens 1987), to test for any differences in the distributions of spectral indices and flux ratios between the Xf-type and Co-s-type knots. For both the parameters, we are unable to detect any statistically significant differences between the two offset classes. Specifically, the p -values are 0.16 and 0.25 for spectral index and flux ratio, respectively, with the null hypothesis being that the two distributions belong to the same parent population.

4.2. Jet orientation scheme

To further interpret the measured offsets (expressed in a sky-projected form in Table 4) we require an estimate of orientation angle in order to compute de-projected offsets. A few methods exist to measure the orientations for kpc-scale jets or pc-scale jets. For example, Marin & Antonucci (2016) use the ratio of radio core to lobe luminosity to determine the orientation of kpc-scale jets while Drouart et al. (2012) use it for pc-scale jets. A few authors have proposed using optical emission lines from the central AGN to determine the pc-scale jet orientations (e.g., Risaliti et al. 2011; Matthews et al. 2017; Yong et al. 2020). However, most of these methods only apply to restricted redshift ranges. Moreover, the optical emission line data is absent for several sources in our sample and the proposed methods measure much larger angles for pc-scale jets than what their superluminal motions imply.

Hence, for 29 sources with a measured value of superluminal speed, we first estimate the upper limit on its pc-scale jet angle. We then convert it to an upper limit on the kpc-scale jet by numerically solving the conversion equations given in Conway & Murphy (1993); Singal (2016). The required inputs are (i) the position angle difference between kpc jets, and pc-scale jets, which we measure using VLBI images obtained from NED⁶, and (ii) the intrinsic pc-kpc jet bend, which we take as 5°. We omitted three superluminal sources, 3C 66B, B2 0737+313 and 4C -03.79, from this analysis due to lack of numerical convergence. For these three and the remaining sources, following Paper I we adopt a spectral class-based orientation scheme to assign representative upper limits on the jet’s angle to the line of sight. In this scheme, CDQs are assigned 15°, LDQs 30°, and FR-II (BLRG) 60° and FR II (NLRG) 90°. Furthermore, for all features where the jet displays a projected bend larger than 20°, we increment the derived/assumed angle by 5° for CDQs, 10° for LDQs and 20° for FR-IIIs.

4.3. De-projected offsets

⁶ NASA Extragalactic Database, <https://ned.ipac.caltech.edu/>

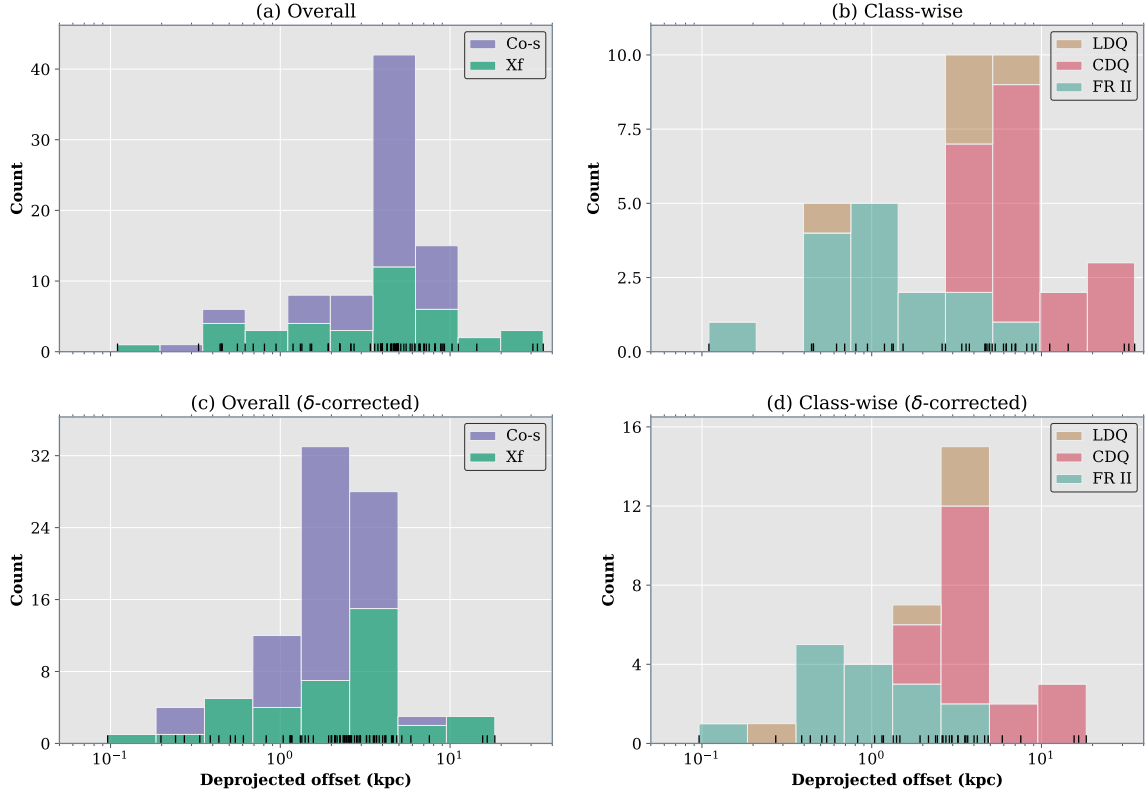


Figure 5. Stacked-histograms for de-projected offsets (kpc), plotted on a log scale, for knots in FR II-type sources. (a) shows the histograms for Xf-type and Co-s-type offsets for all the FR II-type sources. Co-s type knots are plotted by assuming a $0.15''$ offset, also distributed like the Xf-types. The histograms roughly describe a unimodal profile peaking at ≈ 4 kpc, suggesting similar knot sizes and formation mechanisms. (b) shows only the Xf-type offsets, grouped into their respective subclasses; CDQs and LDQs peak at higher values than FR-IIs, which may suggest an intrinsic difference between knots in quasars and FR-IIs. Alternatively, we can interpret this difference as a result of moving knots where their relativistic motion increases the observed offset by a factor of δ . (c) and (d) show the δ -corrected counterparts of the top panels where we assume $\Gamma = 1.25$ to estimate δ . The corrected-offsets are distributed more uniformly across classes and peak at ≈ 2 kpc, which is a better lower-limit on the sizes of knots (see section 4.3 for discussion).

Figure 5a shows the histogram for de-projected Xf-type offsets, de-projected using the upper limits from section 4.2. We also stack the histograms for Co-s-type knots, estimated from a constant angular offset of $0.15''$, which is an upper limit to any offset present in them. Both histograms peak at ≈ 4 kpc. Interestingly, this value is similar to the typical sizes of radio knots found in nearby FR II jets (e.g., Kataoka et al. 2008; Clautice et al. 2016). If not a coincidence, it suggests that most of the observed knots have similar structures, and presumably, a single process produces them. Put another way, the radio knots at lower-redshifts, if resolved along the jet, generally appear extended (e.g., Kataoka et al. 2008; Clautice et al. 2016), while their structure at higher-redshifts remains indeterminate due to limited instrumental resolution. Furthermore, as discussed in 3.2, nearly all the deconvolved X-ray knots show no evidence for extended structures at any redshift. Therefore, the similarity of

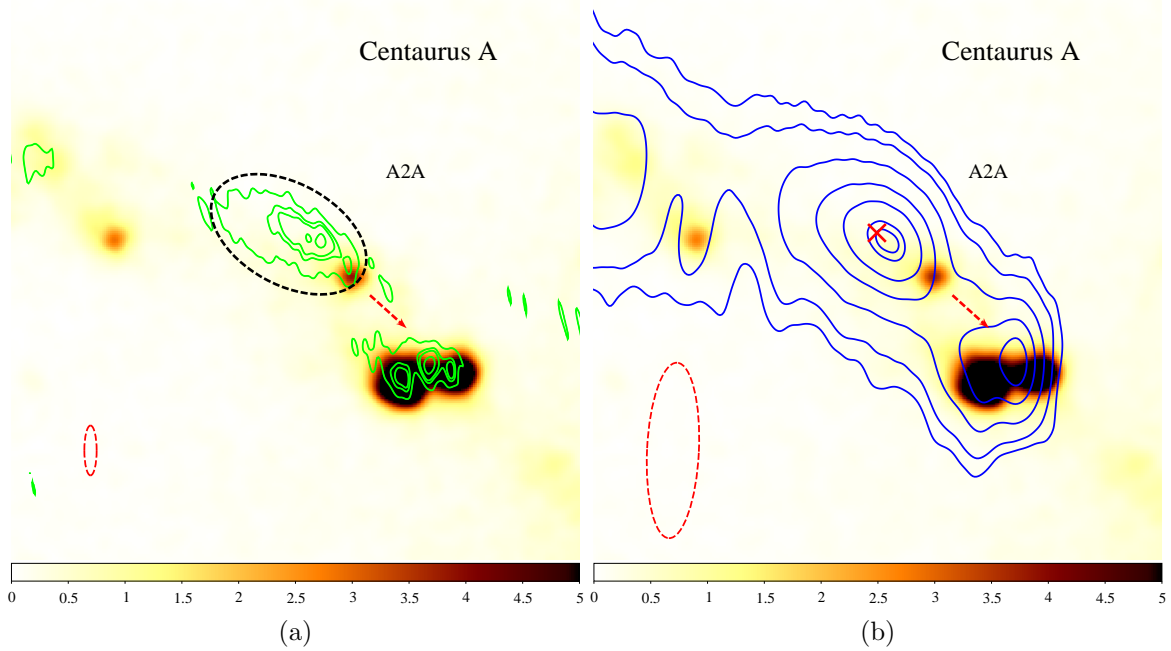


Figure 6. Demonstrating how similar offsets imply similar linear sizes using Centaurus A. With the smoothed *Chandra* X-ray image in the background, the VLA 8.4 GHz A and B-config contours are overlaid on the left and right panels, respectively. The beam size is shown at the bottom left on each image and the red-dashed arrow leads to the core. A-config resolves the radio knot A2A while the B-config produces a point-like knot with its peak located near the weighted centroid of the resolved knot (indicated with a red X), measured using the black-dashed ellipse, producing an X-ray/radio peak-to-peak offset. That means when a knot like A2A—with extended radio and compact X-ray emitting regions—becomes unresolved, it produces an offset, which is a lower limit on the knot’s size. Hence, similar offsets imply similar structures.

offsets in resolved and unresolved radio knots, and with magnitudes comparable to the resolved low-redshift knot sizes, indicates a similarity in their morphology: extended structure in the radio with a relatively more compact structure in the X-rays.

We demonstrate this inference in Figure 6 with the *Chandra* X-ray image and the VLA 8.4 GHz radio images of a nearby FR-I type jet, Centaurus A. The left panel shows the smoothed X-ray image of knot A2A (Hardcastle et al. 2003) overlaid with the A-config radio contours (beam size: $0.77'' \times 0.19''$, -0.3° PA) while the right panel shows the B-config radio contours (beam size: $2.76'' \times 0.80''$, -3.3° PA). A red-dashed arrow leads to the core in both the panels. The A-config radio observation resolves the knot across and along the jet, while the B-config observation, with a lower resolution than its A-config counterpart, shows a point-like structure, thereby producing a typical peak-to-peak X-ray/radio offset. Furthermore, the radio peak in the B-config image lies near the centroid of the knot’s brightness distribution (indicated with a red “X” in the right panel), measured using the dashed-ellipse in the A-config image. That means, when an extended radio knot becomes unresolved (while the X-ray knot remains compact), and unless the radio knot’s brightness varies significantly along its

length, its centroid would lie roughly at its center, creating an offset roughly half its length. Hence, similar offsets would imply similar spatial extents.

Despite a roughly unimodal profile of the overall de-projected offset distribution, the offsets in quasars (CDQ and LDQ) appear to be slightly larger than FR-II type sources (see Fig. 5b). The assumed angles for quasars in our orientation scheme can be smaller than their actual angles, which would result in larger offsets for quasars. Alternatively, the quasar knots in our sample, which lie at higher redshifts, could be intrinsically larger than their lower-redshift, misaligned counterparts, FR-II knots. However, it is unclear with the current understanding how the sizes of knots could increase with redshift. One physically motivated explanation could be that these knots are separate moving portions of plasma moving with at least mildly-relativistic speeds, embedded in an outer flow (e.g., Stawarz et al. 2004; Kataoka et al. 2008), which we detail in the next section. In this case, relativistic effects would magnify the observed offsets by a factor of δ (see e.g., Jester 2008). To check the applicability of the moving-knots scenario to the observed offsets, we correct the de-projected offsets by dividing by an estimated value of δ for each source. Here we set $\Gamma=1.25$ ($\beta=0.6$) based on the limits on kpc-scale bulk Lorentz factor ($\Gamma \approx 1.18 - 1.49$) derived from radio data (Wardle & Aaron 1997; Mullin & Hardcastle 2009). We show the resulting histogram of corrected offsets in the bottom panels of Fig. 5. The overall distribution becomes less dispersed and peaks at ≈ 2 kpc, which is roughly half of the typical knot sizes of ≈ 4 kpc (e.g., Kataoka et al. 2008). The δ -corrected class-wise histograms also indicate similar offsets across all the spectral classes, which, within the errors of the assumed angles and the bulk Lorentz factor, can be read as evidence for the moving-knots scenario.

4.4. *Knot formation mechanism*

Initially, the knots in FR II-type jets were thought to be produced by stationary re-confinement shocks (e.g., Komissarov & Falle 1998), which, however, lack a natural way to explain offsets. Stawarz et al. (2004) suggested the knots are separate faster-moving parts of the jet, presumably produced by a possible intermittent activity in the central engine (e.g., Bridle et al. 1986, 1989; Clarke et al. 1992); see Godfrey et al. (2012) in this context. A forward-reverse shock between faster and slower moving parts of the jet would produce the observed multiwavelength emission. However, Kataoka et al. (2008) note in a detailed study of 3C 353, that it is unclear why the two shocks produce different electron energy populations. They suggest the knots are slower and heavier moving blobs of plasma (produced by intermittent activity) embedded in a faster and lighter outer flow. A forward-reverse shock develops at the upstream end of the blob, where the reverse shock travels in the faster outer flow producing X-rays, while the radio emission coincides with the blob.

Although this model explains a few features of knots in FR II-type jets, including Xf-type offsets, it fails to explain why the transverse brightness profiles of the radio knots

in 3C 353 imply emission from a surface instead of a blob (Swain 1997). (Added: This can be clearly seen in Figure 5.12 in Swain (1996), which shows an edge-filtered radio image of 3C 353, where emission from all knots peaks on jet boundaries. Furthermore, nearly all of the knots show a bridge-like structure on their upstream end that connects the edges of the jet. Their X-ray emission is observed upstream of the bridges (Kataoka et al. 2008), where the jet’s outer flow presumably shocks the blob’s upstream end. This may suggest that we need a different picture.)

One possibility is that the X-ray-emitting electrons accelerated at the upstream edge of the plasma blob flow along its surface blob, presumably forming a shear layer, while emitting synchrotron radiation progressively at longer wavelengths. This simple advection, however, leads to offsets of ~ 100 kpc (Bai & Lee 2003) contrary to the observed offsets of a few kpc. Instead, accelerated plasma undergoes multiple interactions (compression or turbulence) while re-joining the outer flow, which would alter the brightness distribution and result in the observed morphology. Moreover, if synchrotron electrons produce the observed X-rays, their shorter lifetimes than their radio counterparts can also explain the relatively smaller emitting regions in X-rays than in the radio. Alternatively, the radio plasma can also diffuse into an already existing shear layer.

This advection through a shear layer scenario also fits two more observed properties of jets:

1. Magnetic fields are parallel (i.e., negligible radial component) to the jet in their outer layers while perpendicular in the inner regions of several jets (e.g., Bridle & Perley 1984; Bridle et al. 1986; Swain et al. 1998). It is possible for a shock at the upstream end of the blob to compress the plasma and produce a magnetic field parallel to the shock front (for a recent review, see Tavecchio 2021b) in the inner parts, while it can be parallel to the jet in the outer parts due to the presumed shear layer (e.g., Urrin 2006).
2. Optical polarization studies on knots of nearby jets like 3C 273 reveal high polarization either on jet-edges or near their maxima (Perlman et al. 2020) in the central parts of the jet. Depending on the mass density of the blob, most of the observed optical emission could be produced in a few different ways. For example, by a forward shock in the blob (e.g., Stawarz et al. 2004), or by a shear layer between the outer flow and the blob (e.g., Ostrowski et al. 2002), or by the synchrotron cooled X-ray electrons. Interestingly, similar features are also observed in FR I jets (e.g., Perlman et al. 2020, and the references therein) where the knots could be produced by stationary obstacles obstructing the jet flow (e.g., Hardcastle et al. 2003; Perlman et al. 2006; Avachat et al. 2016; Snios et al. 2019).

4.4.1. Constraints on the pattern speed of knots

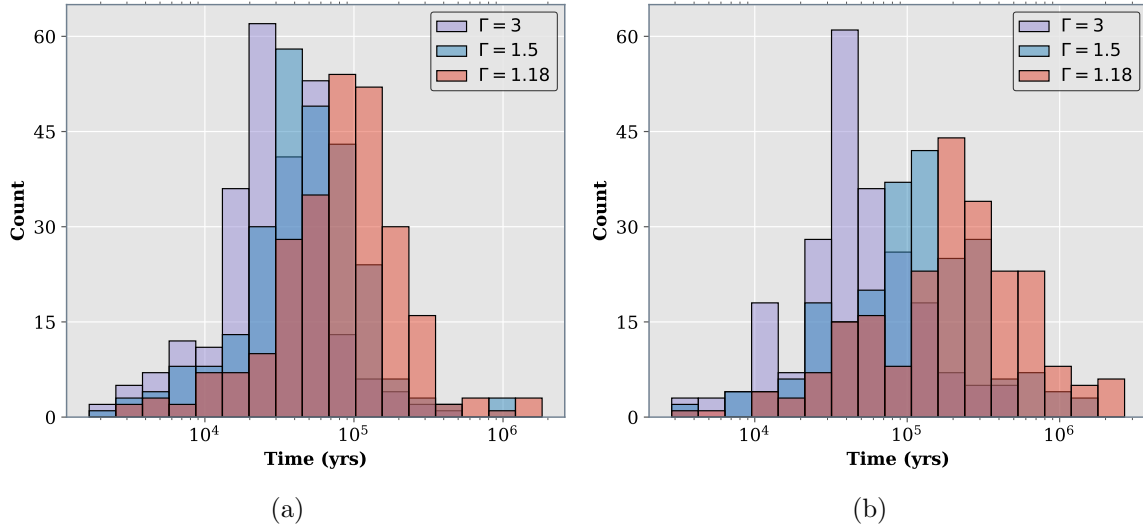


Figure 7. Histograms of knot-ejection timescales derived using inter-knot distances for different bulk Lorentz factors. (a) shows the histogram for timescales measured using the orientation scheme adopted in section 4.2 where the mean is $\approx 10^5$ yrs for $\Gamma = 1.18$, while smaller by a factor of 3 for $\Gamma = 1.5, 3$. (b) shows the same but with all the angles of quasars set to an unrealistic value of 5° . The distribution peaks above 10^5 yrs for $\Gamma = 1.18, 1.5$, while it remains roughly similar for $\Gamma = 3$, suggesting the knots can at most be mildly relativistic if an intermittent activity in the central engine is producing them.

Reynolds & Begelman (1997) suggested that an intermittent activity on timescales of $\geq 10^5$ yrs in the central engine with active jet production on periods of $\sim 10^4$ yrs can explain the observed distribution of radio-jet sizes. Accretion disk models with thermal-viscous instability (e.g., Siemiginowska & Elvis 1997) also indicate similar timescales for jet activity. Based on these works, Stawarz et al. (2004) suggested modulated jet activity produces the observed knotty morphology in radio jets. If the moving-knot model is viable at all, we can use the inter-knot distances to constrain their bulk Lorentz factor.

To derive this constraint, we measure the length of the jet segment between any two adjacent radio-knots for each source in our sample and de-project them using the orientation scheme discussed in section 4.2. Each segment is δ -corrected and converted into a timescale using a set of three bulk Lorentz factors. Figure 7a plots the resulting distribution for each of $\Gamma = 1.18, 1.5$ and 3 where it peaks about $\approx 10^5$ yrs for $\Gamma = 1.18$, while it peaks at about 3×10^4 yrs for $\Gamma = 1.5$ and 3, which is about three times smaller than the expected value. Because knots from CDQs and LDQs form the majority in our sample, our orientation scheme may be underestimating the de-projected lengths leading to smaller periods. To test if that is the case, we fix the inclinations of all the quasar knots to 5° , which is highly unlikely, and re-plot them in Figure 7b. The distributions now become wider with peaks above $\gtrsim 10^5$ yrs for $\Gamma = 1.18, 1.5$. However, it still peaks at about 3×10^4 yrs for $\Gamma = 3$. That means if the radio knots represent slow-moving blobs in the jet produced by modulated jet-

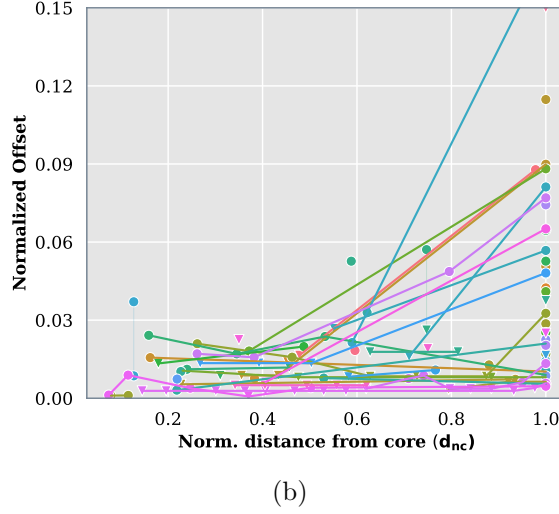


Figure 8. Normalized offsets in knots and hotspots of FR II-type jets plotted against the normalized distance from the core, showing a loose trend of offsets increasing with distance. The moving-knot model can produce this increase if a forward-moving shock determines the radio peak in the blob.

activity, they can at most be mildly-relativistic ($\Gamma \lesssim 1.5$). This limit is consistent with the bulk Lorentz factors derived from radio data (Wardle & Aaron 1997; Mullin & Hardcastle 2009), and also with the upper limits on proper motions ($\Gamma < 2.9$) of the kpc-scale optical knots in 3C 273 (Meyer et al. 2017). Moreover, if the X-ray emitting plasma is roughly at rest in the blob (knot) frame, it questions the large bulk Lorentz factors invoked to explain the observed X-ray emission in one-zone models.

4.4.2. Offsets vs. distance from the core

Figure 8 shows offsets in knots and hotspots (discussed in section 4.7) plotted against distance from the core, both normalized with the total length of the jet. Each jet is assigned a different color, and Xf-type and Co-s-type components are indicated with circles and triangles, respectively. Similar to Paper I we only observe a loose trend of offsets increasing with distance from the core, even with a larger sample. In 16 of 24 jets with at least one knot and a hotspot, the offset in the hotspot exceeds the maximum offset in knots; the count increases to 20 if we consider δ -corrected knot-offsets (see section 4.7). Suppose the offsets increase with distance from the core, and environmental effects presumably (e.g., jet-deflection) modify this trend. In that case, the radio peak must be moving further away from the X-ray peak as observed in the resolved knots of 3C 353 (Kataoka et al. 2008), with intrinsically larger offsets in hotspots. This trend can be reproduced in the moving-knot model if a forward shock propagating within the blob establishes the radio peak. As a result, the radio peak would move further away from the blob’s upstream edge with time, increasing the offset. Despite the qualitative match of the moving-blob model with several observed properties of jets, further theoretical investigations and more advanced numerical simulations are clearly necessary to confirm this and other speculations.

4.5. Flux Ratio

The observed offsets challenge one-zone models and clearly indicate the need for multi-zone models. However, offsets alone are insufficient to establish the exact emission mechanism in multi-zone models. One way to differentiate between synchrotron and IC/CMB modes is by studying X-ray/radio flux ratios. Because of the differences in beaming patterns, IC/CMB mode experiences enhanced beaming at smaller viewing angles (e.g., [Dermer 1995](#); [Harris et al. 2002b](#)) than the synchrotron radiation. Hence, closely aligned knots may show larger flux ratios than their misaligned counterparts. Moreover, due to the stronger dependence of IC/CMB on the Doppler factor compared to synchrotron, in a simplified scenario, the flux ratio may also smoothly decline along a decelerating jet. Below we test for any such systematic trends in the flux ratios of FR II-type knots in our sample.

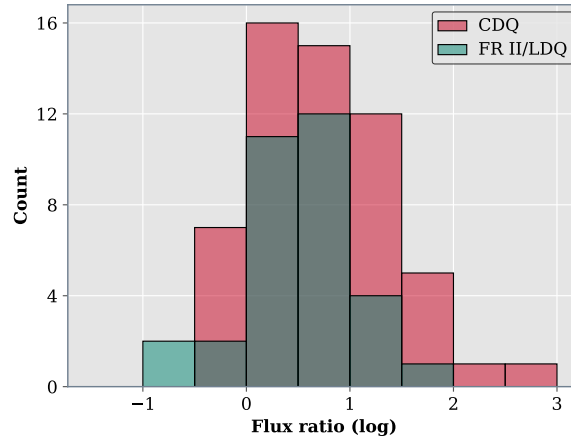


Figure 9. Histograms for log-scaled flux ratios of knots in CDQs and LDQ/FR II sources. A 2-sample AD test between the two groups reveals no statistically significant difference, suggesting that IC/CMB’s contribution to the X-ray emission may be minimal.

4.5.1. Test for differences in flux ratio distributions of aligned and misaligned sources

We first test for any differences in flux ratios of knots by dividing them into two groups. One with knots from CDQs, which are commonly believed to be viewed at small angles to our line of sight, and the other from their misaligned counterparts, the FR IIs and LDQs. Under this division, we might expect a significant difference in flux ratios between these two groups for simple one-zone IC/CMB mode of X-ray emission. Table 4 lists the X-ray flux density, evaluated at 1 keV, and the radio flux density along with its respective frequency for individual sources.

Figure 9 shows the flux ratio distributions for the two groups on a log-scale. A 2-sample AD test is unable to detect a difference between the two distributions (p -value > 0.25) at a high significance. Here the null hypothesis states that the two distributions are drawn from a single population. However, a large imbalance between the number of samples in each group (CDQ: 64, LDQ/FR II: 32) results in low

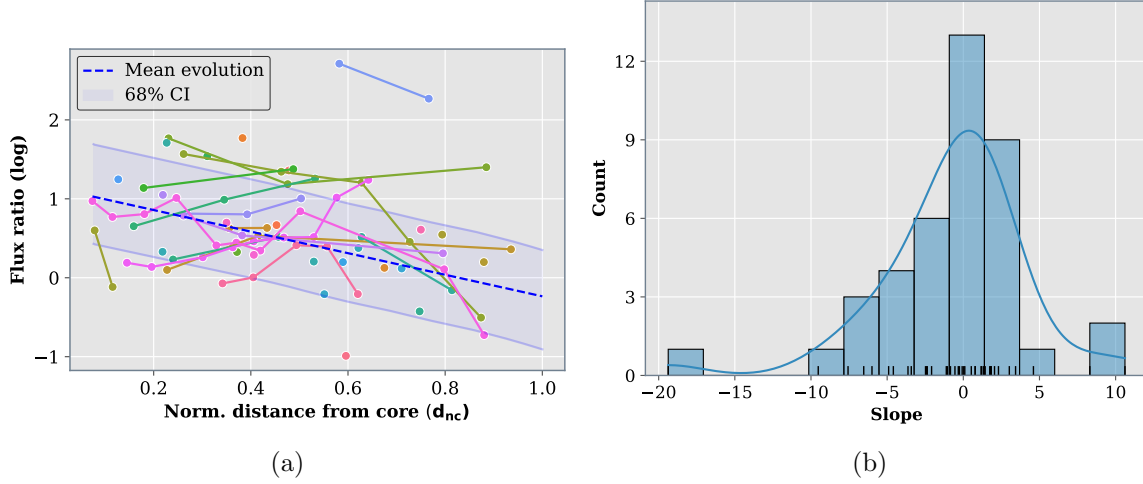


Figure 10. Trends in flux ratios. (a) shows flux ratio plotted against normalized distance from the core. Components from each jet are assigned the same color and joined with a solid line. The blue-dashed line shows the linear fit, which describes a general trend where the flux ratio decreases along the jet. The blue-shaded region indicates its 68% confidence interval. (b) shows the histogram of slopes for each line segment plotted in (a), with a peak near zero. Only the slopes for 16 out of the 34 segments lie below zero, indicating the declining trend is only marginally significant.

statistical power [<0.3 (see Table 1 in Razali et al. 2011)]. Put another way, this test has a $>70\%$ chance to incorrectly accept the null hypothesis even when there is an intrinsic difference. At least twice the number of present observations of knots in both the groups are required to confirm the presence (or absence) of any flux ratio differences with high statistical power.

4.5.2. Evolution of flux ratio along the jet

We next search for any trends associated with the flux ratio. To understand the general evolution of flux ratio along X-ray jets while accounting for the wide range of orientations and jet-lengths in our sample, we consider the relation between flux ratio and distance from the core, normalized by the jet’s total length. The left panel in Figure 10 shows the flux ratio plotted against the normalized distance, and the data points for individual jets are joined with solid lines. We perform a linear regression on the flux ratios of knots and obtain the following equation:

$$\log_{10} R = 1.14^{+0.13}_{-0.13} - 1.37^{+0.17}_{-0.17} \times d_{nc} \quad (2)$$

where R is the flux ratio and d_{nc} is the normalized distance from the core. The uncertainties correspond to the 1σ values. The blue dashed line indicates the fitted model in Figure 10 and the blue-shaded region its 68% confidence interval (CI). The slope of Eq. 2 indicates a mean flux ratio decline by a factor of $\sim 23^{+11}_{-8}$ between the inner and outer regions of the jet, which is slightly higher than what is observed in representative FR II sources like 3C 353 (Kataoka et al. 2008). To estimate the significance of this trend, we measured the slope of each line segment (59 total seg-

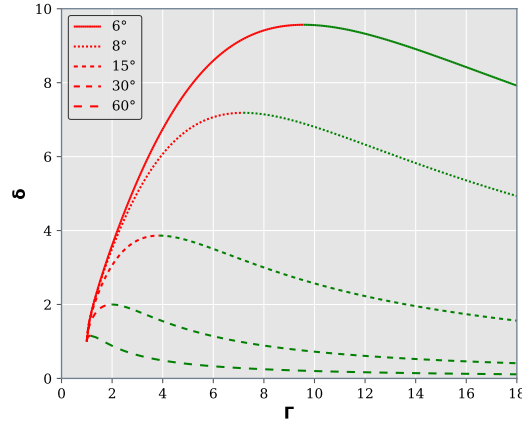


Figure 11. δ vs. Γ for different inclination angles. A jet decelerating in the red zone of each curve experiences reduced δ while it rises in the green zone.

ments) in Figure 10a. Their histogram, shown in Figure 10b, describes a unimodal distribution peaking at ≈ 0 with only 21 out of 40 (52%) segments lying below zero, indicating the measured declining trend is only marginally significant. It is possible, however, that the sample is contaminated by sources with non-jet sources of X-ray emission (for example those with shock-heated gas), which will modify the flux ratios. Deeper observations of jets would allow us to confirm via spectral fitting whether the X-rays are likely from the jet or another source.

4.5.3. Does a decelerating jet explain a decreasing flux ratio?

Under the IC/CMB scenario for X-ray production, a decreasing δ along the jet could result in a declining X-ray/Radio flux ratio since IC/CMB has a stronger dependence on δ than synchrotron due to differences in their beaming patterns. However, this is only true for jets with small inclination angles and fails to hold for misaligned jets. Specifically, for a jet aligned at an angle θ to our line of sight, deceleration can lower δ only when Γ falls below $\Gamma < 1/\sin \theta$ while the opposite happens when it remains above $\Gamma > 1/\sin \theta$. To see this visually, in Figure 11 we have plotted the theoretical curves of δ vs. Γ for different alignment angles (θ). Any deceleration decreases δ in the red zone while the converse happens in the green zone.

For a jet with $\theta=6^\circ$, if a knot requires, for example, $\Gamma=15$ to explain the observed X-ray flux, the jet must decelerate to below $\Gamma \lesssim 5$ at the next knot before any deceleration can reduce the flux ratio. However, the cold matter required to decelerate the jets by such large values can sometimes be implausibly high (Hardcastle 2006). Although a smaller deceleration in the red zone can reduce δ by an equal amount, the range of Γ within these zones is generally insufficient to reproduce the observed X-ray flux under IC/CMB. Furthermore, traditional one-zone IC/CMB interpretations of X-rays assume θ remains constant throughout the jet's extent. At $\Gamma=10$, δ decreases from about 10 to 7 even with a small change in θ , for instance, from $\theta=4^\circ$ to $\theta=6^\circ$,

which we may falsely perceive as deceleration. Hence, fine-tuned angles are unreasonable given the absence of any *straight* jets in our entire sample. Finally, in the case of highly-misaligned jets (e.g., $\theta=60^\circ$ curve in Fig. 11) where any deceleration practically always increases δ , no evidence for smoothly rising X-ray and radio fluxes along such jets has been reported so far. The absence of such observations independently rules out simple one-zone IC/CMB models and warrants the need for a multi-zone emission model, as previously suggested in different contexts (e.g., Stawarz et al. 2004; Jester et al. 2006; Siemiginowska et al. 2007; Kataoka et al. 2008).

4.6. Is there a wavelength-based beaming?

The previous two sections have evaluated flux ratios in the context of a one-zone IC/CMB model. Alternatively, to reconcile the small bulk Lorentz factors inferred from radio observations with large values required in IC/CMB models, a “spine-sheath” structure in the jet, with an X-ray-emitting fast spine surrounded by a radio-emitting slow sheath, has been suggested (e.g. Hardcastle 2006; Jester et al. 2006). Although this model explained the observed X-ray emission in a few jets, it sometimes required unrealistically large bulk Lorentz factors (e.g., Jester et al. 2006). In a different context, (Konar & Hardcastle 2013) find a fast spine ($\Gamma \gtrsim 10$) is necessary to explain similar injection spectral indices during different jet-production episodes of nearby double-double radio galaxies (DDRG).

These spine-sheath models were only evaluated in the case of a few jets, and it is unclear in general whether X-rays and radio can come from a fast spine and a slow sheath, respectively. Below we test whether the bulk Lorentz factors of X-ray and radio-emitting plasmas differ using the luminosity distributions for resolved knots.

The observed luminosity (L_ν^{obs}) from an isotropically emitting optically thin source with rest-frame luminosity $L_\nu^{in} \propto \nu^{-\alpha}$, moving with a bulk Lorentz factor Γ along an angle θ to our line of sight is given by (e.g., Blandford & Königl 1979; Jester 2008)

$$L_\nu^{obs} = \begin{cases} L_\nu^{in} \delta^{3+\alpha} (1+z)^{(1-\alpha)} & \text{(Discrete blob)} \\ L_\nu^{in} \delta^{2+\alpha} (1+z)^{(1-\alpha)} & \text{(Continuous flow)} \end{cases} \quad (3)$$

Because radio knots show extended structures in a wide range of redshifts (e.g., Kataoka et al. 2008; Siemiginowska et al. 2007), we approximate them as cylindrical blobs and use the first expression in Eq. 3 for radio in the following discussion. However, we consider both expressions for X-rays due to uncertainty in their emission geometry.

Figure 12 shows the X-ray and radio luminosity distributions in the left and right panels, respectively, and are color-coded based on their spectral class. The bottom panel shows the mean and 1σ limits for each class at each wavelength. The radio luminosity values are multiplied by a factor of 1.26 to enable easier comparison. Let us first consider the distributions in radio. The mean luminosity for FR II knots is $\sim 10^{40}$ ergs s $^{-1}$ and $\sim 10^{42}$ ergs s $^{-1}$ for CDQ and LDQ knots, both indicating a difference

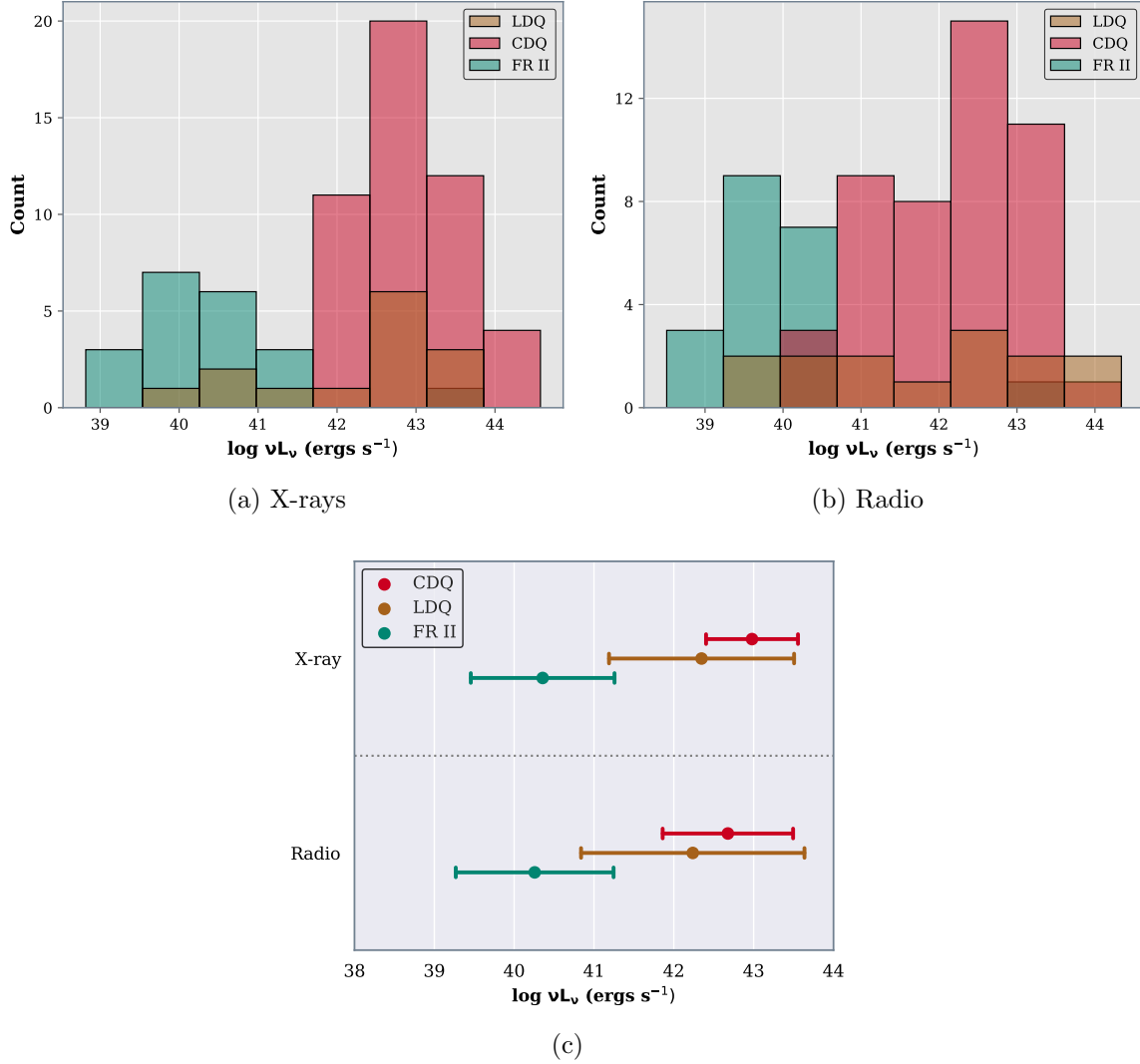


Figure 12. Class-wise histograms for (a) X-ray and (b) radio (right panel) luminosity of knots in FR II-type sources. (c) shows the mean values of each class at each wavelength, where the radio luminosity values are nudged to the right by 0.4 units (multiplied by 1.26) for easier comparison. The similarity in inter-class distance between the distributions (measured using the AD test statistic) at X-ray and radio wavelengths suggests that bulk Lorentz factors for both the emitting plasmas are similar.

of about 2 decades between FR II and quasar knot populations. If we assume all the FR-II knots align at 60° to our line of sight and all the quasar knots at 5° , the luminosity of an FR II knot with $\alpha = 0.8$ and $\Gamma = 1.8$ when it aligns at 5° , i.e., when it is *observed* as a quasar knot, increases by about 2 orders of magnitude. That means if the rest-frame luminosity of all the radio knots belong to a single parent population, beaming effects alone are sufficient to explain most of the observed dispersion in luminosity distributions. We quantify the magnitude of its effect as the sum of AD test-statistic measured between all the two-class combinations from the three spectral classes—the test statistic increases with a rise in the population’s average bulk Lorentz

factor. We measure a value of 34.96 ± 0.35 for the current sample, estimating errors via bootstrapping and assuming 30% error on the flux ratios.

On the other hand, the mean X-ray luminosity for FR II knots is about $\sim 10^{40.5}$ ergs s $^{-1}$, while it is about $\sim 10^{42.5}$ ergs s $^{-1}$ and $\sim 10^{43}$ ergs s $^{-1}$ for CDQ and LDQ knots, respectively. These values place the mean luminosity difference between FR II and quasar knots in the range of 2-2.5 decades. Similar to radio, the X-ray luminosity of a knot with $\alpha = 0.8$, $\Gamma = 2.1$, when approximated as a discrete blob, increases by ~ 2.5 orders of magnitude when its alignment changes from 60° to 5° ; continuous flow-like geometry requires $\Gamma \sim 1.8$. The magnitude of the beaming effect as quantified by the AD test-statistic for the X-ray knot population is 36.35 ± 0.65 and differs from the radio population's statistic 34.96 ± 0.35 only at the 1.1σ -level. That means the bulk Lorentz factors of X-ray and radio-emitting plasmas must be similar contrary to the large differences required in spine-sheath IC/CMB models.

The conclusions drawn here are independent of the assumed orientations. For example, if we assume quasar knots align at 15° and FR II-type knots at 90° , $\Gamma \sim 1.5$ is required in the radio while it becomes $\Gamma \sim 1.5$ (discrete blob) and $\Gamma \sim 1.75$ (continuous flow) in the X-rays.

We emphasize that the bulk Lorentz factors are similar only for the emitting plasmas and not the jet material that carries it. For example, the shocked plasma in the moving-knot model can be at rest in the slow-moving blob's frame, while the outer flow producing the shock can be much faster. Hence, this result is still consistent with the requirement for a faster spine in DDRGs.

The mean redshift for FR II knots is 0.13 ± 0.31 while it is 0.81 ± 0.41 and 0.75 ± 0.67 for CDQ and LDQ knots, respectively. Our analysis ignores any redshift-related enhancements in the intrinsic X-ray luminosity of knots. For instance, an IC/CMB component could become comparable to an already existing synchrotron component at higher redshift (e.g., [Zhu et al. 2019](#)), further reducing the beaming requirement and the bulk Lorentz factor. Finally, if the X-ray/radio bulk Lorentz factors and spectral indices are similar, and their emitting their emission geometries are similar, the flux ratio only weakly depends on beaming ($R \propto \delta^{\alpha_x - \alpha_r}$). That means differences in the X-ray/radio intrinsic luminosity ratio must provide the major contribution to the observed 2-3 orders of magnitude spread in the flux ratio's distribution (see [Fig. 9](#)). This spread is consistent with the observed offsets that indicate spatially separate X-ray/radio-emitting regions and, therefore, independent plasma conditions, producing a large scatter in intrinsic luminosity ratios.

4.7. Offsets in hotspots

Although we mainly focus on studying offsets in knots of FR II-type sources, we briefly discuss the offsets in hotspots for completeness. [Figure 13](#) shows the histograms of de-projected Xf-type offsets in hotspots, stacked with Co-s-type offsets by assuming a $0.15''$ angular offset. The Xf-type offsets are also the predominant type of offsets

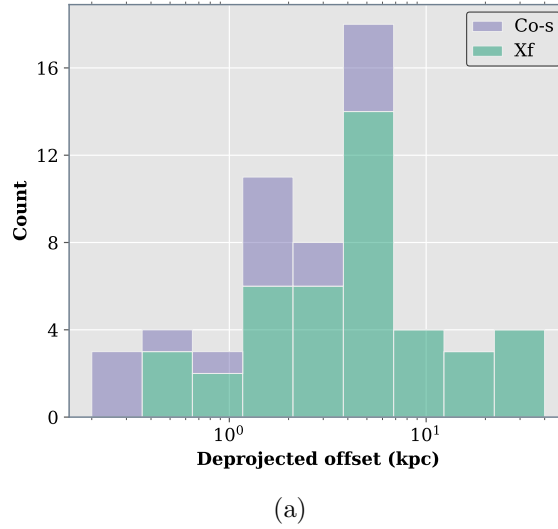


Figure 13. Histograms of de-projected Xf-type offsets in hotspots, stacked with Co-s-type hotspots assuming a $0.15''$ angular offset. Unlike offsets in knots, the Xf-type and Co-s-type hotspots may indicate different structures (see section 4.7).

in hotspots, similar to the knots in FR II-type jets. 43 out of the 63 hotspots in our sample show Xf-type offsets, ruling out simple one-zone IC (CMB or SSC) or synchrotron models, while 17 show Co-s-type offsets. The remaining three hotspots also show offsets, however, we cannot determine the type of offset, i.e., Xf or Rf-type, due to the uncertainty in the direction of their jets at this point. Hence, we indicate them as “Amb” offset-type in table 4.

Upper limits on offsets in Co-s-type hotspots, unlike in the case of knots, are distributed on the left side of the Xf-type’s roughly unimodal distribution. Projection and distance-related effects may be reducing any offsets in Co-s-type hotspots to below the detectable level. A 2-sample AD test also reveals no difference (p -value=0.25) between the flux ratios of the two types of hotspots, suggesting a possible intrinsic structural similarity between them. However, the redshift distributions for both kinds of hotspots are similar with means of 0.71 ± 0.55 and 0.65 ± 0.37 , respectively; each offset-type group also contains roughly equal proportions of FR II and quasar jets. These common traits suggest projection and distance-related effects are probably minimal, and possibly different mechanisms produce Xf and Co-s-type hotspots.

Interestingly, the mean de-projected offset in hotspots and knots are similar (≈ 4 kpc, see sec. 4.3). Moreover, a 2-sample AD test reveals no difference between their distributions (p -value > 0.25), suggesting a possible similarity in their multi-wavelength morphology. However, with the current physical understanding, it is unclear why the two offset distributions are similar when we expect entirely different processes to produce them. One possibility is that the orientations of knots and hotspots differ in most if not all the jets due to the larger likelihood of jets getting deflected in the turbulent hotspot region. To test this possibility, we modified the alignment angle

for each hotspot by adding a random angle between -15° and $+15^\circ$ while keeping the knot-angles unchanged and re-performed the AD test 10,000 times. None of the cases reported a p -value less than 0.14, ruling out the jet-deflection scenario. Alternatively, if we use the δ -corrected knot-offsets (with $\Gamma = 1.25$), we find the expected difference at the 0.2% significance level (although with low statistical power), further supporting the moving-knot model.

5. SUMMARY AND CONCLUSIONS

We used a statistical tool called LIRA to analyze a sample of 77 *Chandra*-detected X-ray jets to detect X-ray/radio offsets in individual features. We required an offset to be at least 1σ -level above $0.15''$ to be statistically significant. Our analysis of 164 components revealed 94 offsets with this criterion, where 58 of these are newly reported. Of the 114 FR II-type knots considered in this study as well as Paper I, we find 48 X-ray-first (Xf-type) offsets, 8 Radio-first (Rf-type) offsets, and 56 knots, which were co-spatial to within $0.15''$ (Co-s-type). Considering hotspots (bright terminal knots) separately, out of 69 considered in this paper and Paper I together, 49 are Xf-type offsets, 20 are Co-s-type offsets, and none are Rf-type. In the case of FR I-type sources, in total, we analyzed 30 knots and detected 20 Xf-type, 5 Rf-type, and 8 Co-s-type knots.

The predominance of Xf-type offsets in FR II-type knots questions the applicability of one-zone models. Although Co-s-type knots occur in similar numbers, they are mostly found in closely-aligned and higher redshift jets. A 2-sample AD test reveals no difference between the distributions of flux ratio and X-ray spectral index for Xf-type and Co-s-type knots. These considerations suggest both kinds of knots are intrinsically similar, and projection and distance effects may be reducing any observable offsets below the detectable level.

The distribution of offsets in FR II-type knots, de-projected using a simple orientation scheme based on the spectral classification of sources, roughly peak at ~ 4 kpc; the Co-s-type knots with assumed angular offset of $0.15''$ also shows a similar distribution. These offsets are also similar to the sizes of low-redshift radio knots, suggesting most if not all knots possess a similar morphology with an extended radio and compact X-ray structures. Adopting a simple ‘moving-knot’ model further reduces the effective mean offset to ~ 2 kpc and inter-class dispersion in the detected offsets.

We speculate that a modified version of the moving-knot model, previously proposed by Kataoka et al. (2008), can explain the observed offsets and multiple other observed properties of jets. The bulk Lorentz factor of radio knots, as implied by inter-knot distances, can at most be mildly relativistic ($\lesssim 1.5$) even with extreme jet-angle constraints. This speed is consistent with the limits derived using radio observations (e.g., Mullin & Hardcastle 2009). Finally, we find a loose trend of offsets increasing

with distance from the core, which can be explained with the moving-knot model by invoking a forward shock in the blob.

We find no difference between the flux ratio distributions of closely aligned (CDQs) and misaligned (LDQs and FR IIs) sources, indicating IC/CMB may be less likely to be the dominant X-ray emission mechanism. The flux ratio appears to decline with distance from the core in general (with marginal significance). Although a decelerating jet with IC/CMB can explain this trend, it generally requires unrealistic conditions. Furthermore, we measure the beaming effect on the dispersion of knot luminosity distributions as the sum of AD test statistic computed between the distributions of CDQ, LDQ, and FR II classes. Here we assume the intrinsic luminosity of all the knots in X-rays and radio belong to the same individual parent populations. The test statistic differs between X-rays and radio only at the 1.1σ -level, suggesting similar bulk Lorentz factors for the emitting plasmas.

These results indicate the need for two or multi-zone emission models that, unfortunately, increase the number of model parameters but provide more flexibility in explaining the observations. We summarize below the general properties of knots that future models must account for:

1. The X-rays peak and decay before the radio in most knots, requiring spatially separated emitting regions.
2. The radio appears to be more extended than the X-ray emission, which is generally unresolved in *Chandra* observations, and both the emitting plasmas have similar bulk Lorentz factors.
3. There is evidence that the radio-emitting plasma occupies a surface layer surrounding the jet instead of the entire cross-section (Swain et al. 1998). On the other hand, the X-rays appear in the central regions of transversely-resolved jets (e.g., Kataoka et al. 2008).
4. Radio polarization measurements indicate magnetic fields parallel to the jet in the outer regions while perpendicular to the jet in the inner regions (e.g., Swain et al. 1998; Bridle et al. 1994).

Hotspots predominantly show Xf-type offsets (43 out of 69). Although we find no difference between the flux ratio distributions of Xf-type and Co-s-type hotspots, hotspots in both groups are located at similar redshifts and comprise similar mixtures of aligned and misaligned sources. These similarities suggest that projection or distance-related effects are unlikely to reduce any offsets to produce Co-s-type hotspots, and the two types of hotspots possibly have different structures. The distributions of Xf-type offsets in knots and hotspots of FR II-type sources are similar; however, they differ for the moving-knot scenario.

APPENDIX

Table 5. List of all *Chandra* detected X-ray jets

Name	IAU Name	R.A. (J2000) hh:mm:ss	decl. (J2000) dd:mm:ss	z	β_{app}^a	Scale (kpc/'')	Class ^b	Reference
Sources analyzed in this work								
3C9	0017+154	+00:20:25.0	+15:40:54.7	2.012		8.57	LDQ	Fabian et al. (2003a)
3C15	0034+014	+00:37:04.0	-01:09:08.5	0.073		1.40	FRI (NLRG)	Kataoka et al. (2003)
3C31	0104+321	+01:07:25.0	+32:25:45.0	0.017		0.34	FRI (LERG)	Hardcastle et al. (2002)
4C+01.02	0106+013	+01:08:39.0	+01:35:00.3	2.099	26.83	8.43	CDQ	Hogan et al. (2011)
3C47	0133+207	+01:36:24.0	+20:57:27.4	0.425	6.41	5.50	LDQ	Hardcastle et al. (2004)
PKS 0144-522	0144-522	+01:46:48.6	-52:02:33.5	0.098		1.86	Q	Marshall et al. (2018)
4C+35.03	0206+355	+02:09:39.0	+35:47:50.9	0.037		0.72	FR I (RG)	Worrall et al. (2001)
PKS0208-512	0208-512	+02:10:46.0	-51:01:02.9	0.999		8.04	CDQ	Marshall et al. (2005)
3C66B	0220+427	+02:23:11.0	+43:00:31.2	0.022	1.03	0.43	FRI (LERG)	Hardcastle et al. (2001)
4C+28.07	0234+285	+02:37:52.0	+28:48:08.9	1.213	27.33	8.36	CDQ	Marshall et al. (2011)
3C78	0305+039	+03:08:26.2	+04:06:39.3	0.029	0.13	0.58	FR I (LERG)	Harwood & Hardcastle (2012)
3C83.1	0315+416	+03:18:16.0	+41:51:27.9	0.025		0.50	FRI (LERG)	Sun et al. (2005)
3C88	0325+023	+03:27:54.2	+02:33:42.0	0.030		0.61	FR I (NLRG)	Sun (2009)
PKS0405-12	0405-113	+04:07:48.0	-12:11:36.6	0.574		6.50	CDQ	Sambruna et al. (2004)
PKS0413-21	0413-210	+04:16:04.0	-20:56:27.5	0.808		7.54	CDQ	Marshall et al. (2005)
3C111	0415+379	+04:18:21.0	+38:01:35.8	0.049	8.42	0.95	FR II (BLRG)	Hogan et al. (2011)
3C120	0430+052	+04:33:11.0	+05:21:15.6	0.033	9.08	0.65	FR I (BLRG)	Harris et al. (2004b)
3C123	0433+295	+04:37:04.0	+29:40:13.7	0.218		3.49	FR II (LERG)	Hardcastle et al. (2001)
PKS 0454-46	0454-463	+04:55:51.0	-46:15:58.7	0.858		7.70	CDQ	Marshall et al. (2011)
PKS0605-08	0605-085	+06:08:00.0	-08:34:49.9	0.870	32.81	7.70	CDQ	Sambruna et al. (2004)
PKS0637-752	0637-752	+06:35:46.0	-75:16:16.8	0.651	11.40	6.90	CDQ	Chartas et al. (2000)
B20738+313	0738+313	+07:41:11.0	+31:12:00.2	0.631	11.09	6.90	CDQ	Siemiginowska et al. (2003b)

Table 5 continued on next page

Table 5 (continued)

Name	IAU Name	R.A. (J2000) hh:mm:ss	decl. (J2000) dd:mm:ss	z	β_{app}^a	Scale (kpc/'')	Class ^b	Reference
OJ +248	0827+243	+08:30:52.0	+24:10:59.8	0.939	24.67	7.90	CDQ	Jorstad & Marscher (2004)
4C+29.30	0836+299	+08:40:02.0	+29:49:00.5	0.064		1.20	FRI RG	Sambruna et al. (2004)
3C207	0837+133	+08:40:47.0	+13:12:23.0	0.680	13.32	7.10	LDQ	Brunetti et al. (2002)
OJ287	0851+202	+08:54:49.0	+20:06:30.6	0.306	20.06	4.48	BL Lac	Marscher & Jorstad (2011)
PKS0920-397	0920-397	+09:22:46.4	-39:59:35.0	0.591	30.79	8.50	CDQ	Marshall et al. (2005)
3C228	0947+145	+09:50:10.8	+14:20:00.6	0.552		6.62	FR II (NLRG)	Hardcastle et al. (2004)
Q0957+561	0957+561	+10:01:21.0	+55:53:56.5	1.410		8.50	LDQ	Chartas et al. (2002)
PKS1030-357	1030-357	+10:33:08.0	-36:01:56.8	1.455		8.53	CDQ	Marshall et al. (2005)
PKS1045-188	1045-188	+10:48:07.0	-19:09:35.7	0.595	10.86	6.64	CDQ	Hogan et al. (2011)
PKS1055+201	1055+201	+10:58:18.0	+19:51:50.9	1.110	10.46	8.20	LDQ	Schwartz et al. (2006)
3C254	1111+408	+11:14:38.0	+40:37:20.3	0.734		7.30	LDQ	Donahue et al. (2003)
PKS1127-145	1127-145	+11:30:07.0	-14:49:27.4	1.180	31.62	8.30	CDQ	Siemiginowska et al. (2002)
PKS1136-135	1136-135	+11:39:11.0	-13:50:43.6	0.554		6.40	LDQ	Sambruna et al. (2002)
3C263	1137+660	+11:39:57.0	+65:47:49.4	0.656	2.31	7.00	LDQ	Hardcastle et al. (2002)
3C265	1142+318	+11:45:29.0	+31:33:49.4	0.811		7.55	FR II (NLRG)	Bondi et al. (2004)
4C+49.22	1150+497	+11:53:24.0	+49:31:06.9	0.334	18.17	4.80	CDQ	Sambruna et al. (2002)
PKS1202-262	1202-262	+12:05:33.0	-26:34:04.5	0.789	10.97	7.48	CDQ	Marshall et al. (2005)
3C270.1	1218+339	+12:20:33.9	+33:43:12.1	1.528		8.69	Q	Wilkes et al. (2012)
M84	1222+131	+12:25:04.0	+12:53:13.1	0.003		0.08	FRI (IERG)	Harris et al. (2002a)
4C+21.35	1222+216	+12:24:55.0	+21:22:46.4	0.432	27.95	5.60	CDQ	Jorstad & Marscher (2006)
M87	1228+216	+12:30:49.0	+12:23:28.0	0.004	6.30	0.08	FRI (NLRG)	Marshall et al. (2002)
PKS1229-02	1229-021	+12:32:00.0	-02:24:05.3	1.045		8.10	CDQ	Tavecchio et al. (2007)
3C277.3	1251+278	+12:54:12.0	+27:37:34.0	0.085		1.67	FR II (HERG)	Worrall et al. (2016)
4C+52.27	1317+520	+13:19:46.0	+51:48:05.8	1.060		8.15	CDQ	Jorstad & Marscher (2006)
3C287.1	1330+022	+13:32:53.3	+02:00:45.7	0.216		3.62	FR II (BLRG)	Balmaverde et al. (2012)
PKS1335-127	1334-127	+13:37:40.0	-12:57:24.7	0.539	22.67	6.33	CDQ	Hogan et al. (2011)
4C+19.44	1354+195	+13:57:04.0	+19:19:07.4	0.720	9.84	7.20	CDQ	Sambruna et al. (2004)
3C294	1404+344	+14:06:44.0	+34:11:25.1	1.786		8.50	FR II (NLRG)	Fabian et al. (2003b)

Table 5 continued on next page

Table 5 (continued)

Name	IAU Name	R.A. (J2000) hh:mm:ss	decl. (J2000) dd:mm:ss	z	β_{app}^a	Scale (kpc/'')	Class ^b	Reference
3C295	1409+524	+14:11:21.0	+52:12:09.0	0.450	5.70	5.70	FR II (NLRG)	Massaro et al. (2013)
3C299	1419+419	+14:21:05.6	+41:44:48.5	0.367	5.25	5.25	FR II (NLRG)	Massaro et al. (2010)
PKS1421-490	1421-490	+14:24:32.0	-49:13:54.0	0.662	6.98	6.98	Q	Gelbord et al. (2005)
3C303	1441+522	+14:43:03.0	+52:01:37.3	0.141	2.50	2.50	FR II (BLRG)	Kataoka et al. (2003)
PKS1510-08	1510-089	+15:12:50.0	-09:05:59.7	0.361	47.00	5.00	CDQ	Sambruna et al. (2004)
3C325	1549+628	+15:49:58.4	+62:41:21.7	1.135	8.44	8.44	FR II	Salvati et al. (2008)
4C+00.58	1603+001	+16:06:13.0	+00:00:27.0	0.059	1.10	1.10	LDQ	Hodges-Kluck et al. (2010)
3C330	1609+660	+16:09:37.0	+65:56:43.6	0.550	6.40	6.40	FR II (NLRG)	Hardcastle et al. (2002)
4C+15.55	1622+158	+16:25:14.4	+15:45:21.9	1.406	8.66	8.66	FR II	Stockton et al. (2006)
3C346	1641+173	+16:43:49.0	+17:15:49.0	0.161	2.74	2.74	FRI (NLRG)	Worrall & Birkinshaw (2005)
3C345	1641+399	+16:42:59.0	+39:48:37.0	0.594	24.64	6.60	CDQ	Sambruna et al. (2004)
4C+69.21	1642+690	+16:42:08.0	+68:56:39.7	0.751	24.90	7.30	CDQ	Sambruna et al. (2004)
3C351	1704+605	+17:04:41.0	+60:44:30.7	0.372	5.10	5.10	LDQ	Brunetti et al. (2001)
[HB89] 1800+440	1800+440	+18:01:32.0	+44:04:21.9	0.663	21.85	6.98	CDQ	Hogan et al. (2011)
4C+56.27	1823+568	+18:24:07.1	+56:51:01.5	0.664	26.98	7.19	Q	Marshall et al. (2018)
3C380	1828+487	+18:29:32.0	+48:44:46.6	0.692	15.36	7.11	FR II	Marshall et al. (2005)
1849+670	1849+670	+18:49:16.0	+67:05:41.7	0.657	31.60	6.95	CDQ	Hogan et al. (2011)
4C+73.18	1928+738	+19:27:48.0	+73:58:01.6	0.302	22.37	4.40	CDQ	Sambruna et al. (2004)
3C403	1949+023	+19:52:16.0	+02:30:24.4	0.059	1.13	1.13	FR II (NLRG)	Kraft et al. (2005)
S52007+777	2007+777	+20:05:31.0	+77:52:43.0	0.342	4.40	4.80	BL Lac	Sambruna et al. (2008)
PKS2101-49	2101-490	+21:05:01.0	-48:48:46.5	1.040	8.12	8.12	CDQ	Marshall et al. (2005)
PKS2152-69	2152-699	+21:57:06.0	-69:41:23.7	0.028	0.56	0.56	FR II RG	Ly et al. (2005)
4C+08.64	2209+080	+22:12:02.0	+08:19:16.5	0.485	5.98	5.98	CDQ	Jorstad & Marscher (2006)
4C-03.79	2216-038	+22:18:52.0	-03:35:36.9	0.901	6.91	7.81	(FRI/II) CDQ	Hogan et al. (2011)
3C452	2243+394	+22:45:49.0	+39:41:15.7	0.081	1.50	1.50	FR II (NLRG)	Hardcastle et al. (2004)
3C454.3	2251+158	+22:53:58.0	+16:08:53.6	0.859	25.40	7.70	CDQ	Marshall et al. (2005)

Sources from reference

Table 5 continued on next page

Table 5 (*continued*)

Name	IAU Name	R.A. (J2000) hh:mm:ss	decl. (J2000) dd:mm:ss	z	β_{app}^a	Scale (kpc/'')	Class ^b	Reference
3C33	0106+130	+01:08:53.0	+13:20:13.8	0.060		1.14	FR II (NLRG)	Kraft et al. (2007)
Pictor A	0518-458	+05:19:50.0	-45:46:44.5	0.035		0.69	FR II (BLRG)	Wilson et al. (2001)
3C227	0945+076	+09:47:45.0	+07:25:20.6	0.086		1.59	FR II (BLRG)	Hardcastle et al. (2007)
3C273	1226+023	+12:29:07.0	+02:03:08.6	0.158	19.19	2.70	CDQ	Marshall et al. (2001)
3C327	1600+021	+16:02:27.0	+01:57:56.2	0.104		1.89	FR II	Hardcastle et al. (2007)
3C353	1717+009	+17:20:28.0	-00:58:47.0	0.030		0.60	FR II	Kataoka et al. (2008)
3C390.3	1845+797	+18:42:09.0	+79:46:17.2	0.056	2.57	1.08	FR II (BLRG)	Hardcastle et al. (2007)
Cyg A	1957+405	+19:59:28.0	+40:44:01.9	0.056	1.20	1.07	FR II RG	Wilson et al. (2000)
4C +74.26	2043+749	+20:42:37.0	+75:08:02.5	0.104		1.90	LDQ	Erlund et al. (2007)
3C445	2221-020	+22:23:50.0	-02:06:12.4	0.056		1.10	FR II RG	Perlman et al. (2009)

Remaining sources

3C6.1	0013+790	+00:16:31.0	+79:16:49.9	0.840		7.84	FR II (NLRG)	Hardcastle et al. (2004)
3C13	0031+391	+00:34:14.6	+39:24:16.6	1.351		8.63	FR II (NLRG)	Wilkes et al. (2013)
3C16	0035+130	+00:37:44.6	+13:19:55.0	0.405		5.57	FR II	Massaro et al. (2013)
3C17	0035-024	+00:38:21.0	-02:07:40.7	0.220		3.64	FR II (BLRG)	Massaro et al. (2009)
3C19	0038+328	+00:40:55.0	+33:10:08.0	0.482		6.16	FR II (LERG)	Massaro et al. (2015)
3C29	0055+016	+00:57:34.9	-01:23:27.9	0.045		0.89	FR I (LERG)	Massaro et al. (2012)
NGC315	0055+300	+00:57:49.0	+30:21:08.8	0.016	0.81	0.32	FR I RG	Worrall et al. (2003)
3C41	0123+239	+01:26:44.4	+33:13:11.2	0.795		7.70	FR II (HERG)	Massaro et al. (2018)
3C52	0145+532	+01:48:29.0	+53:32:35.4	0.290		4.47	FR II (HERG)	Massaro et al. (2010)
3C54	0152+435	+01:55:30.2	+43:45:55.4	0.827		7.80	FR II (HERG)	Massaro et al. (2018)
3C61.1	0210+860	+02:22:35.0	+86:19:06.2	0.188		3.32	FR II (HERG)	Massaro et al. (2010)
3C65	0220+397	+02:23:43.2	+40:00:52.5	1.176		8.49	FR II (HERG)	Wilkes et al. (2013)
3C68.2	0231+313	+02:34:23.9	+31:34:17.5	1.575		8.69	FR II (HERG)	Wilkes et al. (2013)
WISE J031552.09-190644.2	0313-192	+03:15:52.0	-19:06:44.3	0.067		1.27	FR I RG	Keel et al. (2006)

Table 5 *continued on next page*

Table 5 (continued)

Name	IAU Name	R.A. (J2000) hh:mm:ss	decl. (J2000) dd:mm:ss	z	β_{app}^a	Scale (kpc/'')	Class ^b	Reference
3C105	0404+033	+04:07:16.5	+03:42:25.8	0.089		1.71	FR II	Massaro et al. (2010)
3C109	0410+110	+04:13:40.0	+11:12:13.8	0.306		4.50	FR II (BLRG)	Hardcastle et al. (2004)
3C129	0445+449	+04:49:09.0	+45:00:39.3	0.021		0.42	FR I RG	Harris et al. (2002b)
3C133	0459+252	+05:02:58.5	+25:16:25.1	0.278		4.35	FR II (HERG)	Massaro et al. (2010)
PKS0521-36	0521-365	+05:22:58.0	-36:27:30.8	0.055		1.06	BL Lac	Birkinshaw et al. (2002)
WISE J053239.00+073243.2	0529+075	+05:32:39.0	+07:32:43.3	1.254	23.26	8.40	CDQ	Hogan et al. (2011)
3C154	0610+260	+06:13:50.1	+26:04:36.7	0.580		6.77	Q	Massaro et al. (2018)
3C171	0651+542	+06:55:14.8	+54:09:00.1	0.238		3.89	FR II (HERG)	Massaro et al. (2010)
3C173.1	0702+749	+07:09:18.0	+74:49:31.8	0.292		4.30	FR II (LERG)	Hardcastle et al. (2004)
3C179	0723+679	+07:28:12.0	+67:48:47.5	0.846	8.99	7.70	LDQ	Sambruna et al. (2004)
3C181	0725+147	+07:28:10.3	+14:37:36.2	1.382		8.65	Q	Wilkes et al. (2013)
B3 0727+409	0727+409	+07:30:51.3	+40:49:50.8	2.500	6.61	8.27	Q	Simionescu et al. (2016)
4C+25.21	0730+257	+07:33:08.8	+25:36:25.1	2.686		8.14	Q	McKeough et al. (2016)
DA240	0745+56	+07:48:37.0	+55:48:58.0	0.036		0.70	-	-
QSO B0748+126	0748+126	+07:50:52.0	+12:31:04.8	0.889	18.84	7.98	Q	Marshall et al. (2018)
3C189	0755+379	+07:58:28.0	+37:47:11.8	0.043		0.83	FR I RG	Worrall et al. (2001)
3C191	0802+013	+08:04:48.0	+10:15:23.7	1.956		8.60	Q	Erlund et al. (2006)
4C +05.34	0805+046	+08:07:57.5	+04:32:34.5	2.877		7.99	Q	McKeough et al. (2016)
3C200	0824+294	+08:27:25.4	+29:18:44.9	0.458		6.00	FR II (LERG)	Hardcastle et al. (2004)
QSO J0833+0959	0830+101	+08:33:22.5	+09:59:41.1	3.713		7.33	Q	Marshall et al. (2018)
TXS0833+585	0833+585	+08:37:22.4	+58:25:01.8	2.101	14.17	8.53	Q	McKeough et al. (2016)
3C212	0855+143	+08:58:41.0	+14:09:43.9	1.049		8.10	LDQ	Aldcroft et al. (2003)
3C210	0855+280	+08:58:10.0	+27:50:51.6	1.169		8.48	FR II (HERG)	Gilmour et al. (2009)
3C213.1	0858+292	+09:01:05.3	+29:01:46.9	0.194		3.33	FR II (LERG)	Massaro et al. (2010)
4C+47.29	0859+470	+09:03:04.0	+46:51:04.1	1.465	16.41	8.68	Q	Marshall et al. (2018)
3c 215	0903+169	+09:06:31.9	+16:46:11.9	0.412		5.64	Q	Hardcastle et al. (2004)
PKS0903-573	0903-573	+09:04:53.0	-57:35:05.8	0.695		7.12	CDQ	Marshall et al. (2005)
6C0905+39	0905+399	+09:08:16.9	+39:43:26.0	1.883		8.63	FR II (HERG)	Erlund et al. (2008)

Table 5 continued on next page

Table 5 (continued)

Name	IAU Name	R.A. (J2000) hh:mm:ss	decl. (J2000) dd:mm:ss	z	β_{app}^a	Scale (kpc/'')	Class ^b	Reference
PMN J0909+0354	0906+041	+09:09:15.9	+03:54:43.0	3.431		7.66	Q	Ighina et al. (2022)
3C219	0917+458	+09:21:09.0	+45:38:57.4	0.174		2.90	FR II RG (HERG)	Comastri et al. (2003)
3C220.2	0927+362	+09:30:33.5	+36:01:24.2	1.157		8.47	Q	Stuadi et al. (2018)
3C225B	0939+139	+09:42:15.4	+13:45:50.5	0.580		6.77	FR II (HERG)	Massaro et al. (2018)
4C +55.17	0954+556	+09:57:38.2	+55:22:57.8	0.900		8.01	Q	Tavecchio et al. (2007)
3C234	0958+290	+10:01:49.5	+28:47:09.0	0.185		3.21	FR II	Massaro et al. (2012)
4C+13.41	1004+130	+10:07:26.0	+12:48:56.2	0.240		3.76	LDQ	Miller et al. (2006)
3C238	1008+066	+10:11:00.4	+06:24:39.7	1.405		8.66	FR II (HERG)	Stuadi et al. (2018)
3C 239	1008+467	+10:11:45.3	+46:28:18.8	1.781		8.60	FR II (HERG)	Jimenez-Gallardo et al. (2020)
7C 1013+2053	1013+208	+10:16:44.3	+20:37:47.3	3.114		7.80	Q	Snios et al. (2021)
3C245	1040+123	+10:42:44.6	+12:03:31.3	1.028	0.60	8.28	Q	Sambruna et al. (2004)
PKS1046-409	1046-409	+10:48:38.0	-41:13:59.6	0.620		6.78	CDQ	Marshall et al. (2005)
3C 249	1059-009	+11:02:03.8	-01:16:16.7	1.554		8.61	LDQ	Jimenez-Gallardo et al. (2020)
3C 257	1120+057	+11:23:09.4	+05:30:18.5	2.474		8.24	FR II	Jimenez-Gallardo et al. (2020)
3C264	1142+195	+11:45:05.0	+19:36:22.7	0.022		0.43	FR I (LERG)	Perlman et al. (2010)
3C268.1	1157+732	+12:00:19.2	+73:00:45.7	0.970		8.17	FR II (NLRG)	Massaro et al. (2015)
3C268.2	1158+318	+12:00:59.1	+31:33:27.9	0.362		5.21	FR II (HERG)	Massaro et al. (2012)
NGC4261	1216+061	+12:19:23.0	+05:49:30.8	0.007		0.15	FR I RG	Chiaberge et al. (2003)
B3 1239+376	1239+376	+12:42:09.8	+37:20:05.7	3.819		7.25	Q	McKeough et al. (2016)
3C275.1	1241+266	+12:43:58.0	+16:22:53.2	0.555		6.40	LDQ	Crawford & Fabian (2003)
3C280	1254+476	+12:56:57.0	+47:20:19.9	0.996		8.00	FR II (HERG)	Donahue et al. (2003)
3C 280.1	1258+404	+13:00:33.4	+40:09:07.3	1.667		8.62	LDQ	Jimenez-Gallardo et al. (2020)
3C281	1305+069	+13:07:54.0	+06:42:14.3	0.602		6.70	LDQ	Crawford & Fabian (2003)
PKS1311-270	1311-270	+13:13:47.4	-27:16:49.3	2.260		8.44	Q	McKeough et al. (2016)
4C+11.45	1318+113	+13:21:18.8	+11:06:50.0	2.179		8.49	Q	McKeough et al. (2016)
CenA	1322-428	+13:25:28.0	-43:01:08.8	0.002		0.02	FRI RG	Kraft et al. (2000)
4C+65.15	1323+655	+13:25:30.0	+65:15:13.5	1.625		8.60	LDQ	Miller & Brandt (2009)
CenB	1343-601	+13:46:49.0	-60:24:29.9	0.013		0.26	FRI RG	Marshall et al. (2005)

Table 5 continued on next page

Table 5 (*continued*)

Name	IAU Name	R.A. (J2000) hh:mm:ss	decl. (J2000) dd:mm:ss	z	β_{app}^a	Scale (kpc/'')	Class ^b	Reference
3C293	1350+316	+13:52:17.8	+31:26:46.5	0.045		0.93	FR I (LERG)	Massaro et al. (2010)
QSO B1402+044	1402+044	+14:05:01.1	+04:15:35.8	3.215		7.73	Q	Snios et al. (2021)
3C296	1414+110	+14:16:53.0	+10:48:27.7	0.024		0.47	FR I (LERG)	Hardcastle et al. (2005b)
3C297	1414-037	+14:17:24.0	-04:00:47.5	1.406		8.66	Q	Stuardi et al. (2018)
PKS 1418-064	1418-064	+14:21:07.8	-06:43:56.4	3.689		7.35	Q	McKeough et al. (2016)
B3 1428+422	1428+422	+14:30:23.7	+42:04:36.5	4.715		6.62	Q	Cheung et al. (2012)
3C305	1448+634	+14:49:21.6	+63:16:14.0	0.042		0.85	FR II	Hardcastle et al. (2012)
3C313	1508+080	+15:11:00.0	+07:51:50.0	0.461		6.02	FR II (HERG)	Massaro et al. (2013)
TXS1508+572	1508+572	+15:10:03.0	+57:02:44.0	4.300		6.90	Q	Siemiginowska et al. (2003a)
AP Lib	1514-241	+15:17:42.0	-24:22:19.5	0.049		0.94	BL Lac	Kaufmann et al. (2013)
3C321	1529+242	+15:31:44.0	+24:04:19.0	0.096		1.80	FR II (NLRG)	Hardcastle et al. (2004)
3C 322	1533+557	+15:35:01.3	+55:36:52.3	1.681		8.61	FR II	Jimenez-Gallardo et al. (2020)
3C324	1547+215	+15:49:49.0	+21:25:38.1	1.206		8.40	FR II (HERG)	Hardcastle et al. (2004)
3C 326.1	1553+202	+15:56:10.2	+20:04:20.7	1.825		8.59	RG	Jimenez-Gallardo et al. (2020)
3C327.1	1602+014	+16:04:45.3	+01:17:51.0	0.462		6.02	FR II (HERG)	Massaro et al. (2013)
QSO B1607+1819	1607+183	+16:10:05.3	+18:11:43.5	3.122		7.80	Q	Snios et al. (2021)
3C334	1618+177	+16:20:21.8	+17:36:24.0	0.555	3.36	6.63	Q	Hardcastle et al. (2004)
3C341	1626+738	+16:28:04.0	+27:41:43.0	0.448		5.92	FR II (HERG)	Massaro et al. (2013)
NGC6251	1637+826	+16:32:32.0	+82:32:16.5	0.025		0.49	FRI/II (LERG)	Evans et al. (2005)
3C349	1658+371	+16:59:29.5	+47:02:44.1	0.205		3.47	FR II (HERG)	Massaro et al. (2010)
4C+62.29	1745+624	+17:46:14.0	+62:26:54.7	3.889		7.20	LDQ	Cheung et al. (2006)
7C 1754+6737	1754+678	+17:54:22.3	+67:37:34.6	3.600		7.42	Q	McKeough et al. (2016)
3C368	1802+110	+18:05:06.5	+11:01:35.1	1.131		8.44	FR II (HERG)	Massaro et al. (2015)
3C371	1807+698	+18:06:51.0	+69:49:28.1	0.051	18.17	0.98	BL Lac	Pesce et al. (2001)
TXS1834+612	1834+612	+18:35:19.7	+61:19:40.0	2.274		8.43	Q	McKeough et al. (2016)
3C402	1940+504	+19:41:46.0	+50:35:48.4	0.026		0.53	FR I	Massaro et al. (2012)
3C 418	2037+511	+20:38:37.0	+51:19:12.4	1.686	6.86	8.61	Q	Reddy et al. (2021)
4C+23.56	2104+233	+21:07:14.8	+23:31:45.0	2.483		8.29	Q	Blundell & Fabian (2011)

Table 5 *continued on next page*

Table 5 (*continued*)

Name	IAU Name	R.A. (J2000) hh:mm:ss	decl. (J2000) dd:mm:ss	z	β_{app}^a	Scale (kpc/'')	Class ^b	Reference
PKs2123-463	2123-463	+21:26:31.0	-46:05:47.9	1.670		8.56	CDQ	Marshall et al. (2011)
3C436	2141+279	+21:44:11.7	+28:10:19.0	0.214		3.58	FR II (HERG)	Massaro et al. (2010)
3C437	2145+151	+21:47:25.1	+15:20:37.5	1.480		8.68	FR II	Massaro et al. (2015)
PKS2155-152	2155-152	+21:58:06.0	-15:01:09.3	0.672	21.46	7.02	CDQ	Hogan et al. (2011)
PKS2201+044	2201+044	+22:04:18.0	+04:40:02.0	0.027		0.54	BL Lac	Sambruna et al. (2007)
4C+31.63	2201+315	+22:03:15.0	+31:45:38.3	0.295	8.81	4.37	CDQ	Hogan et al. (2011)
NGC7385	2247+313	+22:49:54.6	+11:36:30.8	0.028		0.52	FR I	Rawes et al. (2015)
PKS 2255-282	2255-282	+22:58:06.0	-27:58:21.3	0.926	6.15	7.88	CDQ	Marshall et al. (2011)
3C458	2310+050	+23:12:54.4	+05:16:46.0	0.289		4.46	FR II (HERG)	Massaro et al. (2012)
3C465	2335+46	+23:38:29.0	+27:01:55.9	0.029		0.58	FR I	Hardcastle et al. (2005a)
2345-167	2345-167	+23:48:03.0	-16:31:12.0	0.576	13.50	6.54	CDQ	Hogan et al. (2011)
3C470	2356+437	+23:58:35.9	+44:04:45.6	1.653		8.69	FR II	Hogan et al. (2011)
PKSJ2310-437		+23:10:42.0	-43:47:34.3	0.089		1.60	FR I	Bliss et al. (2009)
PSO J352.4034-15.3373		+23:29:36.8	-15:20:14.5	5.840			Q	Connor et al. (2021)
PSO J047.4478+27.2992		+03:09:47.4	+27:17:57.6	6.100		5.79	Q	Snios et al. (2021)

^aThe maximum apparent superluminal motions are compiled from Keenan et al. (2021)

^bThe class column gives a radio jet morphology descriptor: Fanaroff-Riley I or II, CDQ (core dominated quasar), LDQ (Lobe dominated quasar), BL Lac, and an optical spectroscopic designation: LERG (low-excitation radio galaxy), HERG (high-excitation radio galaxy), NLRG (Narrow-line radio galaxy), BLRG (broad-line radio galaxy)

A. EXCLUDED SOURCES

Besides high- z jets, lack of spatially-correlated features and jets with closely-spaced knots are the two main reasons for exclusion. Here we present examples of sources from the two categories in Figure 14 where each panel shows an X-ray image with the corresponding VLA radio contours overlaid on top. The top panels show examples for the first type where (a) shows AP Librae with spatially-overlapping radio and X-ray jets but with no correlation in their brightnesses, and (b) shows 4C+13.41 with X-ray and radio jets but mostly non-overlapping. Figure 14(c) shows 3C 371 as an example for the second type where all the features are closely-spaced (separation $< 1''$) that preclude constructing large enough ROIs around each component to accurately measure offsets.

Figure 15(a) shows the redshift distribution for all the 199 X-ray jets with the sources considered for offset analysis in Paper I and this paper. (b) shows the stacked histogram of redshift only for the sources considered for offset analysis with the FR I-type colored orange and the FR-II type colored blue.

Because we mainly focus on understanding the nature of X-ray emission from FR II-type sources, to understand the impact of several excluding sources, we plotted their redshift distributions in 15(c). As can be seen, the FR II radio galaxies form the major portion of the excluded sources. In section 4.5, we find no significant evidence for difference between the flux ratios of FR II/LDQ and CDQ knots, although with a low statistical power due to the small sample size. In section 4.3, we find similar offsets in FR II and quasar knots that become more uniform if the knots are moving. Hence, unless the offsets and flux ratios of any knots in the excluded FR II are significantly lower than their included counterparts, the trends found in Section 4 will remain unaltered.

B. NOTES ON INDIVIDUAL SOURCES

3C 9 (Figure 1): This is an intermediate redshift LDQ ($z=2.01$) with a knotty jet. The jet bends towards west at knot H, which produces the brightest radio feature in the jet, presumably interacting with the large-scale gas clouds (Fabian et al. 2003a) and producing an internal shock. This knot shows an Xf-type offset of $0.29''$ (2.49 kpc) .

3C 15 (Figure 16): This is an FR I source. The X-ray emission brightens at the so-called *flaring* region (e.g., Hardcastle et al. 2001) while the radio peaks $0.657''$ (0.92 kpc) further downstream at knot B, showing an Xf-type offset. On the other hand, the X-rays coincide with the radio in knot C.

3C 31 (Figure 17): This is an FR I source. The jet most likely flares and decelerates near the radio knot B (Hardcastle et al. 2002). The X-ray centroid lies $0.77''$ (0.26 kpc) upstream of the radio peak in knot B. Despite the presence of

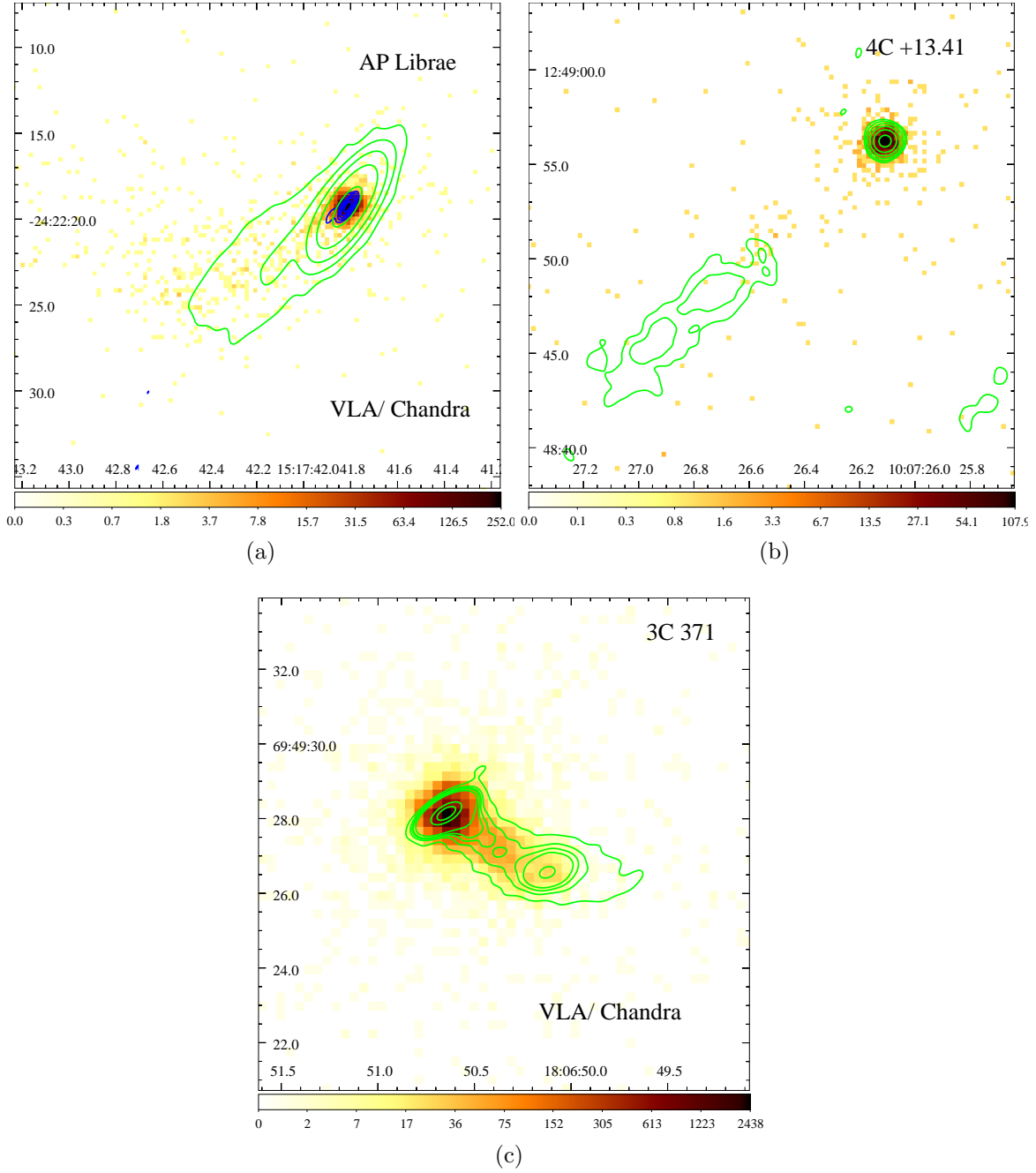


Figure 14. Examples of sources excluded from analysis. The top panels show examples for jets with no spatially-correlated X-ray radio features. (a) X-ray image (bin: 0.5) of AP Librae overlaid with 1.4 GHz VLA radio contours, where both the jets lie along the same position angle but show not correlated features (b) X-ray image of 4C +13.41 with the VLA 8.4 GHz radio contours overlaid. The X-ray and radio jets are mostly spatially disjoint. (c) X-ray image of 3C 371 with the VLA 4.8 GHz radio contours overlaid. The small inter-knot spacing (separation $< 1''$) prevents accurately measuring the centroids on LIRA images.

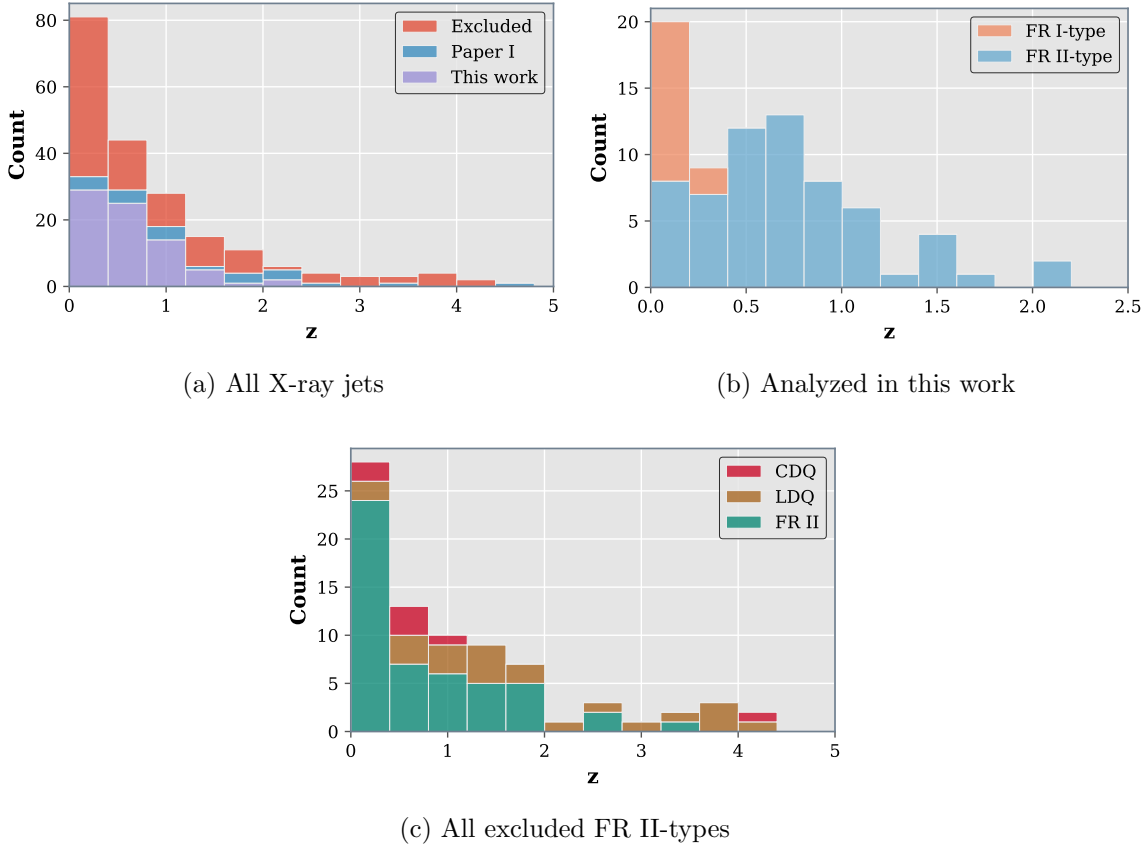


Figure 15. Redshift distribution for X-ray jets. (a) shows the stacked histogram of redshift for all the 199 X-ray jets compiled in this work; sources included and excluded from the offset analysis are colored blue and gray, respectively. (b) shows the class-wise stacked histogram of redshift for the sources considered for offset analysis; FR I-type and FR II-type are colored orange and blue, respectively. (c) shows the stacked redshift distributions of excluded FR II-type sources, divided into individual spectral classes.

significant X-ray emission further downstream of knot B, we exclude it from offset analysis due to lack of clear association with the radio morphology.

4C+01.02 (Figure 18): This is an intermediate redshift ($z=2.01$) CDQ. The jet makes an apparent bend to the southwest at knot B where the X-ray centroid and the radio peak coincide. It is possible that the jet presumably aligns closer to our line of sight (Kharb et al. 2012). On the other hand, the southern hotspot (SHS) shows a $0.40''$ (3.37 kpc) Xf-type offset.

3C 47 (Figure 19): This is an LDQ. The jet makes a sharp apparent bend to the west at SHS where the X-ray centroid coincides with the radio peak. Although the radio jet travels further down terminating in a fainter peak, it lacks any significant X-ray emission.

PKS 0144-522 (Figure 20): This is a nearby quasar detected in a recent survey

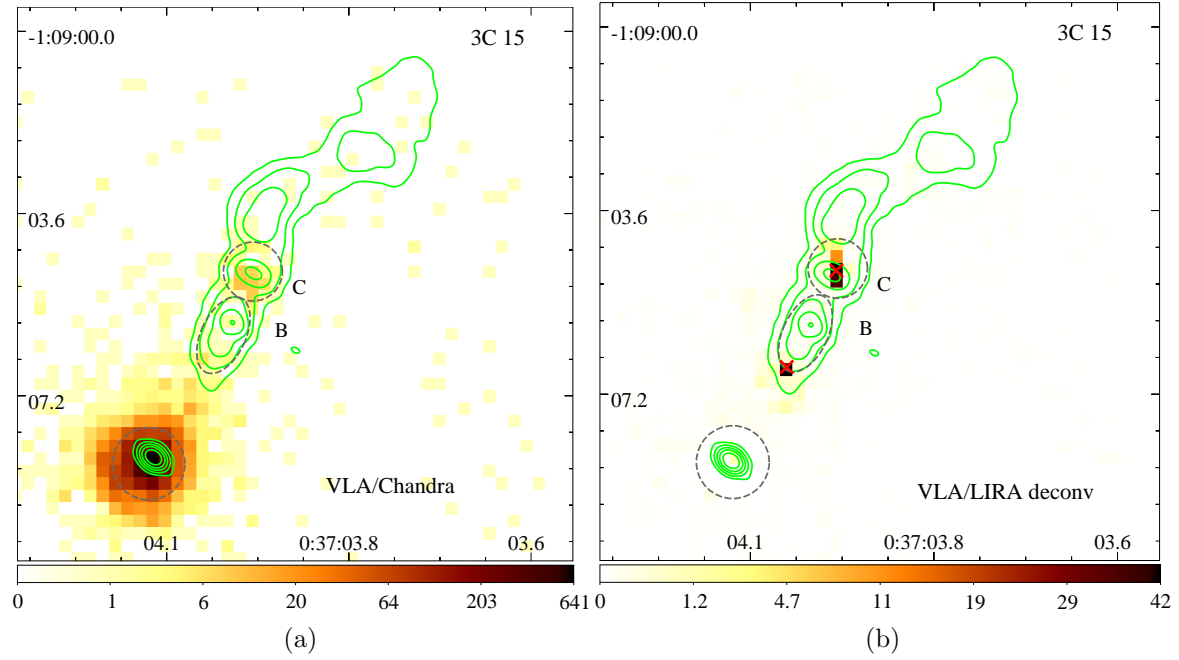


Figure 16. Same as in Fig. 1 but for 3C15. The radio contours are given by 0.2, 0.8, 2.0, 4.0, 8.0 mJy beam⁻¹.

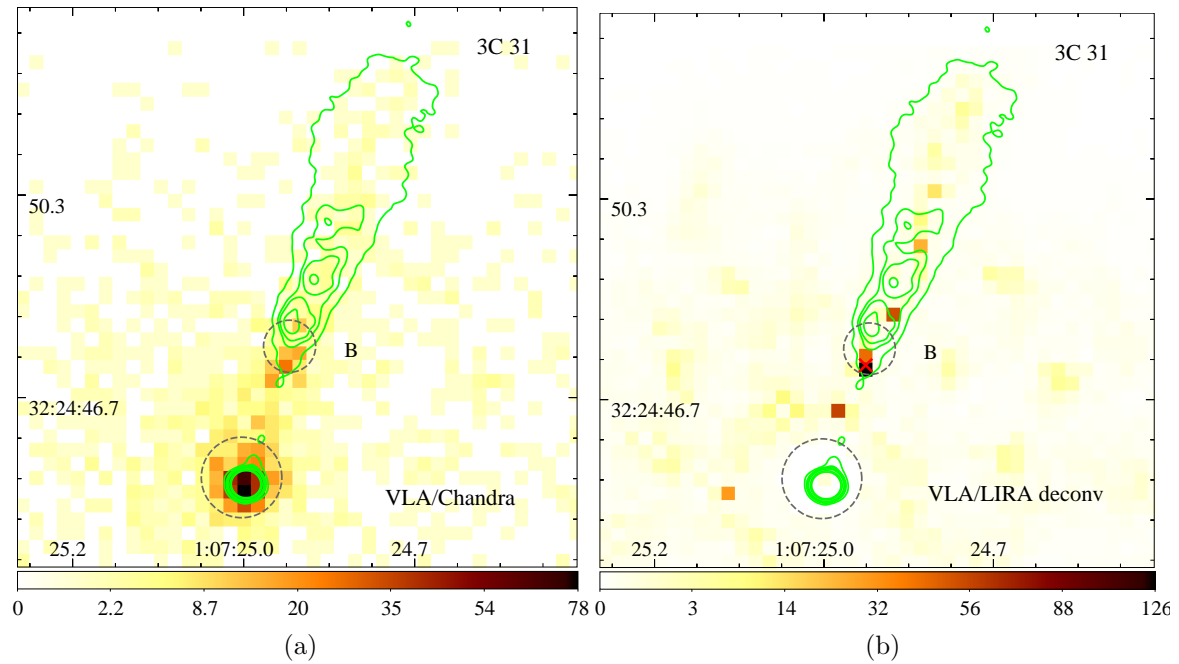


Figure 17. Same as in Fig. 1 but for 3C 31. The radio contours are given by 0.1, 0.3, 0.4, 0.6, 0.8, 2.0, 3.5 mJy beam⁻¹.

(Marshall et al. 2018). The radio map shows a faint jet an inner knot an extension to the southeast of the core. The inner knot, A, shows no offset, while only little X-ray emission is seen beyond this knot.

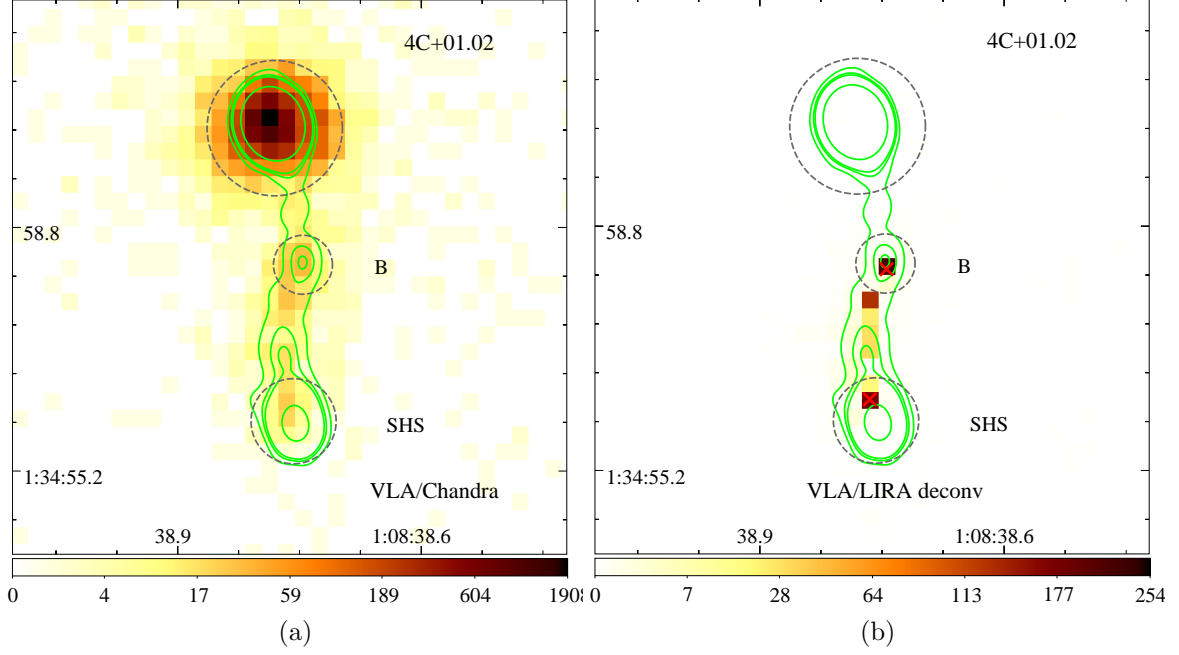


Figure 18. Same as in Fig. 1 but for 4C +01.02. The radio contours are given by 1.5, 4.0, 6.0, 50.0 mJy beam⁻¹.

4C+35.03 (Figure 21): This is an FR I source. The knot A, unlike the typical knots in FR I jets, shows a $0.37''$ (0.27 kpc) Rf-type offset. We exclude the remaining X-ray emission from our analysis due to absence of any radio components.

PKS 0208-512 (Figure 22): This is a CDQ. The radio and X-ray images show a compact extended structure to the southeast of the core. (Perlman et al. 2011) use high resolution ATCA images to find no clear X-ray/radio spatial correlation in this structure. In K3, which lies further downstream, the X-ray centroid coincides with the radio peak.

3C 66B (Figure 23): This is an FR I source. The jet flares at knot B (Hardcastle et al. 2001). We find two distinct peaks in this region, one, upstream of knot B and also downstream of knot x, and, two, $0.422''$ (0.18 kpc) to its southeast, which is the presumed obstacle (see 3.1). We exclude the upstream X-ray knot from our analysis due to its unclear association with the two radio peaks x and B. Further downstream, knot C shows a $0.29''$ (0.12 kpc) Xf-type offset while the X-rays coincide with the radio in knot E.

4C+28.07 (Figure 24): This is a CDQ. We exclude the inner jet from offset analysis due to the small separation ($< 1''$) between the radio knots. Nevertheless, the rough coincidence between the X-ray peaks in averaged LIRA images and their radio coun-

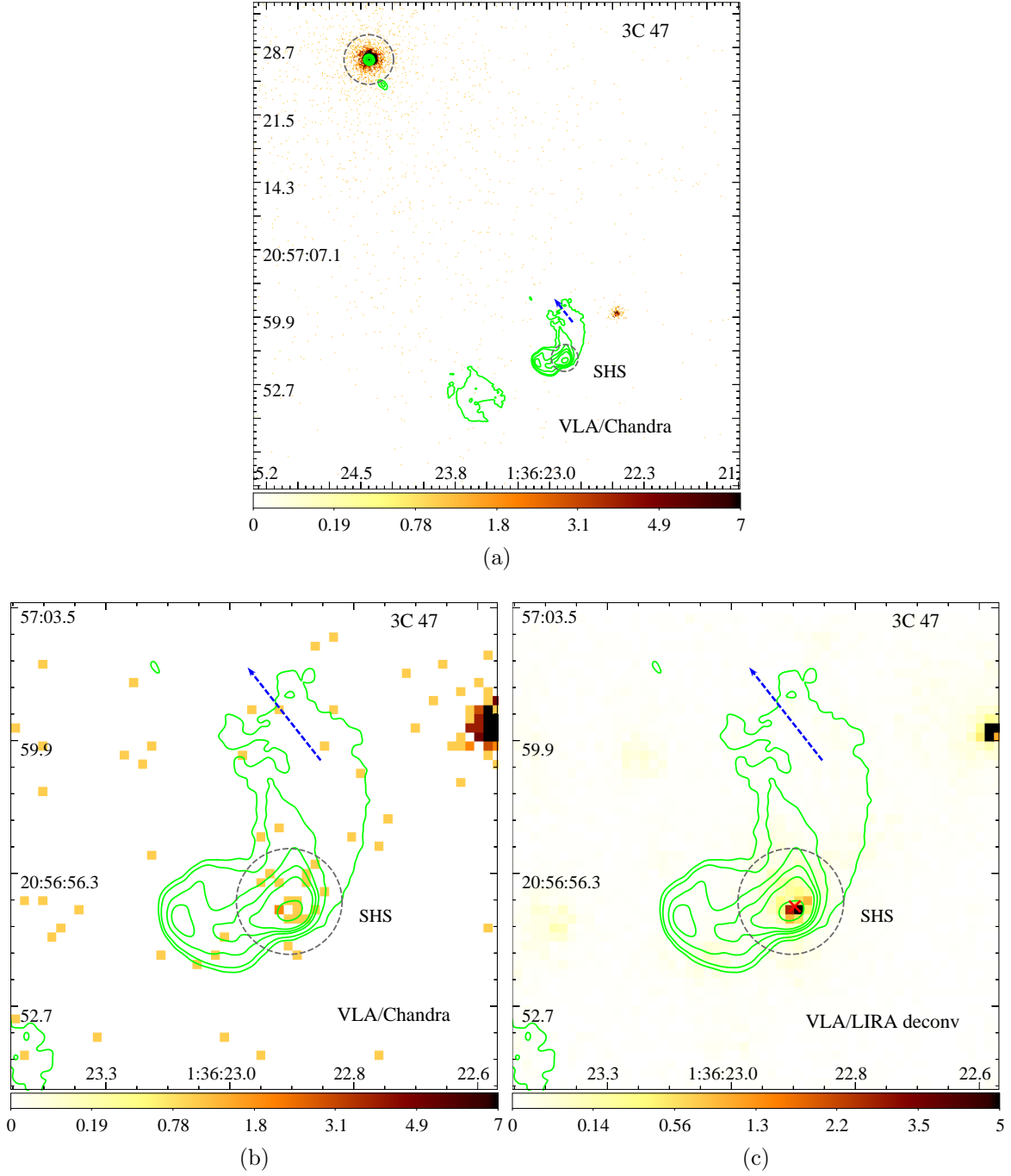


Figure 19. Same as in Fig. 1 but for 3C 47. The radio contours are given by 0.2, 0.5, 2.0, 4.0, 8.0, 40.0 mJy beam^{-1} .

terparts in knots C and D suggest a Co-s-type offset. We identify an X-ray feature $0.366''$ (3.06 kpc) upstream of NHS-a where the jet presumably enters the turbulent hotspot region.

3C 78 (Figure 25): This a nearby FR I radio galaxy. We present core-subtracted radio map for this source, showing a knotty structure. Due to the proximity of the

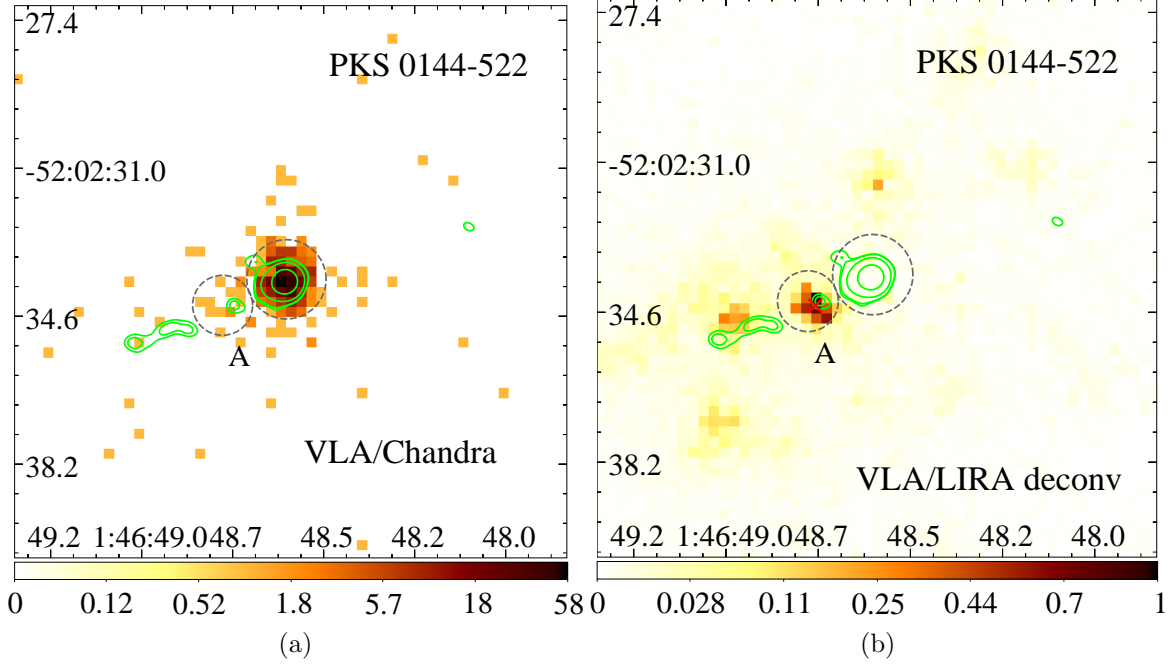


Figure 20. Same as in Fig. 1 but for PKS 0144-522. The radio contours are given by 0.5, 0.7, 4.0, 40.0 mJy beam^{-1} .

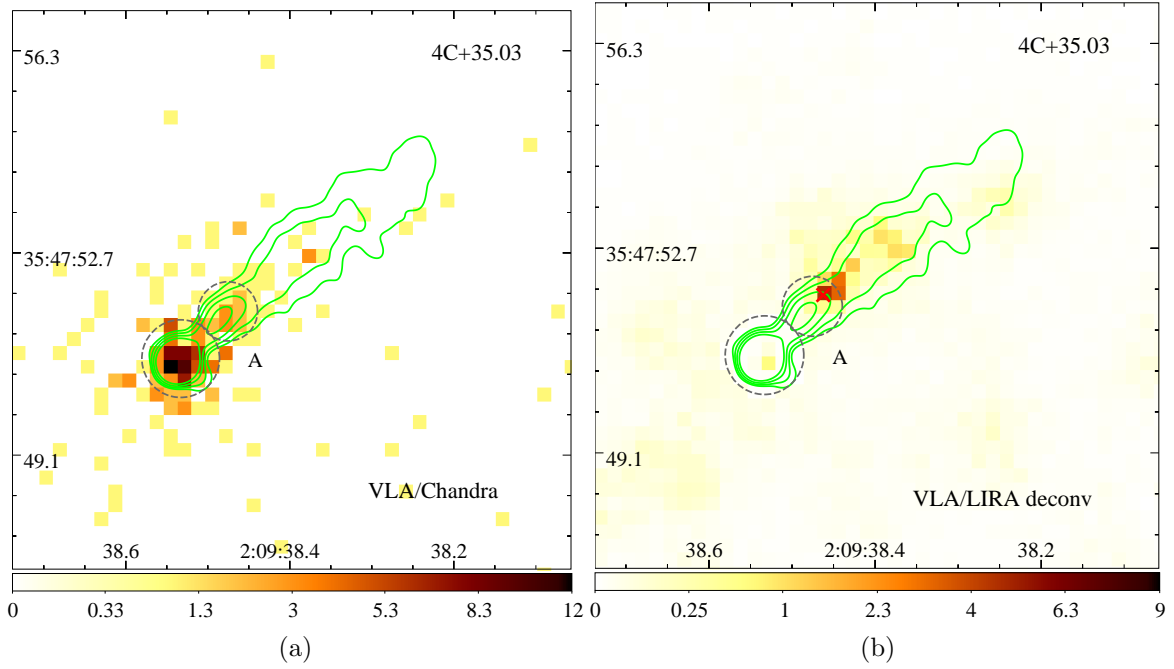


Figure 21. Same as in Fig. 1 but for 4C +35.03. The radio contours are given by 0.5, 1.0, 2.0, 4.0 mJy beam^{-1} .

inner knot to the core, we are unable to detect its X-ray emission in the deconvolved images. However, we find a bright X-ray knot coinciding with its radio counterpart.

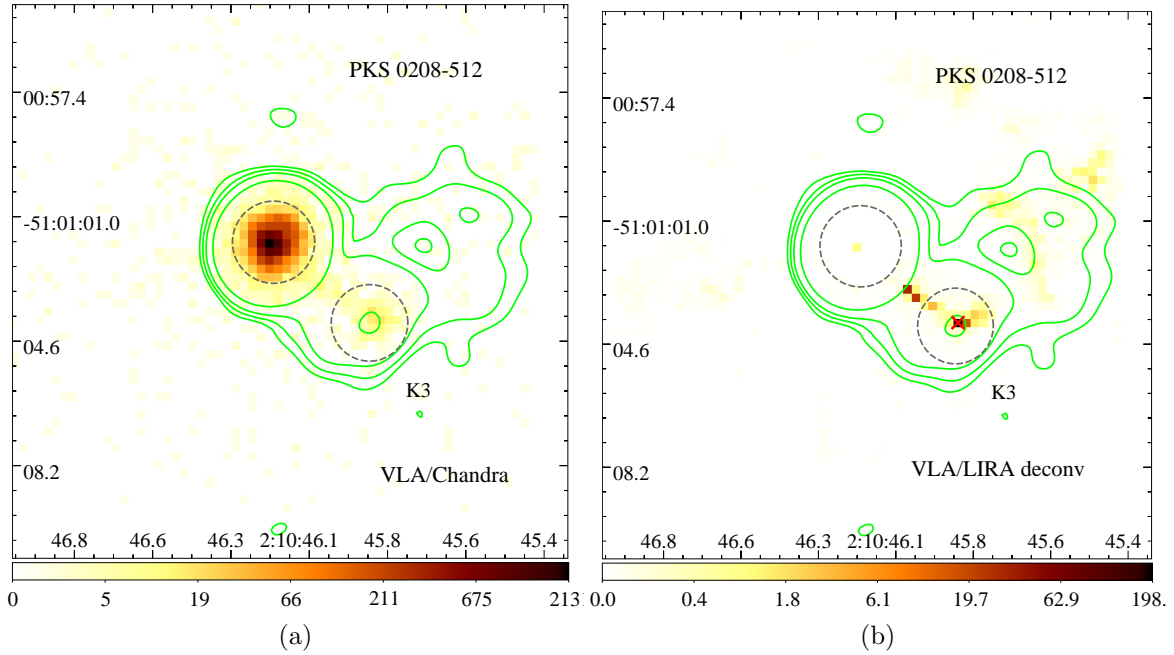


Figure 22. Same as in Fig. 1 but for PKS 0208-512. The radio contours are given by 1.0, 2.0, 4.0, 15.0 mJy beam⁻¹.

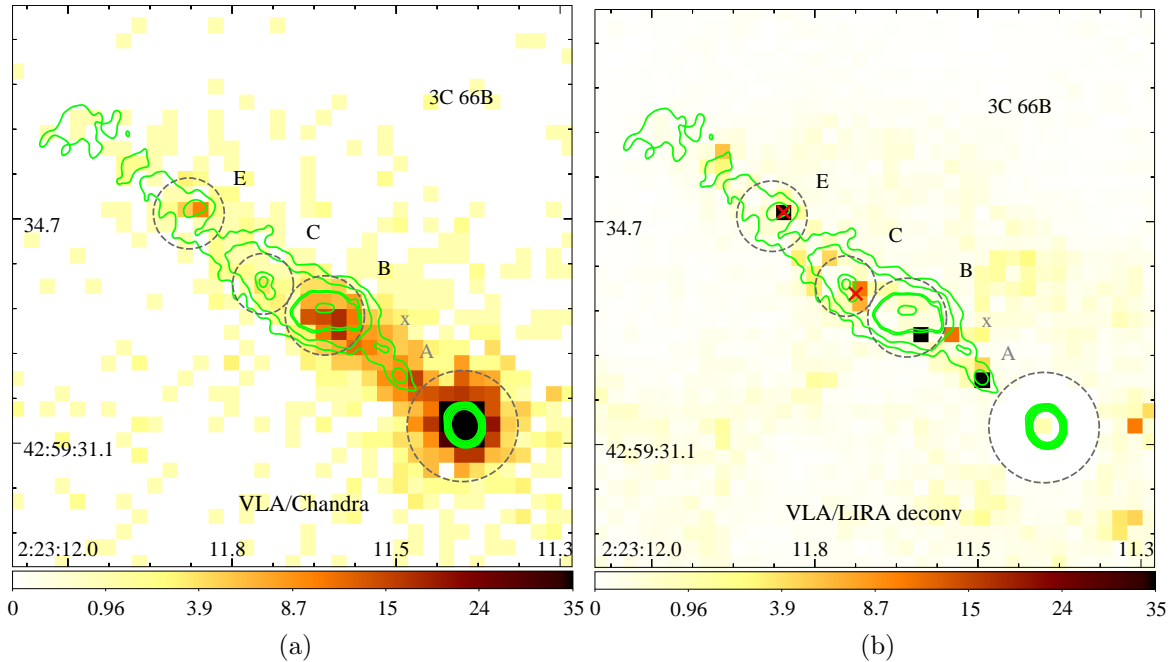


Figure 23. Same as in Fig. 1 but for 3C 66B. The radio contours are given by 0.2, 0.4, 0.8, 0.9, 2.0, 4.0, 8.0 mJy beam⁻¹.

3C 83.1 (Figure 26): This FR I source with a narrow-angle tail morphology. We detect Xf-type offsets in knots E1 and W1 with magnitudes of 0.725'' (0.36 kpc) and 0.65'' (0.32 kpc), respectively.

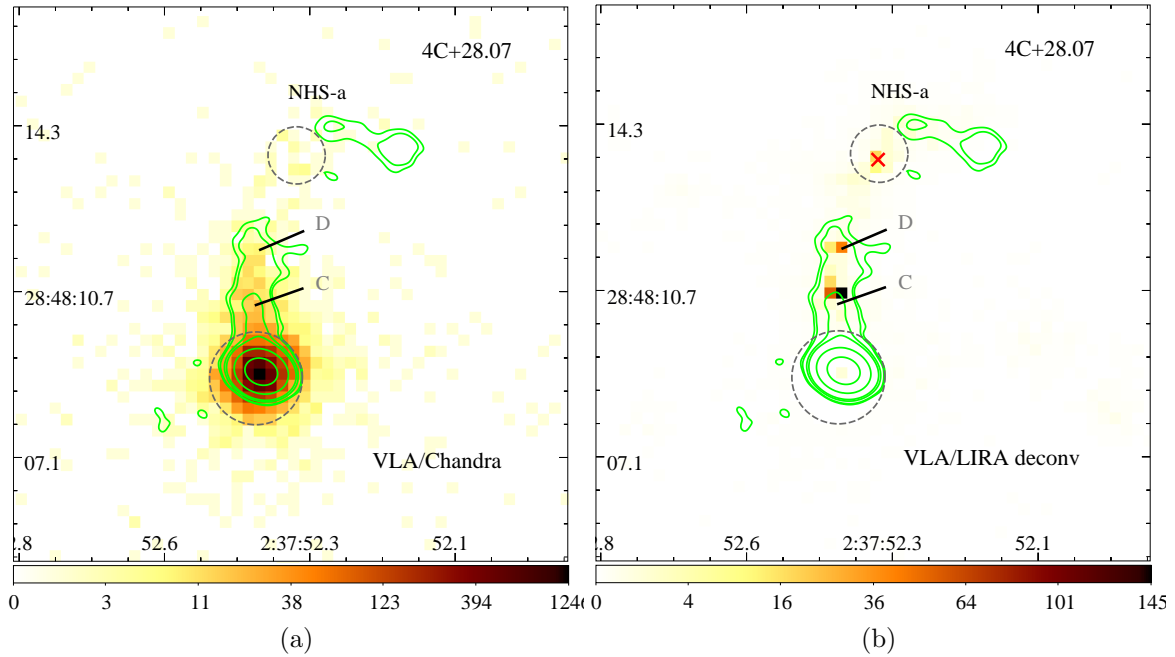


Figure 24. Same as in Fig. 1 but for 4C +28.07. The radio contours are given by 1.0, 1.5, 5.0, 10.0, 100.0, 1000.0 mJy beam⁻¹.

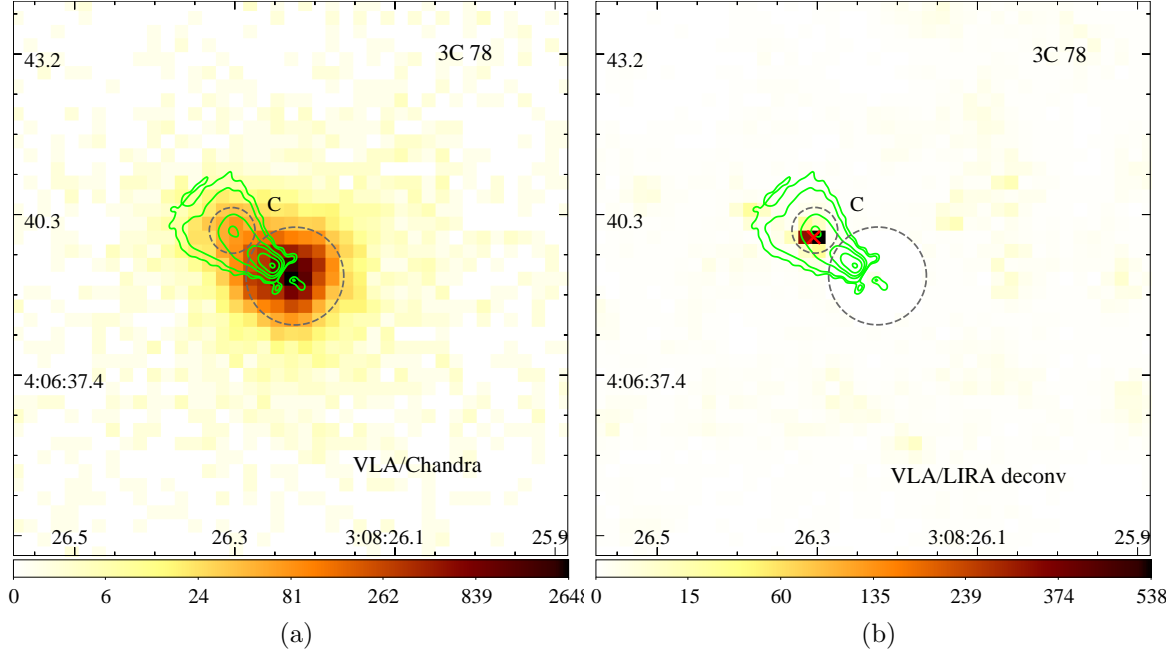


Figure 25. Same as in Fig. 1 but for 3C 78. The radio contours are given by 0.5, 1.0, 5.0, 10.0, 20.0, 35.0 mJy beam⁻¹.

3C 88 (Figure 27): This is an FR I source. The jet makes a sharp turn from the northwest to the southwest at knot C. We find a 1.14'' (0.7 kpc) Xf-type offset

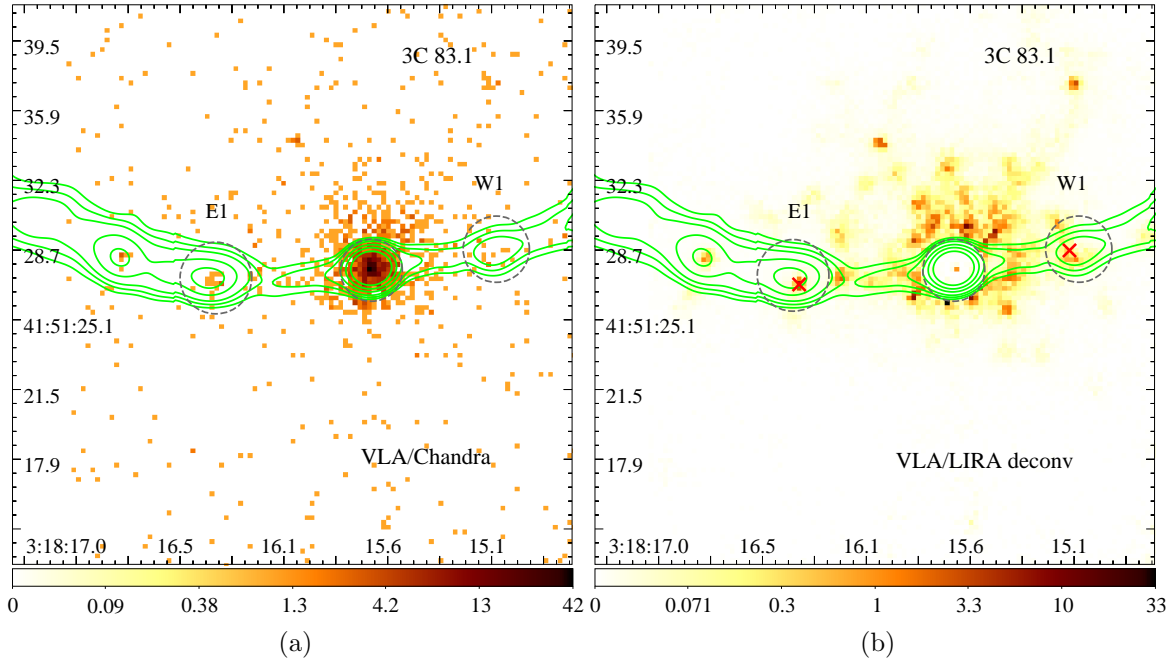


Figure 26. Same as in Fig. 1 but for 3C 83.1. The radio contours are given by 0.17, 0.4, 0.8, 2.0, 4.0, 8.0 mJy beam⁻¹.

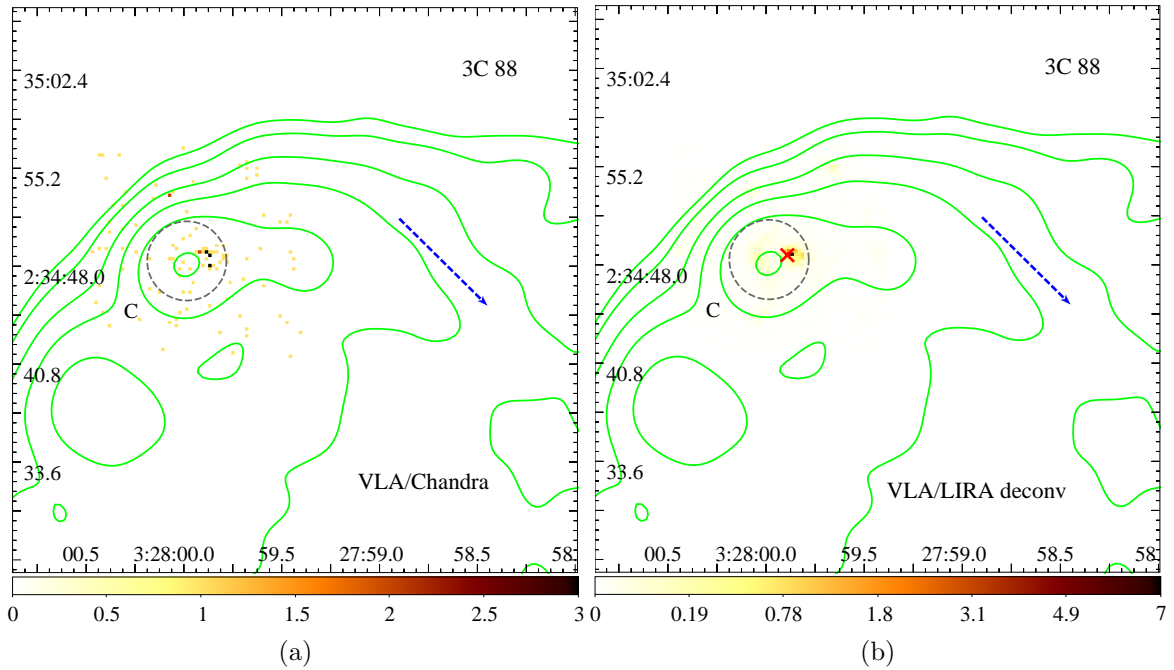


Figure 27. Same as in Fig. 1 but for 3C 88. The radio contours are given by 0.4, 0.8, 2.0, 4.0, 8.0, 18.0 mJy beam⁻¹.

in this knot.

PKS 0405-12 (Figure 28): This is a CDQ. The X-ray centroid in the northern

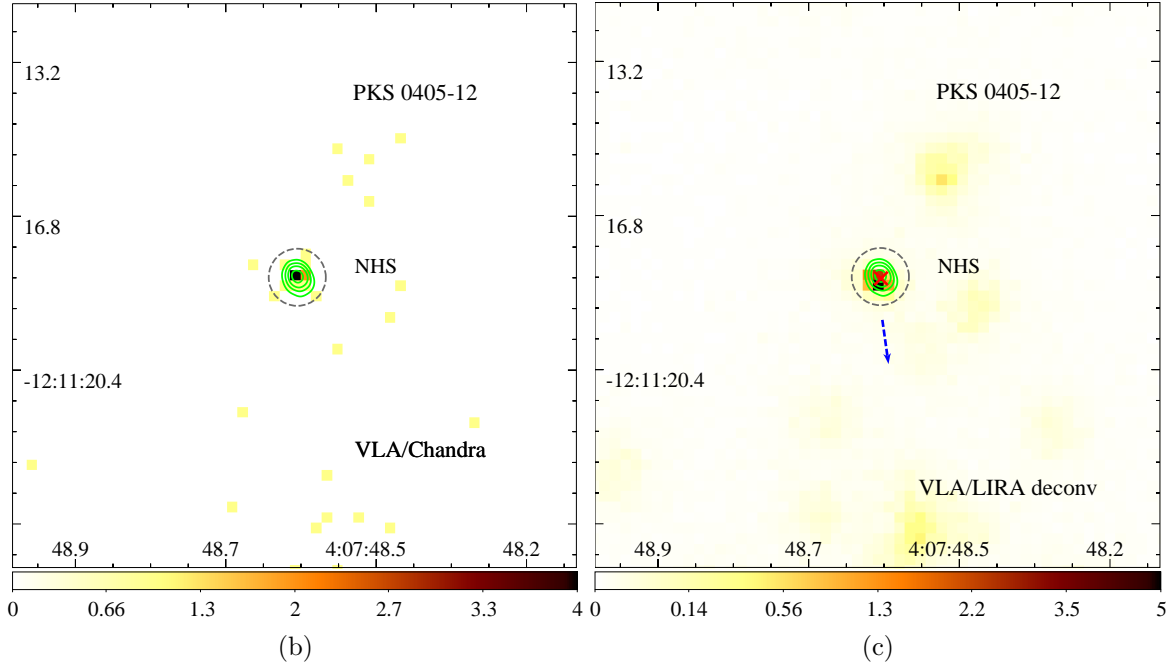
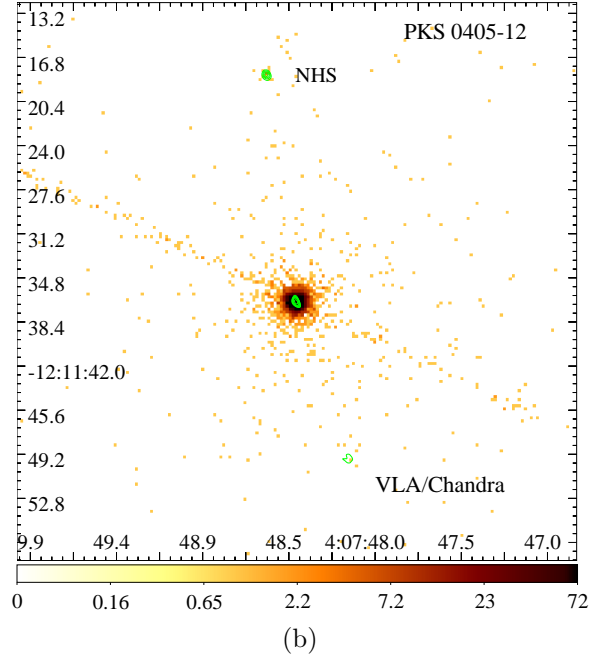


Figure 28. Same as in Fig. 1 but for PKS 0405-12. (a) shows the full image while (b) and (c) show zoomed-in region around the northern hotspot (NHS). The radio contours are given by 4.0, 10.0, 20.0, 40.0, 100.0, 400.0 mJy beam⁻¹.

hotspot (NHS) coincides with the radio peak.

PKS 0413-21 (Figure 29): This is a CDQ. The radio image shows a bright extended feature, denoted as A, to the southwest of the core. The X-ray centroid of this feature lies 0.24'' (1.79 kpc) upstream of its radio peak indicating an Xf-type

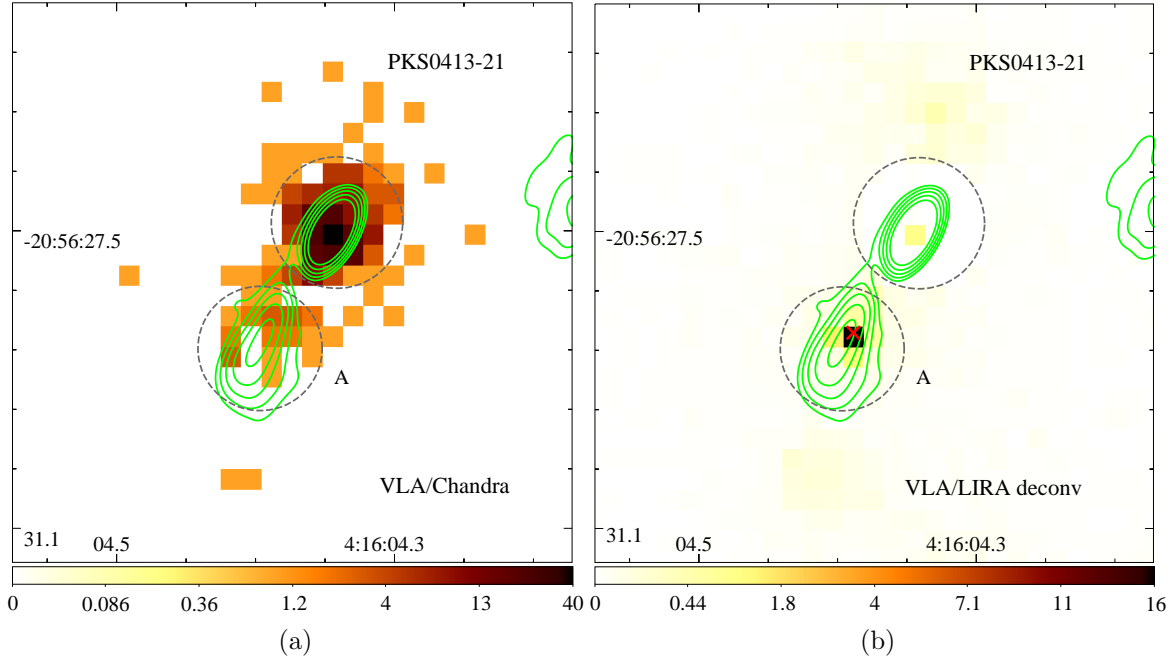


Figure 29. Same as in Fig. 1 but for PKS 0413-21. The radio contours are given by 5.0, 10.0, 20.0, 40.0, 80.0 mJy beam⁻¹.

offset.

3C 111 (Figures 30-33): This is a nearby FR-II jet with about a 120'' long knotty jet. To limit the usage of computational resources, we divide this jet into four parts. We find Xf-type offsets in K9, K14, K30, K61 and NHS, while we find no significant evidence for an offset in K45. Although we also find a offset in K97, we indicate it as Amb-type due to uncertainty in the direction of the jet at this location.

3C 120 (Figure 34): : This is classified as a Seyfert I galaxy, although with an FR I-type jet. We find an Xf-type offset in K4 while the X-ray and radio peaks are within the error limits of each other.

3C 123 (Figure 35): This is an FR II source. The southern radio hotspot is detected in the X-rays whose centroid lies 0.37'' (1.66 kpc) upstream of the radio peak. Although the radio map indicates a precursor-hotspot in the SHS region, we find not X-ray emission.

PKS 0454-463 (Figure 36): This is a CDQ. The southern jet makes a sharp turn from the southwest to the south at knot A. The X-ray centroid of this knot lies within 0.15'' of the radio peak.

PKS 0605-089 (Figure 37): This is a CDQ. The radio image shows a faint in-

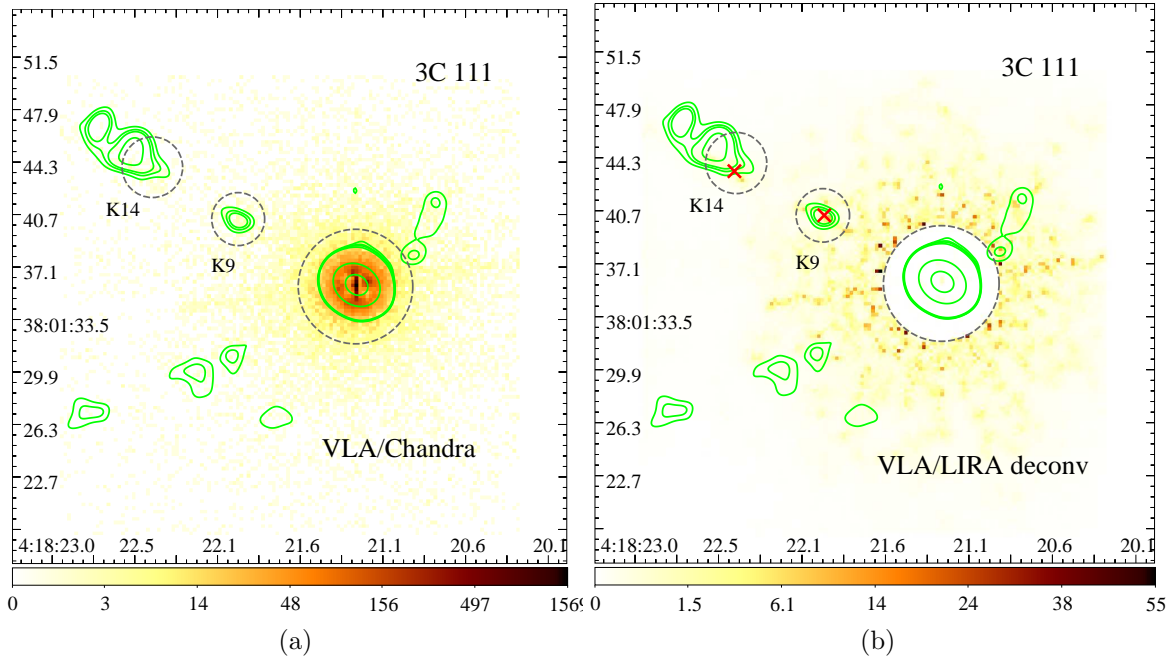
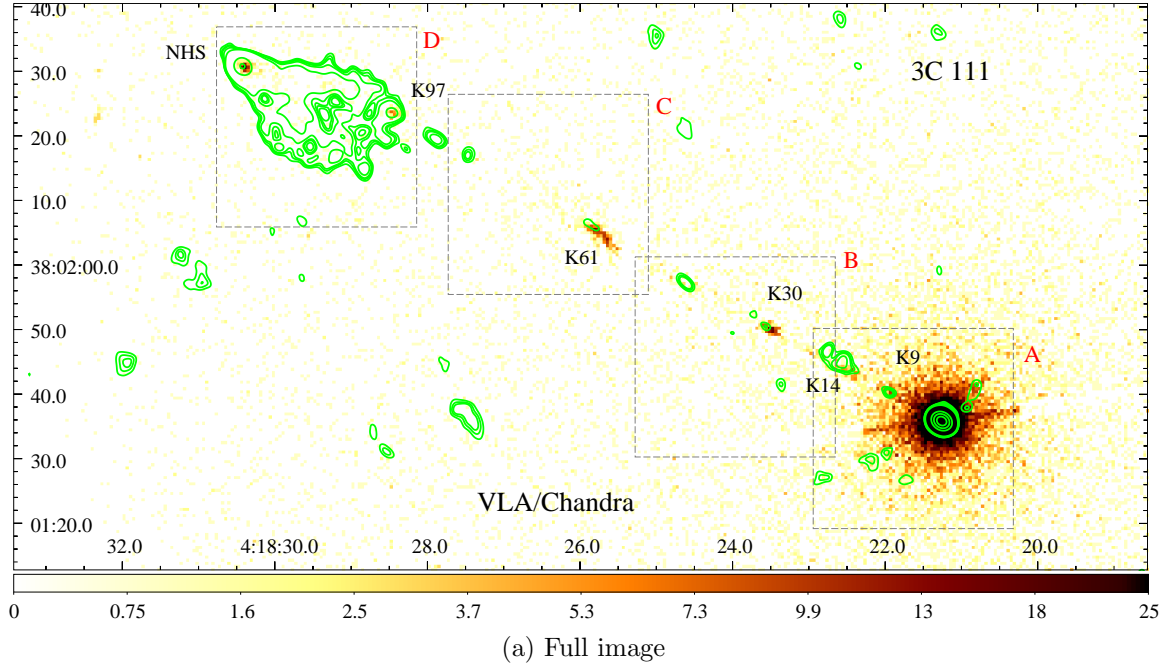


Figure 30. Same as in Fig. 1 but for 3C 111 (part A). The radio contours are given by 1.5, 1.8, 2, 2.5, 100, 500 mJy beam⁻¹.

ner jet followed by a bend to the southwest before terminating in the western hotspot (WHS). We exclude the inner jet from the offset analysis due to small separation ($< 1''$) between the radio knots. WHS shows a $1.02''$ (7.04 kpc) Xf-type offset.

PKS 0637-752 (Figure 38): This is a moderately high-redshift CDQ, and is the first ever jet to be detected by *Chandra* (Chartas et al. 2000; Schwartz et al. 2000). The

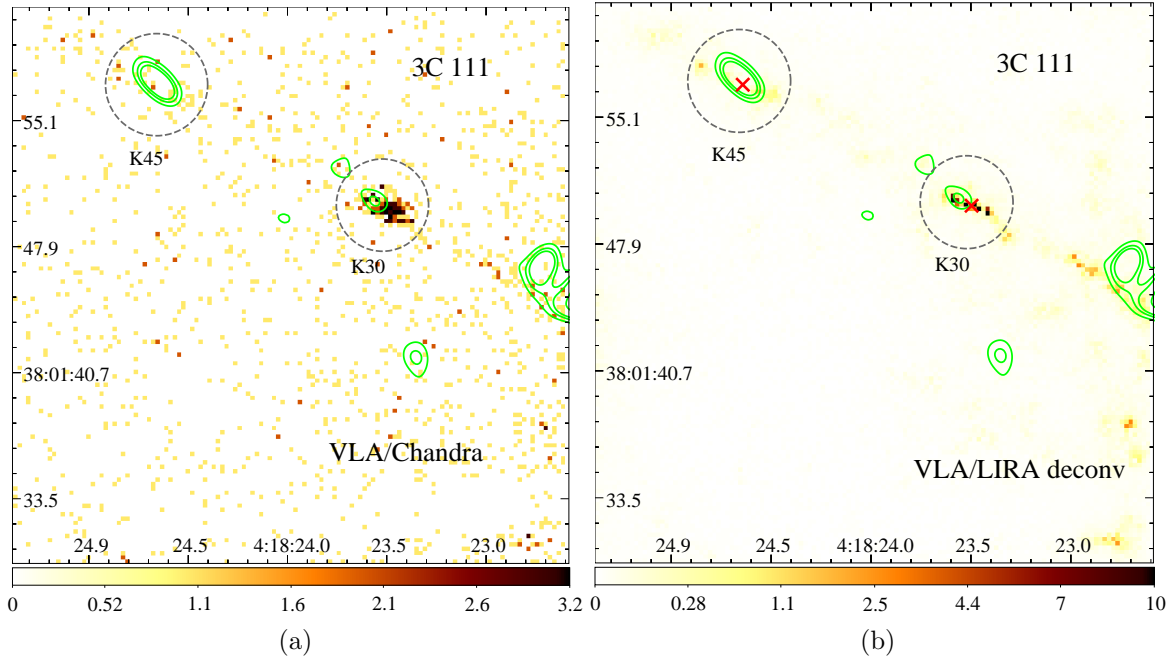


Figure 31. Same as in Fig. 1 but for 3C 111 (part B). The radio contours are given by 1.5, 1.8, 2, 2.5, 100, 500 mJy beam⁻¹.

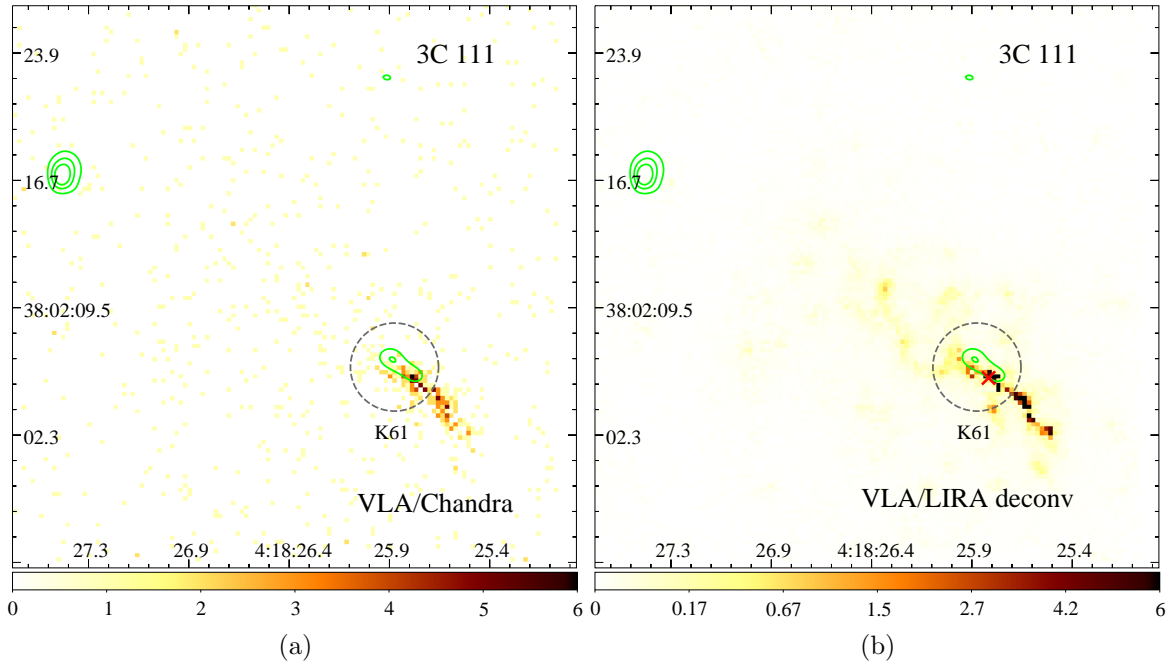


Figure 32. Same as in Fig. 1 but for 3C 111 (part C). The radio contours are given by 1.5, 1.8, 2, 2.5, 100, 500 mJy beam⁻¹.

inner knots are excluded from our analysis due to their close spacing. We find no offsets in knots further down the jet.

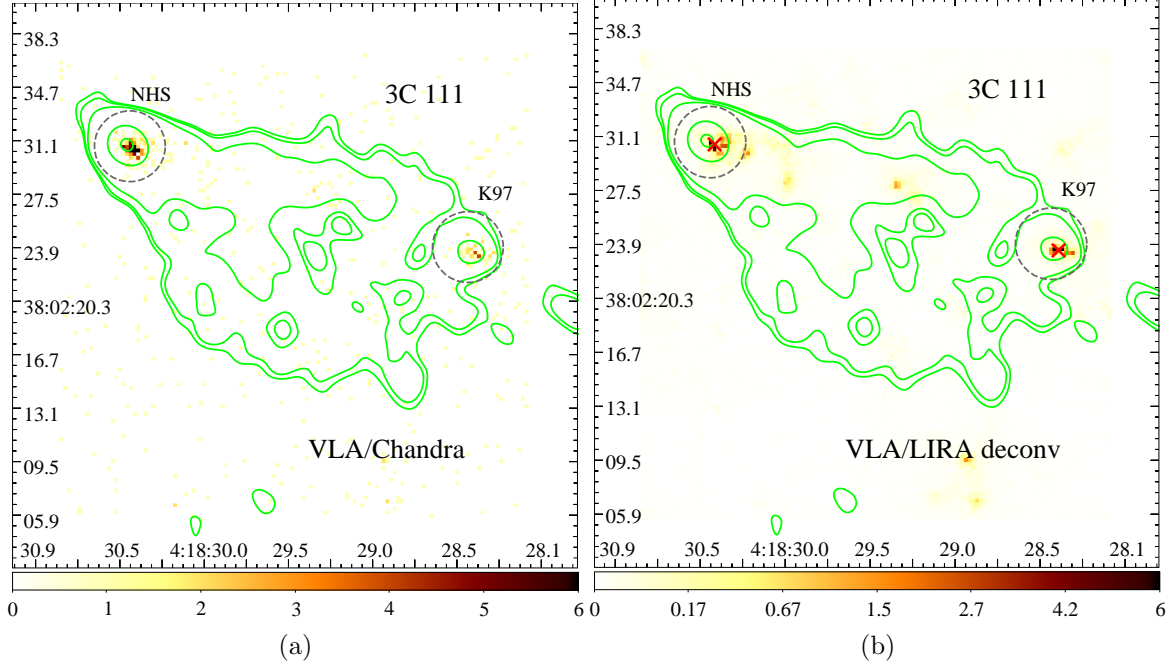


Figure 33. Same as in Fig. 1 but for 3C 111 (part D). The radio contours are given by 1.5, 1.8, 2, 2.5, 100, 500 mJy beam⁻¹.

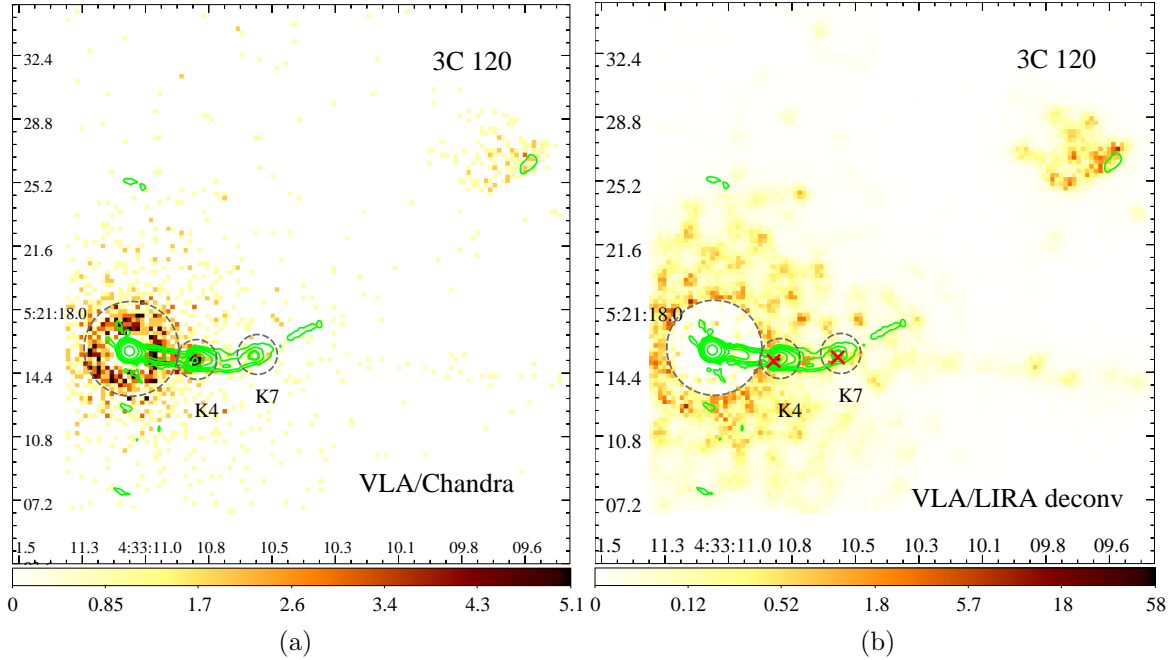


Figure 34. Same as in Fig. 1 but for 3C 120. The radio contours are given by 0.5, 1.0, 1.8, 2.0, 4.0, 8.0, 20.0, 100.0, 1000.0 mJy beam⁻¹.

B2 0738+313 (Figure 39): This is a CDQ. Knot A, which lies roughly midway between the core and the southern hotspot (SHS) shows a 0.54'' (3.73 kpc) Xf-type offset.

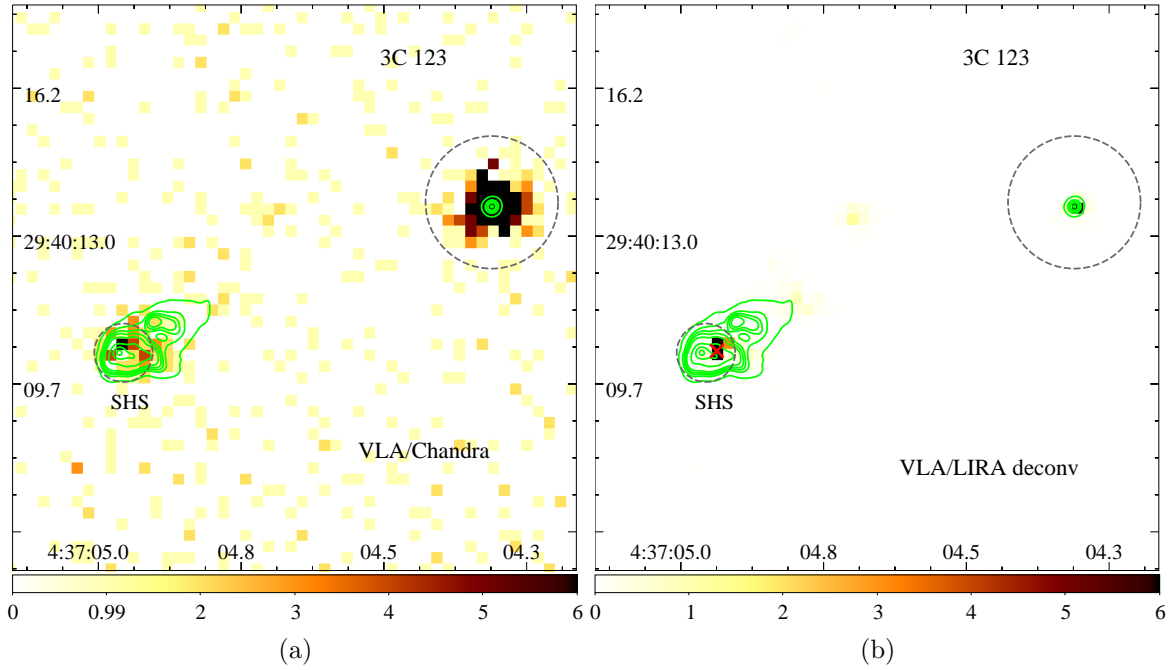


Figure 35. Same as in Fig. 1 but for 3C 123. The radio contours are given by 5.0, 30.0, 50.0, 70.0, 100.0, 200.0, 300.0, 380.0 mJy beam⁻¹.

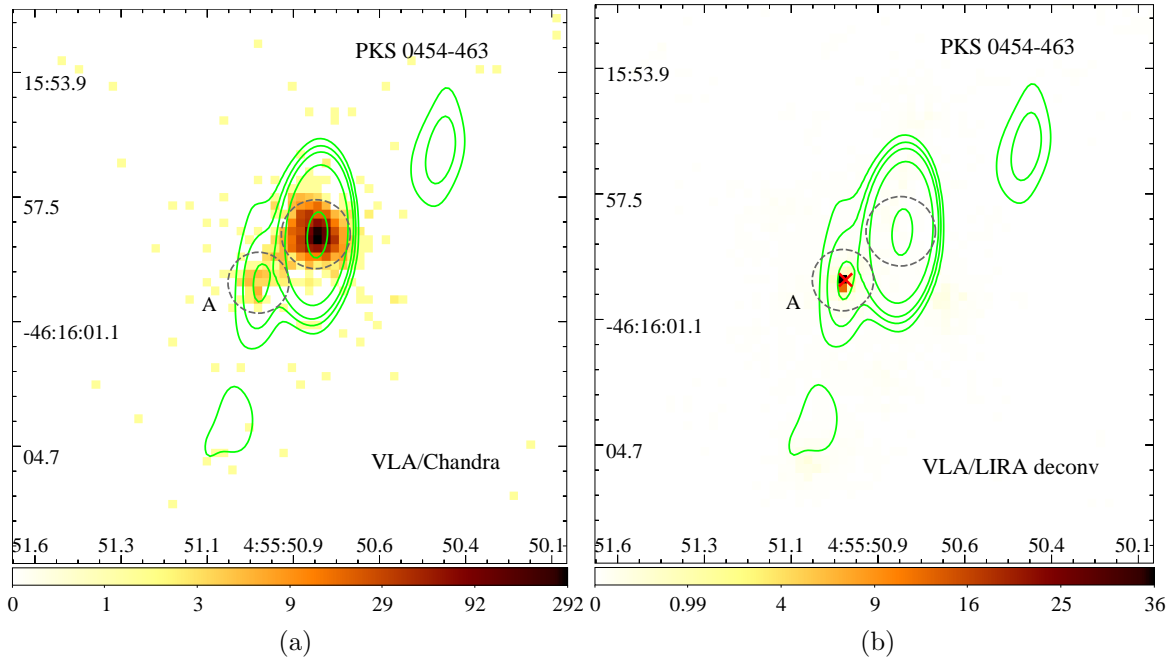


Figure 36. Same as in Fig. 1 but for PKS 0454-46. The radio contours are given by 10.0, 20.0, 35.0, 100.0, 1000.0 mJy beam⁻¹.

OJ 248 (Figure 40): This is a CDQ. The X-ray image shows a one-sided jet to the south without any radio counterpart. It makes a sharp bend to the east where

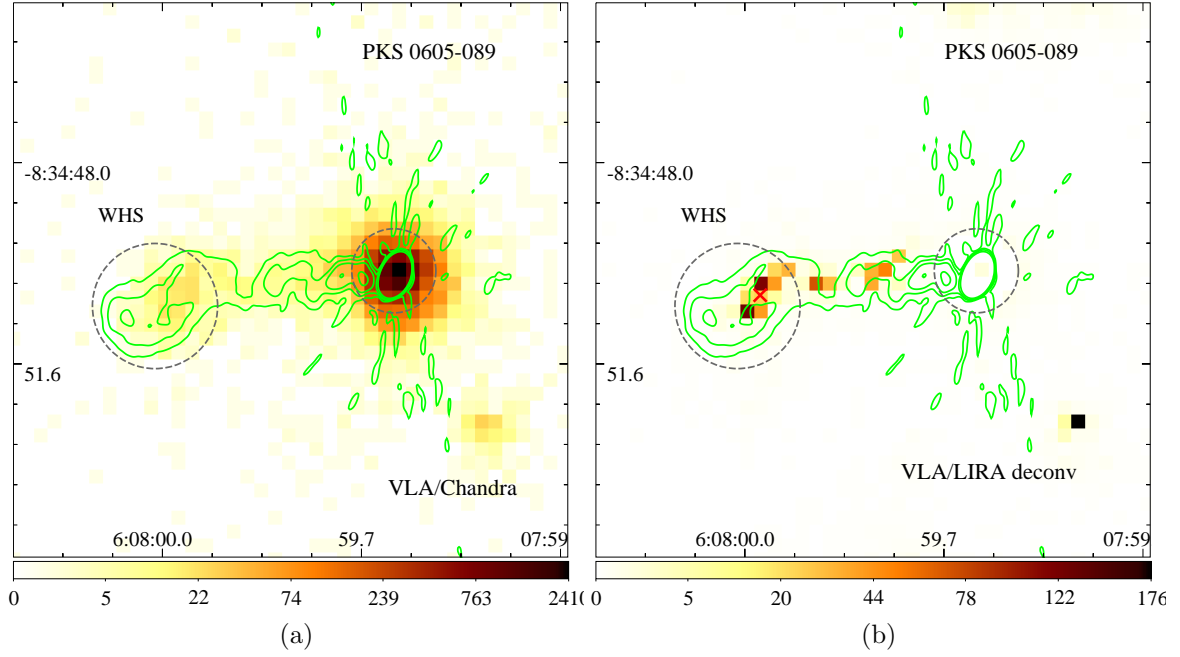


Figure 37. Same as in Fig. 1 but for PKS 0605-089. The radio contours are given by 0.1, 0.3, 0.6, 1.5 mJy beam⁻¹.

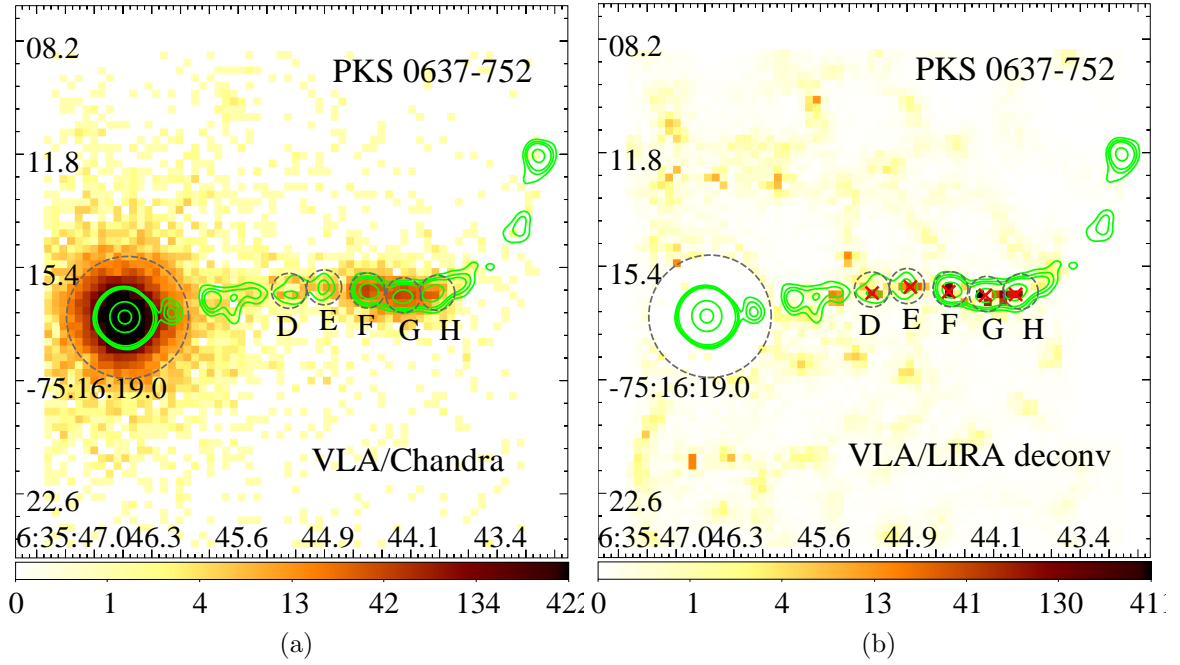


Figure 38. Same as in Fig. 1 but for PKS 0637-752. The radio contours are given by 4.0, 6.0, 8.0, 1.5, 1000.0, 4000.0 mJy beam⁻¹.

the radio jet becomes visible. Knot C2, which lies at this bend, shows a Co-s-type offset. We find a 0.292'' (2.31 kpc) Xf-type offset in knot C4.

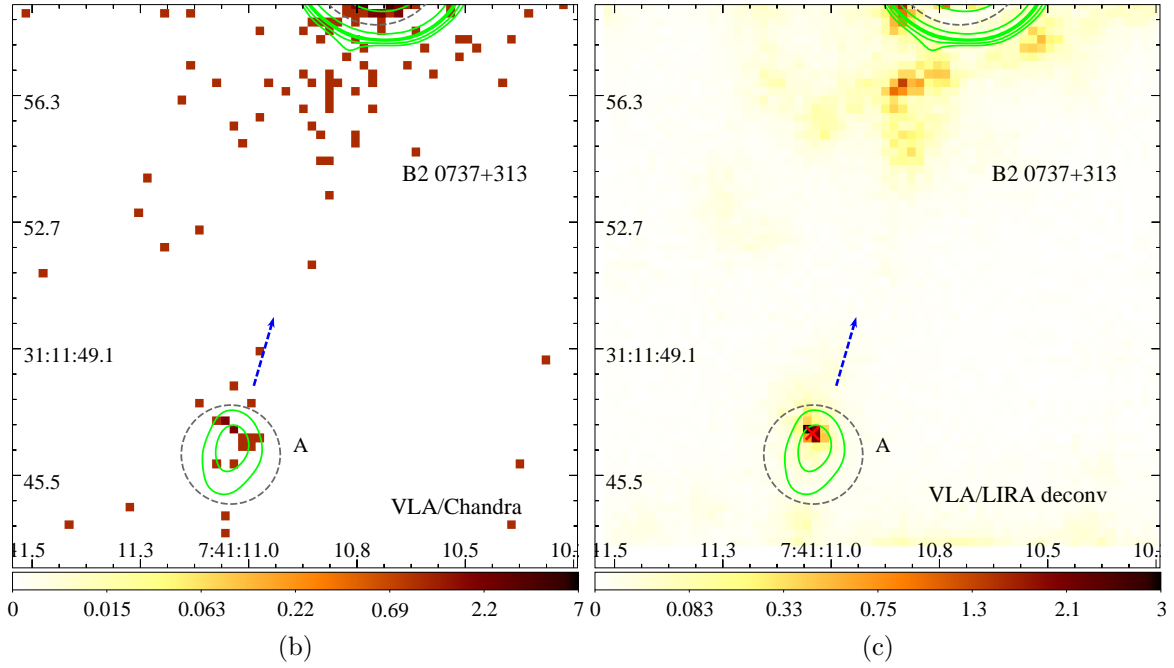


Figure 39. Same as in Fig. 1 but for B2 0738+313. The radio contours are given by 0.1, 0.2, 0.4, 0.5, 0.6, 2.0, 100.0, 1000.0, 2000.0 mJy beam⁻¹.

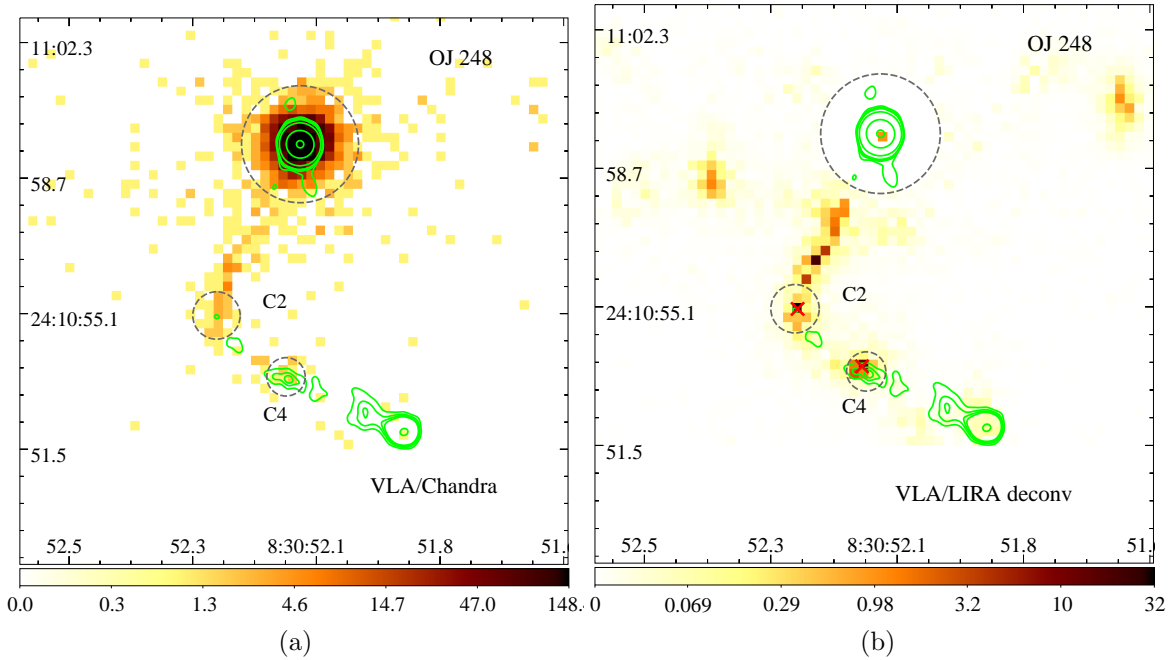


Figure 40. Same as in Fig. 1 but for OJ 248. The radio contours are given by 0.03, 0.06, 0.08, 0.1, 0.4, 10.0, 100.0 mJy beam⁻¹.

4C +29.30 (Figure 41): This is an FR II source. Knot A shows a 0.319'' (0.38 kpc) Xf-type offset, while the two hotspots, NHS-a and SHS, both show no offset.

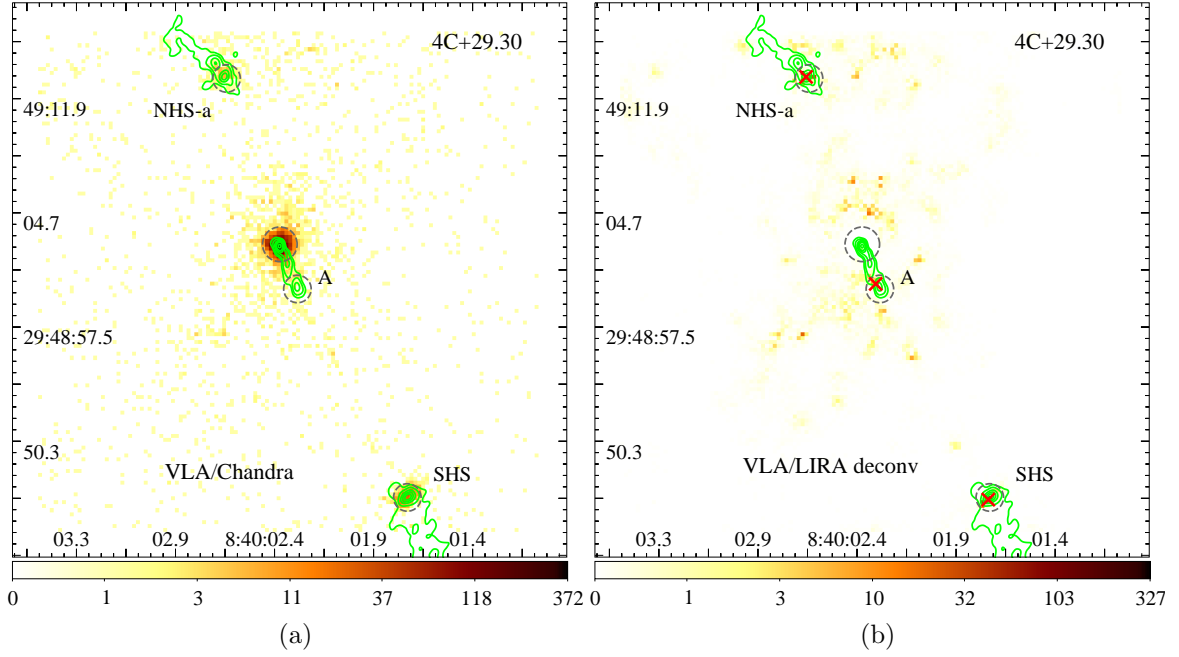


Figure 41. Same as in Fig. 1 but for 4C +29.30. The radio contours are given by 0.5, 1.0, 2.0, 3.0, 4.0, 6.0 mJy beam⁻¹.

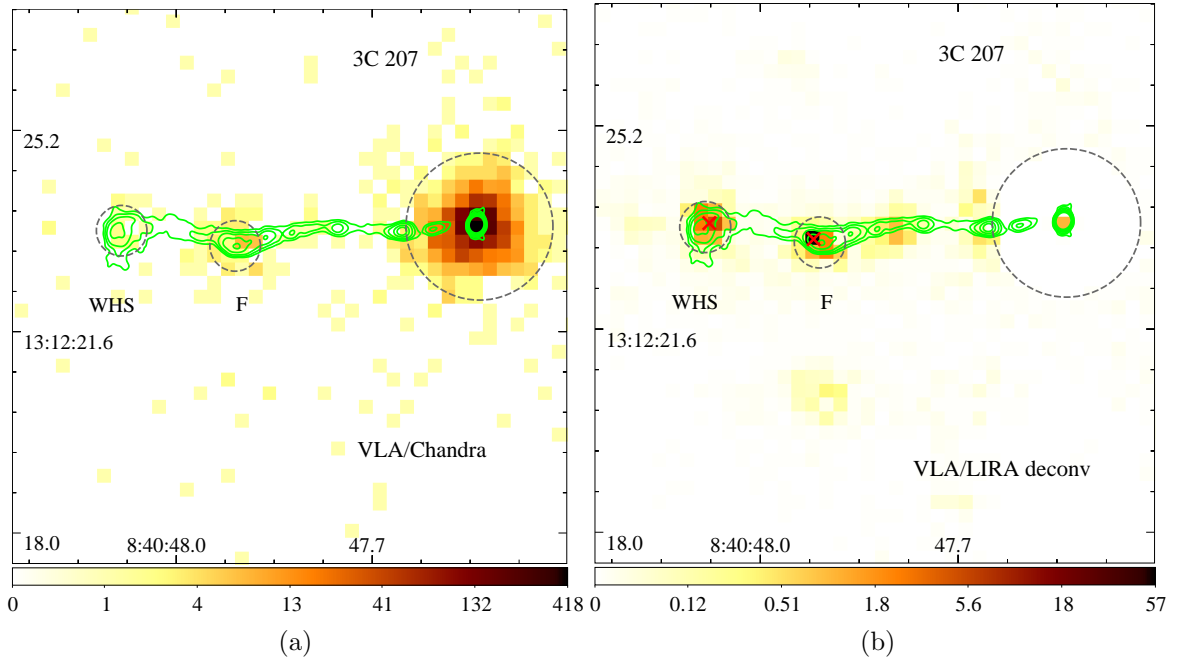


Figure 42. Same as in Fig. 1 but for 3C 207. The radio contours are given by 0.2, 0.4, 0.8, 2.0, 4.0, 8.0, 20.0 mJy beam⁻¹.

3C 207 (Figure 42): This is an LDQ. The jet makes a small projected bend to the southwest at knot F and shows a $0.35''$ (2.48 kpc) Rf-type offset. This is contrary to many knots at apparent jet-bends in our sample that show Xf-type offsets.

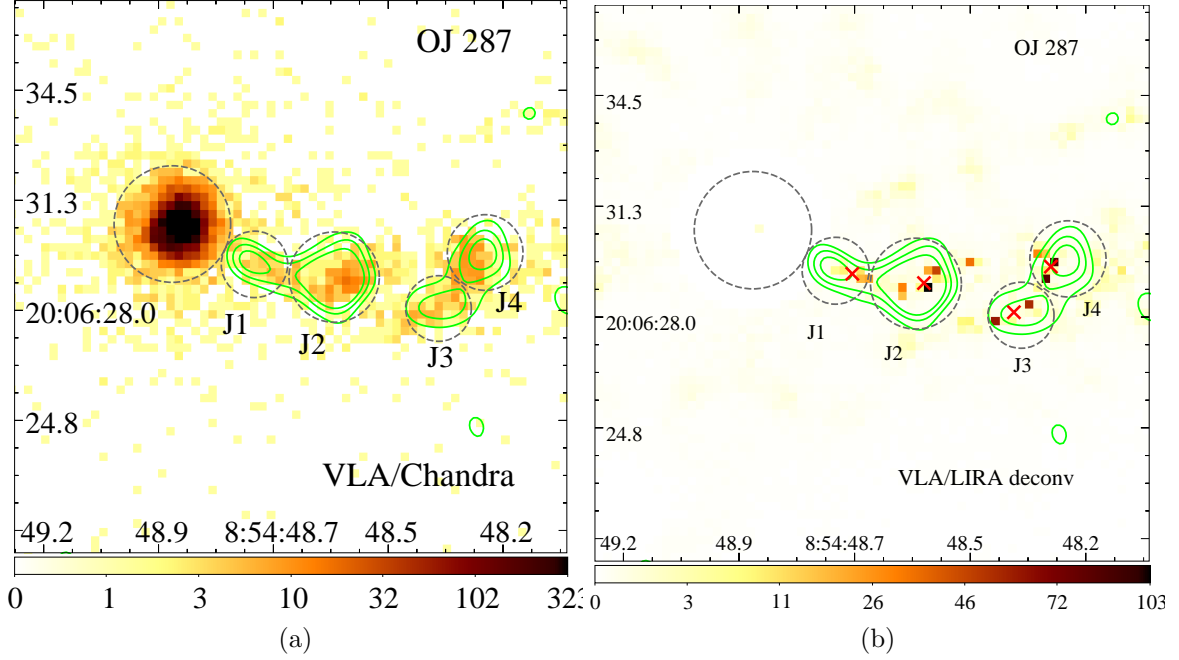


Figure 43. Same as in Fig. 1 but for OJ 287. The radio contours are given by 0.4, 0.6, 0.8 mJy beam⁻¹.

The western hotspot shows a $0.33''$ (2.34 kpc) Xf-type offset.

OJ 287 (Figure 43): This is a BL Lac type object and is one of the few sources in our sample with Rf and Xf-type offsets in the jet. The two knots in the inner jet, A and B, show $0.51''$ (2.3 kpc) and $0.23''$ (1.04 kpc) Rf-type offsets, respectively. On the other hand, two knots in the outer jet, which are detected only in the VLA 1.4 GHz band, show $0.364''$ (1.64 kpc) and $0.471''$ (2.12 kpc) Xf-type offsets, respectively.

PKS 0920-397 (Figure 44): This is a CDQ with a highly aligned jet ($\beta_{app}=30.8$) with near periodic knot spacing similar to PKS 0637-752 (Godfrey et al. 2012). While our LIRA deconvolution is unable to detect emission from the inner knots, we find no offset in knot C and E. Although we find X-ray emission between knots C and E, its radio association is unclear with the current data. The X-ray and radio jet fades away at knot E before re-emerging at the southern hotspot. The X-ray emission peaks $0.81''$ (6.88 kpc) of the radio hotspot.

3C 228 (Figure 45): This is an FR II source. The radio map shows a precursor hotspot followed by the southern hotspot (SHS). The X-ray centroid lies $0.31''$ (2.07 kpc) Xf-type offset upstream of SHS.

QSO 0957+516 (Figure 46): This is a gravitationally-lensed LDQ. We exclude the knot complex upstream of the western hotspot (EHS) from offset analysis due

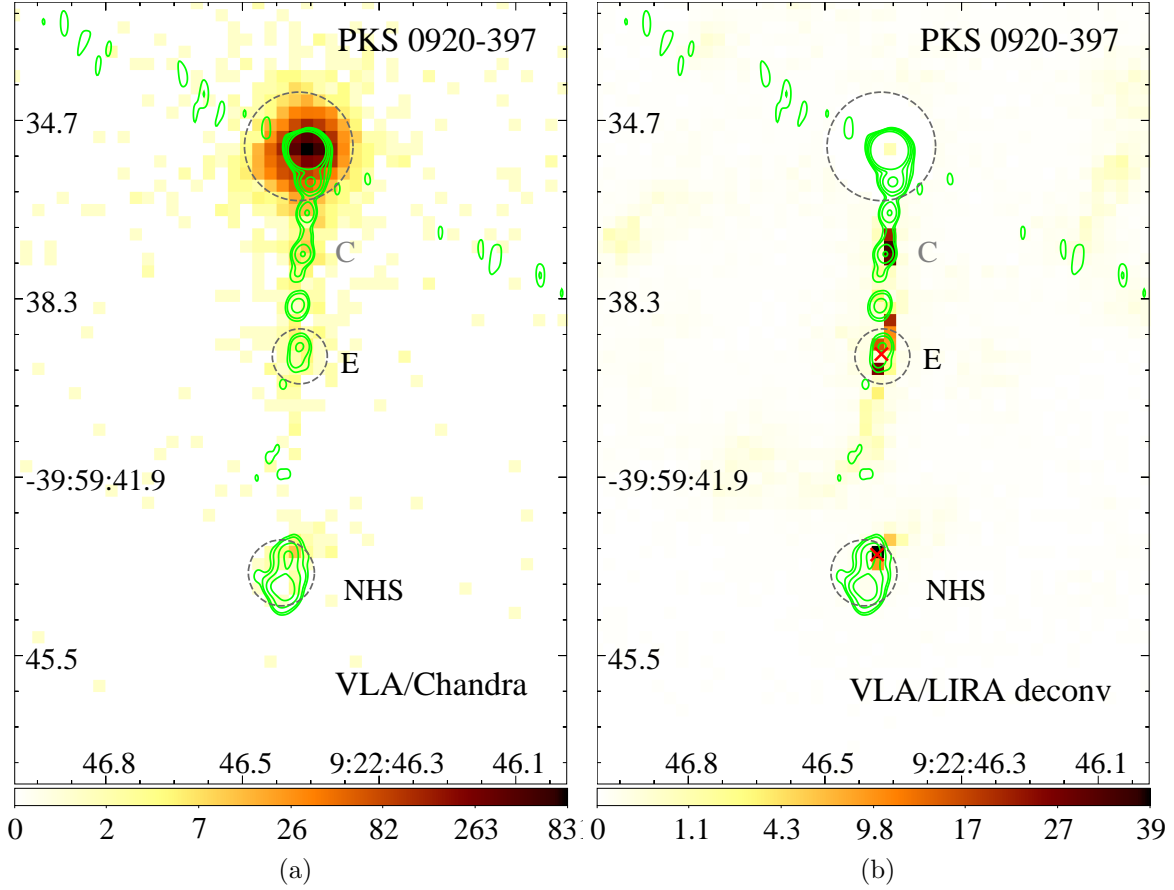


Figure 44. Same as in Fig. 1 but for PKS 0920-397. The radio contours are given by 0.2, 0.4, 0.8, 2.0, 4.0, 8.0, 20.0 mJy beam⁻¹.

to the close separation ($< 1''$) between the radio knots. We find a $0.74''$ (6.29 kpc) Xf-type offset in WHS.

PKS 1030-357 (Figure 47): This is a CDQ. The radio image shows a knotty jet to the southwest where knot B shows a Co-s-type offset, while knot C shows a $0.41''$ (3.48 kpc) Rf-type offset. The radio jet disappears at knot C before re-appearing at knot D. The situation in knot C is similar to 4C+19.44 where the radio jet disappears while the X-ray emission persists further downstream (Harris et al. 2017). Knot D shows a $0.27''$ (2.3 kpc) Xf-type offset where the jet makes a 90° projected-bend towards knot E. Knot E shows a $0.40''$ (3.4 kpc) Rf-type offset where the jet makes another 90° bend to knot F that shows a $0.31''$ (2.64 kpc) Xf-type offset.

PKS 1045-188 (Figure 48): This is a CDQ. We exclude the inner jet from offset analysis due to the small separation ($< 1''$) between the radio knots. Further downstream of the inner jet, the jet makes a 90° projected bend to the east at knot H that shows a $0.21''$ (1.39 kpc) Xf-type offset.

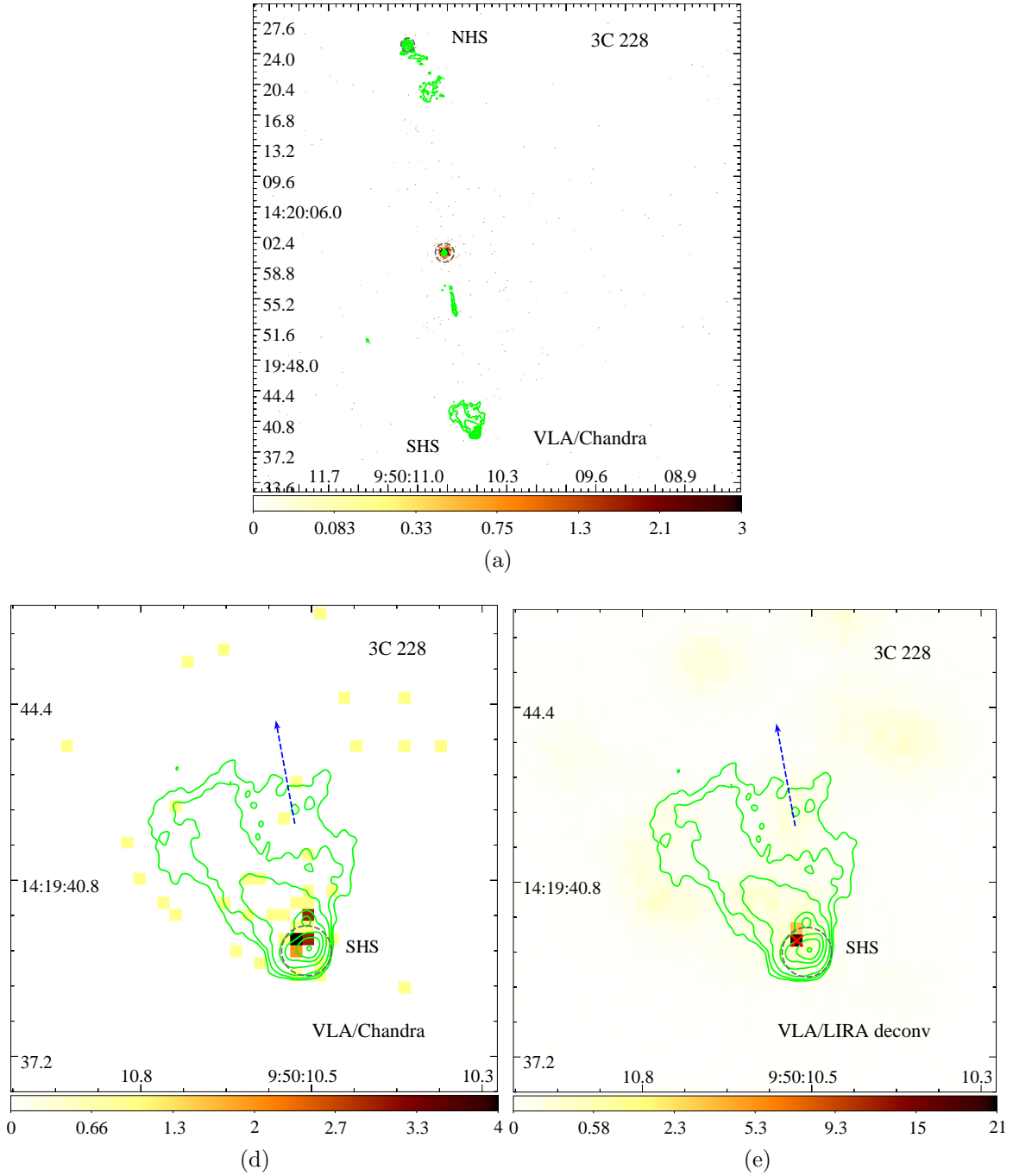


Figure 45. Same as in Fig. 1 but for 3C 228. (a) shows the full image while (b) and (c) zoom into the southern hotspot (SHS). The radio contours are given by 0.2, 0.4, 1.0, 4.0, 10.0, 20.0, 40.0 mJy beam⁻¹.

PKS 1055+201 (Figure 49): This is an LDQ. The deconvolved X-ray image shows a long knotty jet to the north, although with only extremely faint radio emission, terminating in a double-hotspot structure perpendicular to the jet's original direction. Knot A and both the hotspots show no offset.

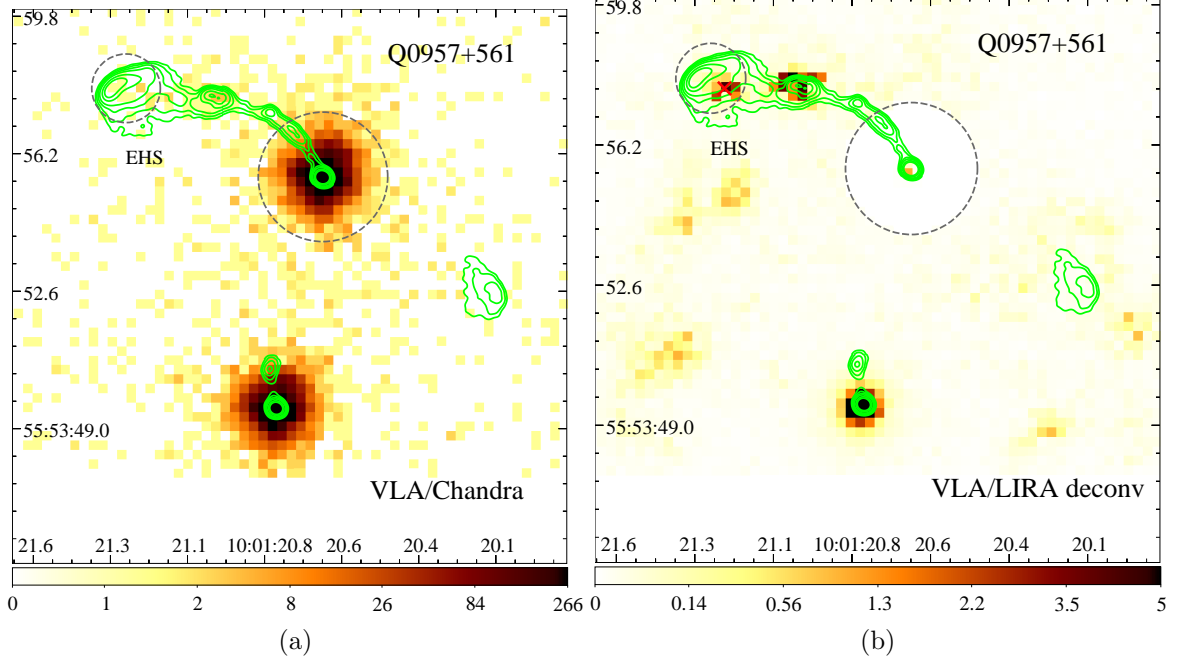


Figure 46. Same as in Fig. 1 but for Q 0957+561. The radio contours are given by 0.1, 0.2, 0.4, 0.8, 2.0, 3.8 mJy beam⁻¹.

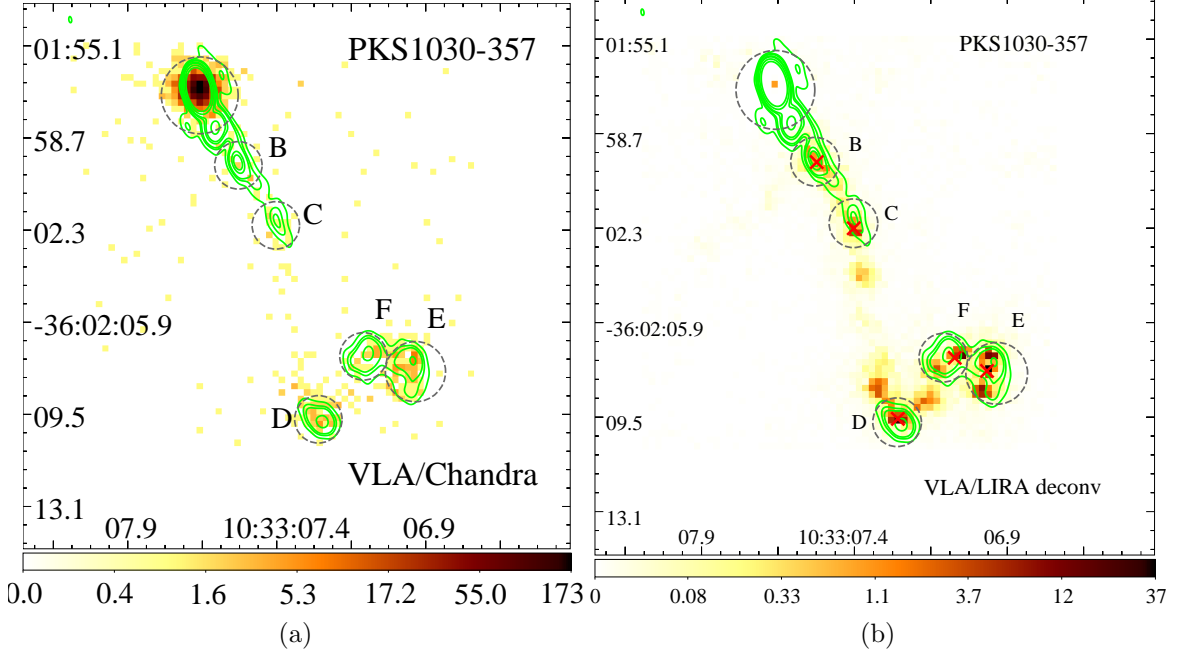


Figure 47. Same as in Fig. 1 but for PKS 1030-357. The radio contours are given by 0.3, 0.6, 0.8, 1.5, 2.0, 4.0, 8.0 mJy beam⁻¹.

3C 254 (Figure 50): This is an LDQ. The eastern hotspot shows a two-peak structure oriented in the north-south direction. The X-ray centroid in this hotspot lies

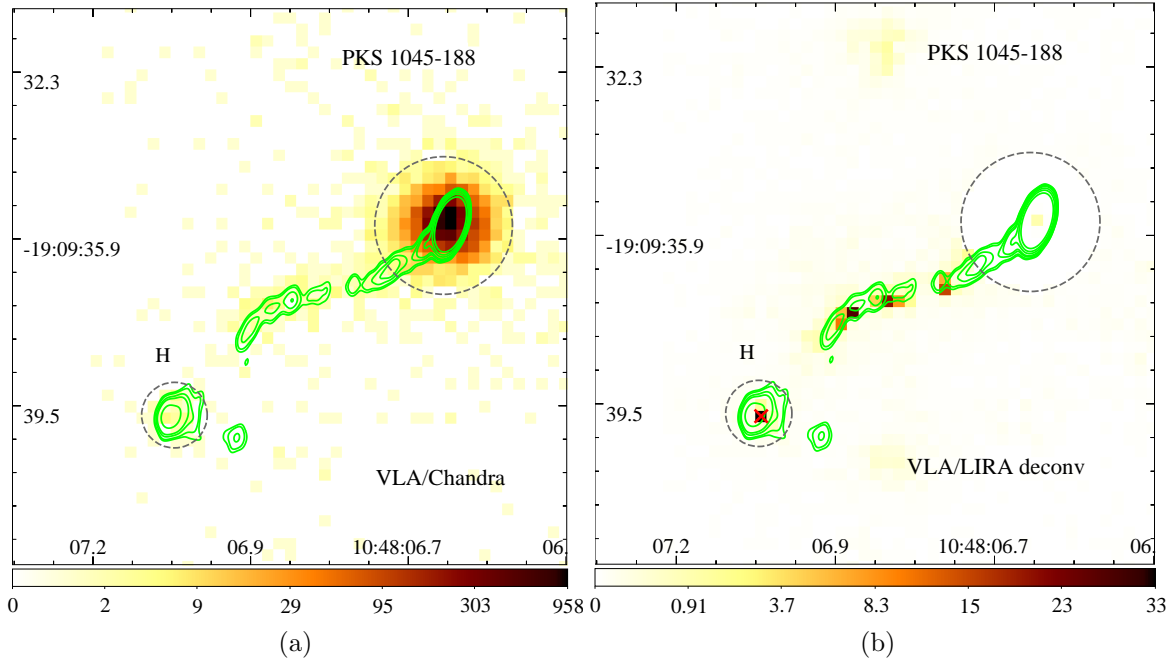


Figure 48. Same as in Fig. 1 but for PKS 1045-188. The radio contours are given by 1.0, 1.5, 0.8, 2.0, 4.0, 8.0, 20.0 mJy beam⁻¹.

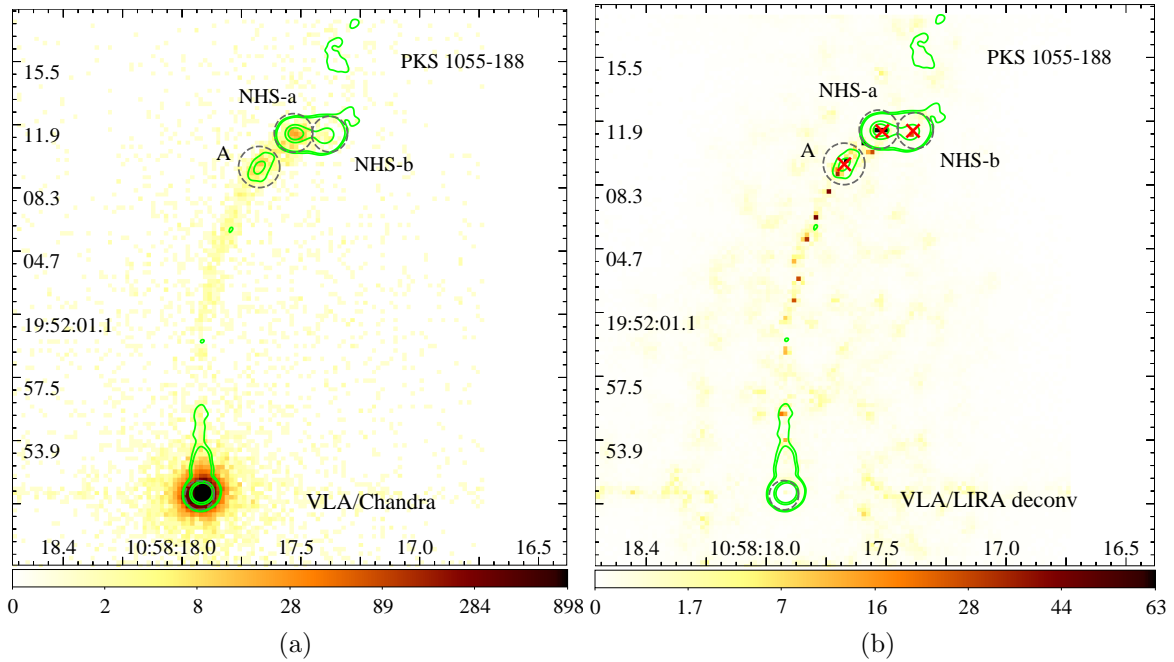


Figure 49. Same as in Fig. 1 but for PKS 1055+201. The radio contours are given by 2.0, 4.0, 100.0, 200.0 mJy beam⁻¹.

0.34'' (2.48 kpc) upstream of the southern radio peak.

PKS 1127-145 (Figure 51): This is a CDQ and has one of the longest X-ray

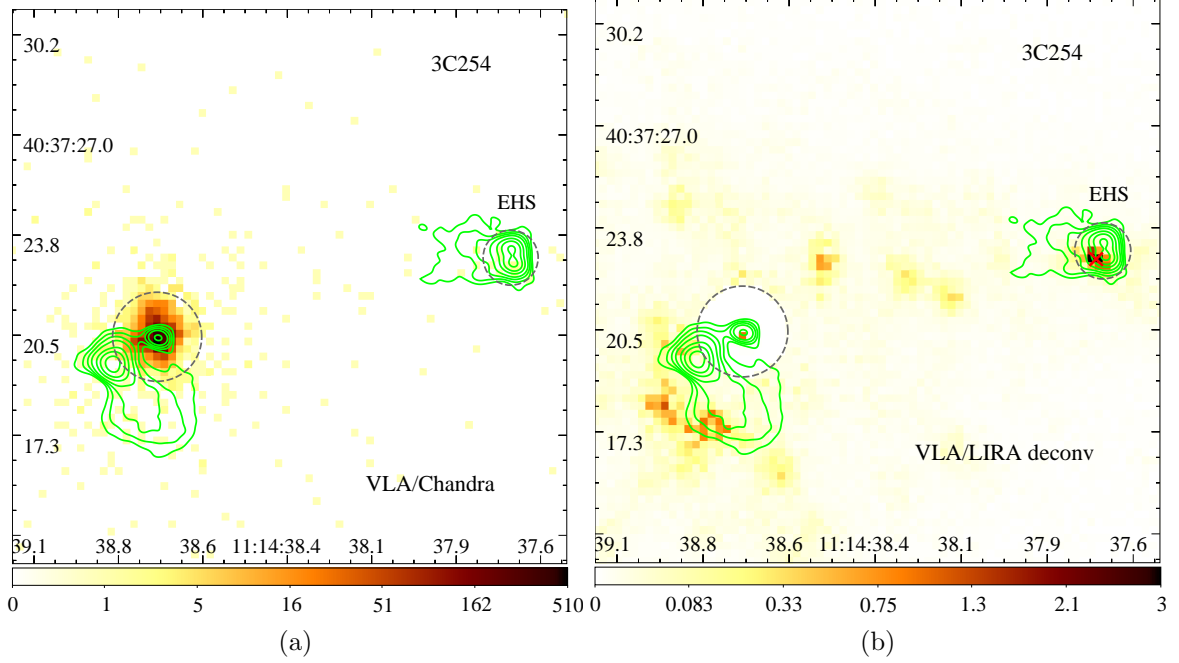


Figure 50. Same as in Fig. 1 but for 3C 254. The radio contours are given by 0.8, 2.0, 4.0, 8.0, 20.0, 40.0, 80.0 mJy beam⁻¹.

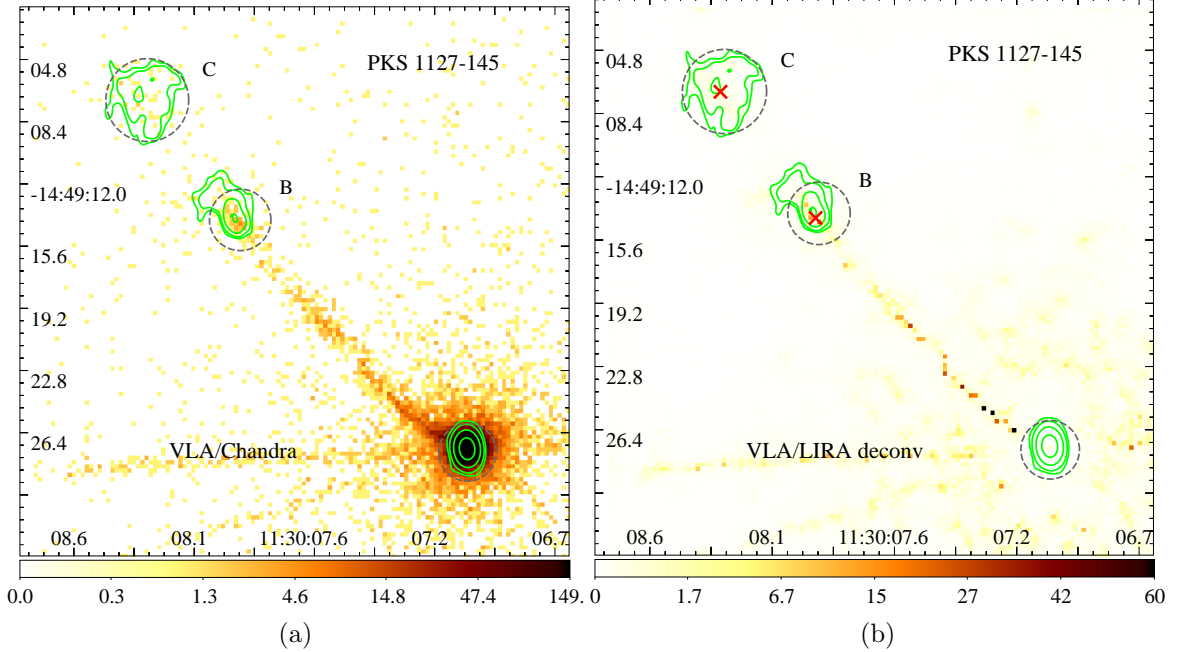


Figure 51. Same as in Fig. 1 but for PKS 1127-145. The radio contours are given by 0.25, 0.4, 0.85, 2.3, 10.0, 100.0, 1000.0 mJy beam⁻¹.

jets known to date. The X-ray image shows a bright inner jet with two knots but without any significant radio emission, and hence are excluded from are analysis. The two outer knots B and C show 0.47'' (3.9 kpc) and 0.50'' (4.15 kpc) Xf-type

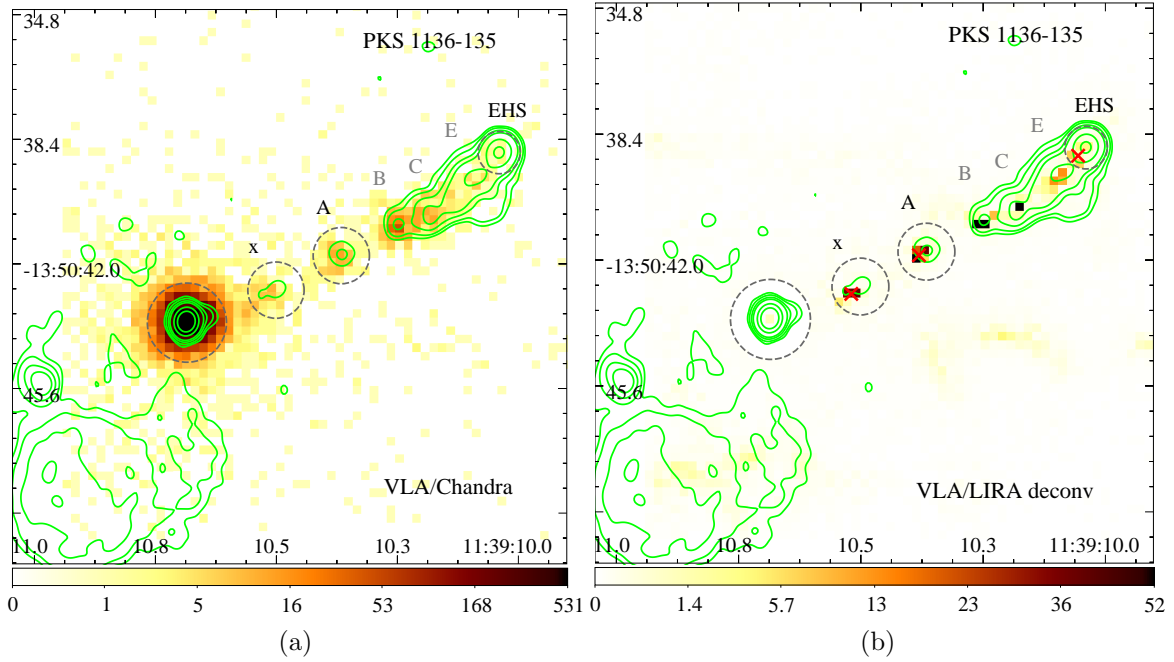


Figure 52. Same as in Fig. 1 but for PKS 1136-135. The radio contours are given by 0.9, 2.0, 5.0, 10.0, 40.0, 100.0 mJy beam⁻¹.

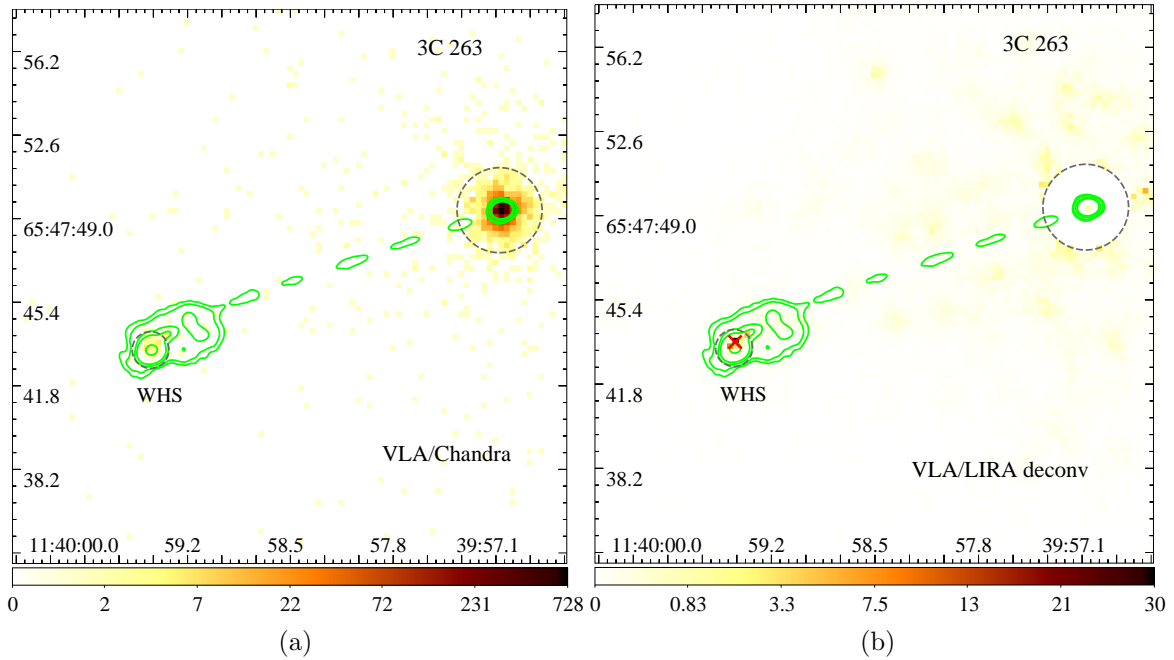


Figure 53. Same as in Fig. 1 but for 3C 263. The radio contours are given by 0.4, 1.0, 4.0, 10.0, 200.0 mJy beam⁻¹.

offsets respectively.

PKS 1136-135 (Figure 52): This is an LDQ. The two knots in the inner jet, x

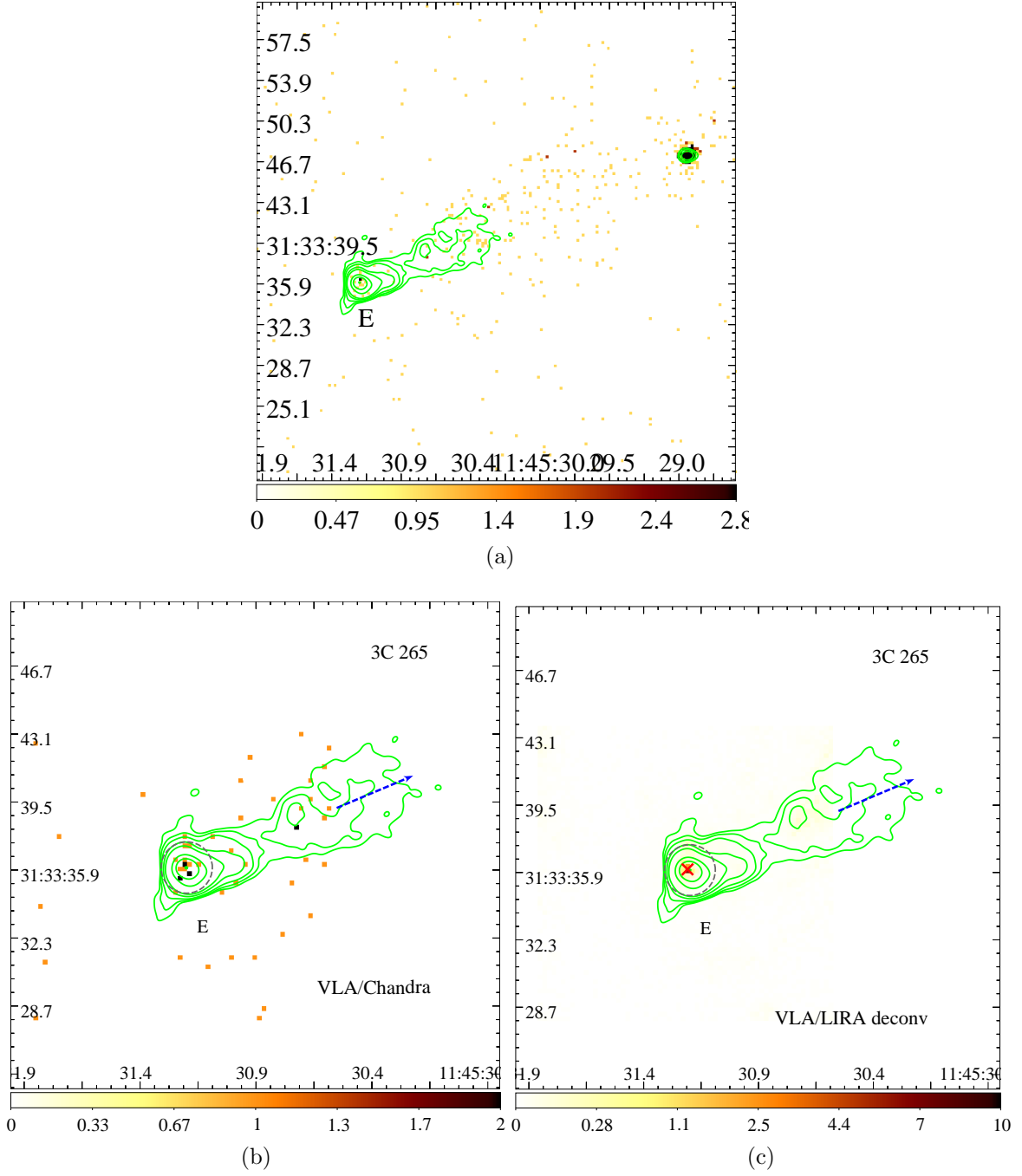


Figure 54. Same as in Fig. 1 but for 3C 265. (a) shows the full image of eastern side jet. (b) and (c) show the zoomed-in region of the eastern hotspot. The radio contours are given by 0.2, 0.4, 0.8, 2.0, 4.0, 20.0, 40.0, 80.0 mJy beam⁻¹.

and A, show $0.37''$ (2.37 kpc) and $0.281''$ (1.8 kpc) Xf-type offsets, respectively. We exclude the knots in the outer jet from offset analysis due to their close separation ($< 1''$), which, although show roughly coincident X-ray and radio peaks. Hence, we tentatively include them under the Co-s-type category. The eastern hotspot (EHS) shows a $0.35''$ (2.24 kpc) Xf-type offset.

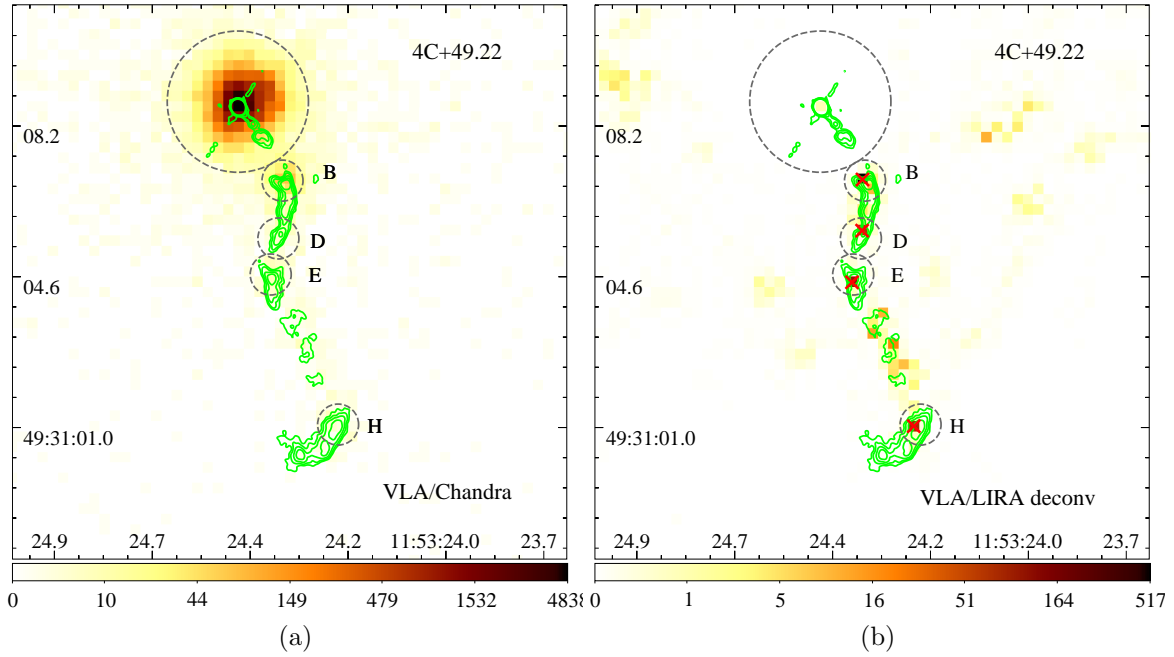


Figure 55. Same as in Fig. 1 but for 4C +49.22. The radio contours are given by 0.05, 0.1, 0.2, 0.4, 0.8 mJy beam⁻¹.

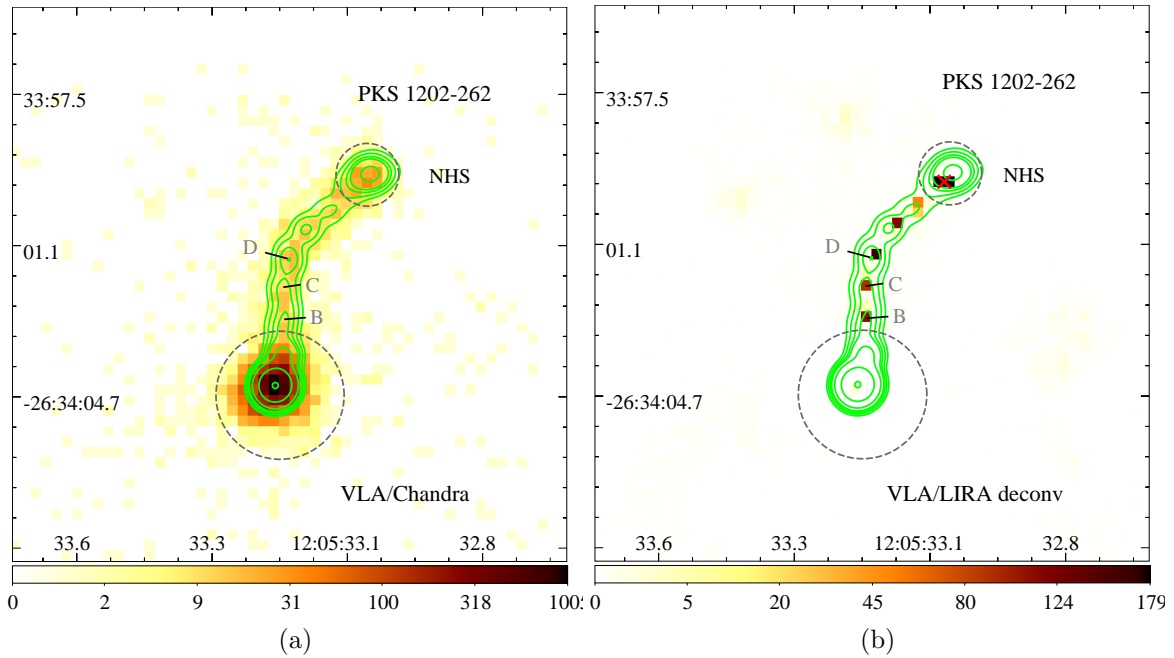


Figure 56. Same as in Fig. 1 but for PKS 1202-262. The radio contours are given by 1.5, 3.0, 5.4, 8.0, 20.0, 100.0, 500.0 mJy beam⁻¹.

3C 263 (Figure 53): This is an LDQ. The radio image shows a knotty radio jet to the southeast although without any X-ray counterpart. The jet terminates in the

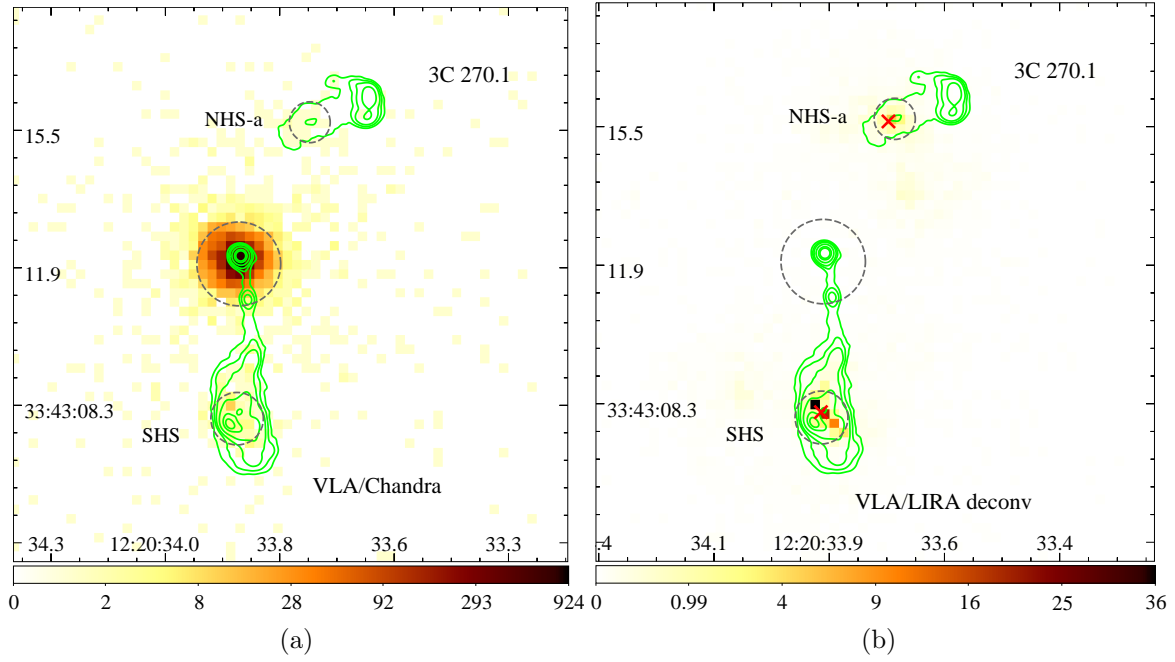


Figure 57. Same as in Fig. 1 but for 3C 270.1. The radio contours are given by 0.1, 0.36, 1.0, 5.0, 22.0, 40.0 mJy beam⁻¹.

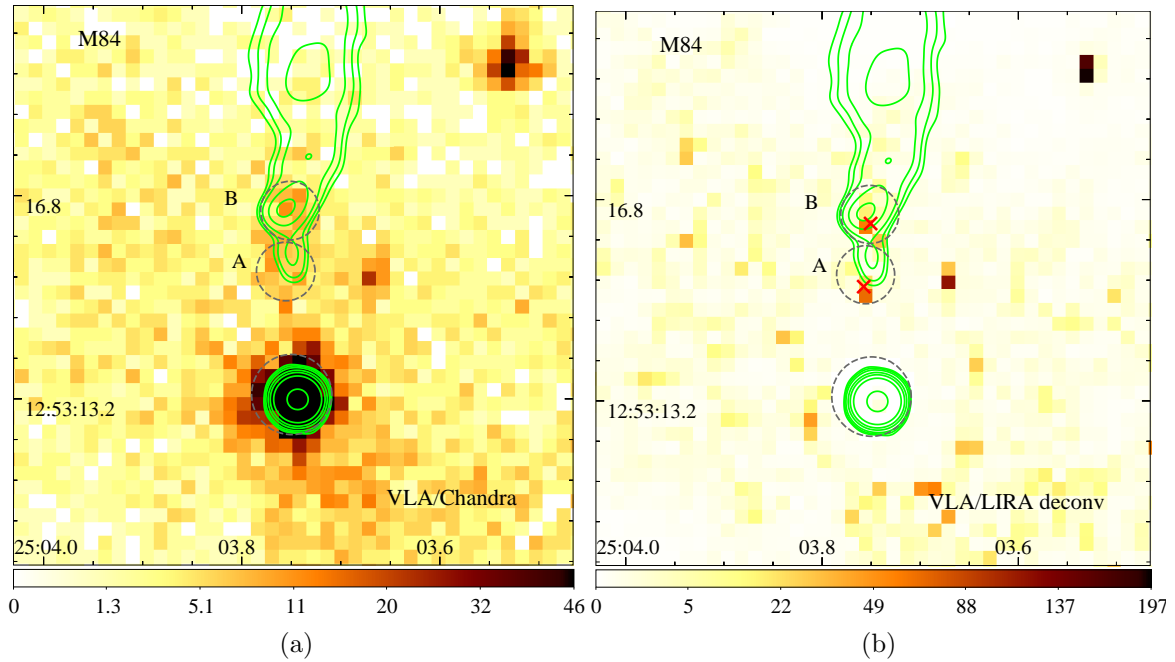


Figure 58. Same as in Fig. 1 but for M84. The radio contours are given by 0.2, 0.4, 0.8, 2.0, 4.0, 10.0, 100.0 mJy beam⁻¹.

western hotspot with a 0.28'' (1.96 kpc) Xf-type offset.

3C 265 (Figure 54): This is an FR II source. Its eastern hotspot (E) shows a

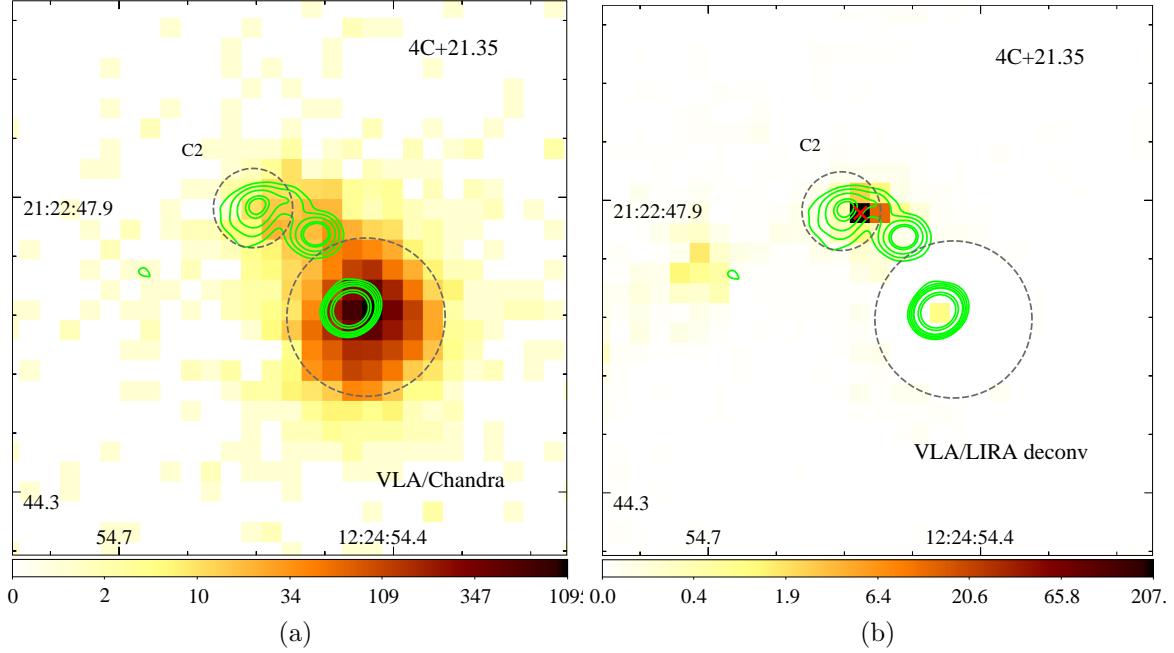


Figure 59. Same as in Fig. 1 but for 4C +21.35. The radio contours are given by 1.0, 2.0, 4.0, 8.0, 10.0, 40.0, 80.0 mJy beam⁻¹.

Co-s-type offset.

4C +49.22 (Figure 55): This is a CDQ. The jet bends from the southwest to the southeast at knot B and shows a 0.197'' (0.95 kpc) Xf-type offset. Knot D, which lies further down, shows a Co-s-type offset. The jet then turns to the southwest at knot E and shows a Co-s-type offset. Knot H, which lies at another apparent bend in the jet, also shows a Co-s-type offset.

PKS 1202-262 (Figure 56): This is a CDQ. We exclude knots in the inner jet from offset analysis due to their small separation ($< 1''$), however, the deconvolved X-ray image shows a knotty structure coinciding with radio knots B, C, D. Hence we tentatively include them under the Co-s-type. Although we find two radio peaks further down the jet, they lie in between the radio peaks, making their radio association ambiguous. The eastern hotspot shows a 0.53'' (4.29 kpc) Xf-type offset.

PKS 1202-262 (Figure 56): This is a CDQ. The radio image shows a one-sided jet to the northeast. We exclude the knots from offset analysis due to their close separation ($< 1''$). The northern hotspot (NHS) shows a 0.28'' (2.09 kpc) Xf-type offset.

3C 270.1 (Figure 57): This is a quasar. As mentioned in section 3, we find a new bar-like structure in the X-rays in the southern hotspot (SHS) region 0.375'' (3.26 kpc) upstream of the radio peak. This bar is presumably the location where the jet loses

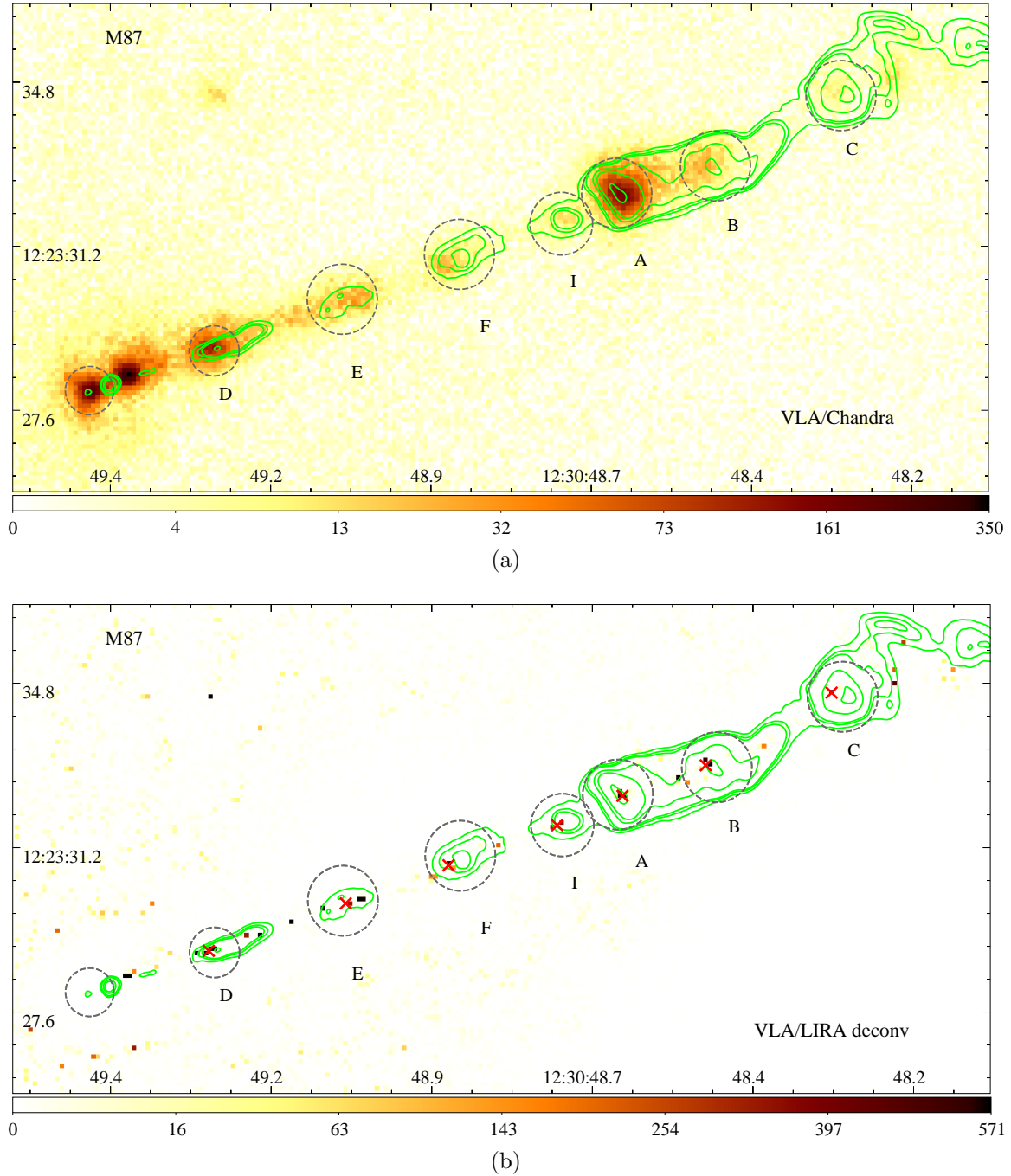


Figure 60. Same as in Fig. 1 but for M87. The radio contours are given by 5.0, 8.0, 23.0, 35.0, 70.0 mJy beam⁻¹.

a major portion of its kinetic energy producing X-rays, similar to 4C +74.26 (Erlund et al. 2007, 2010). A faint knot upstream of the northern hotspot, NHS-a, where the jet presumably enters the turbulent hotspot region, shows a Co-s-type offset.

M84 (Figure 58): This is an FR I source. The radio image shows no radio emission prior to knot A, where the jet presumably flares, and produces a bright knotty jet

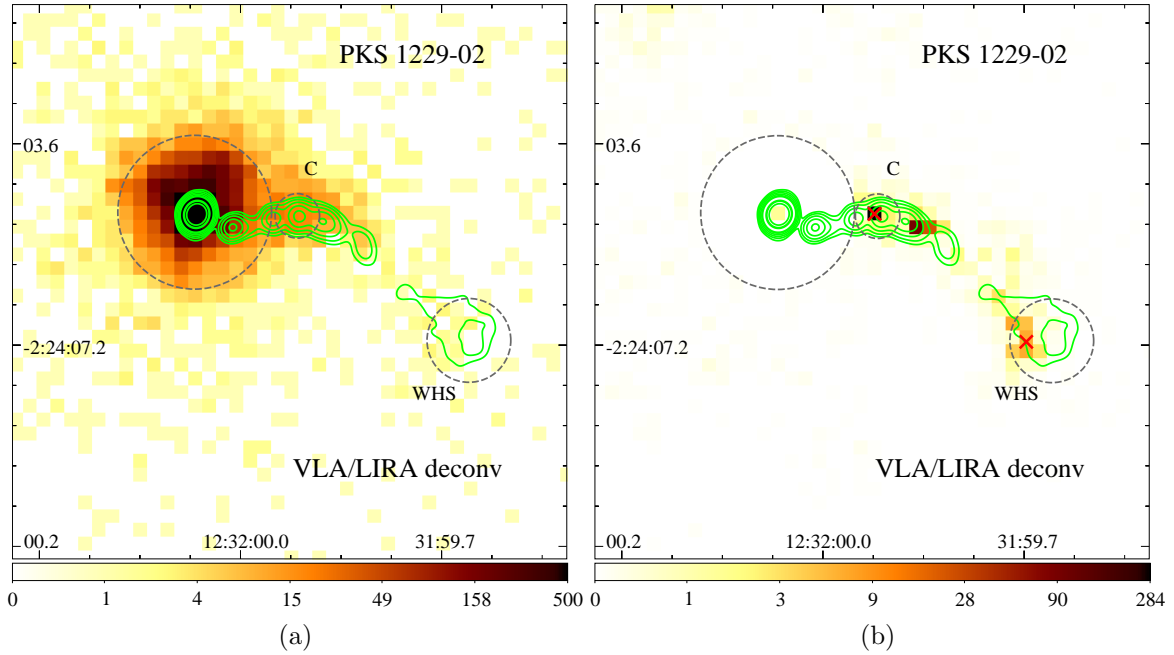


Figure 61. Same as in Fig. 1 but for PKS 1229-02. The radio contours are given by 1.0, 2.0, 4.0, 8.0, 15.0, 20.0, 80.0, 100.0, 200.0 mJy beam⁻¹.

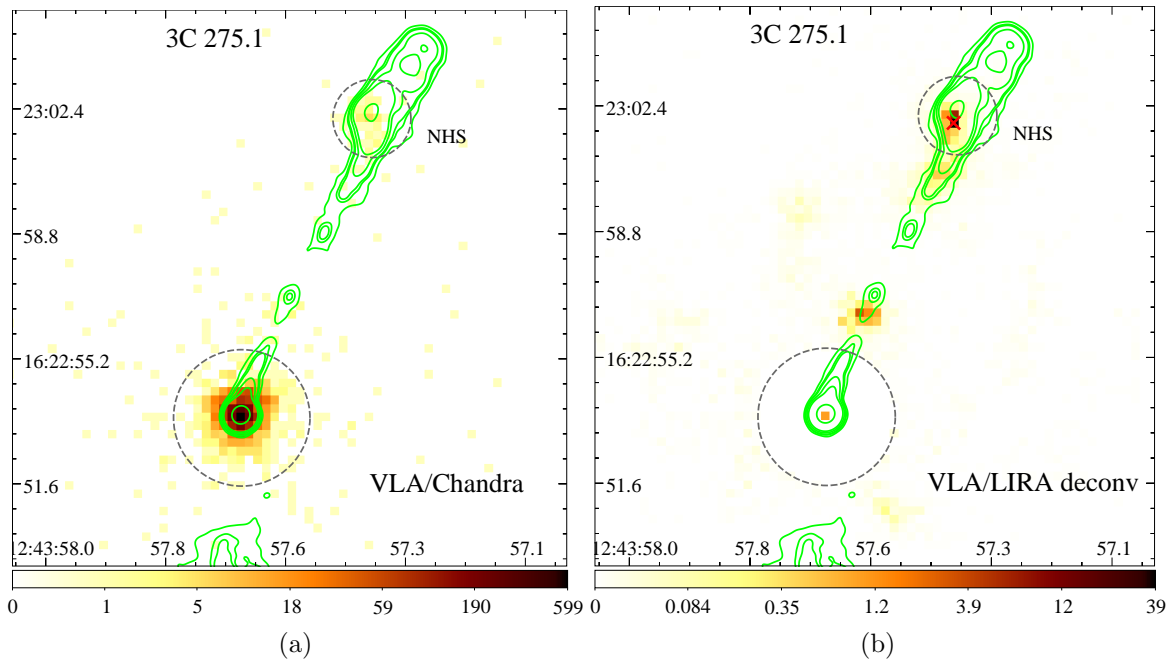


Figure 62. Same as in Fig. 1 but for 3C 275.1. The radio contours are given by 0.4, 0.8, 1.0, 2.0, 4.0, 70.0 mJy beam⁻¹.

further down. We find 0.598''(0.081 kpc) and 1.366'' (0.11 kpc) Xf-type offsets in knot A and B, respectively.

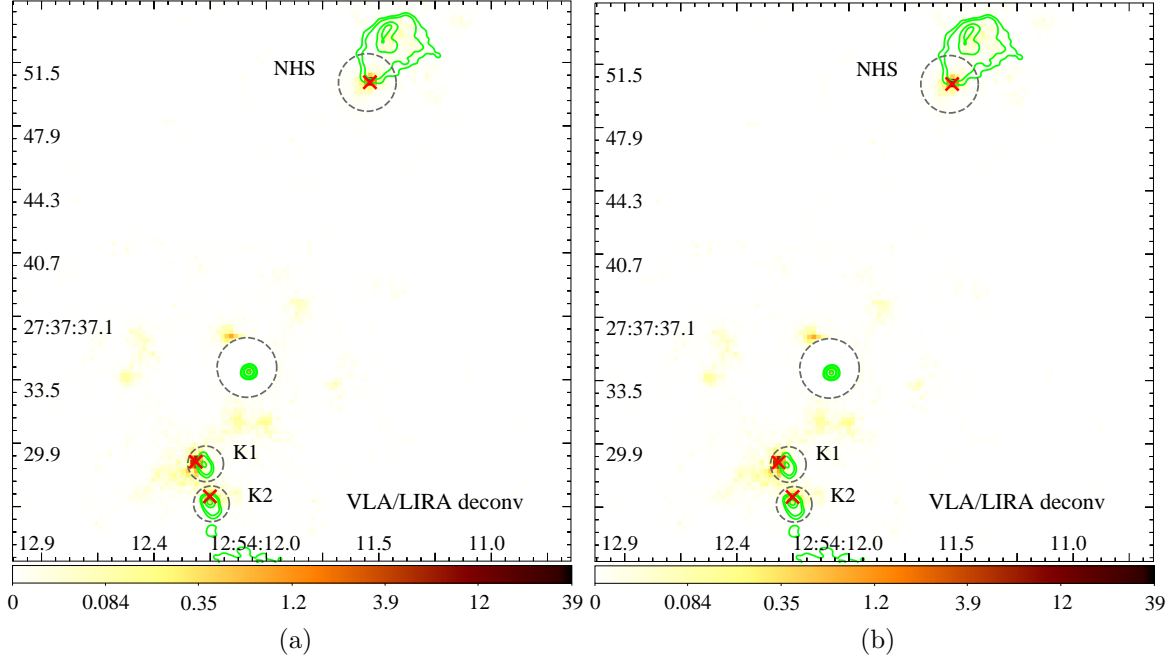


Figure 63. Same as in Fig. 1 but for 3C 277.3. The radio contours are given by 0.5, 1.0, 3.0, 4.5, 10.0 mJy beam⁻¹.

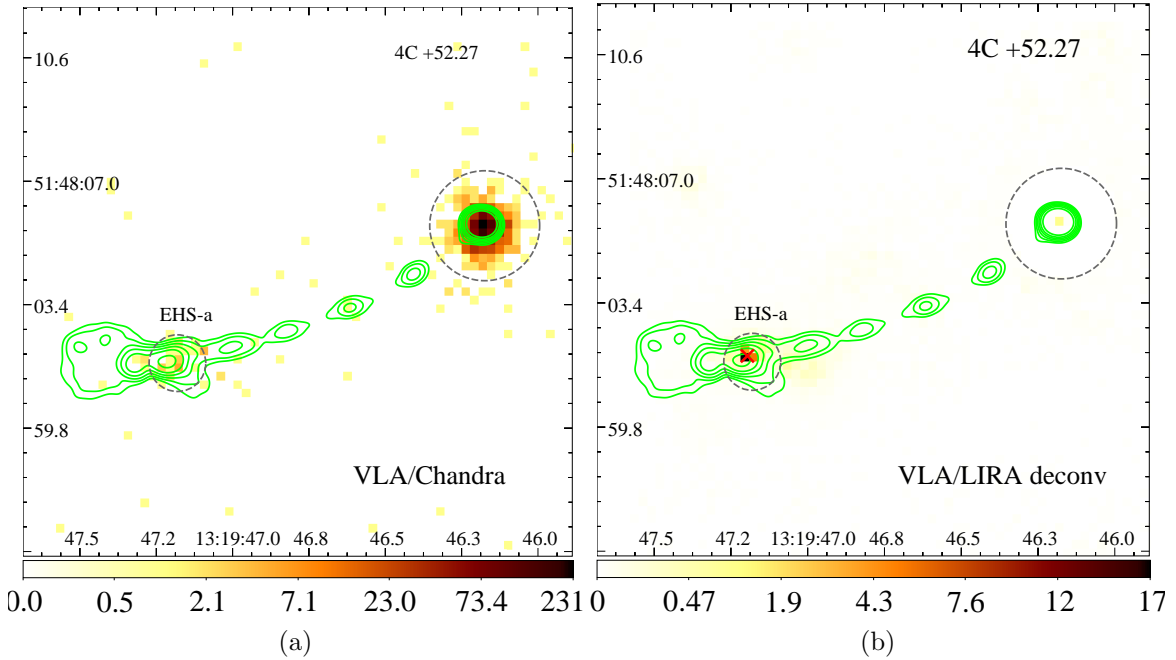


Figure 64. Same as in Fig. 1 but for 4C +52.27. The radio contours are given by 0.5, 1.0, 2.0, 4.0, 8.0, 20.0 mJy beam⁻¹.

4C+21.35 (Figure 59): This is a CDQ. The radio image shows a knotty jet to the northeast of the core turning to the southeast at knot C2. We find a 0.19'' (1.06 kpc) Xf-type offset in knot C2.

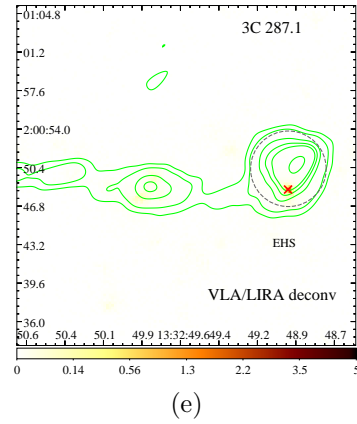
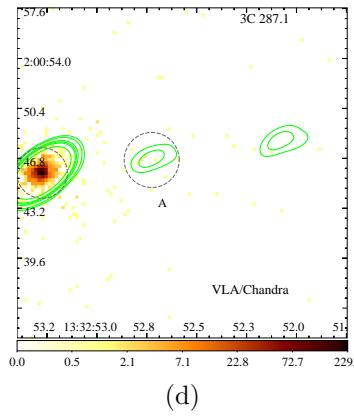
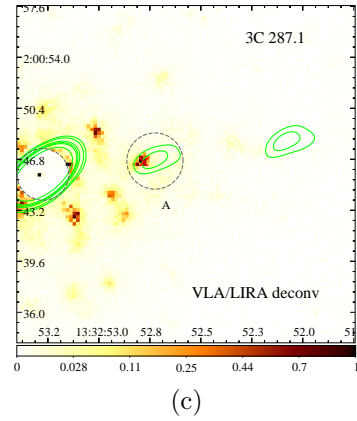
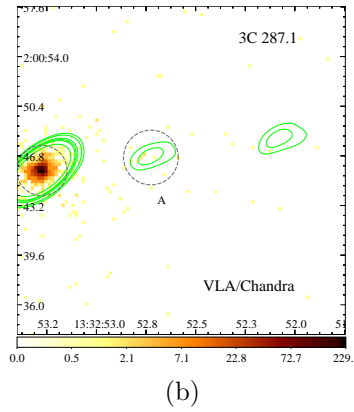
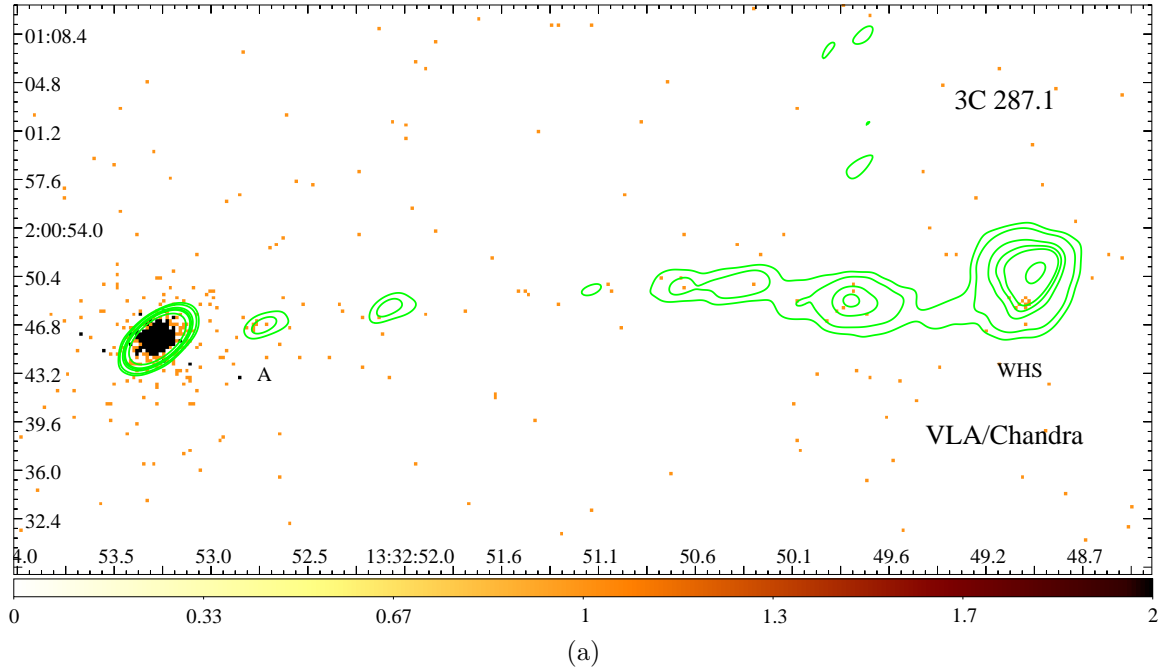


Figure 65. Same as in Fig. 1 but for 3C 287.1. (a) shows the full image while (b), (c) and (d),(e) show the zoomed-in regions around knot A and eastern hotspot (EHS), respectively. The radio contours are given by 0.8, 1.5, 4.0, 6.0, 8.0, 20.0 mJy beam⁻¹.

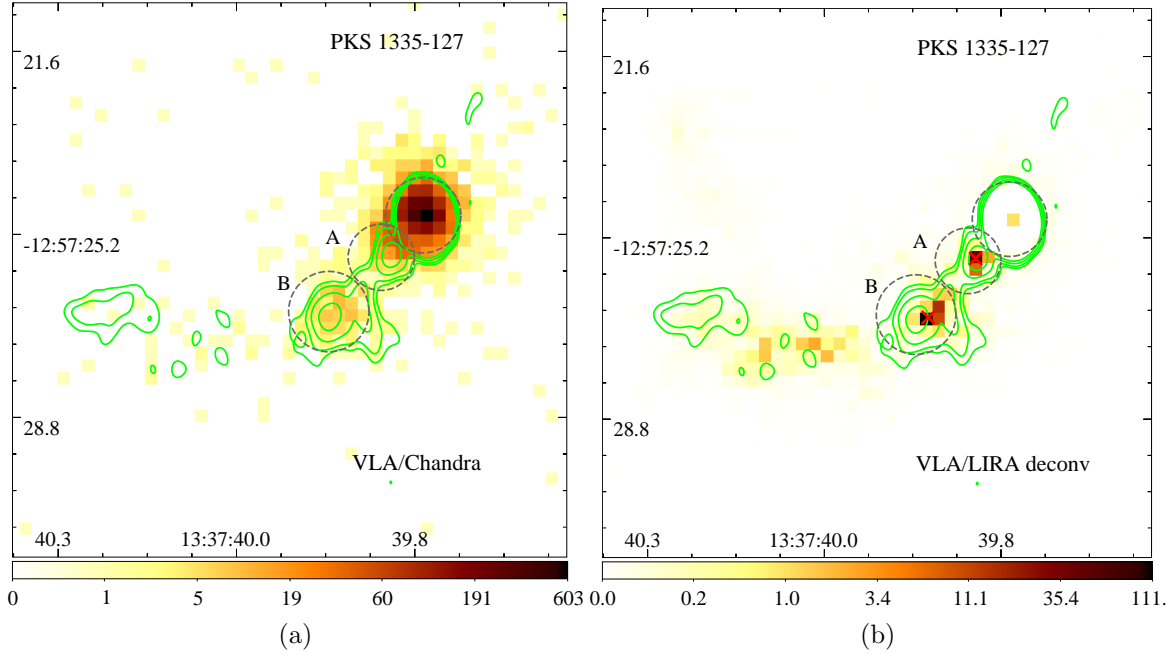


Figure 66. Same as in Fig. 1 but for PKS 1335-127. The radio contours are given by 1.2, 2.0, 4.0, 8.0 mJy beam⁻¹.

M87 (Figure 60): This is a well-studied nearby FR-I jet. Because of its close-proximity and brightness, majority of its *Chandra* observations have many counts. Hence, we considered only one of the observations for our analysis. We find Xf-type offsets in knots B, C, D, F, I while none in knots A and E.

PKS 1229-02 (Figure 61): This is a CDQ. We exclude knots in the inner jet from offset analysis due to their small separation ($< 1''$). The eastern hotspot shows a $0.53''$ (4.29 kpc) Xf-type offset.

3C 275.1 (Figure 62): This is an LDQ. The northern hotspot (NHS) shows a $0.41''$ (2.62 kpc) Xf-type offset.

3C 277.3 (Figure 63): This is an FR II source. A previously cold gas cloud deflects the jet from the southwest to the southeast at knot K1. The X-rays in this knot region are produced by the shock heated cloud (Worrall et al. 2016) and hence we exclude K1 from the offset analysis. The jet bends again at knot K2 where it shows a $0.27''$ (0.45 kpc) Xf-type offset. Similarly, the northern hotspot (NHS) also shows $3.1''$ (5.17 kpc) Xf-type offset.

4C +52.27 (Figure 64): This is a CDQ. The radio image shows a knotty jet to the southeast without any X-ray counterpart. The jet terminates in the eastern

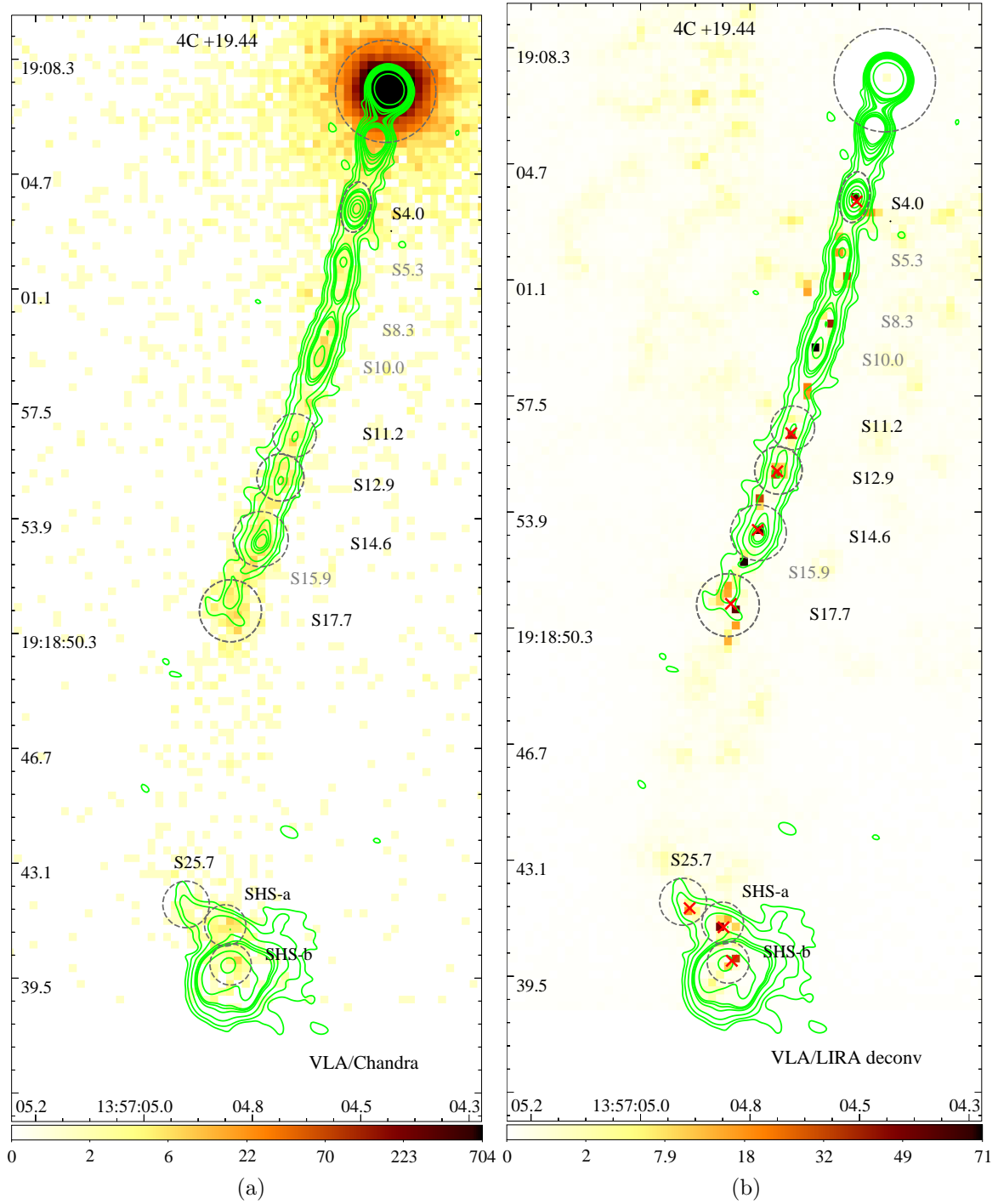


Figure 67. Same as in Fig. 1 but for 4C+19.44. The radio contours are given by 0.25, 0.4, 0.8, 1.6, 2.3, 2, 4, 6, 8, 10, 60 mJy beam⁻¹.

hotspot with a double-peaked structure oriented along the east-west direction. The western peak, EHS-a, shows a 0.22'' (1.79 kpc) Xf-type offset.

3C 287.1 (Figure 65): This is a quasar. The radio image shows a one-sided knotty jet to the west although with significant emission only from knot A. We measure a

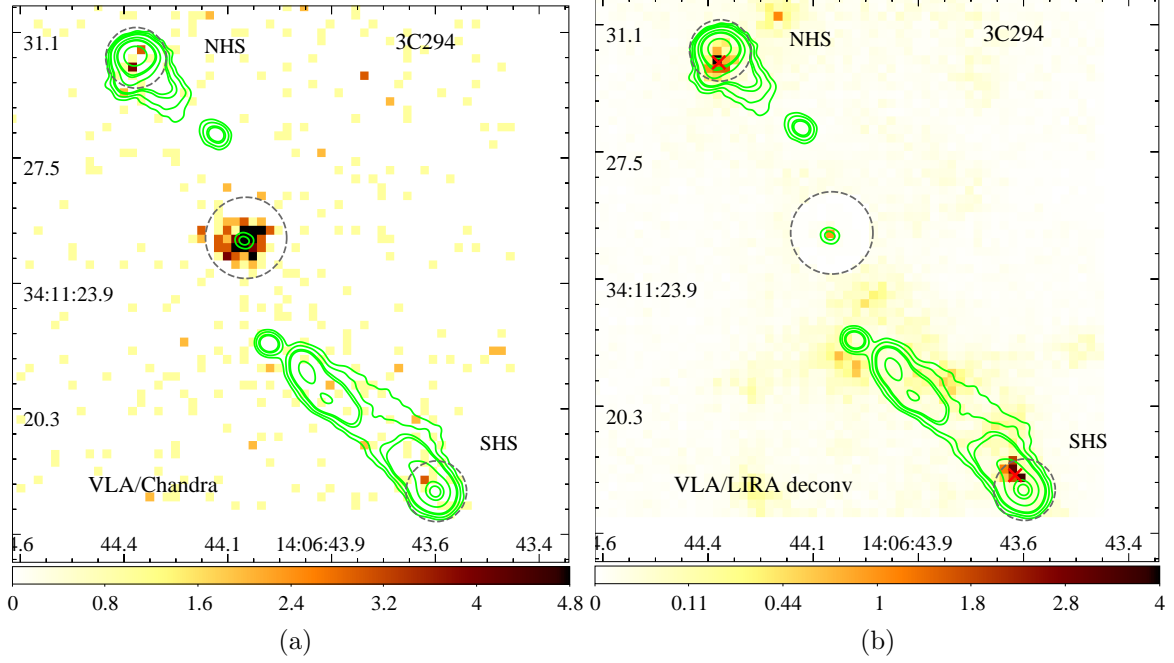


Figure 68. Same as in Fig. 1 but for 3C 294. The radio contours are given by 0.2, 0.4, 0.8, 1.0, 3.5, 8.0, 10.0, 40.0 mJy beam^{-1} .

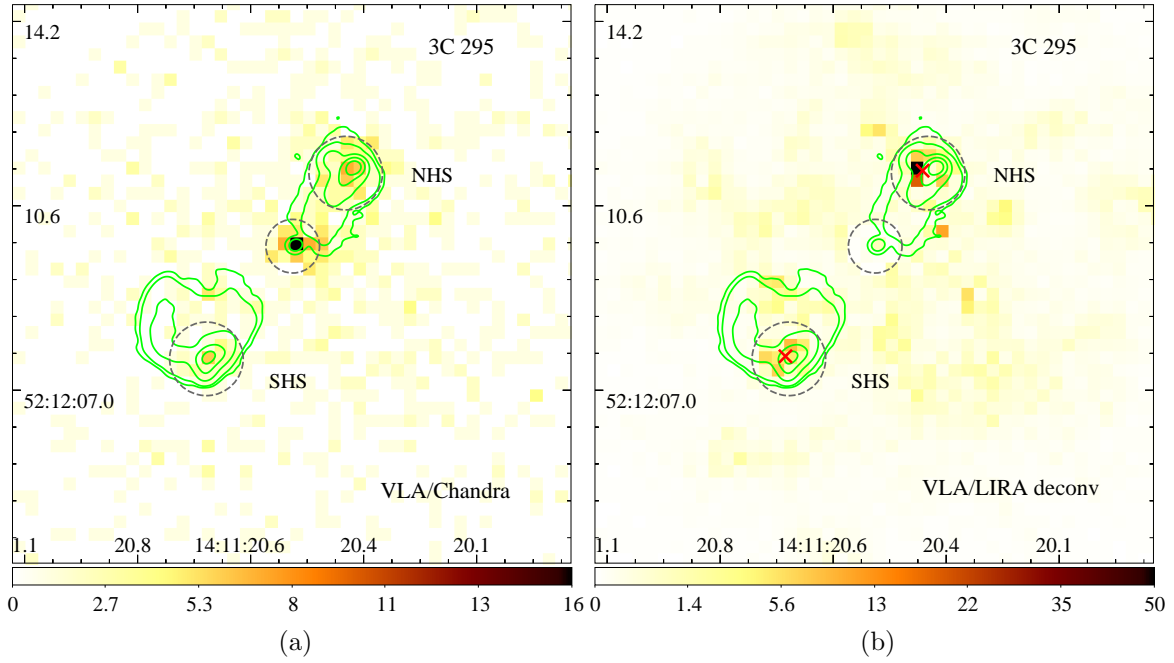


Figure 69. Same as in Fig. 1 but for 3C 295. The radio contours are given by 0.4, 2.0, 20.0, 100.0, 300.0 mJy beam^{-1} .

0.92'' (3.33 kpc) Xf-type in knot A. The jet shows a sharp bend to the north at the eastern hotspot (WHS). We find a 2.39'' (8.65 kpc) Xf-type offset in WHS.

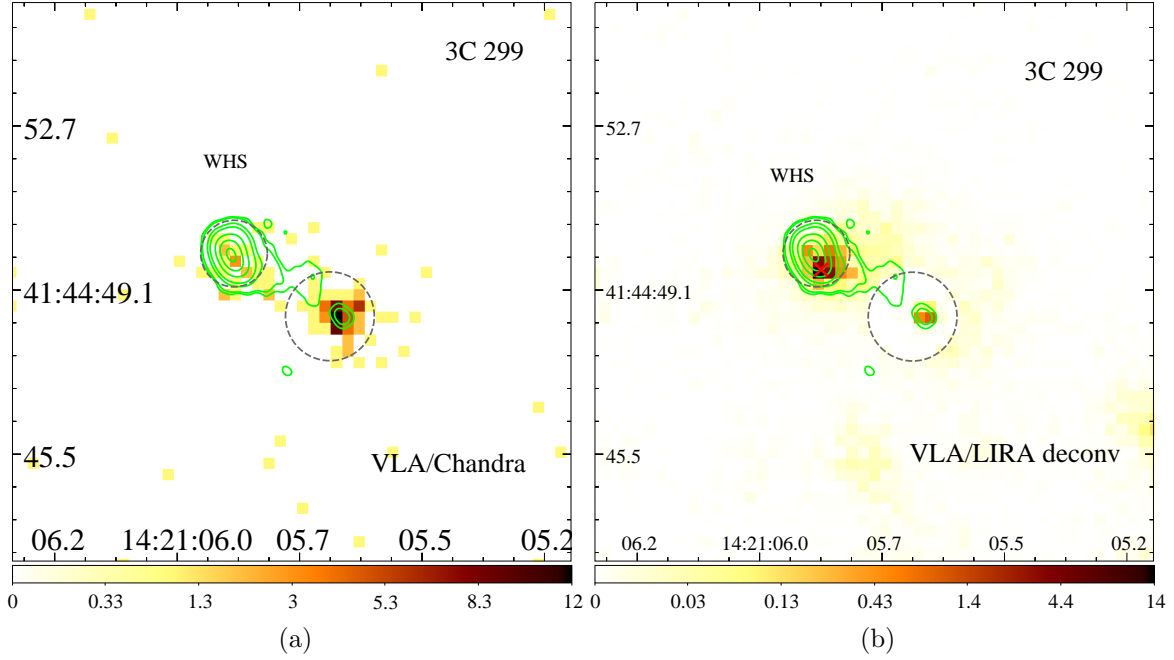


Figure 70. Same as in Fig. 1 but for 3C 299. The radio contours are given by 0.5, 1.0, 8.0, 20.0, 80.0, 200.0, 400.0 mJy beam⁻¹.

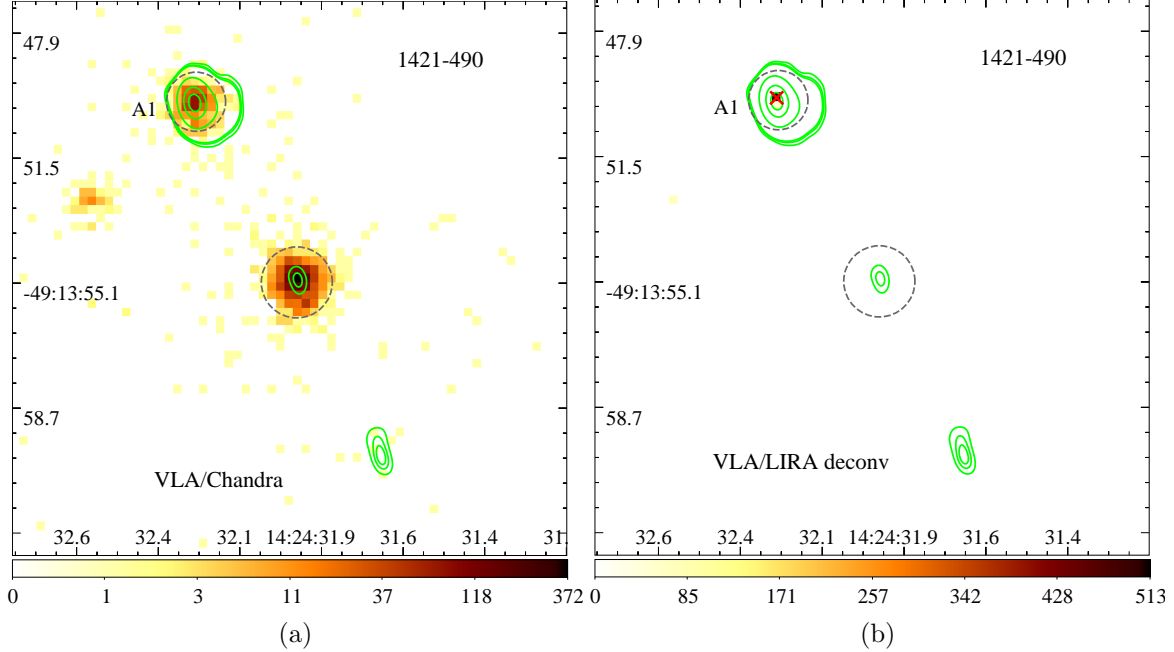


Figure 71. Same as in Fig. 1 but for PKS 1421-490. The radio contours are given by 5, 8, 10, 200, 1000, 2000 mJy beam⁻¹.

PKS 1335-127 (Figure 66): This is a CDQ. The inner knot, A, shows a Co-s-type offset. Further downstream of knot A, the jet makes a sharp turn to the east at knot B showing a 0.22'' (1.39 kpc) Xf-type offset.

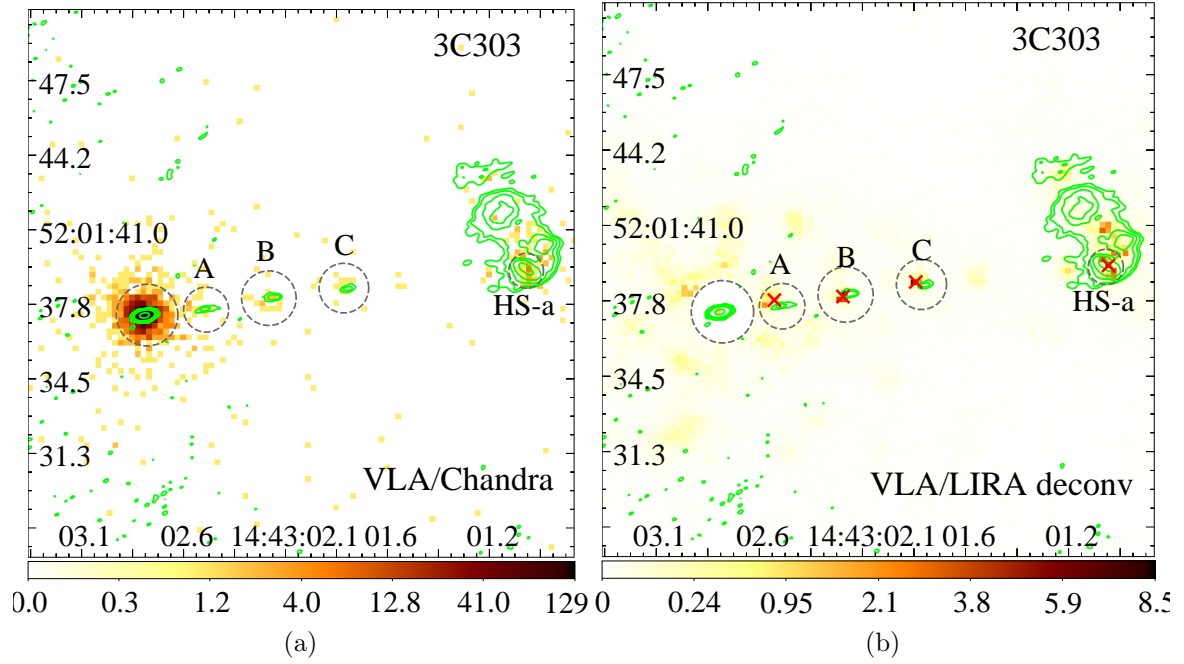


Figure 72. Same as in Fig. 1 but for 3C 303. The radio contours are given by 0.4, 0.8, 2.0, 4.0, 10.0, 100.0 mJy beam⁻¹.

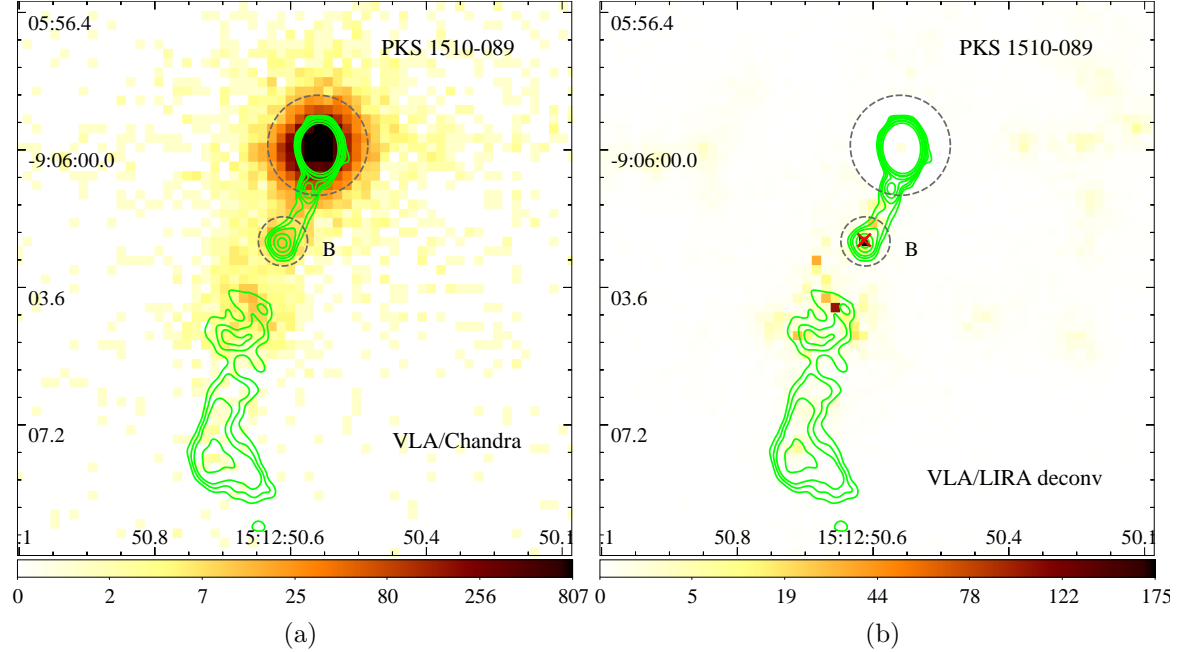


Figure 73. Same as in Fig. 1 but for PKS 1510-08. The radio contours are given by 1.0, 1.5, 2.0, 3.0, 4.0, 8.0, 10.0, 20.0 mJy beam⁻¹.

4C+19.44 (Figure 67): This is CDQ with a 18'' long knotty jet to the southeast. We find no offsets in the inner jet except at knot S17.7, where the X-rays extend past the

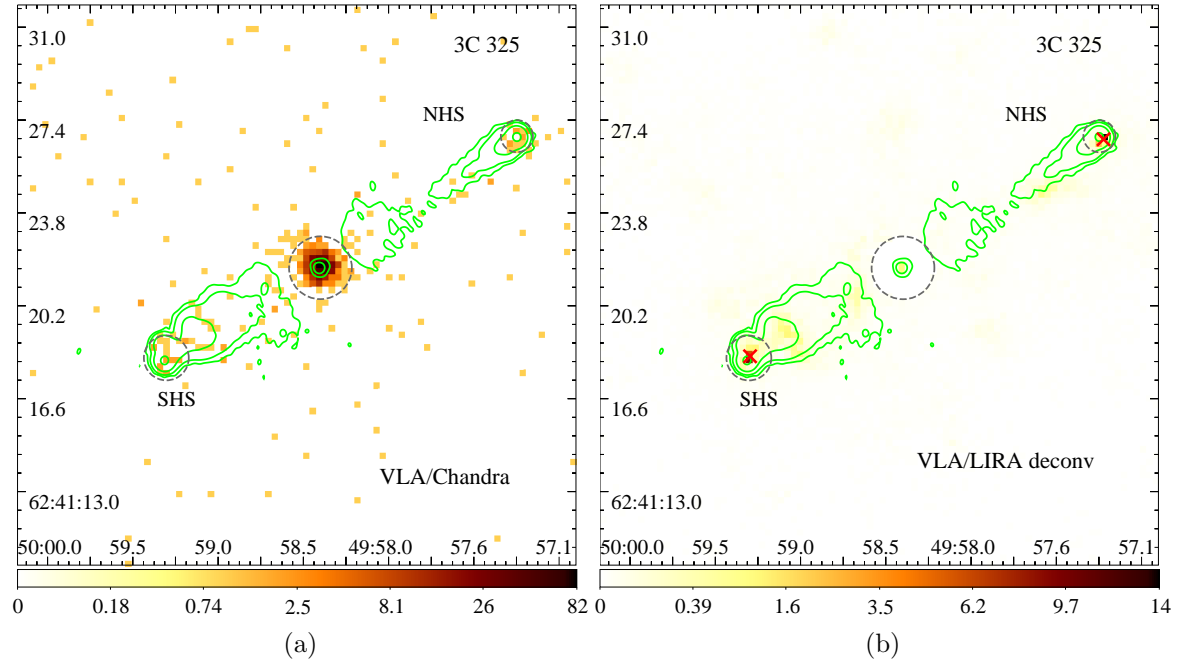


Figure 74. Same as in Fig. 1 but for 3C 325. The radio contours are given by 0.15, 1.0, 10.0, 130.0 mJy beam⁻¹.

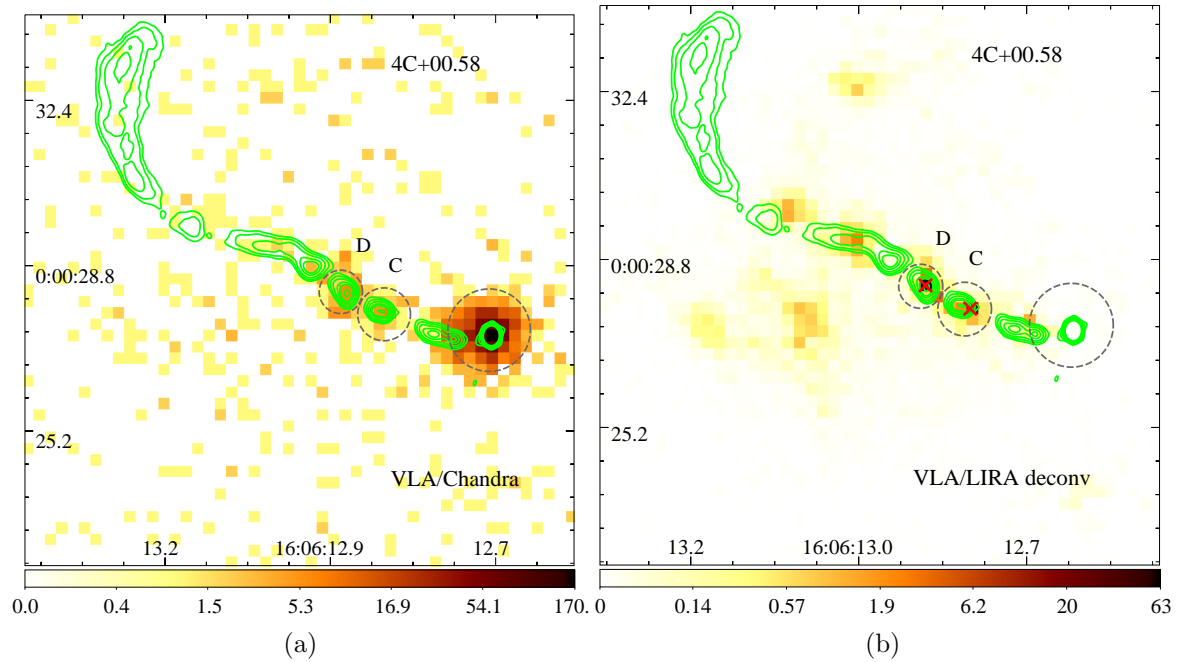


Figure 75. Same as in Fig. 1 but for 4C +00.58. The radio contours are given by 0.1, 0.2, 0.4, 0.8, 1.2, 2.2 mJy beam⁻¹.

radio. As discussed in section 4.1, it is possible that a stationary obstacle interacting presumably produces these X-rays beyond the jet. The jet vanishes at S17.1 and re-emerges at S2.5.7 where X-rays coincide with the radio. Further downstream of

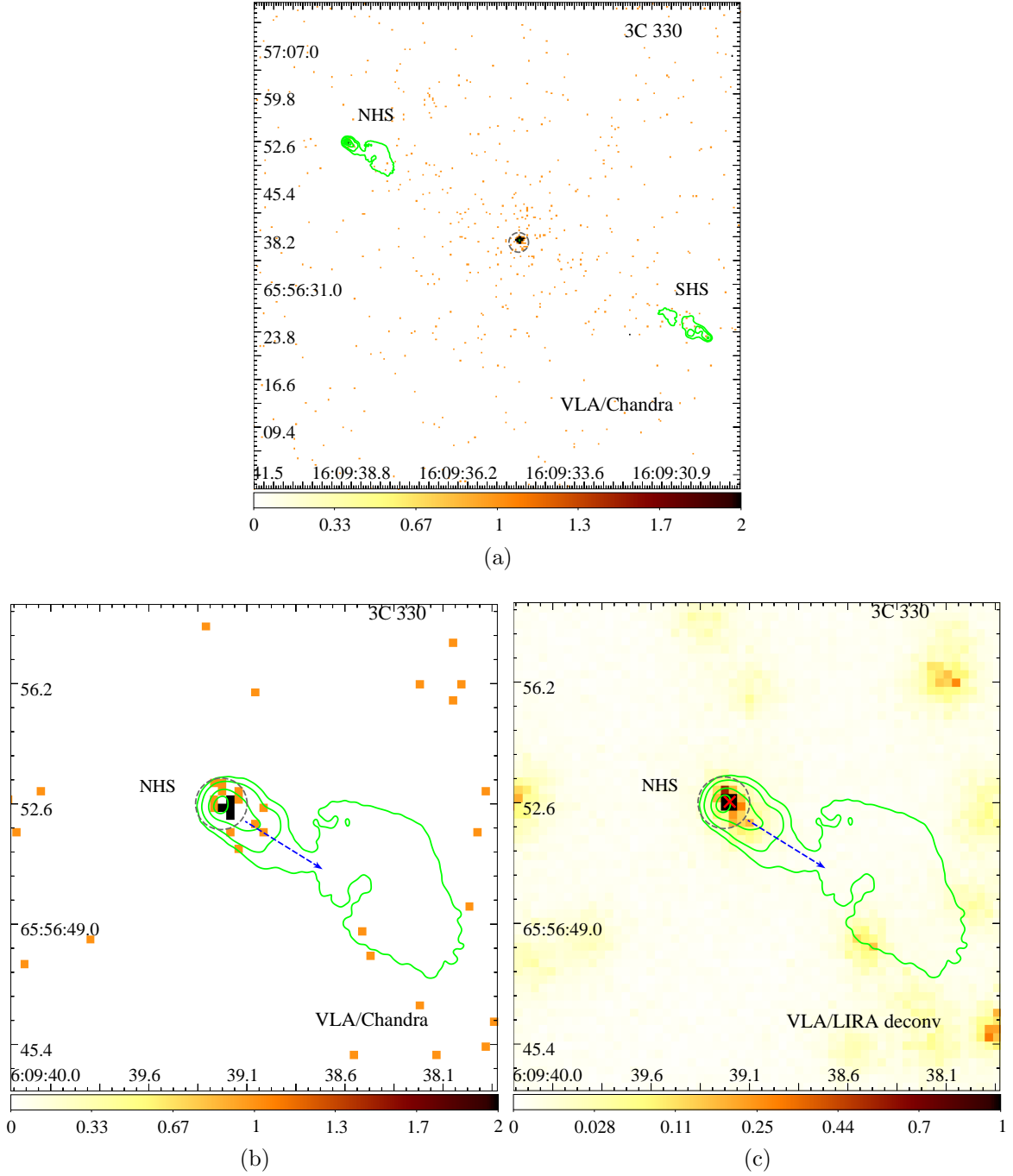


Figure 76. Same as in Fig. 1 but for 3C 330. (a) shows the full image while (b) and (c) zoomed-in regions around the northern hotspot (NHS). The radio contours are given by 0.8, 8.0, 80.0, 200.0 mJy beam⁻¹.

this knot, the jet terminates in a double hotspot-like structure (SHS), where X-rays coincide with the radio in SHS-a, while they peak 0.275'' (1.98 kpc) upstream of the radio peak in SHS-b.

3C 294 (Figure 68): This is an FR II source. The radio image shows two hotspots to

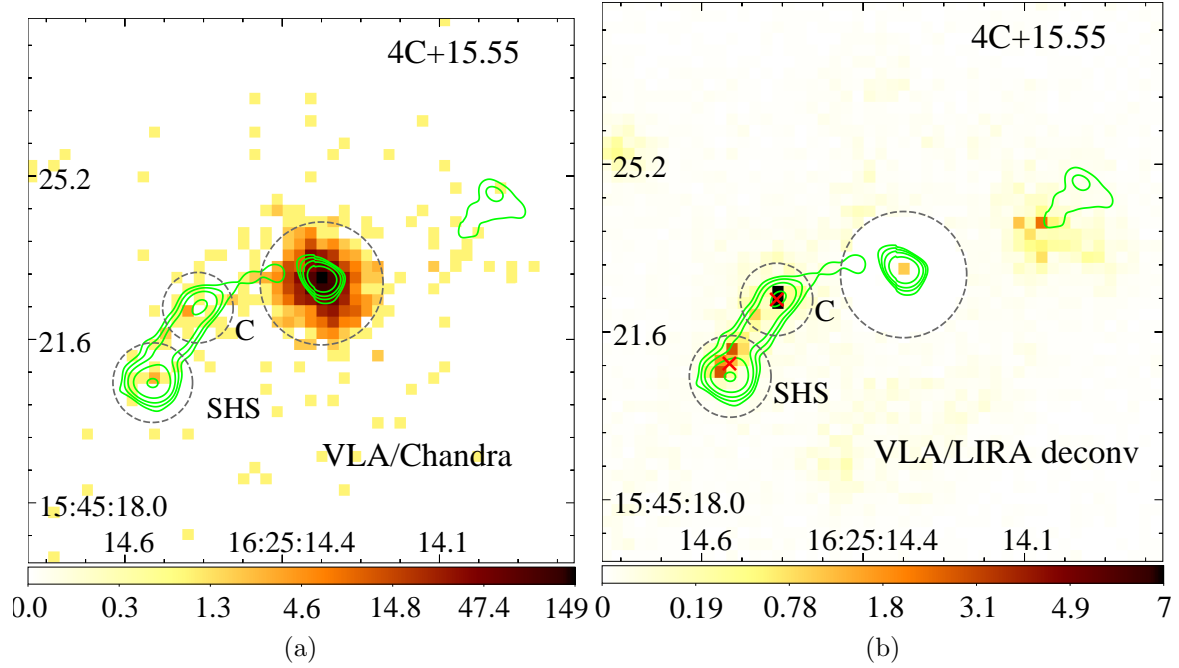


Figure 77. Same as in Fig. 1 but for 4C +15.55. The radio contours are given by 2.0, 4.0, 8.0, 20.0, 80.0 mJy beam⁻¹.

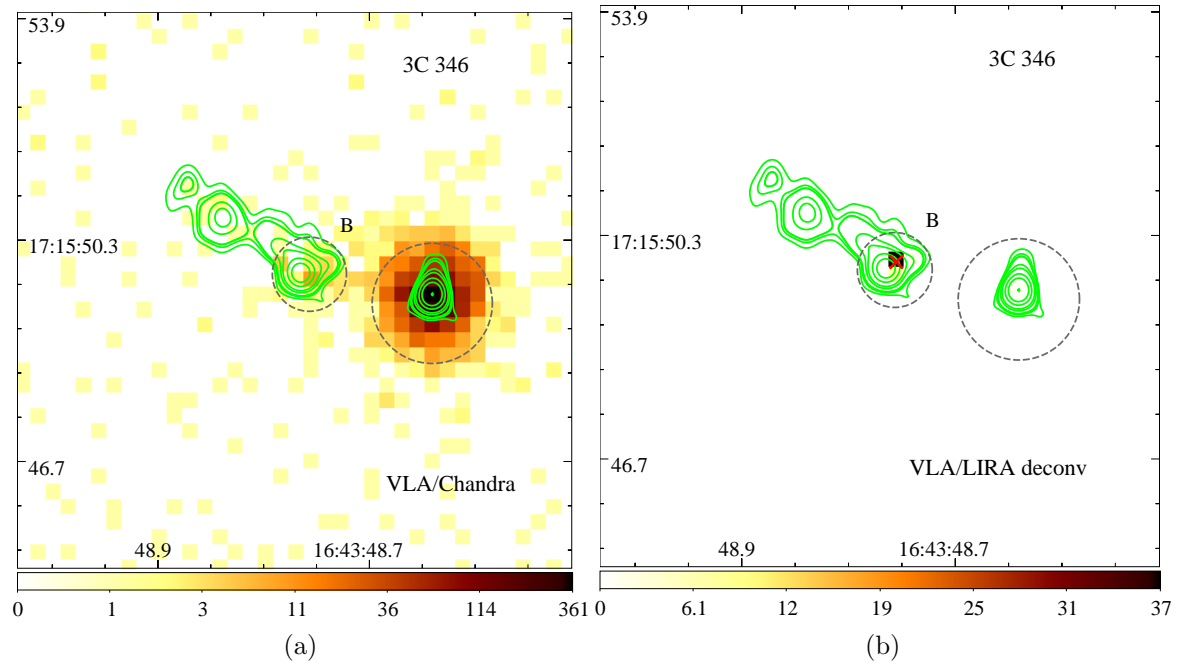


Figure 78. Same as in Fig. 1 but for 3C 346. The radio contours are given by 5.0, 8.0, 10.0, 20.0, 60.0, 10.0, 30.0, 100.0, 200.0 mJy beam⁻¹.

the north and south of the core. The southern hotspot (SHS) shows a $0.50''$ (4.25 kpc) Xf-type offset. The northern jet produces a radio knot before terminating in the northern hotspot. Although the NHS shows a $0.40''$ (3.4 kpc) offset, the X-ray centroid

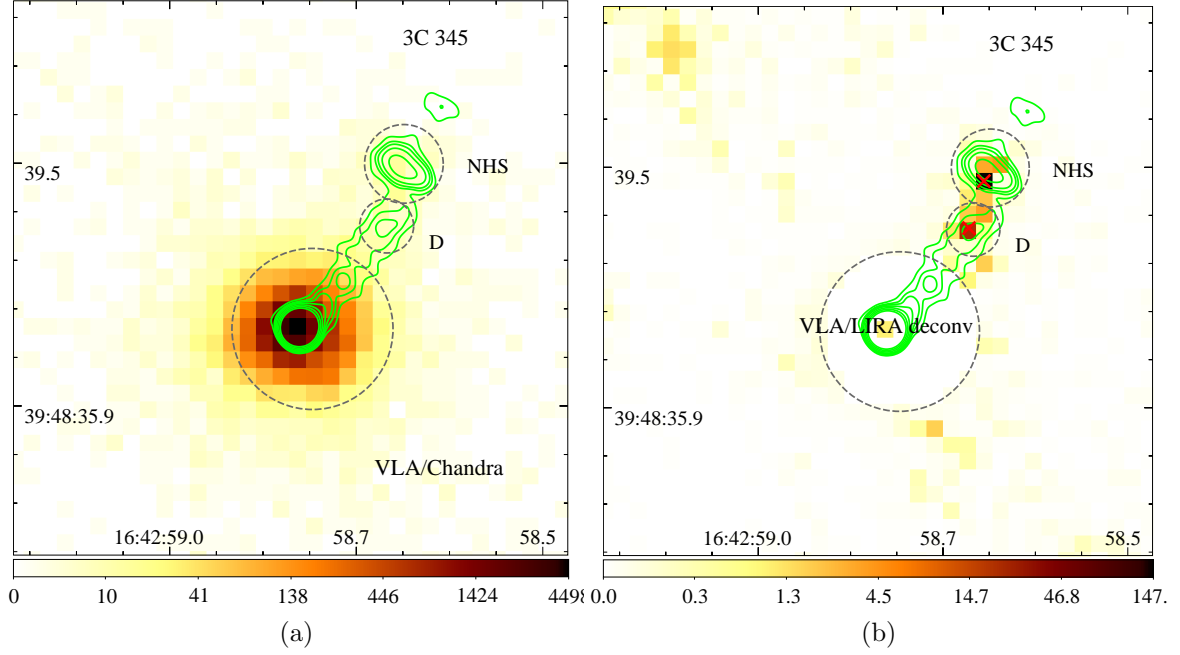


Figure 79. Same as in Fig. 1 but for 3C 345. The radio contours are given by 2.0, 4.0, 6.0, 10.0, 20.0, 40.0, 80.0 mJy beam⁻¹.

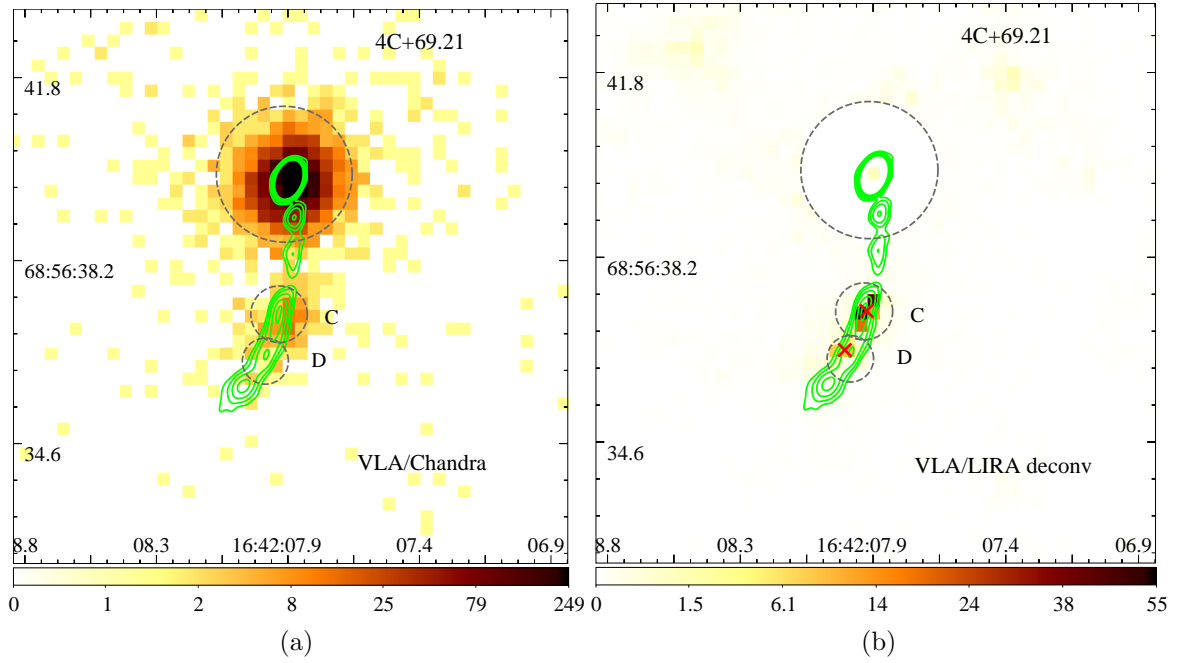


Figure 80. Same as in Fig. 1 but for 4C +69.21. The radio contours are given by 0.5, 1.0, 2.0, 4.0, 6.0, 8.0 mJy beam⁻¹.

does not lie along the line joining this knot and NHS. However, it lies to the southwest of NHS and aligns with elongated radio structure to the southwest of NHS where the jet presumably enters the jet hotspot region. Hence we indicate it as an Xf-type offset.

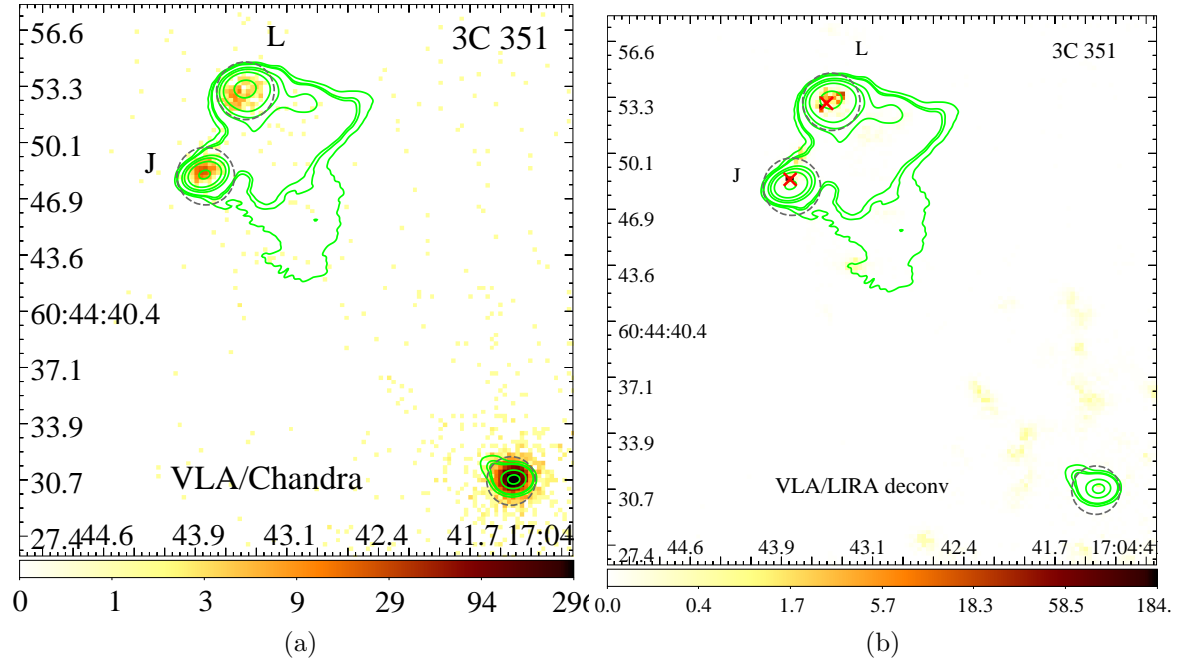


Figure 81. Same as in Fig. 1 but for 3C 351. The radio contours are given by 0.4, 0.8, 1.0, 4.0, 8.0, 20.0, 100.0 mJy beam⁻¹.

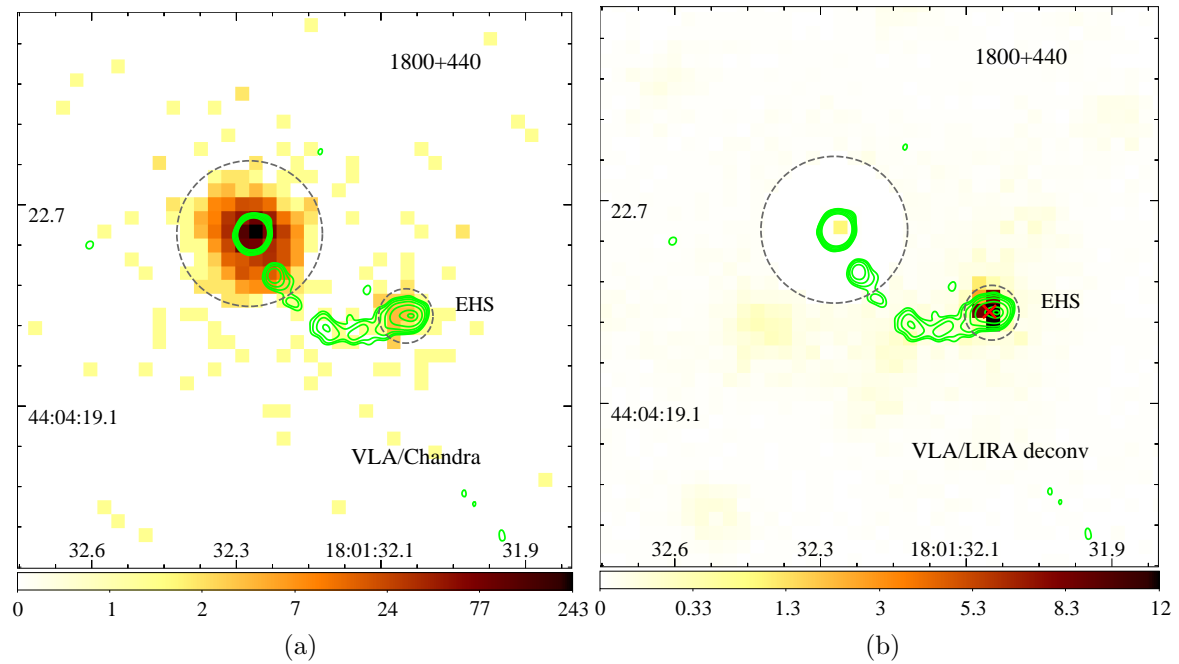


Figure 82. Same as in Fig. 1 but for 1800+440. The radio contours are given by 0.6, 0.8, 1.2, 2.0, 4.0, 8.0, 10.0 mJy beam⁻¹.

3C 295 (Figure 69): This is an FR II jet, embedded in a bright cluster gas. While the northern hotspot (NHS) shows a 0.267'' (1.52 kpc) Xf-type offset, the X-rays

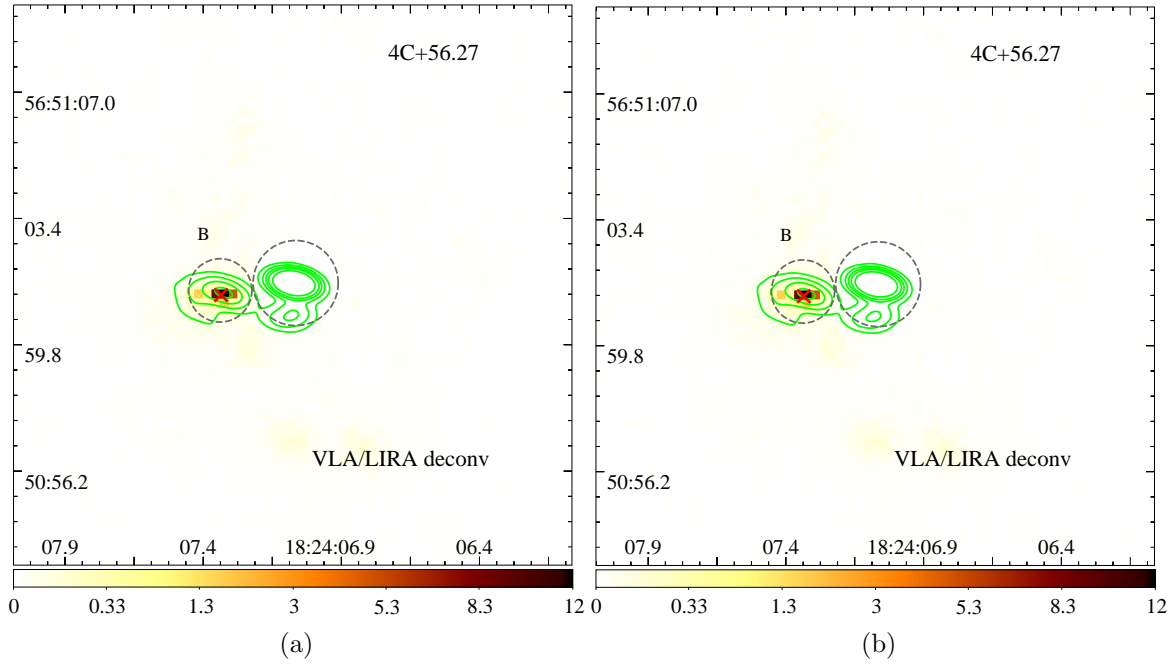


Figure 83. Same as in Fig. 1 but for 4C +56.27. The radio contours are given by 2.0, 8.0, 20.0, 40.0, 1000.0 mJy beam⁻¹.

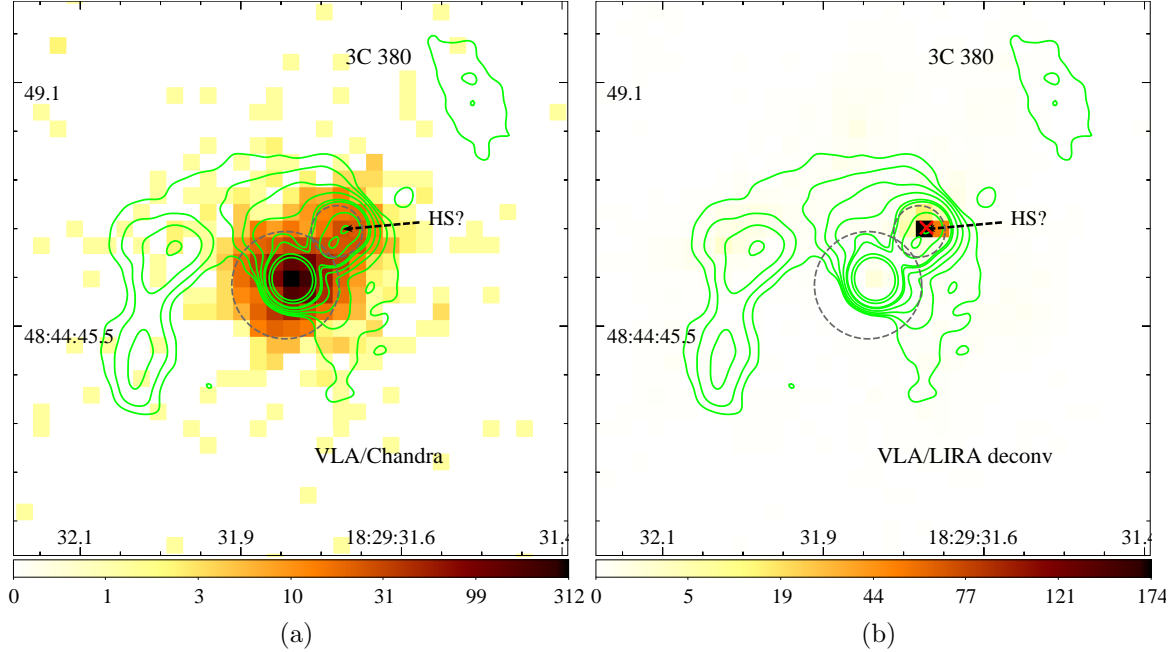


Figure 84. Same as in Fig. 1 but for 3C 380. The radio contours are given by 5.0, 10.0, 20.0, 40.0, 80.0, 100.0, 250.0, 425.0 mJy beam⁻¹.

coincide with the radio in the southern hotspot (SHS).

3C 299 (Figure 70): This is an FR II source. We detect Xf-type offsets in both the

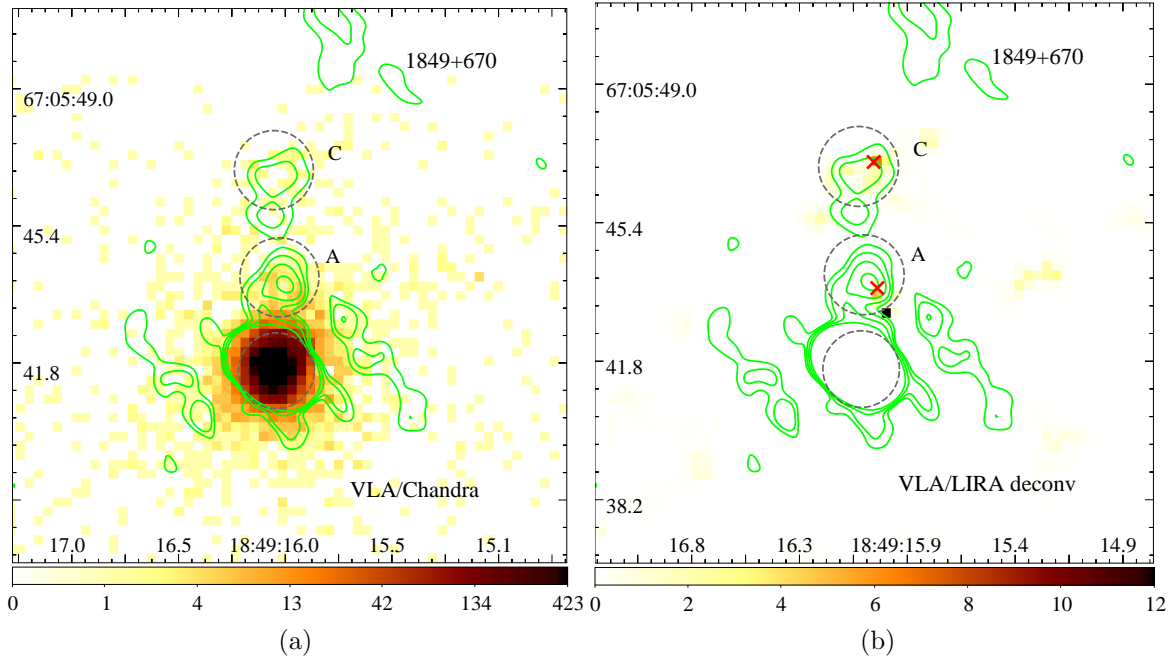


Figure 85. Same as in Fig. 1 but for 1849+670. The radio contours are given by 0.05, 0.1, 0.2, 0.4 mJy beam⁻¹.

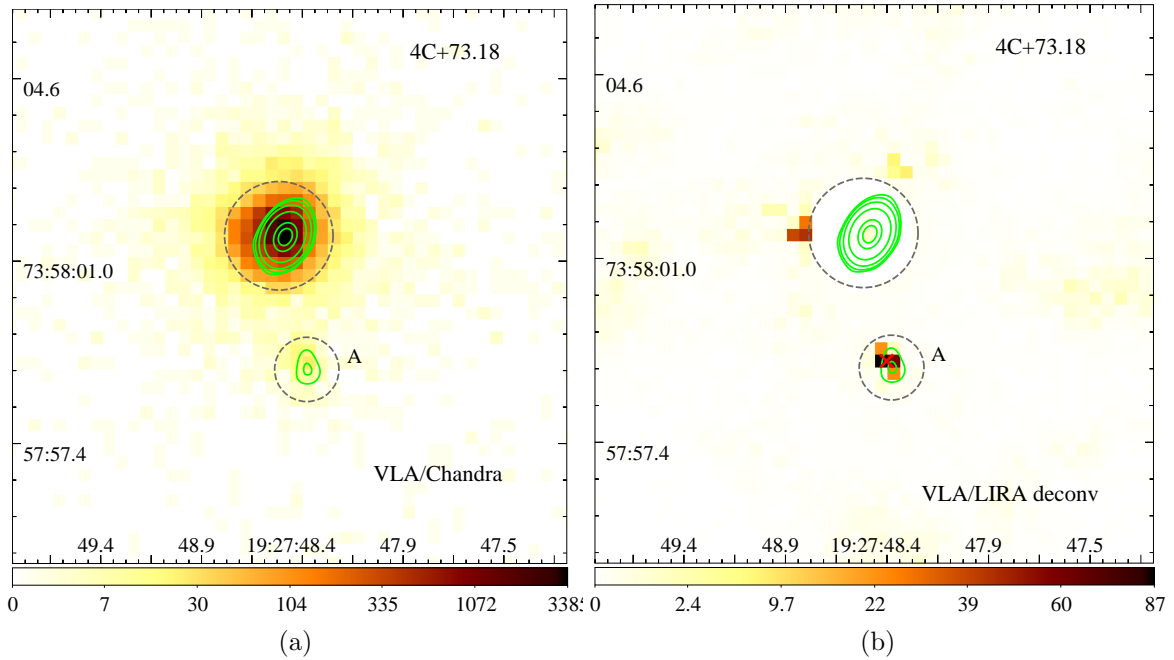


Figure 86. Same as in Fig. 1 but for 4C +73.18. The radio contours are given by 2.0, 4.0, 15.0, 100.0, 1000.0, 2000.0 mJy beam⁻¹.

western (WHS) and the eastern (EHS) hotspot with magnitudes of 0.35'' (1.84 kpc) and 0.33'' (1.73 kpc) , respectively.

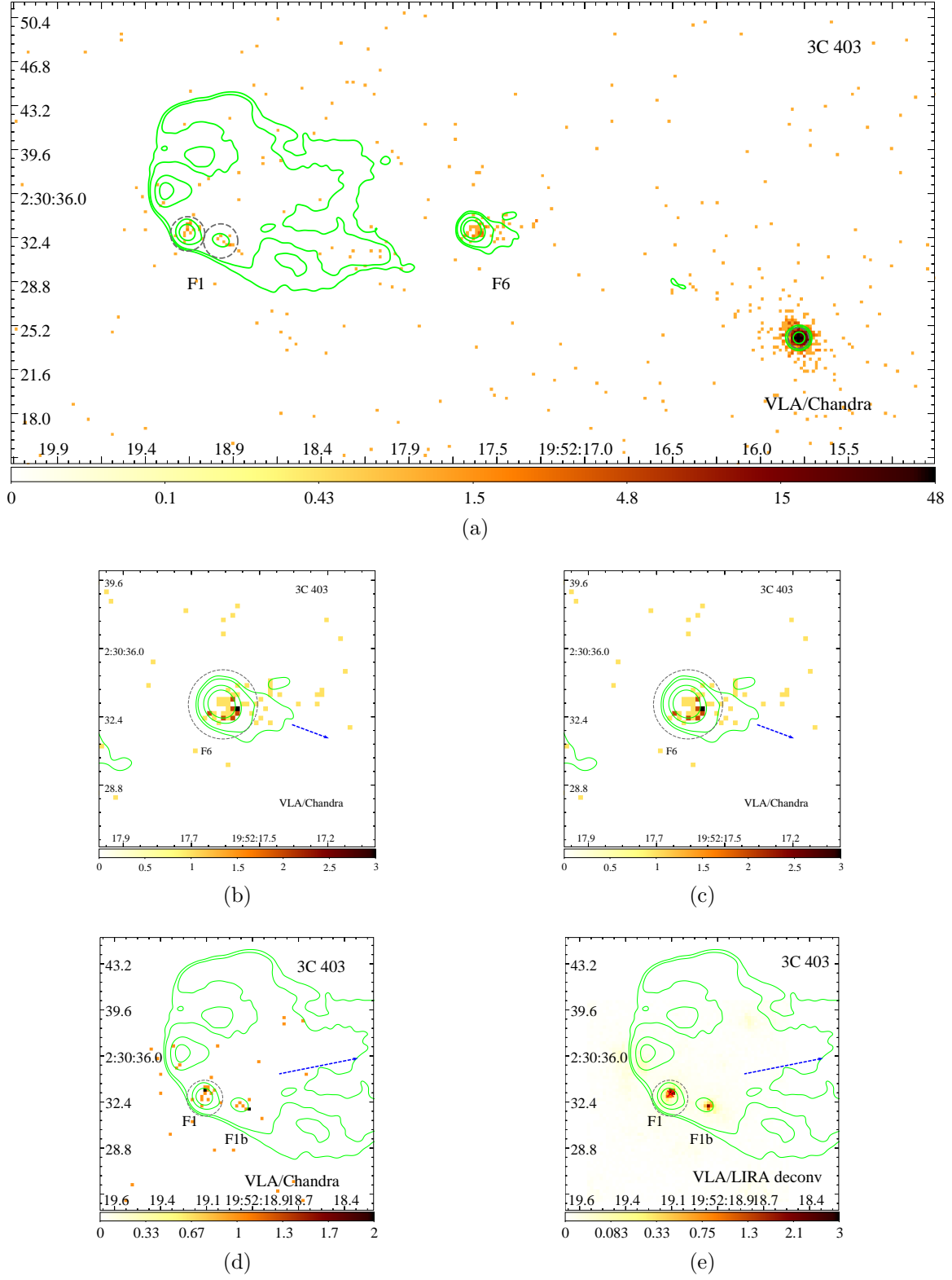


Figure 87. Same as in Fig. 1 but for 3C 403. (a) shows the full image while (b), (c) and (d),(e) show the zoomed-in regions around knot F6 and the western hotspot, respectively. The dashed-blue arrow in panels (d) and (e) indicate the tentative direction of the jet from knot F6. The radio contours are given by 0.4, 0.8, 4.0, 10.0 mJy beam⁻¹.

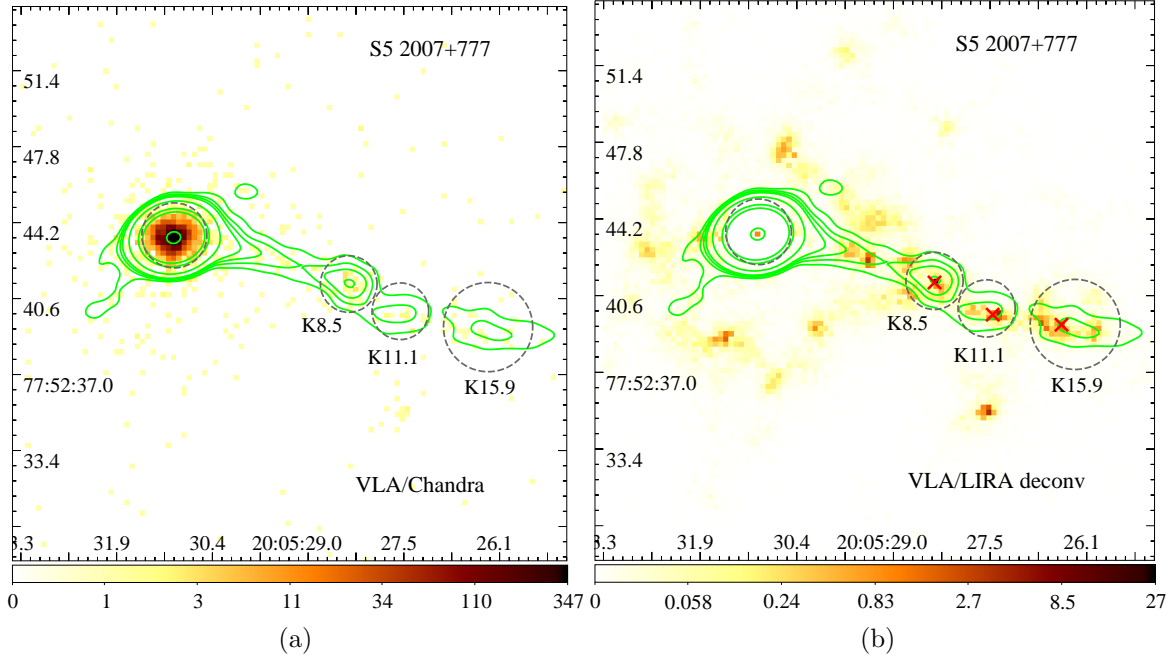


Figure 88. Same as in Fig. 1 but for S5 2007+777. The radio contours are given by 0.5, 1.0, 1.5, 2.2, 8.0, 50.0, 100.0, 1000.0 mJy beam⁻¹.

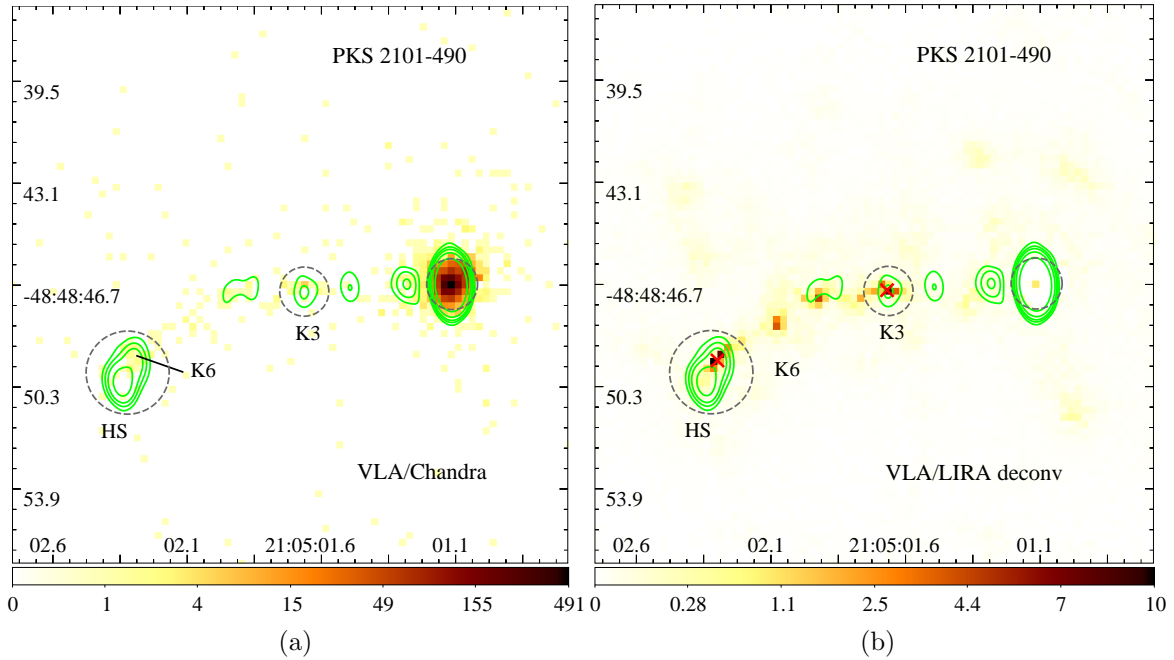


Figure 89. Same as in Fig. 1 but for PKS 2101-490. The radio contours are given by 1.0, 2.0, 3.5, 8.0, 30.0 mJy beam⁻¹.

1421-490 (Figure 71): The northern hotspot (A1) in this source is one of the brightest knots hotspots and is possibly highly-beamed (Godfrey et al. 2009). The X-ray centroid lies with 0.1'' of the radio peak.

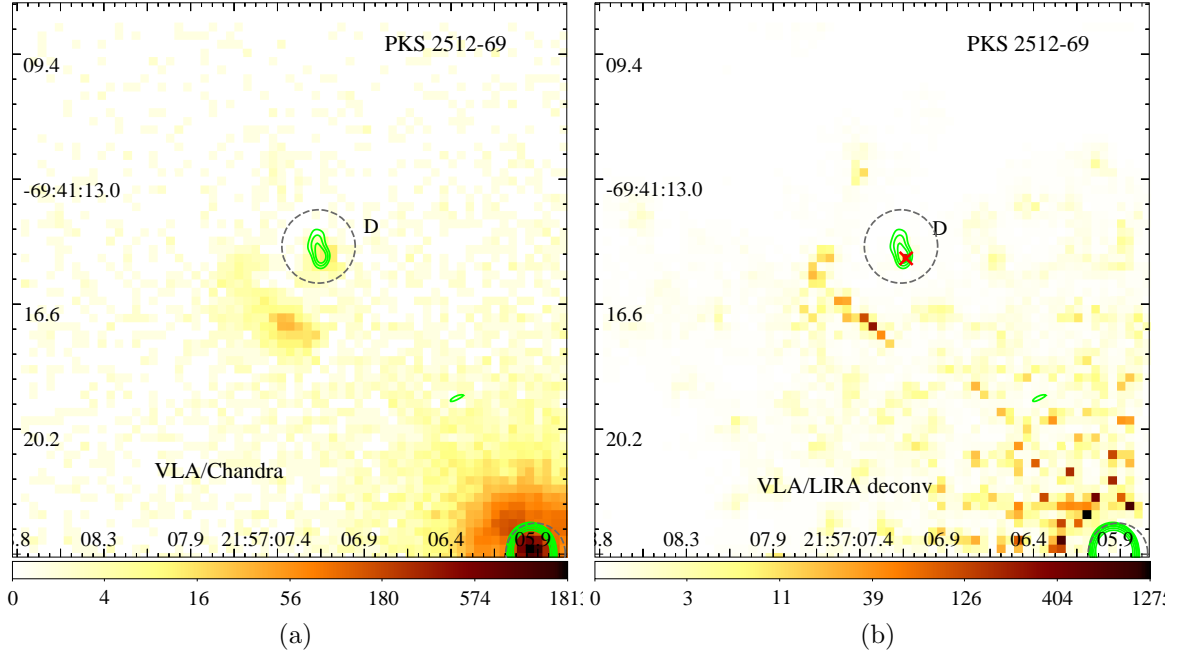


Figure 90. Same as in Fig. 1 but for PKS 2512-69. The radio contours are given by 2.0, 3.0, 4.0, 8.0, 10.0, 20.0, 40.0 mJy beam⁻¹.

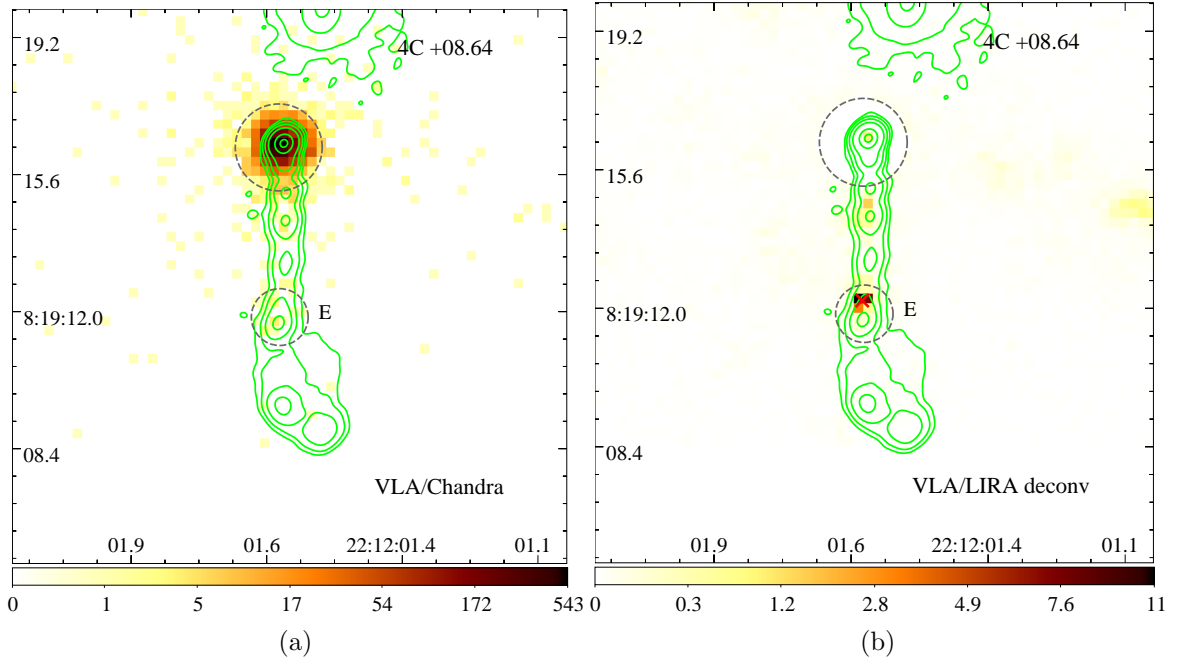


Figure 91. Same as in Fig. 1 but for 4C +08.64. The radio contours are given by 0.7, 2.0, 6.0, 20.0, 100.0, 200.0 mJy beam⁻¹.

3C 303 (Figure 72): This is an FR II source. The radio image shows a knotty jet to the west. Knots A, B and C show 0.46'' (1.15 kpc) , 0.33'' (0.82 kpc) ,

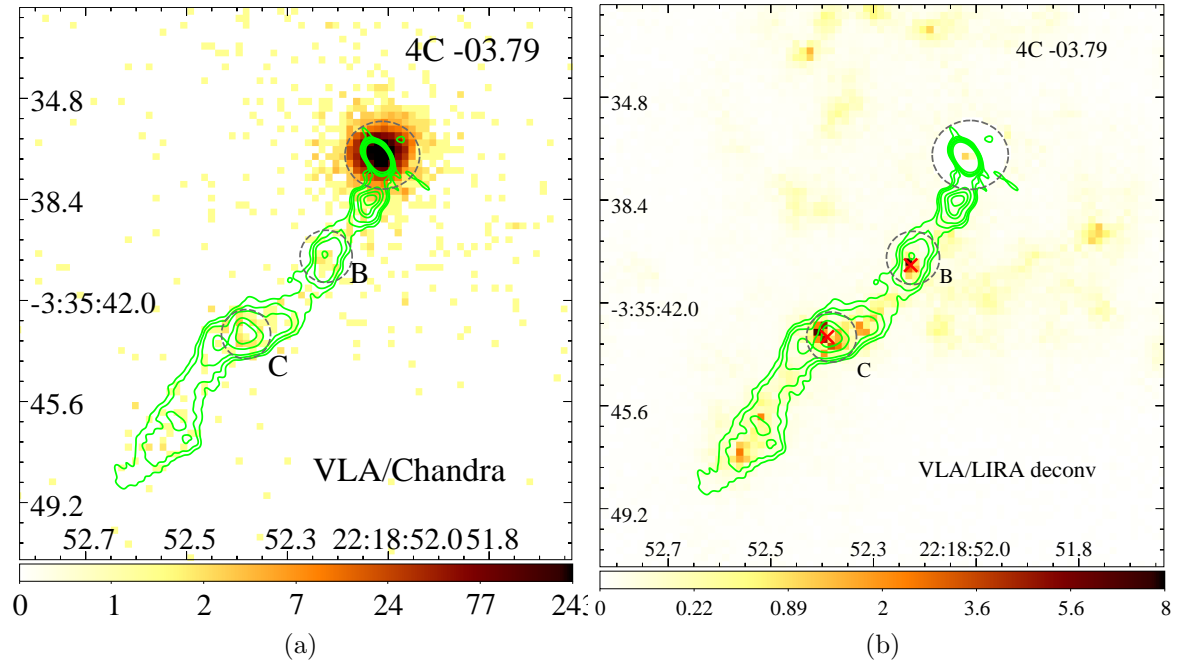


Figure 92. Same as in Fig. 1 but for 4C -03.79. The radio contours are given by 0.1, 0.2, 0.4, 8.0, 1.2, 2.0, 3.0 mJy beam⁻¹.

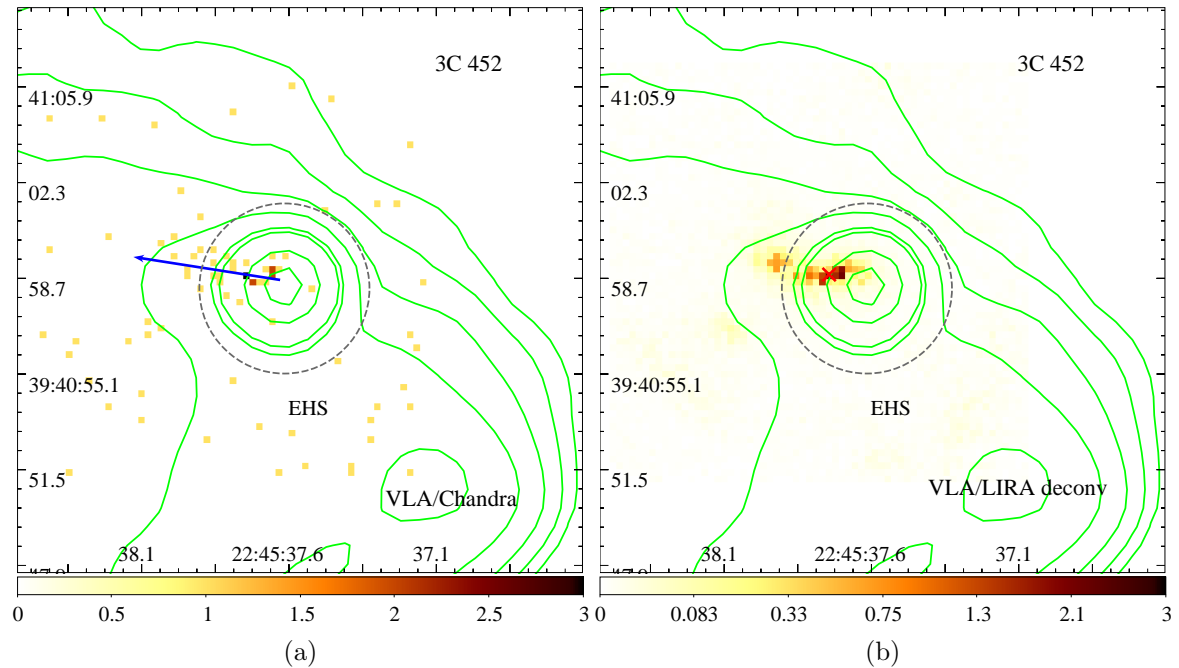


Figure 93. Same as in Fig. 1 but for 3C 452. The radio contours are given by 0.5, 1.0, 2.0, 4.0, 8.0, 10.0, 20.0, 30.0, 40.0 mJy beam⁻¹.

0.46'' (1.15 kpc) Xf-type offsets respectively. The jet makes a sharp bend to the north at HS-a showing a Co-s-type offset.

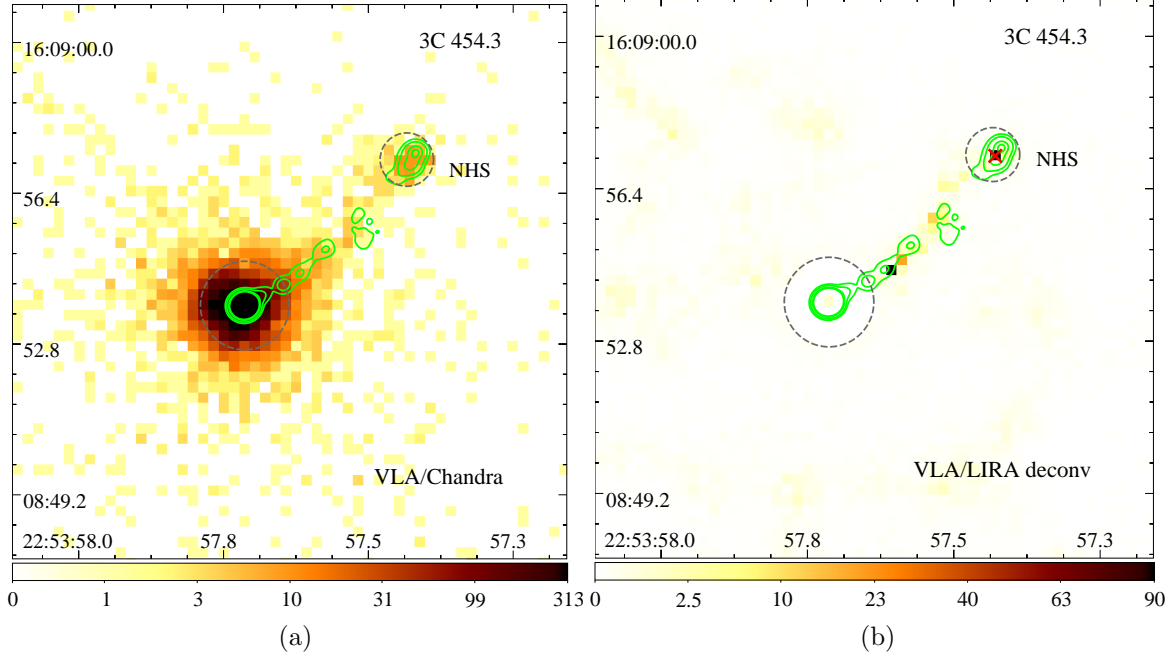


Figure 94. Same as in Fig. 1 but for 3C 454.3. The radio contours are given by 1.0, 4.0, 20.0, 40.0 mJy beam⁻¹.

PKS 1510-089 (Figure 73): This is a CDQ. Knot B shows a Co-s-type offset. We exclude the rest of the jet from offset analysis due to unclear spatial correlation between the X-ray and the radio structures.

3C 325 (Figure 74): This is a double-lobed FR II source oriented in the northeast-southwest direction. We detect a Co-s-type offset in the northern hotspot (NHS). The southern hotspot shows a double-peaked structure aligned roughly in the north-south direction and the southern peak shows a Co-s-type offset.

4C +00.58 (Figure 75): This is an LDQ. The radio image shows a knotty jet to the northwest. The jet bends twice to the northwest at knots C and D, possibly produced by jet-precession (Hodges-Kluck et al. 2010). Knot C shows a 0.21'' (0.23 kpc) Xf-type offset while knot D shows a Co-s-type offset.

3C 330 (Figure 76): This is an FR II source. In the NHS region, the jet makes a sharp turn to the southwest before terminating in the hotspot showing a 0.27'' (1.73 kpc) Xf-type offset.

4C +15.55 (Figure 77): This is a quasar. The radio image shows a faint jet to the southwest making a southerly bend at knot C. This knot shows a Co-s-type offset. The jet terminates in the southern hotspot where we detect a 0.291'' (2.52 kpc) Xf-type offset.

3C346 (Figure 78): This is an FR I source. The jet turns from the southwest to the northwest at knot B and shows a $0.22''$ (0.6 kpc) Xf-type offset.

3C 345 (Figure 79): This is a CDQ. The radio image shows a knotty jet to the northeast. The inner knots are undetected in the deconvolved images due to their proximity to the core. Knot D shows a Co-s-type offset while the northern hotspot NHS shows a $0.17''$ (1.12 kpc) Xf-type offset.

4C +69.21 (Figure 80): This is a CDQ. The radio image shows a knotty jet curving to the southeast. Knots C and D show Co-s-type offsets.

3C 351 (Figure 81): This is an FR II source. The northern lobe shows a double-peaked hotspot structure. Both the hotspots, J and L, show offsets of $0.36''$ (1.84 kpc) and $0.33''$ (1.68 kpc), respectively. However, due to the uncertain direction of the jet, the nature of these offsets remain ambiguous.

1800+440 (Figure 82): This is a CDQ. The radio image shows a knotty jet curving from the southeast to the east but without an X-ray counterpart. The jet terminates in the eastern hotspot (EHS) with a Co-s-type offset.

4C +56.27 (Figure 83): This is a newly identified X-ray jet (Marshall et al. 2018). The radio map shows an inner jet to the south of core that bends to the west at knot B. We find no offset in this knot.

3C 380 (Figure 84): The radio map shows a bright extended structure to the northwest of the core, while the deconvolved X-ray image shows a bright X-ray peak at the terminus of the jet, coincident with a radio peak. While it is unclear whether this structure represents a knot or a hotspot, we tentatively include it in our sample as a hotspot due to its location at the tip of the jet.

1849+670 (Figure 85): This is a hybrid blazar with an FR I jet to the north. The jet sharply turns to the east at knot A. Although we find a $0.39''$ (2.71 kpc) offset in knot A, the position angle of the offset lies perpendicular to the direction of the jet and the X-ray centroid closer lies to the edge of the radio knot. Hence, we label this offset as ambiguous. The jet returns to the northward direction after knot A, where we detect another X-ray knot, C, with a Co-s-type offset.

4C +73.18 (Figure 86): This is a CDQ. The radio image shows a knot, A, with a bright X-ray counterpart. Lower-frequency images presented in Sambruna et al. (2004) reveal a bend at this knot. Knot A shows a $0.24''$ (1.06 kpc) Xf-type offset.

3C 403 (Figure 87): This is an FR II source with a one-sided jet to the northwest. The inner knot, F6, shows a $0.48''$ (0.54 kpc) Xf-type offset. The western radio lobe shows a north-south oriented double-peaked hotspot structure with the southern peak, F1, showing significant X-ray emission. F1, along with a fainter knot F1b, located downstream of F1 along the tentative direction of the jet, show $0.30''$ (0.34 kpc) and $0.36''$ (0.41 kpc) Xf-type offsets, respectively.

S5 2007+777 (Figure 88): This is a BL Lac object. Knot K8.5 shows a Co-s-type offset. The jet slightly bends to the southeast at knot K11.1 that shows a $0.529''$ (2.54 kpc) Rf-type offset while knot 15.9, which lies further down the jet, shows a $0.77''$ (3.7 kpc) Xf-type offset.

PKS 2101-490 (Figure 89): We exclude all knots except K3 due to lack of clear X-ray/Radio correlation. K3 shows no offset while the X-rays peak $0.83''$ (6.72 kpc) upstream of the radio peak, while coincident with a faint radio peak K6.

PKS 2152-69 (Figure 90): This is an FR II source with a one-sided jet to the northwest. The jet interacts with a high-ionization cloud at knot D (Worrall et al. 2012). This knot shows a $0.16''$ ($9 \cdot 10^{-2}$ kpc) Xf-type offset.

4C +08.64 (Figure 91): This is a CDQ with a one-sided jet to the south. The jet bends to the southwest at knot E where the X-rays centroid lies $0.48''$ (2.85 kpc) upstream of its radio peak.

4C -03.79 (Figure 92): This is a hybrid source with a FR I morphology to the south and an FR II to the north. The radio jet is detected on the southern side. Knot B shows a $0.37''$ (2.89 kpc) Rf-type offset. The jet bends to the east at knot C and shows a Co-s-type offset.

3C 452 (Figure 93): This is an FR II source with the X-rays detected in the western hotspot (WHS). The X-ray image shows an extended structure contrary to a point-like appearance in the radio. We find a $1.37''$ (2.06 kpc) Xf-type offset in WHS.

3C 454.3 (Figure 94): This is a well-studied blazar. All the knots in the jet are excluded from offset analysis due to their close separation ($< 1''$). We find a $0.26''$ (2 kpc) Xf-type offset in the northern hotspot (NHS).

ACKNOWLEDGMENTS

We acknowledge financial support from the National Science Foundation under Grant No. 1714380 and NASA Astrophysics Data Analysis Program Grant No. 80NSSC21K0639.

The scientific results reported in this article are based in part on observations made by the Chandra X-ray Observatory and data obtained from the Chandra Data Archive. This research has made use of software provided by the Chandra X-ray Center (CXC) in the application packages CIAO, ChIPS, and Sherpa. The National Radio Astronomy Observatory is a facility of the National Science Foundation operated under cooperative agreement by Associated Universities, Inc. The Australia Telescope Compact Array is part of the Australia Telescope National Facility which is funded by the Australian Government for operation as a National Facility managed by CSIRO. We acknowledge the Gomeroi people as the traditional owners of the Observatory site.

Facilities: VLA, EVLA, CXO, ATCA

Software: CIAO (Fruscione et al. 2006), Sherpa (Freeman et al. 2001, Doe et al. 2007, Burke et al. 2020), ChIPS (Germain et al. 2006), MIRIAD (Sault et al. 1995), CASA (McMullin et al. 2007), ds9 (Joye et al. 2003), LIRA (Esch et al. 2004, Connors et al. 2007, Connors et al. 2011, Stein et al. 2015)

REFERENCES

- | | |
|--|--|
| <p>Aldcroft, T. L., Siemiginowska, A., Elvis, M., et al. 2003, ApJ, 597, 751, doi: 10.1086/378640</p> <p>Atoyan, A., & Dermer, C. D. 2004, The Astrophysical Journal, 613, 151</p> <p>Avachat, S. S., Perlman, E. S., Adams, S. C., et al. 2016, The Astrophysical Journal, 832, 3</p> <p>Bai, J. M., & Lee, M. G. 2003, The Astrophysical Journal Letters, 585, L113</p> <p>Balmaverde, B., Capetti, A., Grandi, P., et al. 2012, Astronomy & Astrophysics, 545, A143</p> <p>Biretta, J., Stern, C., & Harris, D. 1991, The Astronomical Journal, 101, 1632</p> <p>Birkinshaw, M., Worrall, D., & Hardcastle, M. 2002, Monthly Notices of the Royal Astronomical Society, 335, 142</p> <p>Blandford, R., & Königl, A. 1979, The Astrophysical Journal, 232, 34</p> | <p>Blandford, R., Meier, D., & Readhead, A. 2019, Annual Review of Astronomy and Astrophysics, 57, 467</p> <p>Bliss, A. F., Worrall, D. M., Birkinshaw, M., Murray, S. S., & Tananbaum, H. 2009, ApJ, 698, 1061, doi: 10.1088/0004-637X/698/2/1061</p> <p>Blundell, K. M., & Fabian, A. 2011, Monthly Notices of the Royal Astronomical Society, 412, 705</p> <p>Bondi, M., Brunetti, G., Comastri, A., & Setti, G. 2004, MNRAS, 354, L43, doi: 10.1111/j.1365-2966.2004.08398.x</p> <p>Breiding, P., Meyer, E. T., Georganopoulos, M., et al. 2017, The Astrophysical Journal, 849, 95</p> <p>Bridle, A., Perley, R., & Henriksen, R. 1986, The Astronomical Journal, 92, 534</p> <p>Bridle, A. H., Fomalont, E. B., Byrd, G. G., & Valtonen, M. J. 1989, The Astronomical Journal, 97, 674</p> |
|--|--|

- Bridle, A. H., Hough, D. H., Lonsdale, C. J., Burns, J. O., & Laing, R. A. 1994, *The Astronomical Journal*, 108, 766
- Bridle, A. H., & Perley, R. A. 1984, *Annual review of astronomy and astrophysics*, 22, 319
- Brunetti, G., Bondi, M., Comastri, A., et al. 2001, *ApJL*, 561, L157, doi: [10.1086/324764](https://doi.org/10.1086/324764)
- Brunetti, G., Bondi, M., Comastri, A., & Setti, G. 2002, *A&A*, 381, 795, doi: [10.1051/0004-6361:20011462](https://doi.org/10.1051/0004-6361:20011462)
- Butcher, H. R., Van Breugel, W., Miley, G. K., et al. 1980, *Astrophysical Journal*, 235, 749
- Cara, M., Perlman, E. S., Uchiyama, Y., et al. 2013, *The Astrophysical Journal*, 773, 186
- Celotti, A., Ghisellini, G., & Chiaberge, M. 2001, *Monthly Notices of the Royal Astronomical Society*, 321, L1
- Chartas, G., Gupta, V., Garmire, G., et al. 2002, *The Astrophysical Journal*, 565, 96
- Chartas, G., Worrall, D. M., Birkinshaw, M., et al. 2000, *The Astrophysical Journal*, 542, 655
- Cheung, C. C., Stawarz, L., & Siemiginowska, A. 2006, *The Astrophysical Journal*, 650, 679–692, doi: [10.1086/506908](https://doi.org/10.1086/506908)
- Cheung, C. C., Stawarz, L., Siemiginowska, A., et al. 2012, *The Astrophysical Journal*, 756, L20, doi: [10.1088/2041-8205/756/1/120](https://doi.org/10.1088/2041-8205/756/1/120)
- Chiaberge, M., Gilli, R., Macchetto, F. D., Sparks, W. B., & Capetti, A. 2003, *The Astrophysical Journal*, 582, 645
- Clarke, D. A., Bridle, A. H., Burns, J. O., Perley, R. A., & Norman, M. L. 1992, *The Astrophysical Journal*, 385, 173
- Clautice, D., Perlman, E. S., Georganopoulos, M., et al. 2016, *Astrophys. J.*, 826, 109, doi: [10.3847/0004-637X/826/2/109](https://doi.org/10.3847/0004-637X/826/2/109)
- Comastri, A., Brunetti, G., Dallacasa, D., et al. 2003, *MNRAS*, 340, L52, doi: [10.1046/j.1365-8711.2003.06561.x](https://doi.org/10.1046/j.1365-8711.2003.06561.x)
- Connor, T., Bañados, E., Stern, D., et al. 2021, *The Astrophysical Journal*, 911, 120
- Connor, T., Bañados, E., Stern, D., et al. 2021, *ApJ*, 911, 120, doi: [10.3847/1538-4357/abe710](https://doi.org/10.3847/1538-4357/abe710)
- Conway, J., & Murphy, D. 1993, *The Astrophysical Journal*, 411, 89
- Crawford, C., & Fabian, A. 2003, *Monthly Notices of the Royal Astronomical Society*, 339, 1163
- Davis, J. E., Bautz, M. W., Dewey, D., et al. 2012, in *Society of Photo-Optical Instrumentation Engineers (SPIE) Conference Series*, Vol. 8443, *Space Telescopes and Instrumentation 2012: Ultraviolet to Gamma Ray*, ed. T. Takahashi, S. S. Murray, & J.-W. A. den Herder, 84431A, doi: [10.1117/12.926937](https://doi.org/10.1117/12.926937)
- Dermer, C. D. 1995, *The Astrophysical Journal*, 446, L63
- Dermer, C. D., & Atoyan, A. 2004, *The Astrophysical Journal Letters*, 611, L9
- Donahue, M., Daly, R. A., & Horner, D. J. 2003, *The Astrophysical Journal*, 584, 643
- Drouart, G., De Breuck, C., Vernet, J., et al. 2012, *Astronomy & Astrophysics*, 548, A45
- Erlund, M., Fabian, A., Blundell, K. M., Crawford, C., & Hirst, P. 2010, *Monthly Notices of the Royal Astronomical Society*, 404, 629
- Erlund, M., Fabian, A., Blundell, K. M., Moss, C., & Ballantyne, D. 2007, *Monthly Notices of the Royal Astronomical Society*, 379, 498
- Erlund, M. C., Fabian, A., Blundell, K. M., Celotti, A., & Crawford, C. 2006, *Monthly Notices of the Royal Astronomical Society*, 371, 29
- Erlund, M. C., Fabian, A. C., & Blundell, K. M. 2008, *MNRAS*, 386, 1774, doi: [10.1111/j.1365-2966.2008.13209.x](https://doi.org/10.1111/j.1365-2966.2008.13209.x)
- Erlund, M. C., Fabian, A. C., Blundell, K. M., Crawford, C. S., & Hirst, P. 2010, *MNRAS*, 404, 629, doi: [10.1111/j.1365-2966.2010.16304.x](https://doi.org/10.1111/j.1365-2966.2010.16304.x)

- Esch, D. N., Connors, A., Karovska, M., & van Dyk, D. A. 2004, *The Astrophysical Journal*, 610, 1213
- Evans, D. A., Hardcastle, M., Croston, J., Worrall, D., & Birkinshaw, M. 2005, *Monthly Notices of the Royal Astronomical Society*, 359, 363
- Evans, D. A., Fong, W.-F., Hardcastle, M. J., et al. 2008, *ApJ*, 675, 1057, doi: [10.1086/527410](https://doi.org/10.1086/527410)
- Fabian, A. 2012, *Annual Review of Astronomy and Astrophysics*, 50, 455, doi: [10.1146/annurev-astro-081811-125521](https://doi.org/10.1146/annurev-astro-081811-125521)
- Fabian, A. C., Celotti, A., & Johnstone, R. M. 2003a, *MNRAS*, 338, L7, doi: [10.1046/j.1365-8711.2003.06111.x](https://doi.org/10.1046/j.1365-8711.2003.06111.x)
- Fabian, A. C., Sanders, J. S., Crawford, C. S., & Ettori, S. 2003b, *MNRAS*, 341, 729, doi: [10.1046/j.1365-8711.2003.06394.x](https://doi.org/10.1046/j.1365-8711.2003.06394.x)
- Fanaroff, B. L., & Riley, J. M. 1974, *Monthly Notices of the Royal Astronomical Society*, 167, 31P, doi: [10.1093/mnras/167.1.31P](https://doi.org/10.1093/mnras/167.1.31P)
- Freeman, P., Doe, S., & Siemiginowska, A. 2001, in *Society of Photo-Optical Instrumentation Engineers (SPIE) Conference Series*, Vol. 4477, *Astronomical Data Analysis*, ed. J.-L. Starck & F. D. Murtagh, 76–87, doi: [10.1117/12.447161](https://doi.org/10.1117/12.447161)
- Fruscione, A., McDowell, J. C., Allen, G. E., et al. 2006, *Society of Photo-Optical Instrumentation Engineers (SPIE) Conference Series*, Vol. 6270, *CIAO: Chandra's data analysis system*, 62701V, doi: [10.1117/12.671760](https://doi.org/10.1117/12.671760)
- Gelbord, J. M., Marshall, H., Worrall, D., et al. 2005, *The Astrophysical Journal Letters*, 632, L75
- Georganopoulos, M., Perlman, E. S., Kazanas, D., & McEnery, J. 2006, *The Astrophysical Journal Letters*, 653, L5
- Gilmour, R., Best, P., & Almaini, O. 2009, *Monthly Notices of the Royal Astronomical Society*, 392, 1509
- Godfrey, L., Lovell, J., Burke-Spolaor, S., et al. 2012, *The Astrophysical Journal Letters*, 758, L27
- Godfrey, L. E. H., Bicknell, G. V., Lovell, J. E. J., et al. 2009, *ApJ*, 695, 707, doi: [10.1088/0004-637X/695/1/707](https://doi.org/10.1088/0004-637X/695/1/707)
- . 2012, *ApJ*, 755, 174, doi: [10.1088/0004-637X/755/2/174](https://doi.org/10.1088/0004-637X/755/2/174)
- Hardcastle, M., Birkinshaw, M., & Worrall, D. 2001, *Monthly Notices of the Royal Astronomical Society*, 326, 1499
- Hardcastle, M., Worrall, D., Birkinshaw, M., Laing, R., & Bridle, A. 2002, *Monthly Notices of the Royal Astronomical Society*, 334, 182
- Hardcastle, M. J. 2006, *Monthly Notices of the Royal Astronomical Society*, 366, 1465
- Hardcastle, M. J., Birkinshaw, M., Cameron, R. A., et al. 2002, *ApJ*, 581, 948, doi: [10.1086/344409](https://doi.org/10.1086/344409)
- Hardcastle, M. J., Birkinshaw, M., & Worrall, D. M. 2001, *MNRAS*, 326, 1499, doi: [10.1111/j.1365-2966.2001.04699.x](https://doi.org/10.1111/j.1365-2966.2001.04699.x)
- Hardcastle, M. J., Croston, J. H., & Kraft, R. P. 2007, *ApJ*, 669, 893, doi: [10.1086/521696](https://doi.org/10.1086/521696)
- Hardcastle, M. J., Harris, D. E., Worrall, D. M., & Birkinshaw, M. 2004, *ApJ*, 612, 729, doi: [10.1086/422808](https://doi.org/10.1086/422808)
- Hardcastle, M. J., Massaro, F., & Harris, D. E. 2010, *Monthly Notices of the Royal Astronomical Society*, 401, 2697, doi: [10.1111/j.1365-2966.2009.15855.x](https://doi.org/10.1111/j.1365-2966.2009.15855.x)
- Hardcastle, M. J., Sakelliou, I., & Worrall, D. 2005a, *Monthly Notices of the Royal Astronomical Society*, 359, 1007
- Hardcastle, M. J., Worrall, D., Birkinshaw, M., Laing, R., & Bridle, A. 2005b, *Monthly Notices of the Royal Astronomical Society*, 358, 843
- Hardcastle, M. J., Worrall, D. M., Kraft, R. P., et al. 2003, *The Astrophysical Journal*, 593, 169–183, doi: [10.1086/376519](https://doi.org/10.1086/376519)
- Hardcastle, M. J., Massaro, F., Harris, D. E., et al. 2012, *MNRAS*, 424, 1774, doi: [10.1111/j.1365-2966.2012.21247.x](https://doi.org/10.1111/j.1365-2966.2012.21247.x)

- Hardcastle, M. J., Lenc, E., Birkinshaw, M., et al. 2016, *MNRAS*, 455, 3526, doi: [10.1093/mnras/stv2553](https://doi.org/10.1093/mnras/stv2553)
- Harris, D., Carilli, C., & Perley, R. 1994, *Nature*, 367, 713
- Harris, D., Finoguenov, A., Bridle, A., Hardcastle, M., & Laing, R. 2002a, *The Astrophysical Journal*, 580, 110
- Harris, D., Krawczynski, H., & Taylor, G. 2002b, *The Astrophysical Journal*, 578, 60
- Harris, D., Mossman, A., & Walker, R. 2004a, *The Astrophysical Journal*, 615, 161
- . 2004b, *The Astrophysical Journal*, 615, 161
- Harris, D. E., & Krawczynski, H. 2007, in *Revista Mexicana de Astronomia y Astrofisica Conference Series*, Vol. 27, *Revista Mexicana de Astronomia y Astrofisica*, vol. 27, 188. <https://arxiv.org/abs/astro-ph/0604527>
- Harris, D. E., Lee, N. P., Schwartz, D. A., et al. 2017, *The Astrophysical Journal*, 846, 119, doi: [10.3847/1538-4357/aa845c](https://doi.org/10.3847/1538-4357/aa845c)
- Harwood, J. J., & Hardcastle, M. J. 2012, *Monthly Notices of the Royal Astronomical Society*, 423, 1368
- Hodges-Kluck, E. J., Reynolds, C. S., Miller, M. C., & Cheung, C. C. 2010, *ApJL*, 717, L37, doi: [10.1088/2041-8205/717/1/L37](https://doi.org/10.1088/2041-8205/717/1/L37)
- Hogan, B. S., Lister, M. L., Kharb, P., Marshall, H. L., & Cooper, N. J. 2011, *ApJ*, 730, 92, doi: [10.1088/0004-637X/730/2/92](https://doi.org/10.1088/0004-637X/730/2/92)
- Ighina, L., Moretti, A., Tavecchio, F., et al. 2022, *A&A*, 659, A93, doi: [10.1051/0004-6361/202142676](https://doi.org/10.1051/0004-6361/202142676)
- Jester, S. 2008, *Monthly Notices of the Royal Astronomical Society*, 389, 1507
- Jester, S., Harris, D., Marshall, H. L., & Meisenheimer, K. 2006, *The Astrophysical Journal*, 648, 900
- Jimenez-Gallardo, A., Massaro, F., Prieto, M. A., et al. 2020, *ApJS*, 250, 7, doi: [10.3847/1538-4365/aba5a0](https://doi.org/10.3847/1538-4365/aba5a0)
- Jorstad, S. G., & Marscher, A. P. 2004, *ApJ*, 614, 615, doi: [10.1086/423800](https://doi.org/10.1086/423800)
- Jorstad, S. G., & Marscher, A. P. 2006, *Astronomische Nachrichten: Astronomical Notes*, 327, 227
- Kataoka, J., Edwards, P., Georganopoulos, M., Takahara, F., & Wagner, S. 2003, *Astronomy & Astrophysics*, 399, 91
- Kataoka, J., Leahy, J. P., Edwards, P. G., et al. 2003, *A&A*, 410, 833, doi: [10.1051/0004-6361:20031343](https://doi.org/10.1051/0004-6361:20031343)
- Kataoka, J., & Stawarz, L. 2005, *The Astrophysical Journal*, 622, 797
- Kataoka, J., Harris, D., Siemiginowska, A., et al. 2008, *The Astrophysical Journal*, 685, 839
- Kaufmann, S., Wagner, S., & Tibolla, O. 2013, *The Astrophysical Journal*, 776, 68
- Keel, W. C., White, III, R. E., Owen, F. N., & Ledlow, M. J. 2006, *AJ*, 132, 2233, doi: [10.1086/508340](https://doi.org/10.1086/508340)
- Keenan, M., Meyer, E. T., Georganopoulos, M., Reddy, K., & French, O. J. 2021, *MNRAS*, 505, 4726, doi: [10.1093/mnras/stab1182](https://doi.org/10.1093/mnras/stab1182)
- Kharb, P., Lister, M. L., Marshall, H. L., & Hogan, B. S. 2012, *ApJ*, 748, 81, doi: [10.1088/0004-637X/748/2/81](https://doi.org/10.1088/0004-637X/748/2/81)
- Komissarov, S., & Falle, S. 1998, *Monthly Notices of the Royal Astronomical Society*, 297, 1087
- Konar, C., & Hardcastle, M. J. 2013, *Monthly Notices of the Royal Astronomical Society*, 436, 1595, doi: [10.1093/mnras/stt1676](https://doi.org/10.1093/mnras/stt1676)
- Kraft, R., Forman, W., Jones, C., et al. 2000, *The Astrophysical Journal Letters*, 531, L9
- Kraft, R. P., Birkinshaw, M., Hardcastle, M. J., et al. 2007, *ApJ*, 659, 1008, doi: [10.1086/512766](https://doi.org/10.1086/512766)
- Kraft, R. P., Hardcastle, M. J., Worrall, D. M., & Murray, S. S. 2005, *ApJ*, 622, 149, doi: [10.1086/427822](https://doi.org/10.1086/427822)
- Lovell, J. E. J., Tingay, S. J., Piner, B. G., et al. 2000, in *Astrophysical Phenomena Revealed by Space VLBI*, ed. H. Hirabayashi, P. G. Edwards, & D. W. Murphy, 215–218

- Ly, C., De Young, D. S., & Bechtold, J. 2005, *The Astrophysical Journal*, 618, 609
- Marchenko, V., Harris, D. E., Ostrowski, M., et al. 2017, *The Astrophysical Journal*, 844, 11, doi: [10.3847/1538-4357/aa755d](https://doi.org/10.3847/1538-4357/aa755d)
- Marin, F., & Antonucci, R. 2016, *The Astrophysical Journal*, 830, 82
- Marscher, A. P., & Jorstad, S. G. 2011, *ApJ*, 729, 26, doi: [10.1088/0004-637X/729/1/26](https://doi.org/10.1088/0004-637X/729/1/26)
- Marshall, H., Harris, D., Grimes, J., et al. 2001, *The Astrophysical Journal Letters*, 549, L167
- Marshall, H. L., Miller, B. P., Davis, D. S., et al. 2002, *The Astrophysical Journal*, 564, 683, doi: [10.1086/324396](https://doi.org/10.1086/324396)
- Marshall, H. L., Schwartz, D., Lovell, J., et al. 2005, *The Astrophysical Journal Supplement Series*, 156, 13
- Marshall, H. L., Schwartz, D. A., Lovell, J. E. J., et al. 2005, *ApJS*, 156, 13, doi: [10.1086/425578](https://doi.org/10.1086/425578)
- Marshall, H. L., Hardcastle, M. J., Birkinshaw, M., et al. 2010, *The Astrophysical Journal Letters*, 714, L213
- Marshall, H. L., Gelbord, J. M., Schwartz, D. A., et al. 2011, *The Astrophysical Journal Supplement Series*, 193, 15
- Marshall, H. L., Gelbord, J. M., Worrall, D. M., et al. 2018, *ApJ*, 856, 66, doi: [10.3847/1538-4357/aaaf66](https://doi.org/10.3847/1538-4357/aaaf66)
- Massaro, F., Harris, D., Tremblay, G., et al. 2013, *The Astrophysical Journal Supplement Series*, 206, 7
- Massaro, F., Harris, D. E., Chiaberge, M., et al. 2009, *The Astrophysical Journal*, 696, 980, doi: [10.1088/0004-637x/696/1/980](https://doi.org/10.1088/0004-637x/696/1/980)
- Massaro, F., Harris, D., Tremblay, G., et al. 2010, *The Astrophysical Journal*, 714, 589
- Massaro, F., Tremblay, G., Harris, D., et al. 2012, *The Astrophysical Journal Supplement Series*, 203, 31
- Massaro, F., Tremblay, G. R., Harris, D. E., et al. 2012, *ApJS*, 203, 31, doi: [10.1088/0067-0049/203/2/31](https://doi.org/10.1088/0067-0049/203/2/31)
- Massaro, F., Harris, D., Liuzzo, E., et al. 2015, *The Astrophysical Journal Supplement Series*, 220, 5
- Massaro, F., Missaglia, V., Stuardi, C., et al. 2018, *The Astrophysical Journal Supplement Series*, 234, 7, doi: [10.3847/1538-4365/aa8e9d](https://doi.org/10.3847/1538-4365/aa8e9d)
- Matthews, J. H., Knigge, C., & Long, K. S. 2017, *Monthly Notices of the Royal Astronomical Society*, 467, 2571
- McKeough, K., Siemiginowska, A., Cheung, C. C., et al. 2016, *The Astrophysical Journal*, 833, 123, doi: [10.3847/1538-4357/833/1/123](https://doi.org/10.3847/1538-4357/833/1/123)
- McMullin, J., Waters, B., Schiebel, D., et al. 2007, in *ASP Conf. Ser.*, Vol. 376, 127
- Mendoza, S., & Longair, M. 2001, *Monthly Notices of the Royal Astronomical Society*, 324, 149
- Meyer, E. T., & Georganopoulos, M. 2013, *The Astrophysical Journal Letters*, 780, L27
- Meyer, E. T., Georganopoulos, M., Sparks, W. B., et al. 2015, *The Astrophysical Journal*, 805, 154
- Meyer, E. T., Iyer, A. R., Reddy, K., et al. 2019, *The Astrophysical Journal*, 883, L2, doi: [10.3847/2041-8213/ab3db3](https://doi.org/10.3847/2041-8213/ab3db3)
- Meyer, E. T., Petropoulou, M., Georganopoulos, M., et al. 2018, *The Astrophysical Journal*, 860, 9, doi: [10.3847/1538-4357/aabf39](https://doi.org/10.3847/1538-4357/aabf39)
- Meyer, E. T., Petropoulou, M., Georganopoulos, M., et al. 2018, *ApJ*, 860, 9, doi: [10.3847/1538-4357/aabf39](https://doi.org/10.3847/1538-4357/aabf39)
- Meyer, E. T., Sparks, W. B., Georganopoulos, M., et al. 2016, *The Astrophysical Journal*, 818, 195
- . 2017, *Galaxies*, 5, 8
- Miller, B., & Brandt, W. N. 2009, *The Astrophysical Journal*, 695, 755
- Miller, B. P., Brandt, W. N., Gallagher, S., et al. 2006, *The Astrophysical Journal*, 652, 163
- Miller, B. P., Brandt, W. N., Gallagher, S. C., et al. 2006, *ApJ*, 652, 163, doi: [10.1086/507509](https://doi.org/10.1086/507509)

- Mullin, L., & Hardcastle, M. 2009, *Monthly Notices of the Royal Astronomical Society*, 398, 1989
- Ostrowski, M., et al. 2002, *The Astrophysical Journal*, 578, 763
- Padovani, P., Alexander, D. M., Assef, R. J., et al. 2017, *The Astronomy and Astrophysics Review*, 25, doi: [10.1007/s00159-017-0102-9](https://doi.org/10.1007/s00159-017-0102-9)
- Perlman, E. S., Clautice, D., Avachat, S., et al. 2020, *Galaxies*, 8, 71
- Perlman, E. S., Georganopoulos, M., May, E. M., & Kazanas, D. 2009, *The Astrophysical Journal*, 708, 1, doi: [10.1088/0004-637x/708/1/1](https://doi.org/10.1088/0004-637x/708/1/1)
- Perlman, E. S., Padgett, C., Georganopoulos, M., et al. 2006, *The Astrophysical Journal*, 651, 735
- Perlman, E. S., Padgett, C. A., Georganopoulos, M., et al. 2010, *ApJ*, 708, 171, doi: [10.1088/0004-637X/708/1/171](https://doi.org/10.1088/0004-637X/708/1/171)
- Perlman, E. S., Georganopoulos, M., Marshall, H. L., et al. 2011, *ApJ*, 739, 65, doi: [10.1088/0004-637X/739/2/65](https://doi.org/10.1088/0004-637X/739/2/65)
- Perlman, E. S., Georganopoulos, M., Marshall, H. L., et al. 2011, *The Astrophysical Journal*, 739, 65, doi: [10.1088/0004-637x/739/2/65](https://doi.org/10.1088/0004-637x/739/2/65)
- Pesce, J. E., Sambruna, R. M., Tavecchio, F., et al. 2001, *The Astrophysical Journal Letters*, 556, L79
- Pyrzas, S., Steenbrugge, K., & Blundell, K. 2015, *Astronomy & Astrophysics*, 574, A30
- Rawes, J., Worrall, D. M., & Birkinshaw, M. 2015, *Monthly Notices of the Royal Astronomical Society*, 452, 3064, doi: [10.1093/mnras/stv1501](https://doi.org/10.1093/mnras/stv1501)
- Razali, N. M., Wah, Y. B., et al. 2011, *Journal of statistical modeling and analytics*, 2, 21
- Reddy, K., Georganopoulos, M., & Meyer, E. T. 2021, *ApJS*, 253, 37, doi: [10.3847/1538-4365/abd8d7](https://doi.org/10.3847/1538-4365/abd8d7)
- Reynolds, C. S., & Begelman, M. C. 1997, *The Astrophysical Journal*, 487, L135, doi: [10.1086/310894](https://doi.org/10.1086/310894)
- Richstone, D., Ajhar, E., Bender, R., et al. 1998, *nature*, 395, A14
- Risaliti, G., Salvati, M., & Marconi, A. 2011, *Monthly Notices of the Royal Astronomical Society*, 411, 2223
- Russell, H., Fabian, A., Taylor, G., et al. 2012, *Monthly Notices of the Royal Astronomical Society*, 422, 590
- Salvati, M., Risaliti, G., Véron, P., & Woltjer, L. 2008, *Astronomy & Astrophysics*, 478, 121
- Sambruna, R. M., Donato, D., Cheung, C. C., Tavecchio, F., & Maraschi, L. 2008, *ApJ*, 684, 862, doi: [10.1086/589918](https://doi.org/10.1086/589918)
- Sambruna, R. M., Donato, D., Tavecchio, F., et al. 2007, *ApJ*, 670, 74, doi: [10.1086/521972](https://doi.org/10.1086/521972)
- Sambruna, R. M., Gambill, J. K., Maraschi, L., et al. 2004, *The Astrophysical Journal*, 608, 698
- Sambruna, R. M., Gambill, J. K., Maraschi, L., et al. 2004, *ApJ*, 608, 698, doi: [10.1086/383124](https://doi.org/10.1086/383124)
- Sambruna, R. M., Gambill, J. K., Maraschi, L., et al. 2004, *The Astrophysical Journal*, 608, 698–720, doi: [10.1086/383124](https://doi.org/10.1086/383124)
- Sambruna, R. M., Gliozzi, M., Donato, D., et al. 2006, *ApJ*, 641, 717, doi: [10.1086/500526](https://doi.org/10.1086/500526)
- Sambruna, R. M., Maraschi, L., Tavecchio, F., et al. 2002, *The Astrophysical Journal*, 571, 206
- Sault, R. J., Teuben, P. J., & Wright, M. C. H. 1995, in *Astronomical Society of the Pacific Conference Series*, Vol. 77, *Astronomical Data Analysis Software and Systems IV*, ed. R. A. Shaw, H. E. Payne, & J. J. E. Hayes, 433. <https://arxiv.org/abs/astro-ph/0612759>
- Scholz, F. W., & Stephens, M. A. 1987, *Journal of the American Statistical Association*, 82, 918
- Schreier, E., Feigelson, E., Delvaile, J., et al. 1979, *The Astrophysical Journal*, 234, L39
- Schwartz, D., Marshall, H., Lovell, J., et al. 2000, *The Astrophysical Journal Letters*, 540, L69

- Schwartz, D. A., Marshall, H., Lovell, J., et al. 2006, *The Astrophysical Journal Letters*, 647, L107
- Shepherd, M. C. 1997, in *Astronomical Society of the Pacific Conference Series*, Vol. 125, *Astronomical Data Analysis Software and Systems VI*, ed. G. Hunt & H. Payne, 77
- Siemiginowska, A., Bechtold, J., Aldcroft, T. L., et al. 2002, *The Astrophysical Journal*, 570, 543
- Siemiginowska, A., & Elvis, M. 1997, *The Astrophysical Journal*, 482, L9, doi: [10.1086/310673](https://doi.org/10.1086/310673)
- Siemiginowska, A., Smith, R. K., Aldcroft, T. L., et al. 2003a, *The Astrophysical Journal Letters*, 598, L15
- Siemiginowska, A., Stawarz, L., Cheung, C. C., et al. 2007, *ApJ*, 657, 145, doi: [10.1086/510898](https://doi.org/10.1086/510898)
- Siemiginowska, A., Stanghellini, C., Brunetti, G., et al. 2003b, *The Astrophysical Journal*, 595, 643
- Siemiginowska, A., Stawarz, L., Cheung, C. C., et al. 2012, *ApJ*, 750, 124, doi: [10.1088/0004-637X/750/2/124](https://doi.org/10.1088/0004-637X/750/2/124)
- Simionescu, A., Ichinohe, Y., Cheung, C., et al. 2016, *The Astrophysical Journal Letters*, 816, L15
- Singal, Ashok K., E.-m. a. 2016, *Astrophysical Journal*, 827, doi: [10.3847/0004-637X/827/1/66](https://doi.org/10.3847/0004-637X/827/1/66)
- Snios, B., Wykes, S., Nulsen, P. E. J., et al. 2019, *ApJ*, 871, 248, doi: [10.3847/1538-4357/aafaf3](https://doi.org/10.3847/1538-4357/aafaf3)
- Snios, B., Schwartz, D. A., Siemiginowska, A., et al. 2021, arXiv preprint arXiv:2102.12609
- Stanley, E. C., Kharb, P., Lister, M. L., et al. 2015, *The Astrophysical Journal*, 807, 48, doi: [10.1088/0004-637x/807/1/48](https://doi.org/10.1088/0004-637x/807/1/48)
- Stawarz, L., Sikora, M., Ostrowski, M., & Begelman, M. C. 2004, *The Astrophysical Journal*, 608, 95
- Stein, N. M., van Dyk, D. A., Kashyap, V. L., & Siemiginowska, A. 2015, *The Astrophysical Journal*, 813, 66
- Stockton, A., McGrath, E., & Canalizo, G. 2006, *The Astrophysical Journal*, 650, 706
- Stuardi, C., Missaglia, V., Massaro, F., et al. 2018, *The Astrophysical Journal Supplement Series*, 235, 32, doi: [10.3847/1538-4365/aaafcf](https://doi.org/10.3847/1538-4365/aaafcf)
- Sun, M. 2009, *ApJ*, 704, 1586, doi: [10.1088/0004-637X/704/2/1586](https://doi.org/10.1088/0004-637X/704/2/1586)
- Sun, M., Jerius, D., & Jones, C. 2005, *ApJ*, 633, 165, doi: [10.1086/452620](https://doi.org/10.1086/452620)
- Swain, M. R. 1996, PhD thesis, THE UNIVERSITY OF ROCHESTER.
- Swain, M. R. 1997, PhD thesis
- Swain, M. R., Bridle, A. H., & Baum, S. A. 1998, *The Astrophysical Journal Letters*, 507, L29
- Tavecchio, F. 2021a, *Monthly Notices of the Royal Astronomical Society*, 501, 6199
- . 2021b, *Galaxies*, 9, 37
- Tavecchio, F., Maraschi, L., Sambruna, R. M., & Urry, C. M. 2000, *The Astrophysical Journal Letters*, 544, L23
- Tavecchio, F., Maraschi, L., Wolter, A., et al. 2007, *The Astrophysical Journal*, 662, 900
- Uchiyama, Y., Urry, C. M., Coppi, P., et al. 2007, *ApJ*, 661, 719, doi: [10.1086/518089](https://doi.org/10.1086/518089)
- Urpín, V. 2006, *Astronomy & Astrophysics*, 455, 779
- Wardle, J., & Aaron, S. 1997, *Monthly Notices of the Royal Astronomical Society*, 286, 425
- Weisskopf, M. C., Ramsey, B., O'Dell, S. L., et al. 2016, *Results in Physics*, 6, 1179
- Wilkes, B. J., Lal, D. V., Worrall, D. M., et al. 2012, *ApJ*, 745, 84, doi: [10.1088/0004-637X/745/1/84](https://doi.org/10.1088/0004-637X/745/1/84)
- Wilkes, B. J., Kuraszkiewicz, J., Haas, M., et al. 2013, *The Astrophysical Journal*, 773, 15
- Wilson, A., Young, A., & Shopbell, P. 2000, *The Astrophysical Journal Letters*, 544, L27
- Wilson, A. S., & Yang, Y. 2002, *ApJ*, 568, 133, doi: [10.1086/338887](https://doi.org/10.1086/338887)

- Wilson, A. S., Young, A. J., & Shopbell, P. L. 2001, *ApJ*, 547, 740, doi: [10.1086/318412](https://doi.org/10.1086/318412)
- Worrall, D. 2009, *The Astronomy and Astrophysics Review*, 17, 1
- Worrall, D., Birkinshaw, M., & Hardcastle, M. 2001, *Monthly Notices of the Royal Astronomical Society*, 326, L7
- Worrall, D., Birkinshaw, M., & Young, A. 2016, *Monthly Notices of the Royal Astronomical Society*, 458, 174
- Worrall, D., Birkinshaw, M., Young, A., et al. 2012, *Monthly Notices of the Royal Astronomical Society*, 424, 1346
- Worrall, D. M., & Birkinshaw, M. 2005, *MNRAS*, 360, 926, doi: [10.1111/j.1365-2966.2005.09082.x](https://doi.org/10.1111/j.1365-2966.2005.09082.x)
- Worrall, D. M., Birkinshaw, M., & Hardcastle, M. 2003, *Monthly Notices of the Royal Astronomical Society*, 343, L73
- Worrall, D. M., Birkinshaw, M., & Hardcastle, M. J. 2001, *MNRAS*, 326, L7, doi: [10.1046/j.1365-8711.2001.04752.x](https://doi.org/10.1046/j.1365-8711.2001.04752.x)
- Worrall, D. M., Birkinshaw, M., Marshall, H. L., et al. 2020, *MNRAS*, 497, 988, doi: [10.1093/mnras/staa1975](https://doi.org/10.1093/mnras/staa1975)
- Worrall, D. M., Birkinshaw, M., Young, A. J., et al. 2012, *MNRAS*, 424, 1346, doi: [10.1111/j.1365-2966.2012.21320.x](https://doi.org/10.1111/j.1365-2966.2012.21320.x)
- Yong, S. Y., Webster, R. L., King, A. L., et al. 2020, *Monthly Notices of the Royal Astronomical Society*, 491, 1320
- Yuill, R. S. 1971, *Geografiska Annaler. Series B, Human Geography*, 53, 28. <http://www.jstor.org/stable/490885>
- Zhu, S. F., Brandt, W. N., Wu, J., Garmire, G. P., & Miller, B. P. 2019, *MNRAS*, 482, 2016, doi: [10.1093/mnras/sty2832](https://doi.org/10.1093/mnras/sty2832)